Finite Temperature Effects in the Condensates of Dilute Atomic Gases

A thesis submitted in partial fulfillment of

the requirements for the degree of

Doctor of Philosophy

by

Arko Roy

(Roll No. 11330009)

Under the supervision of

Prof. Angom Dilip Kumar Singh

Professor

Theoretical Physics Division

Physical Research Laboratory, Ahmedabad, India.

DISCIPLINE OF PHYSICS

INDIAN INSTITUTE OF TECHNOLOGY GANDHINAGAR

2015

to

Maa, Baba

for all that you have taught me...

Declaration

I declare that this written submission represents my ideas in my own words and where others' ideas or words have been included, I have adequately cited and referenced the original sources. I also declare that I have adhered to all principles of academic honesty and integrity and have not misrepresented or fabricated or falsified any idea/data/fact/source in my submission. I understand that any violation of the above will be cause for disciplinary action by the Institute and can also evoke penal action from the sources which have thus not been properly cited or from whom proper permission has not been taken when needed.

Signature

Name: Arko Roy

(Roll No: 11330009)

Date:

CERTIFICATE

It is certified that the work contained in the thesis titled **"Finite Temperature Effects in the Condensates of Dilute Atomic Gases"** by **Mr. ARKO ROY** (Roll No. 11330009), has been carried out under my supervision and that this work has not been submitted elsewhere for a degree.

Prof. Angom Dilip Kumar Singh
(Thesis Supervisor)
Professor,
Theoretical Physics Division
Physical Research Laboratory,
Ahmedabad, India.

Date:

Acknowledgments

After piling higher and deeper for the past 5 years, now I find that the thing that's the hardest for me to write is writing the acknowledgments. It also, hands down, takes me longer than any other chapter in this thesis. For me, I think the reason I take these acknowledgments so seriously is because it's when I get to put down on paper how truly grateful I am to be surrounded with such great friends, motivating supervisor, an awesome group, and a family that truly makes my life a joy. That's why it is so tough. I also type a lot slower...

To my supervisor, Prof. Angom Dilip Kumar Singh, I consider myself lucky to have got the opportunity to be your graduate student. I am extremely fortunate and privileged to have got to spend so many years in your company. Thank you for all the formal, and incisive discussions on various topics in physics, computer science, and in particular on the area of my thesis all along; I have learned a lot from you. From introducing me to popular articles on medical science through Siddhartha Mukherjee or Atul Gawande; to graffiti painting of Banksy, magazines like New Yorker, and informative websites like aeon.com, to name a few; thank you. I will remain indebted to you for the trust, faith and confidence you had in me right from the inception of any scientific idea to the final execution of the project. It meant a lot to me. *'What is the status?'* was the question that would initiate any conversation kept me motivated and made me enthusiastic to give you a satisfying answer each time. Your truly encouraging words like *'We are heading in the right direction'* or *'Don't worry, you will do well'* before any review or seminar have always helped me to take things in stride and look forward. I wish I could learn the brilliant acumen you have over academic and non-academic matters. Thank you Dilip for being there, for being extremely patient with me.

It was a pleasure to know Dr. Sandeep Gautam at the beginning of my Ph.D. tenure, who by then was a postdoc in our group. I will remain ever grateful to you for all the time you spent, despite your own research, in giving me the first-hand knowledge on the physics of BEC and related numerical techniques; they were so valuable. The long hours of scientific discussions, providing correct references, sharing codes through mail or chat or phone were highly productive and crucial for me. Now I realize that I had asked you the most naive, simple and trivial questions..:P. How fun and tough can debugging a code be, I learned from you; thank you for making me appreciate that. You had been a fantastic and fine trouble-shooter. I could not have expected better than this. Thank you Sandeep, for being extremely helpful and a superb support just at that right point of time.

The first lesson on shock waves, Mach angle, and vortices in classical fluids

from Debolina Dasgupta (currently a Graduate Research Assistant at Department of Aerospace Engineering, Georgia Tech) immensely helped me to understand the various aspects of topological defects in quantum fluids. Thank you so much, they were essential. I take this opportunity to thank Naik (VTech.), Rakesh (UIC), Soumyadeep (Minnesota Univ.) Souvick (UIC), Sayak (Ohio State), Ranjan (IISc), Ankur (Oregon State Univ.), and not to forget Lata (IIT-B) for being so prompt and mailing me the journal articles whenever I had asked for; without your help, I would not have come across several useful and inaccessible papers. A huge part of my research revolved around computers and the men behind the early exposition to the world of Linux were Dr. Siddhartha Chattopadhyay and Dr. Koushik Saha. Thank you Koushik for teaching me how to install OS like Windows/Linux; they were so beneficial. Thank you Siddhartha for divulging the fun of tinkering with the filesystem in Linux. I am deeply indebted to Dr. Shashi Prabhakar for introducing me to the basics of HTML/PHP scripting and helping me out whenever I used to get stuck on a particular step in MATLAB.

I remain grateful to the Director, Dean, Academic Committee for the academic & non-academic support and help I got all throughout. Thank you for providing all the necessary facilities and a homely atmosphere, I will surely cherish my stay at PRL forever. I am thankful to Dr. Bhushit G. Vaishnav for his continual support. A warm thanks to all the faculty members, course-work instructors, research scholars, PDFs of Theoretical Physics Division, and specially the members of DSC for attending my seminars, and giving encouraging remarks on the thesis work. I thank Prof. R. P. Singh, Prof. K. P. Subramanian, Prof. Subroto Mukerjee, and the anonymous external examiners for their constructive feedbacks, suggestions and encouraging comments while reviewing the thesis; they were much-needed and indispensable.

All throughout these brilliant 5 years, I used to share the office space with Avdhesh and Girish Kumar. Thank you for tolerating me despite my gossipy nature, and listen to my ramblings. Let me take this moment to thank Mr. Razaahmed Maniar, Secretary of Theory Office for the numerous help in official matters related to the Division. I will always remember the enormous help I got from Mr. Senthil Babu, Mr. Pradeep Sharma of PRL, and Dr. Nithin V. George, Mr. Piyush Vankar of IIT Gandhinagar (IIT-GN) in all academic & administrative matters. I am deeply indebted to the PRL and IIT-GN Library staff for all the facilities and help they provided. Thank you Dr. T. S. Kumbar of IIT-GN for mailing many interesting articles and allowing me to access the journals subscribed by IIT-GN. I am highly obliged to the American Physical Society, NIST Virtual Library, and Macmillan Publishers Ltd.(on behalf of Nature

Publishing Group) for permitting me to reprint some of their published figures in this thesis. A big thanks to Mr. Samuel Johnson and Mr. Jigar Raval for a smooth and seamless computing experience on PRL HPC, and recently on Vikram-100. Without your help, life would not have been that easy. I thank the other members of the Computer Center, PRL for their endless advice, support and cooperation.

I must thank Abhishek and Koushik for giving me the first hands-on training on cooking. I had an amazing time. Priyanka and Sneha, thank you for baking the most exquisite cakes, for the absolutely yummy and mouth-watering food I have ever had. 'A Bird's Rhapsody' would have remained implausible, but because of you...I am pleased with Tanushree for the awesome dinner treats at her place. Thank you; I enjoyed a lot. I also thank the canteen staff for the tireless effort put in serving food 16×7. I continue to be a foodie because of you all. This thesis would not have been possible without the innumerable late-night parties, hangouts and the amusing time spent together with Tanmoy Chattopadhyay, Monojit, Naveen, Chandan Hati - thank you for the camaraderie. Without you, life would have been so wretched. I am thrilled with all the fun and exciting things we have been able to do together. Ujjal, Gaurava, Lalit; dude, you are just excellent! Your strange quirks are really entertaining; thanks Chandan Gupta and Ribhu for all the photography outings and the criticisms thereafter. I am fortunate to be among so many sensible and responsible guys, specially Deepak, Diptiranjan, Bivin, Jabir, Prahlad and Kuldeep Pandey for taking care of the hostel activities and make it a better one. I am grateful to have had the company of Dr. Susanta Kumar Bisoi, Dr. Sunil Chandra, Dr. Amrendra Pandey, Diganta Kumar for the many initiatives we had taken together and for the several chit-chat sessions. A huge shout to thank all my batchmates and junior & senior colleagues for making my stay at PRL cozy and making the hostel a happening place. I sincerely thank and acknowledge the group members Kuldeep Suthar, Rukmani, Soumik and the intense journal-club sessions with Nabyendu, Sudip, Manpreet, Pankaj, Pradeep for the stimulating discussions on various topics in condensed-matter physics.

For all that I have learned, everything that I have gained, whatever I have achieved - I owe my deepest thanks and express my gratitude to my parents, grandparent for their constant love, support and encouragement. Without you I could not have been so happy.

Arko

Abstract

The stationary state solutions and dynamics of Bose-Einstein condensates (BECs) at $T = 0$ are well described by the Gross-Pitaevskii (GP) equation. BECs of dilute atomic gases have been experimentally achieved at ultracold temperatures of the orders of 10^{-9} K. To include the effects of finite temperature on these condensates one needs to generalize the GP equation. We report here the development of the Hartree-Fock-Bogoliubov theory with the Popov (HFB-Popov) approximation for trapped two-component BECs (TBECs). It is a gapless theory and satisfies the Hugenholtz-Pines theorem. The method is particularly well suited to examine the evolution of the low-lying energy excitation spectra at $T = 0$ and $T \neq 0$. Apart from the two Goldstone modes corresponding to each of the species in quasi-1D TBEC, we show that the third Goldstone mode, which emerges at phase-separation due to softening of the Kohn mode, persists to higher interspecies interaction for density profiles where one component is surrounded on both sides by the other component. These are termed as *sandwich* type density profiles. This is not the case with symmetry-broken density profiles where one species is entirely to the left and the other is entirely to the right which we refer to as *side-by-side* density profiles. However, the third Goldstone mode which appears at phase-separation gets hardened when the confining potentials have separated trap centers. This hardening increases with the increase in the separation of the trap centers in which the TBECs have been confined. Furthermore, we demonstrate the existence of mode bifurcation near the critical temperature. We also examine the role of thermal fluctuations in quasi-1D TBECs of dilute atomic gases. In particular, we use this theory to probe the impact of non-condensate atoms to the phenomenon of phase-separation in TBECs. We demonstrate that, in comparison to $T = 0$, there is a suppression in the phase-separation of the binary condensates at $T \neq 0$. This arises from the interaction of the condensate atoms with the thermal cloud. We also show that, when $T \neq 0$ it is possible to distinguish the phase-separated case from miscible from the trends in the correlation function. However, this is not the case at $T = 0$. In a BEC, a soliton enhances the quantum depletion which is sufficient enough to induce dynamical instability of the system. For phase-separated TBECs with a dark soliton in one of the components, two additional Goldstone modes emerge in the excitation spec-

trum. We demonstrate that when the anomalous mode collides with a higher energy mode it renders the solitonic state oscillatory unstable. We also report soliton induced change in the topology of the density profiles of the TBEC at phase-separation. For quasi-2D BECs, at $T = 0$, we show that with the transformation of a harmonically to toroidally trapped BECs, the energy of the Kohn modes gets damped. This is examined for the case when the radial angular frequencies of the trap are equal. The other instance, when the condensate is asymmetric, the degeneracy of the modes gets lifted. The variation in the anisotropy parameter is accompanied by the damping of the modes, the quasiparticle modes form distinct family of curves; each member being different from the other by the principal quantum number n. When $T \neq 0$, with the production of a toroidally trapped BEC, the maxima of the thermal density tends to coincide with the maxima of the condensate density profiles. This is different from the case of a harmonically trapped BEC in which due to the presence of repulsive interaction between the atoms, the thermal density gets depleted where the condensate atoms are the highest.

Contents

List of Figures

Chapter 1

Introduction

The year 1995 witnessed the first experimental observation of Bose-Einstein condensation (BEC) in trapped dilute atomic gases of ^{87}Rb [1], ^{23}Na [2], ^{7}Li atoms [3]. The remarkable achievements were honored with the 2001 Nobel Prize in Physics, which was awarded jointly to Eric A. Cornell, Wolfgang Ketterle, and Carl E. Wieman "*for the achievement of Bose-Einstein condensation in dilute gases of alkali atoms, and for the early fundamental studies of the properties of the condensates* " [4]. After this seminal achievement, there has been a series of experiments towards realization of BEC in different atoms. Table 1.1 provides the list of atoms which have been cooled and trapped to achieve BEC. These experiments suggest the immense growth in the theoretical and experimental study of quantum gases. Experiments take place at very low but finite temperatures. As a result, presence of thermal or non-condensate atoms is inevitable, and the interactions between the condensate and thermal atoms play a crucial role in thermalization. For instance, temperature plays a significant role during condensate growth, or when the BEC is heated due to strong external perturbations. It is then imperative to have a good knowledge about thermal or non-condensate atoms density to give an appropriate theoretical description of the system. As an example, by now quintessential, one of the first images of ^{87}Rb BEC reported in Anderson *et al.* [1] is shown in Fig. 1.1. The images in the figure represent atomic density distribution in the velocity space as the atoms are cooled below the critical temperature with harmonic confining potential. BECs of ^{87}Rb atoms have also been achieved in toroidal or ring traps shown in Fig. 1.2. As evident from the figures, the condensate fraction is large,

Atom	Year	Groups	References
^{87}Rb	1995	Wieman & Cornell	Anderson *et al.* [1]
^{23}Na	1995	Ketterle	Davis *et al.* [2]
^{7}Li	1995	Hulet	Bradley *et al.* [3]
^{23}Na	1996	Ketterle	Mewes *et al.* [5]
^{1}H	1998	Kleppner & Greytak	Fried *et al.* [6]
^{85}Rb	2000	Wieman & Cornell	Cornish *et al.* [7]
He*	2001	Aspect	Robert *et al.* [8]
^{41}K	2001	Inguscio	Modugno *et al.* [9]
^{133}Cs	2003	Grimm	Weber *et al.* [10]
^{174}Yb	2003	Takahashi	Takasu *et al.* [11]
^{52}Cr	2005	Pfau	Griesmaier *et al.* [12]
^{40}Ca	2009	Sterr	Kraft *et al.* [13]
^{84}Sr	2009	Killian	Escobar *et al.* [14]
^{84}Sr	2009	Schreck	Stellmer *et al.* [15]
^{86}Sr	2010	Schreck	Stellmer *et al.* [16]
^{88}Sr	2010	Killian	Mickelson *et al.* [17]
^{164}Dy	2011	Lev	Lu *et al.* [18]
^{168}Yb	2011	Takahashi	Sugawa *et al.* [19]
^{168}Er	2012	Ferlaino	Aikawa *et al.* [20]

Table 1.1: Experimental observation of BEC in chronological order. Listed here are the atoms which have been Bose condensed till date. The year of achievement and the groups involved are also mentioned. Experiments on ^{87}Rb and ^{23}Na BEC, shown here as the first two entries was awarded the 2001 Nobel Prize in Physics.

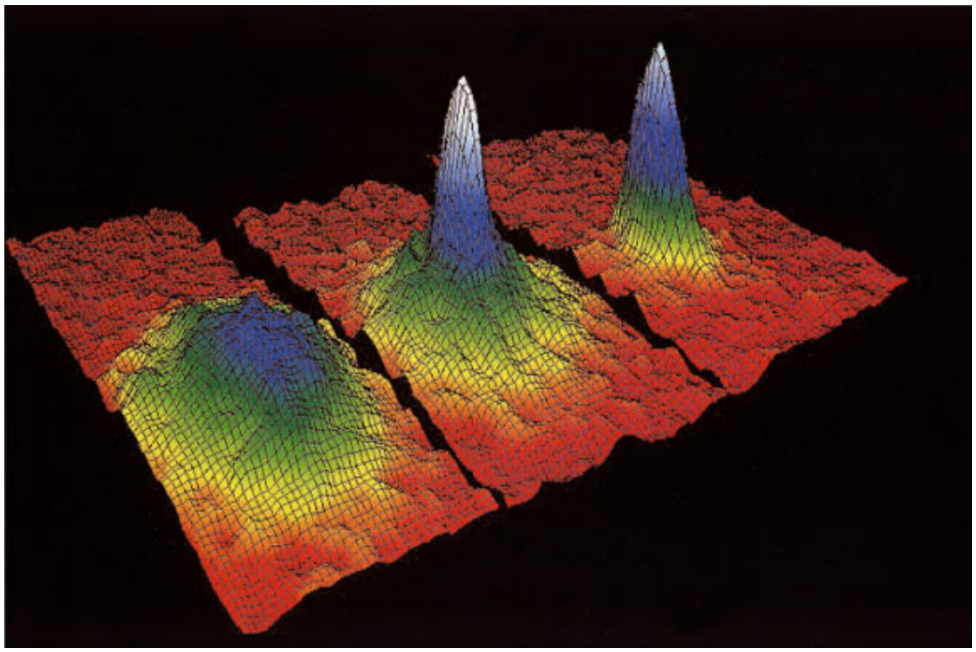

Figure 1.1: False color coded images of the velocity distribution of trapped ^{87}Rb atoms taken with the aid of time-of-flight expansion technique. The left frame corresponds to the velocity distribution just before the appearance of BEC; the center frame, just after the appearance of the condensate; the right frame, after further evaporation leaves a sample of nearly pure condensate. The color corresponds to the number of atoms at each velocity, with red being the fewest and white being the most. Reprinted figure from [E. Cornell, *J. Res. Natl. Inst. Stand. Technol.* **101**, 419 (1996).] Reprinted courtesy of the National Institute of Standards and Technology, U.S. Department of Commerce.

however, the non-condensate atom or thermal atom density is finite. So, studying the effects of finite temperature is essential to develop "high-power" atom lasers [21] using BEC, improve precision measurements based on matter-wave interferometry [22, 23], and in quantum-information processing which relies on the bunch of qubits occupying the same state at zero temperature [24]. In low-dimensional systems the large phase-fluctuations destroy the global coherence of the condensate at finite temperatures even when it is below the critical temperature.

This transforms the true condensate into a superfluid phase also known as quasi-condensate. One needs a finite temperature theory to examine such a transition [25]. To corroborate the experimental results, modelling of BEC at finite temperatures are of utmost importance and an accurate theoretical representation has been a challenging

problem [26].

An important difference of dilute quantum gases, as the name suggests, compared to ordinary gases, liquids and solids is the number density of atoms. The particle density of a typical Bose-condensed atomic cloud is $10^{13} - 10^{15}$ cm^{-3}, whereas it is $\approx 10^{19}$ cm^{-3} for air at room temperature and atmospheric pressure. The atomic density in case of liquids and solids is $\approx 10^{22}$ cm^{-3}. On the contrary, density of nucleons in atomic nuclei is $\approx 10^{38}$ cm^{-3}. Based on the condition that the energy level spacing should be of the order of the thermal energy, in trapped dilute quantum gases, to observe quantum effects the temperature must be 10^{-5} K or even less. In solids, for electrons in metals it is around $10^{4} - 10^{5}$ K, and for phonons it is of the order of 10^{2} K. In atomic nuclei owing to its high particle density the temperature is about 10^{11} K. For the superfluid ^{4}He (discovered in 1938) and ^{3}He (discovered in 1972), the temperatures required are of the order of 1 K and 10^{-3} K for the quantum-mechanical effects to dominate [27].

1.1 Bose-Einstein Condensation

Bosons are quantum particles with integer spin and obey Bose-Einstein statistics. On the other hand, fermions are quantum particles with half-integer spin and obey Fermi-Dirac statistics. The many-body wavefunction for a system of identical bosons is symmetric under interchange of any two particles, and under Bose-Einstein statistics, more than one particle may occupy a single-particle state. The idea of Bose statistics was proposed by Satyendranath Bose in 1924 [28] to derive the black-body radiation spectrum. Albert Einstein extended this to the case of number conserving collection of non-interacting atoms with integer spin [29], where the number of particles is conserved. Photons addressed in Bose's work, on the other hand, are not number conserving. The melding of these two works gave rise to Bose-Einstein statistics. Einstein predicted a very novel feature in the distribution of atomic bosons over the quantized energy levels. At temperatures below the critical temperature $T_{\rm c}$, a finite fraction of the bosons occupy the ground state or the ground state is macroscopically occupied. This is referred to as BEC [30]. Another description of $T_{\rm c}$ is, it is the temperature at which the

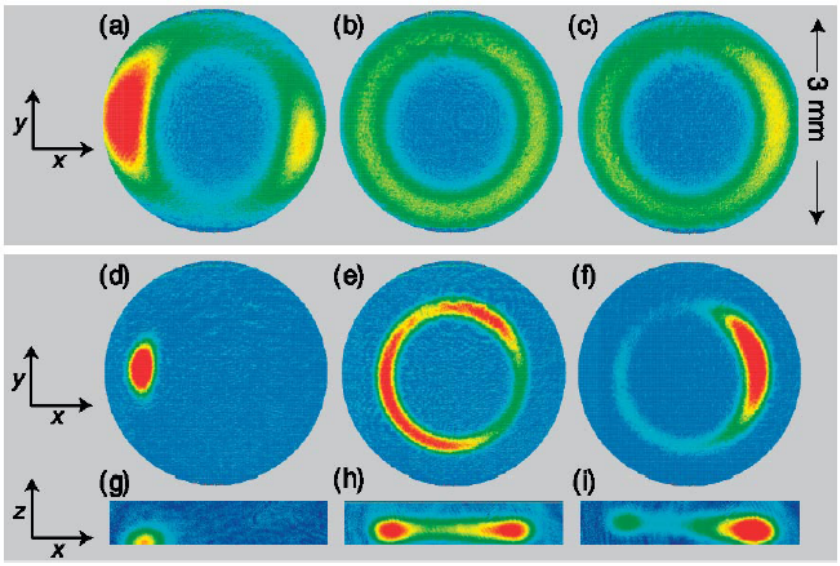

Figure 1.2: Experimental images of condensates of ^{87}Rb atoms in a ring-shaped magnetic trap. (a)-(f) Shown is the top view, and (g)-(i) side view of the absorption images taken 2 ms after switching off the traps. The atoms were trapped either in a quadrupole (Q) ring which is shown in images (a)-(c) or in a time-orbiting ring trap (TORT) shown in images (d)-(i). The color corresponds to intensity of resonant absorption ranging from 0 (blue) to $> 80\%$ (red). Reprinted figure from [Gupta *et al.*, *Phys. Rev. Lett.* **95**, 143201 (2005).] Copyright © 2005 by the American Physical Society.

thermal de Broglie wavelength $\lambda_{\mathrm{dB}} = (2\pi\hbar^2/mk_{\mathrm{B}}T)^{1/2}$ of the atoms, which increases with decreasing temperature, are comparable to the interatomic separation. The atomic wave packets, then, overlap and a macroscopic wavefunction is formed which leads to the formation of BEC.

For an ideal and homogeneous Bose gas in 3-dimension, reaching the value of the phase space density $n\lambda_{\mathrm{dB}}^3 \approx 2.612$ marks the onset of BEC. Here, $n = N/V$ is the number density of the bosons in volume V. The critical temperature for a noninteracting gas of bosons is given by

$$T_{\mathrm{c}} = \frac{2\pi\hbar^2}{mk_B}\left(\frac{n}{2.612}\right)^{2/3}. \tag{1.1}$$

The condensate fraction at temperature T, below T_{c}, is

$$\frac{N_0}{N} = 1 - \left(\frac{T}{T_{\mathrm{c}}}\right)^{3/2}. \tag{1.2}$$

From Eq. 1.1 it is evident that T_{c} is higher for lower mass and higher density bosons.

These were important considerations in choosing spin-polarized Hydrogen as the first candidate atomic gas to obtain BEC.

1.1.1 Off-Diagonal Long-Range Order (ODLRO)

The most important aspect of BEC is the off-diagonal long-range order (ODLRO). A noninteracting system is said to exhibit ODLRO if the single-particle density matrix

$$\rho_1(\mathbf{r},\mathbf{r}') \equiv \mathrm{Tr}\{\hat{\rho}\hat{\psi}^\dagger(\mathbf{r})\hat{\psi}(\mathbf{r}')\} \equiv \langle\hat{\psi}^\dagger(\mathbf{r})\hat{\psi}(\mathbf{r}')\rangle \tag{1.3}$$

has a large eigenvalue, that is an eigenvalue proportional to the total number of particles N. The density operator of the system is represented by $\hat{\rho}$ and $\hat{\psi}^\dagger(\mathbf{r})(\hat{\psi}(\mathbf{r}'))$ is the field operator which corresponds to the creation (annihilation) of a particle at $\mathbf{r}(\mathbf{r}')$. When the system undergoes BEC, the de Broglie wavelength of the bosonic atoms overlap, and a particle at $\mathbf{r}'$ becomes indistinguishable from another particle at $\mathbf{r}$. As a result, $\rho_1(\mathbf{r},\mathbf{r}')$ does not vanish over a long distance $|\mathbf{r}-\mathbf{r}'|$ and the system has spatial coherence. In the thermodynamic limit, for a noninteracting uniform BEC, it has been shown that $\rho_1(\mathbf{r},\mathbf{r}')$ attains the order of N/V as $|\mathbf{r}-\mathbf{r}'| \to \infty$. This confirms ODLRO and implies the formation of BEC [25]. However, for interacting BECs, when single-particle energy levels are not well defined, the reduced single-particle density operator is used instead of single-particle density. It is defined as

$$\hat{\rho}_1 = \mathrm{Tr}_{2,3,\cdots,N}\,\hat{\rho}, \tag{1.4}$$

where, $\mathrm{Tr}_{2,3,\cdots,N}$ denotes the trace over particles $2,3,\cdots,N$. If n_M is the maximum eigenvalue of $\hat{\sigma}_1 \equiv N\hat{\rho}_1$, then BEC occurs when the particles satisfy the Penrose-Onsager criterion [31]

$$\frac{n_\mathrm{M}}{\mathrm{N}} = e^{\mathcal{O}(1)}, \tag{1.5}$$

where, $e^{\mathcal{O}(1)}$ is a positive number of the order of unity. Here, n_M represents the number of condensed bosons and the ratio n_M/N is referred to as the condensate fraction. When the system is inhomogeneous, the condition for ODLRO states that

$$\rho_1(\mathbf{r},\mathbf{r}') \to \psi^*(\mathbf{r})\psi(\mathbf{r}'), \quad |\mathbf{r}-\mathbf{r}'| \to \infty, \tag{1.6}$$

where, $\psi(\mathbf{r})$ is referred to as the condensate wave function, and $\rho_1(\mathbf{r},\mathbf{r}') = \langle\mathbf{r}'|\hat{\rho}_1|\mathbf{r}\rangle$ is the single-particle density matrix. These definitions are valid for both interacting

and noninteracting particles. In addition, the criterion is applicable when the system is inhomogeneous. Hence, the Penrose-Onsager criterion is the most general condition for the existence of BEC in a system.

The experiments with dilute atomic gases are carried out in traps, and the favored trapping potential configurations are well approximated with a harmonic-oscillator potential. If the number of particles is N, and $\omega_x, \omega_y, \omega_z$ are the harmonic oscillator frequencies along the x, y and z directions, the critical temperature

$$T_{\rm c} = \frac{\hbar\varpi}{k_B}\left(\frac{N}{1.202}\right)^{1/3}, \tag{1.7}$$

where, $\varpi = (\omega_x\omega_y\omega_z)^{1/3}$ is the geometric mean of the harmonic oscillator frequencies. At $T_{\rm c}$ an inhomogeneous BEC emerges both in momentum and coordinate space, unlike superfluid helium. This allows development of novel methods to investigate unique features of BEC like temperature dependence of condensate, interference phenomena and so on. Furthermore, the effects of two-body interactions on important measurable properties like density are enhanced in BECs confined in a trapping potential [32].

The concept of BEC plays a key role in the phenomenon of superconductivity, where bosons are pairs of electrons with opposite spin. The other remarkable experimental achievements, in recent times, are observation of BECs with: excitons, which are bound states of an electron and a hole [33]; biexcitons [34]; polaritons, excitons coupled to radiation field in a cavity [35,36]; exciton-polariton [37–39]; magnons [40]; and photon [41,42].

1.1.2 Two-component Bose-Einstein condensates

BECs consisting of atoms of two different species, or two isotopes of the same element, or two different hyperfine states of the same atom are called two-component Bose-Einstein condensates (TBECs). The remarkable feature of TBECs or binary condensates is the phenomenon of phase-separation [43,44]. This relates the system to novel phenomena in nonlinear dynamics and pattern formation, non-equilibrium statistical mechanics, optical systems and phase transitions in condensed matter systems. In TBECs, it is possible to steer the system from miscible to immiscible (phase-

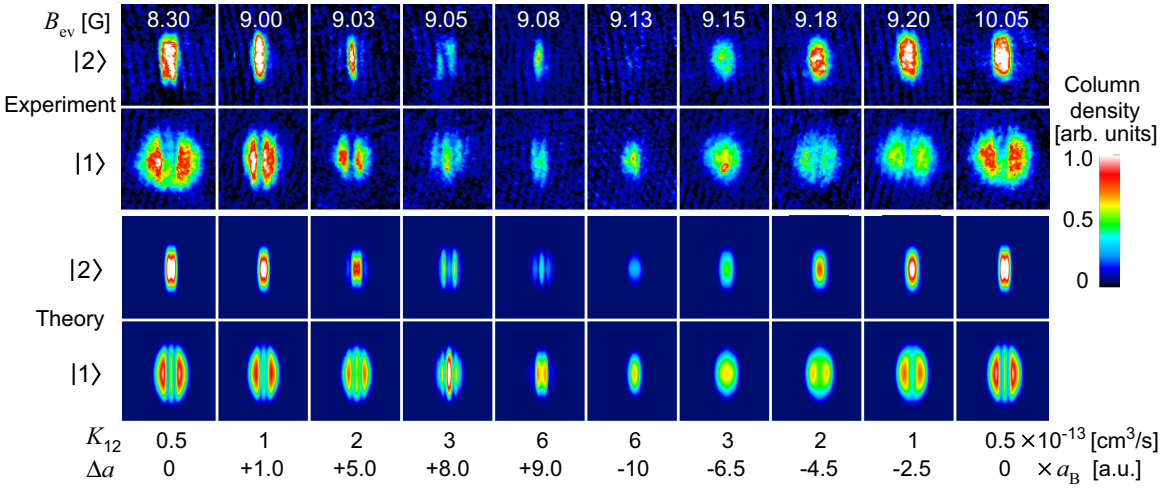

Figure 1.3: Experimental observation of sandwich type density profiles in a TBEC. The images in the first and second panel show the column densities of $|1\rangle \equiv |F = 1, m_F = 1\rangle$ and $|2\rangle \equiv |F = 2, m_F = -1\rangle$ of ^{87}Rb atoms obtained by varying the interspecies scattering length. The images in the third and fourth panel show the density profiles obtained through the numerical solution of GP equation at $T = 0$. Reprinted figure from [Tojo *et al.*, *Phys. Rev. A* **82**, 033609 (2010).] Copyright © 2010 by the American Physical Society.

separated) or vice-versa by tuning the interatomic interactions through Feshbach resonances [45, 46]. Using improved experimental techniques, TBECs have been achieved in several experiments over the last decade. Table 1.2 provides a list of TBECs, which includes all the three types mentioned earlier, achieved till date. The remarkable feature of phase-separation in TBECs has been successfully observed in ^{85}Rb-^{87}Rb [53], different hyperfine states of ^{87}Rb [64] and ^{87}Rb-^{133}Cs [49] condensate mixtures. As an example, Fig. 1.3 shows the experimental image of *sandwich* type TBEC density profiles at phase-separation, the two species are different hyperfine states of ^{87}Rb [64]. The other possible geometry of density distribution is *side-by-side*, Fig. 1.4 shows the density profile of the first experimental realization of this geometry [53]. These have motivated theoretical investigations on stationary states [43, 65], dynamical instabilities [66–68] and collective excitations [69–75]of TBECs.

In the context of excited states in TBECs, it supports coupled dark-bright solitons which makes it richer and more interesting than single-component BECs [76]. The bright soliton, on the other hand, cannot survive in single component BECs with repulsive interaction. It may be mentioned here that, solitons in BECs and TBECs have been

Atom	Year	Groups	References
		Two different species	
^{41}K - ^{87}Rb	2002	Inguscio	Modugno *et al.* [47]
^{87}Rb- ^{133}Cs	2011	Nägerl	Lercher *et al.* [48]
^{87}Rb- ^{133}Cs	2011	Cornish	McCarron *et al.* [49]
^{84}Sr - ^{87}Rb	2013	Schreck	Pasquiou *et al.* [50]
^{23}Na - ^{87}Rb	2013	Wang	Xiong *et al.* [51]
^{39}K - ^{87}Rb	2015	Arlt	Wacker *et al.* [52]
		Two different isotopes	
^{85}Rb - ^{87}Rb	1998	Ketterle	Inouye *et al.* [45]
^{85}Rb - ^{87}Rb	2008	Wieman	Papp *et al.* [53]
^{85}Rb - ^{87}Rb	2011	Cornish	Händel *et al.* [54]
		Two different hyperfine states of the same atom	
^{87}Rb	1997	Wieman	Myatt *et al.* [55]
^{87}Rb	1998	Cornell	Hall *et al.* [56]
^{23}Na	1998	Ketterle	S.-Kurn *et al.* [57]
^{23}Na	1998	Ketterle	Stenger *et al.* [58]
^{87}Rb	2000	Inguscio	Maddaloni *et al.* [59]
^{87}Rb	2001	Aspect	Delannoy *et al.* [60]
^{87}Rb	2006	S.-Kurn	Sadler *et al.* [61]
^{87}Rb	2007	Hall	Mertes *et al.* [62]
^{87}Rb	2009	Hall	Anderson *et al.* [63]
^{87}Rb	2010	Hirano	Tojo *et al.* [64]

Table 1.2: Experimental observation of TBEC. Listed here are the atoms used for achieving TBEC, the year of achievement and the groups involved.

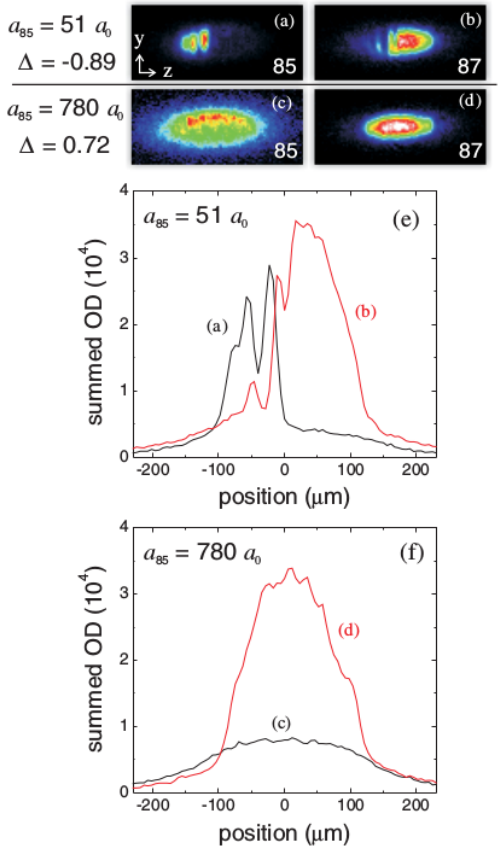

Figure 1.4: Absorption images of ^{85}Rb - ^{87}Rb TBEC showing the miscible and immiscible phases on changing the intraspecies scattering length of ^{85}Rb. (a), (b) show side-by-side, and (c), (d) show miscible density profiles for $a_{85} = 51a_0, 780a_0$ respectively. (e), (f) show optical density of ^{85}Rb - ^{87}Rb TBEC along radial direction. Reprinted figure from [Papp *et al.*, *Phys. Rev. Lett.* **101**, 040402 (2008).] Copyright © 2008 by the American Physical Society.

experimentally achieved either by phase-imprinting method [77] or in two counter-flowing miscible TBECs above a critical velocity [78]. For miscible TBECs, creation and interaction of dark solitons has been theoretically examined in Refs. [79,80]. Families of stable solitonic solutions from coupled GP equations in quasi-1D TBECs at zero temperature have been obtained [81, 82].

1.2 Liquid He and BEC

Superfluidity in liquid He is well known since several decades, however, it is difficult to isolate and examine the properties of condensates as there are strong interatomic interactions. In general, BECs of alkali-metal atoms are weakly interacting and all the atoms are considered to be in the same quantum state. So, mean field approaches provide a good description of the static and dynamic properties of these systems. This is not the case in liquid He, the interatomic interaction induce strong correlations, and mean field approach is not applicable. BECs, used here after in reference to the Bose-Einstein condensates of dilute atomic gases, is unique in the sense that it is a quantum-statistical phase transition. These are excellent systems to probe the condensate state, which was first predicted for ideal Bose gas or noninteracting Bose gas [29, 30]. Interactions are, however, necessary for ^{4}He to exhibit superfluidity.

Although there is a difference between condensates and superfluids, the noticeable features of superfluidity in ^{3}He and ^{4}He are linked and can be explained through the phenomenon of condensation [83–85]. BECs on the other hand are far more dilute and weakly interacting compared to liquid Helium. The low density suppresses three body collisions and makes the atomic gas stable against solidification at very low temperatures. The densities considered are, however, high enough so that the two-body binary elastic collision rate is sufficient to thermalize the system and form a metastable BEC. Another striking feature of BEC and ^{4}He is that both are inviscid and support quantized vortices. According to the two-fluid description of hydrodynamics, at critical temperature and below it, the superfluid and normal component coexist. At lower temperatures, the density of normal component tends to zero, and the superfluid density approaches the total density of the liquid. Near the lambda point or just above the critical temperature, the reverse happens, that is the density of normal component tends to approach the total density and the superfluid density approaches zero. The normal component in a superfluid is identified by the presence of low momenta elementary excitations called phonons which obey Bose statistics. BECs at finite temperatures consists of condensate and non-condensate atomic clouds, the remarkable difference from liquid helium is, in BECs the number of atoms in the non-condensate atomic cloud is smaller

than the condensate by several orders of magnitude. This is due to weak interactions between bosonic atoms in the BEC.

1.3 Spin-polarized Hydrogen

The strong interactions in superfluid liquid Helium enhances quantum fluctuations, and the density of non-condensate atoms is significant at zero temperature. So, it is difficult to probe condensate properties with superfluid Helium. In 1959, Hecht showed that spin-polarized Hydrogen is in the gaseous state till zero temperature, and proposed it as a suitable candidate to observe Bose-Einstein condensate in weakly interacting bosonic gas [86]. The study was based on quantum theory of corresponding states. The proposal, with better theoretical understanding and realizable experimental parameters, appeared in the independent work of Stwalley and Nosanow [87]. This was soon followed by an important step towards observation of atomic Hydrogen condensate with the experimental realization of spin-polarized Hydrogen gas in the high field seeking spin polarization of the ground state by two groups: Silvera and collaborators [88]; and Kleppner and collaborators [89]. The next important step was the proposition of Harald Hess to use the low-field seeking spin states and employ evaporative cooling to achieve lower temperatures [90]. As discussed earlier, the latter was instrumental in observing condensates of dilute alkali-atomic gases. However, there is one basic technical difference in the evaporative cooling as implemented in alkali atoms: a radio frequency flips the spins of the atoms and repels it from the trap [91,92]. The same technique was adopted in the evaporative cooling of spin-polarized Hydrogen atomic gas, and BEC of spin-polarized hydrogen was observed in 1998 [6]. A 2D quasicondensate with atomic hydrogen has also been observed [93].

1.4 Finite Temperature Models

We continue here with the discussion about the different methodologies employed till date to incorporate the effects of finite temperature on BECs of dilute atomic gases. At $T = 0$, neglecting quantum fluctuations, all the atoms are in the condensate state and the total density equals the condensate density. The GP equation is appropriate

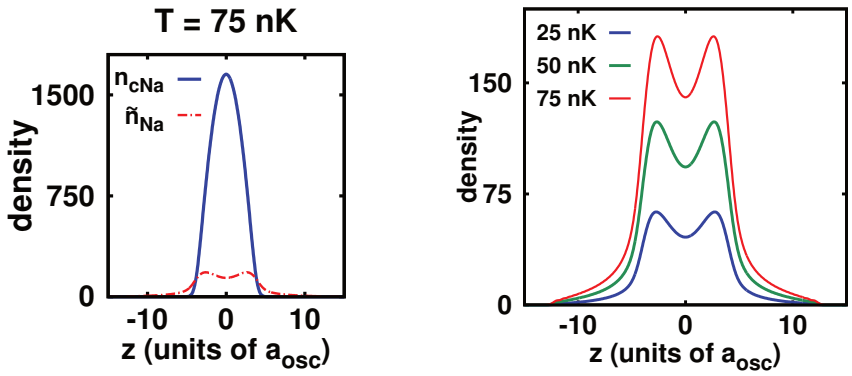

Figure 1.5: The figure on the left shows the equilibrium condensate (blue) and thermal density (red) profile along the axial direction z for a system containing 10^4 ^{23}Na atoms at $T = 75$ nK in a harmonic trap with $(\omega_\perp, \omega_z) = 2\pi \times (40.2, 4.55)$ Hz. The figure on the right shows the variation in thermal density for the same system at $T = 25, 50, 75$ nK. In the plots density is measured in units of $a_{\rm osc}^{-1}$.

to describe the statics and dynamics of Bose-Einstein condensates. However, in the experimental realizations non-condensate atoms coexist with the condensate atoms as these are at finite temperatures, and even at zero temperature, there are non-condensate atoms due to quantum fluctuations. It is therefore, pertinent to generalize the GP equation to account for non-condensate atoms. At $T \neq 0$, as the condensate cloud coexists with the thermal cloud, the interactions between the condensate and non-condensates cloud cannot be ignored. This interaction modifies the equilibrium density profiles of BECs at $T \neq 0$ and plays an important role in the damping of collective modes, and also influences the dynamics of topological defects such as solitons and vortices in BECs. On the theoretical front, it is essential to include the dynamics of both the condensate and thermal densities to accurately reflect the experimental scenarios and modelling such systems is an active area of research. Here we review some of the finite temperature models and point out their essential features.

In the semi-ideal two-gas model proposed in Ref. [94], the condensate part is affected only by the repulsive s-wave interactions between the condensed atoms. The atoms in the thermal or the non-condensate part are considered to be noninteracting and is under the influence of the effective potential constituted by the external trapping potential and the mean-field interaction potential of the condensed atoms. For strong interactions between the condensed atoms, Thomas-Fermi approximation is applicable

and based on the self-consistent Hartree-Fock model, the analytic expressions for the condensate and the thermal component are given by

$$\begin{aligned} n_0(\mathbf{r}) &= \frac{\mu - r^2/2 - 2Un_{\rm T}(\mathbf{r})}{U}\theta(\mu - r^2/2 - 2Un_{\rm T}(\mathbf{r})), \\ n_{\rm T}(\mathbf{r}) &= \frac{1}{\lambda_{\rm T}^3} g_{3/2}(e^{-(-r^2/2+2U[n_0+n_{\rm T}]-\mu)/k_{\rm B}T}). \end{aligned} \tag{1.8}$$

Here, U and $\lambda_{\rm T}$ are the strength of the interatomic interaction and the thermal de Broglie wavelength, respectively, and $g_\alpha(z) = \sum_{j=1}^{\infty} z^j/j^\alpha$ is the Bose function. The coupled Eqns. (1.8) are to be solved self-consistently with the total number of atoms $N = \int d\mathbf{r}[n_0(\mathbf{r}) + n_T(\mathbf{r})]$ as a constraint. Here, n_0 and $n_{\rm T}$ are the condensate density at $T = 0$ and the non-condensate density of bosons, respectively. The chemical potential μ is then determined through N. Furthermore on neglecting U from the thermal atoms in Eqns. (1.8), the explicit expression for chemical potential is

$$\mu = \frac{1}{2}(15Na)^{2/5}\left(\frac{N_0}{N}\right)^{2/5}, \tag{1.9}$$

with a as the scattering length and N_0 as the total number of condensate atoms. The expressions for the condensate fraction N_0/N has also been explicitly calculated in terms of incomplete gamma functions for the temperature ranges $T < T_c$ and $T \approx T_c$ [94].

The non-equilibrium properties during the condensate growth as the trapped atoms are cooled to temperatures below the BEC transition has been studied by Bijlsma *et al.* [95]. They consider the kinetics of both the thermal cloud, and the Hartree-Fock mean-field effects in the condensed and the non-condensed parts. In this model, the total number of atoms and total energy of the system are kept fixed. It is assumed that the thermal component behaves ergodically and that the condensate which is treated within the Thomas-Fermi approximation grows adiabatically [95]. This necessarily implies that the dynamics of the condensate is neglected and the collective excitations are ignored. However, for temperatures of interest, during the growth process these excitations are damped and one can safely assume the condensate to remain in a state that is well-approximated by the quasiequilibrium solution of the GP equation. The non-condensate part, on the other hand, is the solution of a semiclassical Boltzmann equation in the ergodic approximation. This is based on the assumption that the equilibration of atoms within one energy level occurs on a much shorter time scale than

equilibration of atoms between different energy levels. The nonlinear Schrödinger equation for the condensate and a kinetic equation for the thermal component have to be solved self-consistently with the equilibrium density of the condensate determined by the number of atoms in the condensate. However, there are discrepancies between the theoretical estimates and the experimental results which are attributed to deviations from the assumptions made in this model. A full solution of the quantum Boltzmann equation may be a possible remedy to this disparity which is beyond the scope of this theory [95].

As a step towards solving the quantum Boltzmann equation, a coarse-grained Markovian approach based on the Chapman-Enskog-Bogoliubov procedure of nonequilibrium statistical mechanics, has been developed by Walser *et al.* [96]. The kinetic evolution of a trapped condensed bosonic gas of atoms towards equilibrium is described within this model. In particular, the self-consistent master equations for the mean-fields corresponding to the condensate, and the quantum-Boltzmann equation for the normal densities, and anomalous fluctuations have been obtained. These equations generalize the Gross-Pitaevskii equations, and are consistent with the quantum-Boltzmann-equation approach.

Another class of theories to model finite temperature BECs are based on c-field methods. These models consider c-field to represent the coherent condensate field and are simulated using classical stochastic field equations. The incoherent region consists of the high energy modes other than the Bose-degenerate modes. The distribution of particles in this region obey Bose statistics and may contain significant fraction of the total number of particles depending on temperature. The c-field techniques can be classified into three broad categories, namely

1. *Projected GPE (PGPE)* : The time evolution of the system is described classically. It is applicable when thermal effects are large, which holds true when $T \approx T_c$, and quantum fluctuations can be neglected. The GPE is modified with a projection operator which specifies the appropriate energy cut-off such that the energy levels in the c-field region have large occupancies. This technique is used to simulate the c-field region considered to be a microcanonical system, in complete isolation from the external environment, with fixed energy and

number of particles. The coupling between coherent and incoherent region is neglected [26, 97].

2. *Truncated Wigner PGPE (TWPGPE)*: When $T \ll T_c$, the quantum effects dominate over the thermal densities. There exist modes with low occupation number in the c-field region. Noise terms which represent quantum fluctuations are added to the initial conditions. The addition of terms is not exact, but is well approximated by stochastic sampling of a Wigner quasiprobability distribution function for the initial state. Evolution of the system towards equilibrium with this method leads to damping, and deviates from the experimental results. For short time scales or low temperature, this approach provides reliable results [26, 97].

3. *Stochastic GPE (SGPE)* : In this approach, dissipative and dynamical noise terms are added to the GPE. Through these terms the coupling between the modes in the c-field and the incoherent region is taken into account. So that the system attains the correct thermal equilibrium. The high lying modes evolve according to the quantum Boltzmann equation, and the system is described by a member of a grand-canonical ensemble which includes exchange of particles and energy between the coherent and incoherent regions [26, 97]. It should be mentioned here that the solution of SGPE includes both thermal and quantum fluctuations. Unlike TWPGPE, this method does not suffer from spurious damping as the system relaxes to achieve equilibrium.

In addition to the aforementioned formalisms, the nonequilibrium properties of BEC at finite temperatures has been studied within the Zaremba-Nikuni-Griffin (ZNG) formalism [98]. It is based on Kadanoff-Baym formalism of nonequilibrium quantum statistical mechanics using Green's function techniques [99, 100], and incorporates the dynamics of the condensate atoms, collisions between the non-condensate atoms, and the particle-exchange collisions between the condensate and the non-condensate atoms which are essential to describe the state of the Bose system at finite temperatures. The two components, namely the condensate and the non-condensate atoms satisfy different equations of motion which are coupled to each other. In this method the

governing equations of motion are the generalized Gross-Pitaevskii equation which includes the coupling to the thermal cloud, and the quantum Boltzmann equation which subsumes the effects of collisions between the atoms. For a single-species BEC these two equations are

$$i\hbar\frac{\partial\phi}{\partial t} = \left[-\frac{\hbar^2}{2m}\nabla^2 + V_{\rm ext} + g(|\phi|^2 + 2\tilde{n}) - iR\right]\phi, \tag{1.10a}$$

$$\frac{\partial f}{\partial t} + \frac{\mathbf{p}}{m}.\nabla_{\mathbf{r}} f - (\nabla_{\mathbf{r}} U_{\rm eff}).(\nabla_{\mathbf{p}} f) = C_{12}[\phi, f] + C_{22}[f]. \tag{1.10b}$$

Here, the first and second equations are the generalized GP and the quantum Boltzmann equation, respectively, with ϕ as the condensate wavefunction, and $V_{\rm ext}$ as the external trapping potential. The term iR describes the exchange of particles between condensate and thermal cloud, $f = f(\mathbf{p}, \mathbf{r}, t)$ is the Wigner distribution function, and $U_{\rm eff} = 2g[n_c + \tilde{n}]$. Depending on the frequency, and the strength of collisions the Boltzmann equation can be used to address two dynamical regimes namely the a) the collisionless or mean-field dominated, and b) the hydrodynamic or the collision dominated regime. The quantum Boltzmann or kinetic equation describes the evolution of Wigner distribution function $f(\mathbf{p}, \mathbf{r}, t)$ of the non-condensate atoms. The equation includes the collisions between condensate and non-condensate atoms through $C_{12}[\phi, f]$, and collisions between the thermally excited atoms through Uehling-Uhlenbeck $C_{22}[f]$ collision integral. In addition, the continuity equation for the local condensate density embody a source term Γ_{12}, which is connected to $C_{12}[\phi, f]$ through the dissipative term iR [101]. One preeminent reason of using ZNG is, it predicts Kohn mode with reliable accuracy for a trapped Bose gas. The other finite temperature theories, described earlier lead to damped Kohn mode at higher temperatures [102, 103].

The methods mentioned so far do not provide detailed and systematic information about the quasiparticle spectrum. It is, however, possible to examine the equilibrium state solutions of trapped BEC at finite temperature and study the collective excitations through the self-consistent Hartree-Fock-Bogoliubov theory with the Popov (HFB-Popov) approximation. It is a gapless theory and hence, satisfies Hugenholtz-Pines theorem. The method is in particular well suited to examine the evolution of the low-lying modes. For the condensate part, a generalized GP equation which includes interactions between condensate and non-condensate clouds is employed, but

the non-condensate atoms are excluded from the dynamics. If the fluctuations around the condensate part (represented by c-field) are denoted by $\tilde{\psi}$, the three-field correlation function $\langle\tilde{\psi}^{\dagger}\tilde{\psi}\tilde{\psi}\rangle$ is neglected. This theory has been used extensively in single-species BEC to study finite temperature effects and mode energies [104–107], and the results are in good agreement with experimental results [108] at low temperatures. For illustration, Fig. 1.5 shows the equilibrium condensate and non-condensate density profiles of a quasi-1D ^{23}Na BEC obtained using HFB-Popov approximation.

1.5 Objectives of the Present Study

In TBECs, the HFB-Popov approximation has been used in the miscible domain [109] and in this thesis, we use the method to examine equilibrium properties in the phase-separated domain at $T = 0$ and $T \neq 0$. Other works which have examined the finite temperature effects in TBECs use Hartree-Fock treatment with or without trapping potential [110, 111] and semi-classical approach [112]. The list of highlights of the research work done in this dissertation is as follows:

- Extension of the HFB-Popov theory and development of the coupled generalized Gross-Pitaevskii equations to account for the finite temperature effects in binary condensates.
- Prediction of fluctuation-induced instability of a quasi-1D single-species Bose-Einstein condensate with dark soliton.
- Mode evolution of a quasi-1D TBEC at zero temperature in coincident and non coincident trap centers. We have predicted three Goldstone modes at phase-separation for sandwich type density profiles.
- Examination of the interaction induced instability of a quasi-1D TBEC with a dark soliton at zero temperature. At phase-separation we have predicted four Goldstone modes and change in the topology of condensate density profiles due to the presence of soliton.
- Investigation of the evolution of quasiparticle modes, condensate and thermal

density profiles of a quasi-1D TBEC at finite temperature. We have demonstrated the existence of mode bifurcation near the critical temperature.

- Thermal suppression of phase-separation in binary condensates when $T \neq 0$. We also show that, when $T \neq 0$ it is possible to distinguish the phase-separated case from miscible based on the trends in the correlation function.

- Mode evolution of a rotationally symmetric quasi-2D BEC at $T = 0$ as the external trapping potential undergoes transformation from a harmonic to a toroidal geometry. This transition decreases the energy of the Kohn mode.

- Study of quasiparticle modes on steering a rotationally symmetric to an asymmetric quasi-2D BEC at $T = 0$. The asymmetry lifts degeneracy of the modes. For toroidal geometry, with the change in the anisotropy parameter, a new Goldstone mode appears in the quasiparticle excitation spectrum.

- Study of the condensate and non-condensate density profiles of a quasi-2D BEC at $T \neq 0$ on transforming the trapping potential from harmonic to toroidal geometry. For a toroidal trap, the maxima of the condensate and the thermal density profiles tends to coincide.

1.6 Overview of the Chapters

In the next chapter, Chapter 2, we begin with discussion on the GP equation. We then present the development of the Hartree-Fock-Bogoliubov theory with the Popov approximation (HFB-Popov) to address the finite temperature effects in the ground state of a single-species BEC. We then highlight the importance of TBECs, and extend the HFB-Popov theory for a single-species BEC to a binary condensate. Finally, we derive the coupled generalized GP equations for a TBEC, and the Bogoliubov-de Gennes equations to examine the excitation spectrum and the thermal cloud densities.

In Chapter 3, we provide a brief description of spontaneous symmetry breaking (SSB) and the Goldstone modes in non-relativistic systems. Furthermore, based on the HFB-Popov theory, we study mode evolution in a trapped TBEC at $T = 0$ with coincident trap centers. For displaced trap centers, we demonstrate mode hardening.

We then study the effect of a soliton in a TBEC on elementary excitation spectra and predict interaction-induced instability in the system.

In Chapter 4, we examine the finite temperature effects on mode evolution in TBEC and demonstrate the existence of mode bifurcations. We also compute the thermal cloud densities for a binary BEC mixture, and show that thermal fluctuations suppress phase-separation in a TBEC. In addition, we show that at finite temperatures it is possible to distinguish the phase-separated case from the miscible case from the trends in the correlation function.

In Chapter 5, we study the fluctuations in quasi-2D condensates. At $T = 0$, with the transformation of the trapping potential from harmonic to a toroidal geometry BEC by introducing and changing the strength U_0 of a Gaussian beam, we observe the softening of Kohn mode and investigate the behaviour of other low-lying modes. For harmonic trapping potential, the changeover from a rotationally symmetric condensate to an asymmetric one lifts the degeneracy of the modes. We point out that during this change the quasiparticle modes form families of curves with similar slopes. Furthermore, at $T \neq 0$, on varying U_0 the maxima of the condensate and non-condensate density profiles tend to coincide. This is different from the case of BEC in a harmonic trapping potential, in which the non-condensate density has a dip where the condensate density is maximum. Finally, in Chapter 6 we present a possible outlook for future studies.

Chapter 2

Finite Temperature Theory

At zero temperature, the Gross-Pitaevskii (GP) equation, also referred to as the non-linear Schrödinger equation (NLSE), is an apt mean-field theory to describe the statics and dynamics of weakly interacting dilute Bose gases. It was formulated independently by Gross [113, 114], and Pitaevskii [115] to describe bosonic quantum fluids, and in particular, superfluid liquid ^{4}He. It is valid at low temperatures where there is a macroscopic occupation of the lowest energy level, or when BEC is formed. The theory, and it's variations to accommodate multi-species condensates have been used with remarkable success to explain various experimental observations.

In this Chapter we use the second quantization formalism, in which the symmetry associated with the spin-statistics of identical and indistinguishable quantum particles is ensured by the algebra of the quantum field operators. That is, in terms of wave-functions, the operators ensure that the many-particle states of identical bosons and fermions are symmetric and antisymmetric under permutations of particles, respectively. To address the effects of quantum, and thermal fluctuations in the BECs of dilute atomic gases we use a spontaneous symmetry breaking approach. We start with the second quantized form of the Hamiltonian for a dilute, weakly interacting Bose gas, and derive the generalized GP and the coupled Bogoliubov-de Gennes equations. The former describes the condensate wave-function or the order parameter, and the latter is an extension of the Bogoliubov theory at zero temperature to describe the excitations or quasiparticles of the system.

2.1 Single-component BEC

2.1.1 Gross-Pitaevskii equation

At $T = 0$, following Bose-Einstein statistics, all the bosons in an ideal/interacting dilute Bose gas macroscopically occupy a single-particle quantum state. In the case of BEC of dilute atomic gases, as the temperature is decreased, quantum degeneracy sets in when the de Broglie wavelength of the atoms is equal to or larger than the inter-atomic spacing. Neglecting the quantum fluctuations, the condensed state can then be described by a macroscopic wavefunction $\Phi(\mathbf{r}, t)$. By mean-field theory, the static and dynamical properties of $\Phi(\mathbf{r}, t)$, albeit at $T = 0$, can be examined through the Gross-Pitaevskii (GP) equation [27, 116]. It is given by

$$i\hbar\frac{\partial\Phi(\mathbf{r},t)}{\partial t} = \left[-\frac{\hbar^2\nabla^2}{2m} + V_{\rm trap}(\mathbf{r}) + g|\Phi(\mathbf{r},t)|^2\right]\Phi(\mathbf{r},t). \tag{2.1}$$

The trapping potential $V_{\rm trap}$, unless otherwise mentioned, is in general harmonic in nature which is of the form

$$V_{\rm trap}(\mathbf{r}) = \frac{1}{2}m(\omega_x^2x^2 + \omega_y^2y^2 + \omega_z^2z^2), \tag{2.2}$$

where m is the mass of the atom, and ω_x, ω_y, and ω_z are the angular frequencies along x, y, and z directions, respectively. In a spherical trap, the angular frequencies satisfy the condition $(\omega_x = \omega_y = \omega_z \equiv \omega_0)$, whereas for a symmetric pancake shaped or quasi-2D trap it should be $(\omega_x = \omega_y \equiv \omega_\perp \ll \omega_z)$. For a cigar shaped or quasi-1D trap, the trapping frequencies satisfy $(\omega_x = \omega_y \equiv \omega_\perp \gg \omega_z)$. In the latter case, the radial excitation energies are large and the radial degrees of freedom are assumed to be frozen for which $\hbar\omega_\perp \gg \mu$ and $\hbar\omega_\perp \gg k_{\rm B}T$ where μ and T are the chemical potential and temperature of the system, respectively. So, the dynamics and hence the excitations occur only along the axial direction, z-axis, of the trap. The atoms interact through binary collisions. The interaction strength, the third term of Eq. (2.1), is proportional to the condensate density $n_c(\mathbf{r}, t) = |\Phi(\mathbf{r}, t)|^2$ with $g = 4\pi\hbar^2a/m$ as the interaction strength, where a is the s-wave scattering length, and to satisfy stability conditions we consider positive a for the present work. Although, we have neglected quantum fluctuations in the GP equation innate to any quantum system, it is more so

in macroscopic matter waves like BEC. However, BEC experiments are carried out at $T \neq 0$ and thermal fluctuations are unavoidable. Thus Eq. (2.1) needs to be generalized so as to incorporate the effects of the thermal cloud or the non-condensate atoms.

2.1.2 Many-body Hamiltonian

For simplicity, let us first consider quasi-1D system, where $(\omega_x = \omega_y \equiv \omega_\perp \gg \omega_z)$. In this case, we can integrate out the condensate wave function along xy and the dynamics of the BEC is reduced to a quasi-1D system. That is, along the transverse direction the system is limited to the ground state and degrees of freedom are frozen. Excitations, in form of quasiparticles, are present only in the axial direction z [117, 118]. For this system the many-body grand-canonical Hamiltonian describing BEC of N interacting bosons in the second quantized form is

$$\hat{H} = \int dz \hat{\Psi}^\dagger(z,t) \Big[-\frac{\hbar^2}{2m}\frac{\partial^2}{\partial z^2} + V(z) - \mu + \frac{U}{2}\hat{\Psi}^\dagger(z,t)\hat{\Psi}(z,t) \Big] \hat{\Psi}(z,t). \tag{2.3}$$

Here, $\hat{\Psi}$ is the Bose field operator of the single-species BEC that annihilates a boson at the position z and obeys the usual Bose commutation relations

$$\Big[\hat{\Psi}(z,t), \hat{\Psi}^\dagger(z',t)\Big] = \delta(z-z'), \Big[\hat{\Psi}(z,t), \hat{\Psi}(z',t)\Big] = \Big[\hat{\Psi}^\dagger(z,t), \hat{\Psi}^\dagger(z',t)\Big] = 0. \tag{2.4}$$

In Eq. (2.3), $V(z)$ and μ represent the external trapping potential and chemical potential, respectively. The intraspecies interactions is modified to $U = 2g\lambda$, and $\lambda = (\omega_\perp/\omega_z) \gg 1$ is the anisotropy parameter. In other words, higher anisotropy implies stronger effective inter-atomic interactions, and as a consequence enhances fluctuations. Starting with this Hamiltonian, the Heisenberg equation of motion for the Bose field operator is

$$i\hbar\frac{\partial}{\partial t}\hat{\Psi} = \Big[\hat{\Psi}(z,t), \hat{H}\Big] = \hat{h}\hat{\Psi} + U\hat{\Psi}^\dagger\hat{\Psi}\hat{\Psi}, \tag{2.5}$$

where $\hat{h} = (-\hbar^2/2m)\partial^2/\partial z^2 + V(z) - \mu$. For compact notations and when appropriate, we refrain from writing the explicit dependence of $\hat{\Psi}$ on z and t. Since majority of the atoms populate the ground state for the temperature domain pertinent to the experiments, using Bogoliubov approximation [119, 120] the condensate part can be separated out from the Bose field operator $\hat{\Psi}(z,t)$. For condensates in 3D the domain

of validity of the approximation is $T \leqslant 0.65T_c$ [106]. However, for a system of quasi-1D BECs, the anisotropy enhanced interaction should affect a change to the domain of validity, and shall be addressed in the subsequent chapters. The non-condensed or the thermal cloud of atoms are then the fluctuations of the condensate field. Here, T_c is the critical temperature for an ideal Bose gas in a harmonic confining potential.

2.1.3 Bogoliubov approximation

The Bose field operator $\hat{\Psi}$, in general, can be written as a linear combination of a complete set of single-particle wavefunctions $\{\psi_i(z)\}$ as

$$\hat{\Psi}(z,t) = \sum_{i=0} \hat{\alpha}_i(t)\psi_i(z) = \hat{\alpha}_0(t)\psi_0(z) + \sum_{i=1} \hat{\alpha}_i(t)\psi_i(z), \tag{2.6}$$

where $\hat{\alpha}_i$ is the annihilation operator of the ith state of the trapping potential of the system considered and obeys equal time commutation relations

$$\left[\hat{\alpha}_k, \hat{\alpha}_l^\dagger\right] = \delta_{k,l}, \left[\hat{\alpha}_k, \hat{\alpha}_l\right] = \left[\hat{\alpha}_k^\dagger, \hat{\alpha}_l^\dagger\right] = 0. \tag{2.7}$$

In addition, the single-particle wave-functions $\psi_i(z)$ satisfy the normalization condition

$$\sum_k \psi_k(z)\psi_k^*(z') = \delta(z - z'). \tag{2.8}$$

In Fock space, the operation of $\hat{\alpha}_i$ and $\hat{\alpha}_i^\dagger$ on an occupation number state [121] are defined through the equalities

$$\hat{\alpha}_i^\dagger|n_0\, n_1\, \cdots, n_i, \cdots\rangle = \sqrt{(n_i+1)}|n_0\, n_1, \cdots, n_i+1, \cdots\rangle, \tag{2.9a}$$

$$\hat{\alpha}_i|n_0\, n_1, \cdots, n_i, \cdots\rangle = \sqrt{n_i}|n_0\, n_1, \cdots, n_i-1, \cdots\rangle, \tag{2.9b}$$

where n_is are the eigenvalues of the number operator $\hat{\alpha}_i^\dagger\hat{\alpha}_i$, which denotes the number of atoms in the ith single-particle state. BEC occurs when the number of atoms n_0 in the single-particle ground state becomes very large, such that $n_0 \equiv N_0 \gg 1$. Here N_0 is the number of condensate atoms and the ratio N_0/N remains finite in the thermodynamic limit; N is the total number of atoms. To a very good approximation $N_0 \pm 1 \approx N_0$, that is, the two many-particle states with N_0 and $N_0 + 1$ atoms in the condensate are equivalent. This implies that the operators $\hat{\alpha}_0$ and $\hat{\alpha}_0^\dagger$ are c-numbers, so

that we can replace the operators as

$$\hat{\alpha}_0 = \hat{\alpha}_0^\dagger = \sqrt{N_0}. \tag{2.10}$$

This is referred to as Bogoliubov approximation [32, 119]. From Eq. (2.6), and using Eq. (2.10), one can write

$$\hat{\Psi}(z,t) = \sqrt{N_0}\psi_0(z)e^{-i\mu t/\hbar} + \tilde{\psi}(z,t), \tag{2.11}$$

where the first term on the right hand side represents the condensate part and $\tilde{\psi}(z,t) = \sum_{i=1} \hat{\alpha}_i(t)\psi_i(z)$ is the fluctuation operator. Thus one can now write

$$\hat{\Psi} = \phi + \tilde{\psi}, \tag{2.12}$$

where $\phi(z,t) = \sqrt{N_0}\psi_0(z)e^{-i\mu t/\hbar}$ is the condensate wavefunction or the order parameter [104]. It is to be noted that, only the fluctuation operator $\tilde{\psi}$ embodies the operator properties of $\hat{\Psi}$. With this decomposition, the field operator does not possess the same symmetries as the original Hamiltonian. The condensate wavefunction has a well-defined phase, and consequently global $U(1)$ gauge symmetry of the Hamiltonian is broken. Fixing the condensate phase leads to nonconservation of total number of particles, since these are canonically conjugate observables. This is, however fixed, when we work with the grand-canonical Hamiltonian through the inclusion of the chemical potential μ. This ensures that the total number of particles in the system is conserved [122, 123].

2.1.4 Hartree-Fock-Bogoliubov approximation

The operator $\tilde{\psi}$, depending on the system, may represent fluctuations due to thermal excitations, quantum nature of the system, or atoms excited to higher energy internal states due to interactions. Then, using Eq. (2.12) in Eq. (2.3), we obtain the Hartree-Fock-Bogoliubov Hamiltonian

$$\begin{aligned}\hat{H} \;=\; & \int dz \left\{\phi^*\left(\hat{h}-\mu\right)\phi + \tilde{\psi}^\dagger\left(\hat{h}-\mu\right)\tilde{\psi} + \phi^*\left(\hat{h}-\mu\right)\tilde{\psi} + \tilde{\psi}^\dagger\left(\hat{h}-\mu\right)\phi\right\} \\ & + \int dz\, \frac{U}{2}\left\{|\phi|^4 + \left(\phi^*|\phi|^2 + \phi^{*2}\phi\right)\tilde{\psi} + \left(|\phi|^2\phi + \phi^*\phi^2\right)\tilde{\psi}^\dagger \right. \\ & + \phi^{*2}\tilde{\psi}\tilde{\psi} + \phi^2\tilde{\psi}^\dagger\tilde{\psi}^\dagger + 4|\phi|^2\tilde{\psi}^\dagger\tilde{\psi} + 2\phi^*\tilde{\psi}^\dagger\tilde{\psi}\tilde{\psi} + 2\phi\tilde{\psi}^\dagger\tilde{\psi}^\dagger\tilde{\psi} \\ & \left. + \tilde{\psi}^\dagger\tilde{\psi}^\dagger\tilde{\psi}\tilde{\psi}\right\}. \end{aligned} \tag{2.13}$$

We can split the Hamiltonian into terms of different order in fluctuation as $\hat{H} = \hat{H}_0 + \hat{H}_1 + \hat{H}_2 + \hat{H}_3 + \hat{H}_4$, here n in $\hat{H}_n$ denotes the order of the fluctuation operators. The explicit form of the terms are

$$\hat{H}_0 = \int dz\, \phi^* \left(\hat{h} - \mu + \frac{U}{2}|\phi|^2\right) \phi, \tag{2.14a}$$

$$\hat{H}_1 = \int dz\, \phi^* \left(\hat{h} - \mu + U|\phi|^2\right) \tilde{\psi} + \tilde{\psi}^\dagger \left(\hat{h} - \mu + U|\phi|^2\right) \phi, \tag{2.14b}$$

$$\hat{H}_2 = \int dz\, \tilde{\psi}^\dagger \left(\hat{h} - \mu + 2U|\phi|^2\right) \tilde{\psi} + \frac{U}{2} \left(\phi^{*2}\tilde{\psi}\tilde{\psi} + \phi^2 \tilde{\psi}^\dagger \tilde{\psi}^\dagger\right), \tag{2.14c}$$

$$\hat{H}_3 = \int dz\, U \left(\phi^* \tilde{\psi}^\dagger \tilde{\psi}\tilde{\psi} + \phi \tilde{\psi}^\dagger \tilde{\psi}^\dagger \tilde{\psi}\right), \tag{2.14d}$$

$$\hat{H}_4 = \int dz\, \frac{U}{2} \tilde{\psi}^\dagger \tilde{\psi}^\dagger \tilde{\psi}\tilde{\psi}. \tag{2.14e}$$

The equivalent Feynman diagrams of these terms are shown in Fig. 2.1. In the figure the smooth solid and wiggly lines represent the non-condensate and condensate propagator, respectively, and the dashed lines represent the interatomic interaction [123].

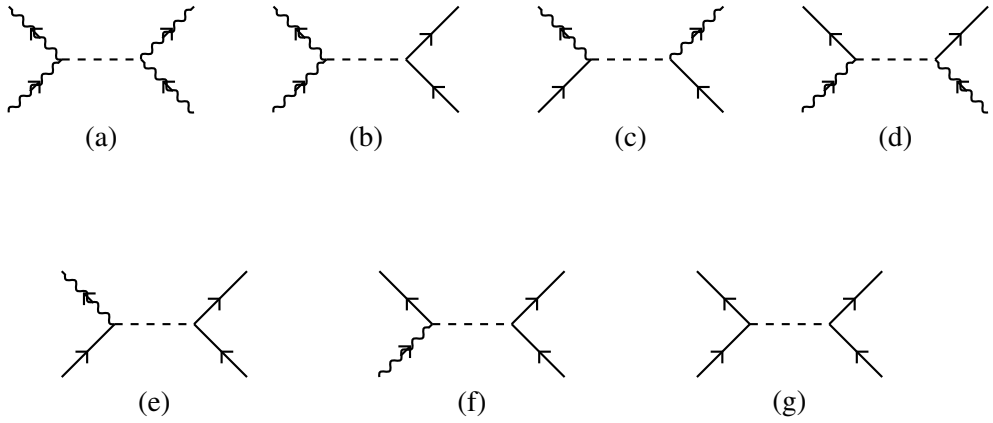

Figure 2.1: Feynman diagrams of scattering processes associated with the term (a) $\phi^*\phi^*\phi\phi$, (b) $\phi^*\phi\tilde{\psi}^\dagger\tilde{\psi}$, (c) $\phi^*\phi^*\tilde{\psi}\tilde{\psi}$, (d) $\phi\phi\tilde{\psi}^\dagger\tilde{\psi}^\dagger$, (e) $\phi^*\tilde{\psi}^\dagger\tilde{\psi}\tilde{\psi}$, (f) $\phi\tilde{\psi}^\dagger\tilde{\psi}^\dagger\tilde{\psi}$, (g) $\tilde{\psi}^\dagger\tilde{\psi}^\dagger\tilde{\psi}\tilde{\psi}$.

The fluctuations, both quantum and thermal, are white noise in character, and the fluctuation operators have zero ensemble average $\langle\tilde{\psi}(z,t)\rangle = \langle\tilde{\psi}^\dagger(z,t)\rangle = 0$ [124]. The condensate wavefunction or the order parameter is normalized as $\int |\phi(z)|^2\, dz = N_0$. Following the decomposition in Eq. (2.12), the second term of Eq. (2.5) can be written as

$$\hat{\Psi}^\dagger\hat{\Psi}\hat{\Psi} = |\phi|^2\phi + 2|\phi|^2\tilde{\psi} + \phi^2\tilde{\psi}^\dagger + \phi^*\tilde{\psi}\tilde{\psi} + 2\phi\tilde{\psi}^\dagger\tilde{\psi} + \tilde{\psi}^\dagger\tilde{\psi}\tilde{\psi}. \tag{2.15}$$

To reduce the interaction terms to quadratic form in fluctuation operators, the last term on the right hand side is approximated, using mean-field approximation and Wick's theorem, as

$$\tilde{\psi}^\dagger\tilde{\psi}\tilde{\psi} \simeq 2\langle\tilde{\psi}^\dagger\tilde{\psi}\rangle\tilde{\psi} + \langle\tilde{\psi}\tilde{\psi}\rangle\tilde{\psi}^\dagger. \tag{2.16}$$

Using the above approximation in Eq. (2.15) we obtain [104]

$$\hat{\Psi}^\dagger\hat{\Psi}\hat{\Psi} = |\phi|^2\phi + 2\left[|\phi|^2 + \langle\tilde{\psi}^\dagger\tilde{\psi}\rangle\right]\tilde{\psi} + \left[\phi^2 + \langle\tilde{\psi}\tilde{\psi}\rangle\right]\tilde{\psi}^\dagger + 2\phi\tilde{\psi}^\dagger\tilde{\psi} + \phi^*\tilde{\psi}\tilde{\psi}. \tag{2.17}$$

The stationary state solution of Eq. (2.5) is obtained by taking the average, and it is given by

$$\hat{h}\phi + U\langle\hat{\Psi}^\dagger\hat{\Psi}\hat{\Psi}\rangle = 0. \tag{2.18}$$

From the definitions of the fluctuation operators as $\langle\tilde{\psi}\rangle = \langle\tilde{\psi}^\dagger\rangle = 0$, we get

$$\langle\hat{\Psi}^\dagger\hat{\Psi}\hat{\Psi}\rangle = |\phi|^2\phi + 2\phi\langle\tilde{\psi}^\dagger\tilde{\psi}\rangle + \phi^*\langle\tilde{\psi}\tilde{\psi}\rangle. \tag{2.19}$$

Thus, with this definition Eq. (2.18) is reduced to

$$\hat{h}\phi(z) + U\left[n_c(z) + 2\tilde{n}(z)\right]\phi(z) + U\tilde{m}(z)\phi^*(z) = 0. \tag{2.20}$$

This is referred to as the generalized Gross-Pitaevskii equation with $n_c = |\phi|^2$, $\tilde{n} \equiv \langle\tilde{\psi}^\dagger\tilde{\psi}\rangle$, and $\tilde{m} \equiv \langle\tilde{\psi}\tilde{\psi}\rangle$ being the local condensate, non-condensate and anomalous density respectively. It is to be emphasized here that Eq. (2.16) neglects particle-exchanging collisions between condensed and thermal atoms. The anomalous average term $\tilde{m}$ is the expectation value of an unequal number of creation and annihilation operators, hence its name. In case of repulsively interacting BECs, $\tilde{m}$ plays a negligible role. But it is crucial in the study of attractive or molecular BECs [26]. The equation of motion of the fluctuation or non-condensate operator is given by

$$i\hbar\frac{\partial\tilde{\psi}}{\partial t} = i\hbar\frac{\partial}{\partial t}(\hat{\Psi} - \phi), \tag{2.21}$$

using Eqs. (2.5), and (2.20) it is simplified to

$$i\hbar\frac{\partial\tilde{\psi}}{\partial t} = \hat{h}\tilde{\psi} + U\left[\hat{\Psi}^\dagger\hat{\Psi}\hat{\Psi} - \langle\hat{\Psi}^\dagger\hat{\Psi}\hat{\Psi}\rangle\right]. \tag{2.22}$$

In the mean field approximation $\tilde{\psi}^\dagger\tilde{\psi} \simeq \langle\tilde{\psi}^\dagger\tilde{\psi}\rangle$, and $\tilde{\psi}\tilde{\psi} \simeq \langle\tilde{\psi}\tilde{\psi}\rangle$, then, the average of the three field operator in the above equation is reduced to

$$\hat{\Psi}^\dagger\hat{\Psi}\hat{\Psi} - \langle\hat{\Psi}^\dagger\hat{\Psi}\hat{\Psi}\rangle \simeq 2\langle\hat{\Psi}^\dagger\hat{\Psi}\rangle\tilde{\psi} + \langle\hat{\Psi}\hat{\Psi}\rangle\tilde{\psi}^\dagger. \tag{2.23}$$

From the above relation, the Eq. (2.22) assumes the form

$$i\hbar\frac{\partial\tilde{\psi}}{\partial t} = \hat{h}\tilde{\psi} + 2Un\tilde{\psi} + Um\tilde{\psi}^{\dagger}, \tag{2.24}$$

where $n \equiv n_c + \tilde{n}$, and $m \equiv \phi^2 + \tilde{m}$. The fluctuations, through the Bogoliubov transformation [119, 120] can be written as a linear combination of the quasiparticle modes or excited states of the condensate as

$$\tilde{\psi}(z,t) = \sum_j \left[u_j(z)\hat{\alpha}_j(z)e^{-iE_jt/\hbar} - v_j^*(z)\hat{\alpha}_j^{\dagger}(z)e^{iE_jt/\hbar}\right], \tag{2.25a}$$

$$\tilde{\psi}^{\dagger}(z,t) = \sum_j \left[u_j^*(z)\hat{\alpha}_j^{\dagger}(z)e^{iE_jt/\hbar} - v_j(z)\hat{\alpha}_j(z)e^{-iE_jt/\hbar}\right]. \tag{2.25b}$$

Here, $\hat{\alpha}_j$ ($\hat{\alpha}_j^{\dagger}$) are the quasiparticle annihilation (creation) operators and satisfy the usual Bose commutation relations, and the subscript j represents the energy eigenvalue index. The functions u and v are in general complex, and referred to as the Bogoliubov quasiparticle amplitudes. An important assumption in the derivations is that the quasiparticles are noninteracting, which is applicable when the condensate is with few excitations. Applying the above transformation to Eq. (2.24), and collecting prefactors of $e^{-iE_jt/\hbar}$ and $e^{iE_jt/\hbar}$, we obtain the following coupled Bogoliubov-de Gennes equations

$$(\hat{h} + 2Un)u_j - Umv_j = E_ju_j, \tag{2.26a}$$

$$-(\hat{h} + 2Un)v_j + Um^*u_j = E_jv_j. \tag{2.26b}$$

The above equations along with Eq. (2.20), are the Hartree-Fock-Bogoliubov (HFB) equations, and are to be solved self-consistently. They form the basis of our study of effect of finite temperature on Bose condensates. Returning to the quasiparticle amplitudes, they satisfy the following orthogonality and symmetry conditions

$$\int dz\left[u_pu_q^* - v_pv_q^*\right] = \delta_{pq}, \tag{2.27a}$$

$$\int dz\left[u_p^*v_q^* - v_p^*u_q^*\right] = 0, \tag{2.27b}$$

$$\int dz\left[u_pv_q - v_pu_q\right] = 0. \tag{2.27c}$$

The number density $\tilde{n}$ of non-condensate particles is then

$$\tilde{n} \equiv \langle\tilde{\psi}^{\dagger}\tilde{\psi}\rangle = \sum_j \left\{[|u_j|^2 + |v_j|^2]N_0(E_j) + |v_j|^2\right\}, \tag{2.28}$$

where $\langle\hat{\alpha}_j^\dagger\hat{\alpha}_j\rangle = (e^{\beta E_j}-1)^{-1} \equiv N_0(E_j)$ with $\beta = 1/k_{\rm B}T$, is the Bose factor of the quasiparticle state with energy E_j at temperature T. However, it should be emphasized that, when $T \to 0$, $N_0(E_j)$'s in Eq. (2.28) vanishes. The non-condensate density is then reduced to

$$\tilde{n} = \sum_j |v_j|^2, \tag{2.29}$$

which is independent of temperature and accounts for the quantum fluctuations. Following similar calculations, the anomalous density is given by

$$\tilde{m} \equiv \langle\tilde{\psi}\tilde{\psi}\rangle = -\sum_j u_j v_j^* [2N_0(E_j)+1] \tag{2.30}$$

The Eq. (2.26) is equivalent to solving a matrix eigenvalue problem of the form

$$E\begin{pmatrix} u \\ v \end{pmatrix} = \begin{pmatrix} \hat{h}+2Un & -Um \\ Um^* & -(\hat{h}+2Un) \end{pmatrix}\begin{pmatrix} u \\ v \end{pmatrix}. \tag{2.31}$$

In this thesis, the quasiparticle amplitudes u_j, v_j's are defined in the basis of the trapping potential, in particular, harmonic oscillator potential. Then,

$$u(z) = \sum_{i=0}^{N_b} c_i\varphi_i(z), \text{ and } v(z) = \sum_{i=0}^{N_b} d_i\varphi_i(z),$$

where, $|\varphi_i\rangle$'s are the harmonic-oscillator eigenstates, c_i and d_is are the expansion coefficients of the mode functions u and v, respectively, and N_b is the number of harmonic oscillator eigenstates chosen to represent the quasi-particle amplitudes. Thus, the matrix form of Eq. (2.31) is

$$E\begin{pmatrix} c_0 \\ \vdots \\ c_{N_b} \\ d_0 \\ \vdots \\ d_{N_b} \end{pmatrix} = \begin{pmatrix} \mathcal{L}_{00} & \cdots & \mathcal{L}_{0N_b} & -\mathcal{B}_{00} & \cdots & -\mathcal{B}_{0N_b} \\ \vdots & \ddots & \vdots & \vdots & \ddots & \vdots \\ \mathcal{L}_{N_b0} & \cdots & \mathcal{L}_{N_bN_b} & -\mathcal{B}_{N_b0} & \cdots & -\mathcal{B}_{N_bN_b} \\ \mathcal{B}_{00} & \cdots & \mathcal{B}_{0N_b} & -\mathcal{L}_{00} & \cdots & -\mathcal{L}_{0N_b} \\ \vdots & \ddots & \vdots & \vdots & \ddots & \vdots \\ \mathcal{B}_{N_b0} & \cdots & \mathcal{B}_{N_bN_b} & -\mathcal{L}_{N_b0} & \cdots & -\mathcal{L}_{N_bN_b} \end{pmatrix}\begin{pmatrix} c_0 \\ \vdots \\ c_{N_b} \\ d_0 \\ \vdots \\ d_{N_b} \end{pmatrix}, \tag{2.32}$$

where $\mathcal{L}_{pq} = \int \varphi_p(z)(\hat{h}+2Un)\varphi_q(z)\,dz$, and $\mathcal{B}_{pq} = \int \varphi_p(z)Um\varphi_q(z)\,dz$ are the matrix elements. The matrix is non-Hermitian and non-symmetric with a dimension of $2(N_b+1)\times 2(N_b+1)$, so it can have both real and complex eigenvalues depending on

the physical parameters of the system under study. The eigenvalue spectrum obtained from the diagonalization of the matrix has an equal number of positive and negative eigenvalues E_j's.

2.1.5 Hartree-Fock-Bogoliubov-Popov approximation

The HFB theory is gapped, there is a finite energy gap in the excitation spectrum, and violates Hugenholtz-Pines theorem [125]. According to the theorem, it is necessary that the energy spectrum arising from a theory based on symmetry-breaking should be gapless. To be precise, it should cost zero energy to excite the lowest mode, known as the Goldstone mode and corresponds to a rotation of the condensate phase. The energy gap in HFB theory arises from the approximate factorization of the operator averages. In particular, the inclusion of the anomalous average $\tilde{m}$ makes HFB theory ultraviolet divergent, which is an unavoidable outcome of the inconsistent treatment of atom-atom collisions through contact potential. One way to resolve the divergence is to regularize $\tilde{m}$ by subtracting the contributions from energy modes. Although the contribution from $\tilde{m}$ and $\tilde{n}$ are comparable, a consistent analysis of the condensate and non-condensate requires going beyond the quadratic Hamiltonian approximation. Details on the short comings of HFB method are discussed in Refs. [26, 126–130]. As an immediate solution is, in a heuristic way, ignoring the $\tilde{m}$ term, which is also known Popov approximation. It is a gapless finite temperature approximation which satisfies Hugenholtz-Pines theorem. Thus the equations under HFB-Popov approximation are

$$\hat{h}\phi(z) + U\left[n_c(z) + 2\tilde{n}(z)\right]\phi(z) = 0, \tag{2.33a}$$

$$(\hat{h} + 2Un)u_j - U\phi^2 v_j = E_j u_j, \tag{2.33b}$$

$$-(\hat{h} + 2Un)v_j + U\phi^{*2}u_j = E_j v_j, \tag{2.33c}$$

where, as mentioned earlier, $\tilde{n}$ is the non-condensate density. The order parameter ϕs and the non-condensate density $\tilde{n}$s are then calculated self-consistently using the above coupled equations [105, 106, 131, 132].

2.1.6 Local-Density approximation

The HFB-Popov equations, Eq. (2.33), can also be solved using the semiclassical WKB approximation, which in this context is referred to as *local-density approximation* (LDA) [133, 134]. For a quasi-1D system where z represents the axial direction, this approximation is equivalent to setting

$$\begin{aligned} u_j(z) \to u(p,z)e^{i\chi(z)} \quad , \quad v_j(z) \to v(p,z)e^{i\chi(z)}, \\ \sum_j \cdots \quad \to \quad \int \frac{dp}{2\pi}, \end{aligned} \tag{2.34}$$

where χ defines the local phase of the condensate and its gradient is the momentum $p = \partial\chi/\partial z$. The Bogoliubov quasiparticle amplitudes, as discussed earlier, are normalized as $|u(p,z)|^2 - |v(p,z)|^2 = 1$. In this limit, one assumes that $u(z)$ and $v(z)$ vary slowly, so the first order derivatives of u and v, and second order derivatives of χ are neglected. The Bogoliubov-de Gennes equations, then, assume the form

$$\left[\frac{p^2}{2m} + V(z) - \mu + 2Un(z)\right] u(p,z) - Un_c(z)v(p,z) = \epsilon(p,z)u(p,z), \tag{2.35a}$$

$$-\left[\frac{p^2}{2m} + V(z) - \mu + 2Un(z)\right] v(p,z) + Un_c(z)u(p,z) = \epsilon(p,z)v(p,z). \tag{2.35b}$$

For simplification define Hartree-Fock energy as $\epsilon_{\rm HF}(p,z) = p^2/2m + V - \mu + 2Un(z)$. With this definition

$$\epsilon_{\rm HF}(p,z)u(p,z) - Un_c(z)v(p,z) = \epsilon(p,z)u(p,z), \tag{2.36a}$$

$$-\epsilon_{\rm HF}(p,z)v(p,z) + Un_c(z)u(p,z) = \epsilon(p,z)v(p,z). \tag{2.36b}$$

This can be written as a matrix eigenvalue equation

$$\begin{pmatrix} \epsilon_{\rm HF} - \epsilon & -Un_c \\ Un_c & -\epsilon_{\rm HF} - \epsilon \end{pmatrix} \begin{pmatrix} u \\ v \end{pmatrix} = 0. \tag{2.37}$$

The characteristic or the secular equation gives the dispersion relation

$$\epsilon^2 = \epsilon_{\rm HF}^2 - U^2 n_c^2. \tag{2.38}$$

From Eq. (2.36) and using the normalization condition, mentioned earlier, we get

$$u^2 = \frac{\epsilon_{\rm HF} + \epsilon}{2\epsilon}; v^2 = \frac{\epsilon_{\rm HF} - \epsilon}{2\epsilon}. \tag{2.39}$$

The non-condensate density in the LDA, similar to Eq. (2.28), is then given by

$$\tilde{n} = \frac{1}{2\pi}\int dp\left[(|u|^2+|v|^2)N_0(\epsilon)+|v|^2\right], \tag{2.40}$$

where the momentum integral replaces the summation over the excited energy states in Eq. (2.28). This is applicable when the level spacing of the high-lying momentum states are small. Furthermore, the excitation energies considered must be much larger than the level spacing of the external trapping potential, that is, $k_{\rm B}T \gg \hbar\omega_{\rm HO}$. Substituting u and v, we get

$$\tilde{n} = \frac{1}{2\pi}\int dp\left[\frac{\epsilon_{\rm HF}}{\epsilon}\left(\frac{1}{e^{\beta\epsilon}-1}+\frac{1}{2}\right)-\frac{1}{2}\right]. \tag{2.41}$$

Using Eq. (2.38) the density of non-condensate atoms with LDA is

$$\tilde{n} = \frac{1}{2\pi}\int dp\left[\frac{\epsilon_{\rm HF}}{\epsilon}\left(\frac{1}{e^{\beta\epsilon}-1}+\frac{1}{2}\right)-\frac{1}{2}\right]\Theta(\epsilon_{\rm HF}^2-U^2n_c^2). \tag{2.42}$$

One may also use LDA for the entire energy excitation spectra and not just for the high-lying modes. In which case, the condensate must also be treated semiclassically like Thomas-Fermi (TF) approximation. So that the entire theory, describing the condensate and non-condensate atoms, is semiclassical at finite temperature and consistent. This scheme is applicable only when $Na \gg a_{\rm HO}$ (in the case of dilute ultracold atoms this corresponds to $N \approx 10^6$ with a density of $10^{12}-10^{14}$ cm^{-3}). Here $a_{\rm HO} = (\hbar/m\omega_{\rm HO})^{1/2}$ is the oscillator length scale associated with the geometric mean $\omega_{\rm HO}$ of the angular trapping frequencies [32]. Under the TF approximation, the kinetic energy term is neglected and the condensate density is

$$n_c = \left(\frac{\mu - V - 2U\tilde{n}}{U}\right)\Theta(\mu - V - 2U\tilde{n}). \tag{2.43}$$

The properties of Heaviside step function give rise to two possible cases: first, when $\mu < V + 2U\tilde{n}$, then $n_c = 0$ and hence, $\epsilon(p,z) = p^2/2m + V - \mu + 2U\tilde{n}(z)$; and second when $\mu > V + 2U\tilde{n}$, $\epsilon_{\rm HF} = p^2/2m + V - \mu + 2U\tilde{n}(z) + 2Un_c(z) = p^2/2m + Un_c$. Thus using Eq. (2.38) we get,

$$\epsilon = \left[\left(\frac{p^2}{2m}+Un_c\right)^2 - U^2n_c^2\right]^{1/2}. \tag{2.44}$$

To use the above semiclassical expressions for BECs in which TF approximation is not applicable, a threshold energy $\epsilon_{\rm th}$ is to be defined. It is defined such that, below $\epsilon_{\rm th}$

the quasiparticle excitations solve Eq. (2.33). For modes lying above $\epsilon_{\rm th}$, LDA can be used to obtain $\tilde{n}$. The total non-condensate density $\tilde{n}$ at finite temperature can thus be written as [122, 135]

$$\tilde{n}(z) = \sum_j \tilde{n}_j(z)\Theta(\epsilon_{\rm th} - E_j) + \int_{\epsilon_{\rm th}}^{\infty} d\epsilon\, \tilde{n}(\epsilon, z) \tag{2.45}$$

Using Eq. (2.42) and transforming the integration in momentum space to integration in terms of ϵ, we get

$$\begin{aligned}
\tilde{n}(\epsilon, \mathbf{r}) &= \frac{m^{1/2}}{2\sqrt{2}\pi} \int_{\epsilon_{\rm th}}^{\infty} d\epsilon \left(\sqrt{\epsilon^2 + U^2 n_c^2} + \mu - V - 2Un\right)^{-1/2} \left(\frac{1}{e^{\beta\epsilon} - 1} + \frac{1}{2}\right) \\
&- \frac{m^{1/2}}{4\sqrt{2}\pi} \int_{\epsilon_{\rm th}}^{\infty} d\epsilon\, \epsilon \left(\sqrt{\epsilon^2 + U^2 n_c^2} + \mu - V - 2Un\right)^{-1/2} / \sqrt{\epsilon^2 + U^2 n_c^2} \\
&= \frac{m^{1/2}}{2\sqrt{2}\pi} \int_{\epsilon_{\rm th}}^{\infty} d\epsilon \left(\sqrt{\epsilon^2 + U^2 n_c^2} + \mu - V - 2Un\right)^{-1/2} \\
&\times \left\{\frac{1}{e^{\beta\epsilon} - 1} + \frac{1}{2} - \frac{\epsilon}{2\sqrt{\epsilon^2 + U^2 n_c^2}}\right\}
\end{aligned} \tag{2.46}$$

The value of $\epsilon_{\rm th}$ depends on the problem of interest, and hence, must be chosen with care. It is worth mentioning here that for high-lying modes $> \epsilon_{\rm th}$ HFB-Popov theory and LDA do not differ much, and the reason is, the Bose-Einstein distribution factors for these states are small. However, the difference between these two approaches will be much more pronounced for the low-lying modes when the energy level spacing is larger, and cannot be approximated as a continuum. Thus for calculation of non-condensate density, HFB-Popov approximation is far more reliable.

2.2 Two-component BEC

We here generalize the finite temperature theory employed for the one-component system to an interacting two-component BEC. At $T = 0$, excluding quantum fluctuations, the total wavefunction of the TBEC is given by

$$\Phi(\mathbf{r}_1, \cdots, \mathbf{r}_{N_1}; \mathbf{r}'_1, \cdots, \mathbf{r}'_{N_2}) = \prod_{k=1}^{N_1} \psi_1(\mathbf{r}_k) \prod_{j=1}^{N_2} \psi_2(\mathbf{r}'_j). \tag{2.47}$$

Here $\mathbf{r}_k$ and $\mathbf{r}'_j$ denote the position of the particles of species 1 and species 2 respectively, with N_1 and N_2 as the number of particles of the constituent species. The

single-particle wave functions are given by ψ_1 and ψ_2. Furthermore, the single-particle wavefunction are normalized to unity so that the condensate wavefunctions belonging to each of the species are given by $\phi_1 = \sqrt{N_1}\psi_1$ and $\phi_2 = \sqrt{N_2}\psi_2$. Unlike in a single-component BEC, atoms of species 1 interact with atoms of species 2 which makes the system richer and allows the existence of different phases. For such a system, the energy functional reads

$$E = E_1 + E_2 + E_{12}, \tag{2.48}$$

where, E_1 and E_2 are the usual single-species energy functionals for species 1 and species 2, respectively. The term E_{12} arises due to the presence of the interspecies interaction. Thus the energy of the TBEC is given by

$$E = \int d\mathbf{r}\left[\sum_{k=1}^{2}\left(\frac{\hbar^2}{2m_k}|\nabla\phi_k|^2 + V_k(\mathbf{r})|\phi_k|^2 + \frac{1}{2}U_{kk}|\phi_k|^4\right) + U_{12}|\phi_1|^2|\phi_2|^2\right]. \tag{2.49}$$

Here m_k is the mass of the bosonic atom of species k, and V_k is the usual external harmonic trapping potential. The interaction strengths are given by $U_{kj} = 2\pi\hbar^2 a_{kj}/m_{kj}$, where $m_{kj}^{-1} = m_k^{-1} + m_j^{-1}$ is the reduced mass for an atom k and an atom j. Using these definitions we obtain the coupled time-independent Gross-Pitaevskii equations for a TBEC

$$\left[-\frac{\hbar^2}{2m_k}\nabla^2 + V_k(\mathbf{r}) + \sum_{j=1}^{2}U_{kj}|\phi_j|^2\right]\phi_k = \mu_k\phi_k, \tag{2.50}$$

when the energy functional $\varepsilon = E - \sum_k \mu_k N_k$ is variationally minimized with ϕ_k^* as the parameters of variation. The above Eq. (2.50) forms the starting point of our analysis of binary condensates at $T \neq 0$. Using the stability conditions, at equilibrium, depending upon the strength of the interatomic interactions, the condensates may either overlap spatially or phase-separate. The emergence of such different phases makes it drastically different from the usual single-species BEC and motivates us to study binary mixtures at $T \neq 0$. For these studies, as mentioned earlier we first solve Eqns. (2.50), and then we use HFB-Popov approximation to calculate the thermal cloud densities. At $T \neq 0$, along with the two coherent condensate clouds, there exist the incoherent non-condensate clouds belonging to each of the species. Apart from the interaction between the condensate and non-condensate cloud of the same species, interaction between

the condensate atoms of one species and the non-condensate of the other species also exists. The presence of an increased number of interaction terms in such a system makes it complicated and poses difficulty to theoretically model it. In the present work, we have assumed the thermal clouds of both the species are static, and consider temperature less than the lower critical temperature among the two. We present here a detailed description of the generalization of the coupled $T = 0$ Gross-Pitaevskii equations to $T \neq 0$. For simplicity, we consider a quasi-1D trap in which the radial degrees of freedom have been integrated out.

2.2.1 HFB approximation for the TBEC

Consider the grand-canonical Hamiltonian of a mixture of two interacting BECs, like in Eq. (2.3), for a quasi-1D trap it can be written as

$$\begin{aligned}\hat{H} &= \sum_{k=1,2}\int dz\hat{\Psi}_k^\dagger(z,t)\Big[-\frac{\hbar^2}{2m_k}\frac{\partial^2}{\partial z^2}+V_k(z)-\mu_k+\frac{U_{kk}}{2}\hat{\Psi}_k^\dagger(z,t)\hat{\Psi}_k(z,t)\Big]\hat{\Psi}_k(z,t)\\ &+ U_{12}\int dz\hat{\Psi}_1^\dagger(z,t)\hat{\Psi}_2^\dagger(z,t)\hat{\Psi}_1(z,t)\hat{\Psi}_2(z,t),\end{aligned} \tag{2.51}$$

where $k = 1, 2$ is the species index, $\hat{\Psi}_k$'s are the Bose field operators of the two different species, and μ_k's are the chemical potentials. The strength of intra- and interspecies interactions are $U_{11} = 8\pi\hbar^2 a_{11}\lambda/m_1$, $U_{22} = 8\pi\hbar^2 a_{22}\lambda/m_2$, and $U_{12} = (4\pi\hbar^2 a_{12}\lambda)/(2m_{12})$, respectively, where $\lambda = (\omega_\perp/\omega_z) \gg 1$ is the anisotropy parameter. In this thesis we consider all the interactions as repulsive, that is $a_{kk}, a_{12} > 0$. The Heisenberg equation of motion for the Bose field operator $\hat{\Psi}_k(z)$ in case of binary condensates in two-component notation is

$$i\hbar\frac{\partial}{\partial t}\begin{pmatrix}\hat{\Psi}_1\\ \hat{\Psi}_2\end{pmatrix}=\begin{pmatrix}\hat{h}_1+U_{11}\hat{\Psi}_1^\dagger\hat{\Psi}_1 & U_{12}\hat{\Psi}_2^\dagger\hat{\Psi}_1\\ U_{12}\hat{\Psi}_1^\dagger\hat{\Psi}_2 & \hat{h}_2+U_{22}\hat{\Psi}_2^\dagger\hat{\Psi}_2\end{pmatrix}\begin{pmatrix}\hat{\Psi}_1\\ \hat{\Psi}_2\end{pmatrix}, \tag{2.52}$$

where $\hat{h}_k = (-\hbar^2/2m_k)\partial^2/\partial z^2 + V_k(z) - \mu_k$. Similar to a single-component BEC, employing Bogoliubov approximation in a TBEC system, field operators can be written as $\hat{\Psi}_k(z,t) = \phi_k(z) + \tilde{\psi}_k(z,t)$, where $\phi_k(z)$ is a c-field and represents the condensate, and $\tilde{\psi}_k(z,t)$ is the fluctuation part of the kth species. We can write the total field

operator as

$$\begin{aligned}\begin{pmatrix}\hat{\Psi}_1\\ \hat{\Psi}_2\end{pmatrix} &= \begin{pmatrix}\phi_1\\ \phi_2\end{pmatrix} + \begin{pmatrix}\tilde{\psi}_1\\ \tilde{\psi}_2\end{pmatrix}, \\ \Rightarrow \hat{\Psi} &= \Phi + \tilde{\Psi},\end{aligned} \tag{2.53}$$

where Φ and $\tilde{\Psi}(z)$ are the condensate and fluctuation operator in two-component notations. Using the expression of $\hat{\Psi}_k$, we can separate the Hamiltonian as $\hat{H} = \sum_{k=1,2}\sum_{n=1}^{4}\hat{H}_n^k$, where $0 \leqslant n \leqslant 4$ denotes the order of the fluctuation operators. There are ten terms, and these are

$$\begin{aligned}
\hat{H}_0^1 &= \int dz\, \phi_1^*\left(\hat{h}_1 - \mu_1 + \frac{U_{11}}{2}|\phi_1|^2 + \frac{U_{12}}{2}|\phi_2|^2\right)\phi_1, \\
\hat{H}_0^2 &= \int dz\, \phi_2^*\left(\hat{h}_2 - \mu_2 + \frac{U_{22}}{2}|\phi_2|^2 + \frac{U_{12}}{2}|\phi_1|^2\right)\phi_2, \\
\hat{H}_1^1 &= \int dz\, \phi_1^*\left(\hat{h}_1 - \mu_1 + U_{11}|\phi_1|^2 + U_{12}|\phi_2|^2\right)\tilde{\psi}_1 + \tilde{\psi}_1^\dagger\left(\hat{h}_1 - \mu_1 + U_{11}|\phi_1|^2 + U_{12}|\phi_2|^2\right)\phi_1, \\
\hat{H}_1^2 &= \int dz\, \phi_2^*\left(\hat{h}_2 - \mu_2 + U_{22}|\phi_2|^2 + U_{12}|\phi_1|^2\right)\tilde{\psi}_2 + \tilde{\psi}_2^\dagger\left(\hat{h}_2 - \mu_2 + U_{22}|\phi_2|^2 + U_{12}|\phi_1|^2\right)\phi_2, \\
\hat{H}_2^1 &= \int dz\, \tilde{\psi}_1{}^\dagger\left(\hat{h}_1 - \mu_1 + 2U_{11}|\phi_1|^2 + U_{12}|\phi_2|^2\right)\tilde{\psi}_1 + \frac{U_{11}}{2}\left(\phi_1^{*2}\tilde{\psi}_1\tilde{\psi}_1 + \phi_1^2\tilde{\psi}_1^\dagger\tilde{\psi}_1^\dagger\right) \\
&\quad + \frac{U_{12}}{2}\left(\phi_1^*\phi_2^*\tilde{\psi}_1\tilde{\psi}_2 + \phi_1^*\phi_2\tilde{\psi}_2^\dagger\tilde{\psi}_1 + \phi_1\phi_2^*\tilde{\psi}_1^\dagger\tilde{\psi}_2 + \phi_1\phi_2\tilde{\psi}_1^\dagger\tilde{\psi}_2^\dagger\right), \\
\hat{H}_2^2 &= \int dz\, \tilde{\psi}_2{}^\dagger\left(\hat{h}_2 - \mu_2 + 2U_{22}|\phi_2|^2 + U_{12}|\phi_1|^2\right)\tilde{\psi}_2 + \frac{U_{22}}{2}\left(\phi_2^{*2}\tilde{\psi}_2\tilde{\psi}_2 + \phi_2^2\tilde{\psi}_2^\dagger\tilde{\psi}_2^\dagger\right) \\
&\quad + \frac{U_{12}}{2}\left(\phi_1^*\phi_2^*\tilde{\psi}_1\tilde{\psi}_2 + \phi_1^*\phi_2\tilde{\psi}_2^\dagger\tilde{\psi}_1 + \phi_1\phi_2^*\tilde{\psi}_1^\dagger\tilde{\psi}_2 + \phi_1\phi_2\tilde{\psi}_1^\dagger\tilde{\psi}_2^\dagger\right), \\
\hat{H}_3^1 &= \int dz\, U_{11}\left(\phi_1^*\tilde{\psi}_1^\dagger\tilde{\psi}_1\tilde{\psi}_1 + \phi_1\tilde{\psi}_1^\dagger\tilde{\psi}_1^\dagger\tilde{\psi}_1\right) + \frac{U_{12}}{2}\left(\phi_1^*\tilde{\psi}_2^\dagger\tilde{\psi}_1\tilde{\psi}_2 + \phi_2^*\tilde{\psi}_1^\dagger\tilde{\psi}_1\tilde{\psi}_2\right. \\
&\quad \left.+\phi_1\tilde{\psi}_1^\dagger\tilde{\psi}_2^\dagger\tilde{\psi}_2 + \phi_2\tilde{\psi}_1^\dagger\tilde{\psi}_2^\dagger\tilde{\psi}_1\right) \\
\hat{H}_3^2 &= \int dz\, U_{22}\left(\phi_2^*\tilde{\psi}_2^\dagger\tilde{\psi}_2\tilde{\psi}_2 + \phi_2\tilde{\psi}_2^\dagger\tilde{\psi}_2^\dagger\tilde{\psi}_2\right) + \frac{U_{12}}{2}\left(\phi_1^*\tilde{\psi}_2^\dagger\tilde{\psi}_1\tilde{\psi}_2 + \phi_2^*\tilde{\psi}_1^\dagger\tilde{\psi}_1\tilde{\psi}_2\right. \\
&\quad \left.+\phi_1\tilde{\psi}_1^\dagger\tilde{\psi}_2^\dagger\tilde{\psi}_2 + \phi_2\tilde{\psi}_1^\dagger\tilde{\psi}_2^\dagger\tilde{\psi}_1\right) \\
\hat{H}_4^1 &= \int dz\, \frac{U_{11}}{2}\tilde{\psi}_1^\dagger\tilde{\psi}_1^\dagger\tilde{\psi}_1\tilde{\psi}_1 + \frac{U_{12}}{2}\tilde{\psi}_1^\dagger\tilde{\psi}_2^\dagger\tilde{\psi}_1\tilde{\psi}_2 \\
\hat{H}_4^2 &= \int dz\, \frac{U_{22}}{2}\tilde{\psi}_2^\dagger\tilde{\psi}_2^\dagger\tilde{\psi}_2\tilde{\psi}_2 + \frac{U_{12}}{2}\tilde{\psi}_1^\dagger\tilde{\psi}_2^\dagger\tilde{\psi}_1\tilde{\psi}_2
\end{aligned} \tag{2.54}$$

The Feynman diagrams corresponding to the scattering processes due to intraspecies interactions U_{11}, U_{22} and interspecies interaction U_{12} are shown in Fig. 2.2 and Fig. 2.3, respectively. Using the definition of field operator from Eq. (2.53) in Eq. (2.52), the

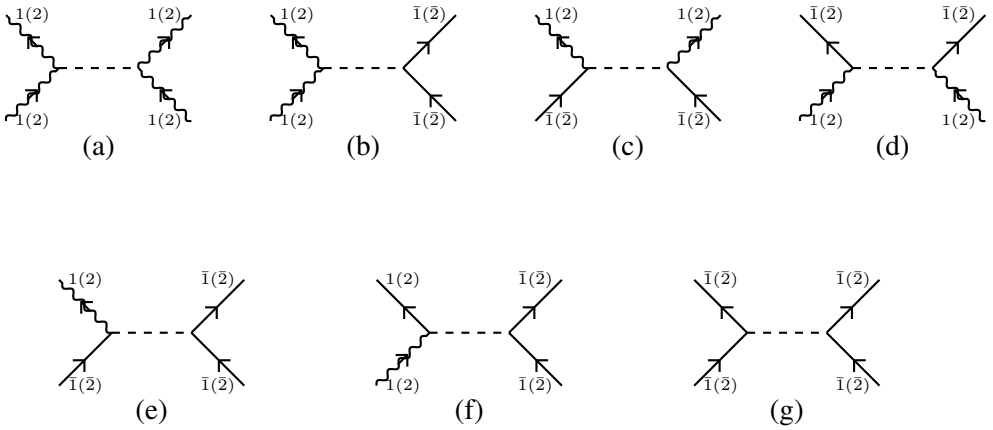

Figure 2.2: Various scattering processes solely due to the intraspecies interactions U_{11} and U_{22}. Here '1', '2', '$\bar{1}$', and '$\bar{2}$' represent ϕ_1, ϕ_2, $\tilde{\psi}_1$, and $\tilde{\psi}_2$, respectively. The smooth solid lines denote the non-condensate propagator, the wiggly lines represent the condensate propagator and the broken lines represent the interaction.

Heisenberg equation of motion for the first species ($k = 1$) is

$$\begin{aligned} i\hbar\frac{\partial(\phi_1+\tilde{\psi}_1)}{\partial t} &= \Big[\frac{-\hbar^2}{2m_1}\nabla^2\phi_1 - \frac{\hbar^2}{2m_1}\nabla^2\tilde{\psi}_1 + V_1\phi_1 + V_1\tilde{\psi}_1 \\ &\quad + U_{11}\hat{\Psi}_1^\dagger\hat{\Psi}_1\hat{\Psi}_1 + U_{12}\hat{\Psi}_2^\dagger\hat{\Psi}_2\hat{\Psi}_1 - \mu_1\phi_1 - \mu_1\tilde{\psi}_1\Big]. \end{aligned} \tag{2.55}$$

The interaction terms in the equation can be written in terms of c-number and fluctuation operators as

$$\hat{\Psi}_1^\dagger\hat{\Psi}_1\hat{\Psi}_1 = |\phi_1|^2\phi_1 + 2|\phi_1|^2\tilde{\psi}_1 + 2\phi_1\tilde{\psi}_1^\dagger\tilde{\psi}_1 + \phi_1^*\tilde{\psi}_1\tilde{\psi}_1 + \phi_1^2\tilde{\psi}_1^\dagger + \tilde{\psi}_1^\dagger\tilde{\psi}_1\tilde{\psi}_1, \tag{2.56a}$$

$$\begin{aligned} \hat{\Psi}_2^\dagger\hat{\Psi}_2\hat{\Psi}_1 &= |\phi_2|^2\phi_1 + |\phi_2|^2\tilde{\psi}_1 + \phi_2^*\tilde{\psi}_2\phi_1 + \phi_2^*\tilde{\psi}_2\tilde{\psi}_1 + \tilde{\psi}_2^\dagger\phi_2\phi_1 + \tilde{\psi}_2^\dagger\phi_2\tilde{\psi}_1 \\ &\quad + \tilde{\psi}_2^\dagger\tilde{\psi}_2\phi_1 + \tilde{\psi}_2^\dagger\tilde{\psi}_2\tilde{\psi}_1. \end{aligned} \tag{2.56b}$$

For the same reasons as in the single-component BEC $\langle\tilde{\psi}_k\rangle = \langle\tilde{\psi}_k{}^\dagger\rangle = 0$. Thus the expectation value of the product of operators are

$$\langle\hat{\Psi}_1^\dagger\hat{\Psi}_1\hat{\Psi}_1\rangle = |\phi_1|^2\phi_1 + \phi_1^*\langle\tilde{\psi}_1\tilde{\psi}_1\rangle + 2\phi_1\langle\tilde{\psi}_1^\dagger\tilde{\psi}_1\rangle + \langle\tilde{\psi}_1^\dagger\tilde{\psi}_1\tilde{\psi}_1\rangle, \tag{2.57a}$$

$$\begin{aligned} \langle\hat{\Psi}_2^\dagger\hat{\Psi}_2\hat{\Psi}_1\rangle &= |\phi_1|^2\phi_1 + \phi_2^*\langle\tilde{\psi}_2\tilde{\psi}_1\rangle + \phi_2\langle\tilde{\psi}_2^\dagger\tilde{\psi}_1\rangle + \phi_1\langle\tilde{\psi}_2^\dagger\tilde{\psi}_2\rangle \\ &\quad + \langle\tilde{\psi}_2^\dagger\tilde{\psi}_2\tilde{\psi}_1\rangle. \end{aligned} \tag{2.57b}$$

Taking, $\langle\tilde{\psi}_2\tilde{\psi}_1\rangle = \langle\tilde{\psi}_2^\dagger\tilde{\psi}_1\rangle = 0$, the equation of motion of the condensate of the first

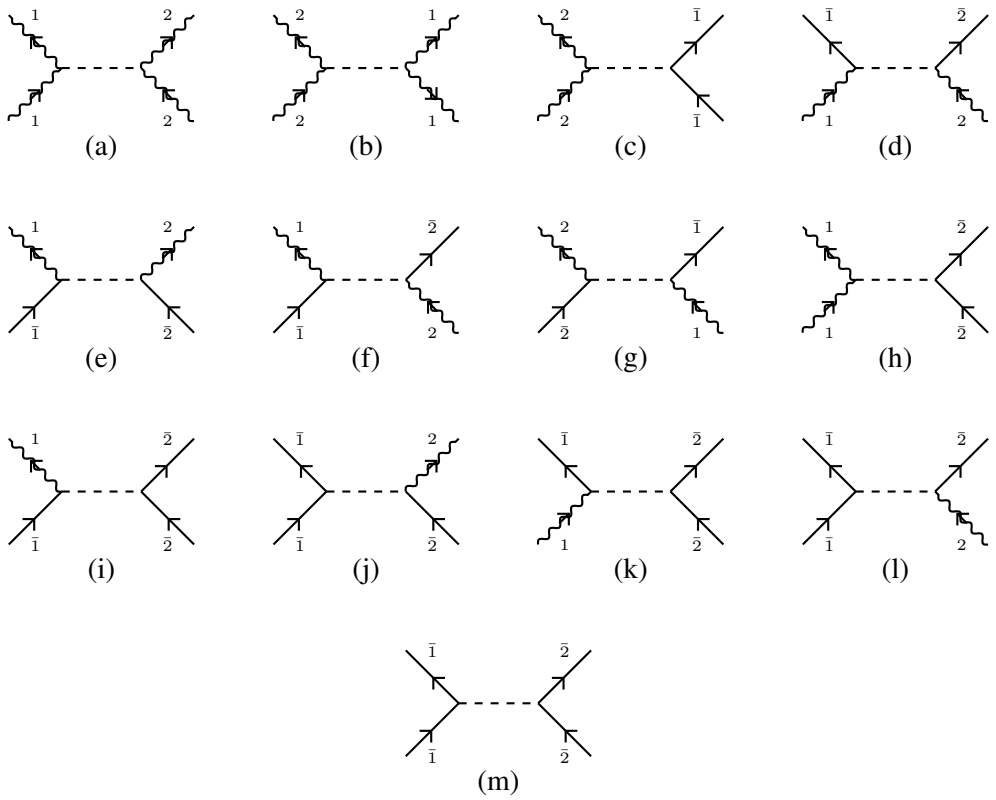

Figure 2.3: Various scattering processes arising due to the interspecies interactions U_{12}.

species is obtained by taking the average of Eq. (2.55) which is given by

$$\begin{aligned} i\hbar\frac{\partial\phi_1}{\partial t} &= \left[-\frac{\hbar^2}{2m_1}\nabla^2 + V_1 - \mu_1\right]\phi_1 + U_{11}\left[n_{1c} + 2\tilde{n}_1\right]\phi_1 + U_{11}\tilde{m}_1\phi_1^* \\ &+ U_{12}\left[n_{2c} + \tilde{n}_2\right]\phi_1 + \langle\tilde{\psi}_1^\dagger\tilde{\psi}_1\tilde{\psi}_1\rangle + \langle\tilde{\psi}_2^\dagger\tilde{\psi}_2\tilde{\psi}_1\rangle. \end{aligned} \tag{2.58}$$

Similarly, the equation of motion for the condensate of the second species is given by,

$$\begin{aligned} i\hbar\frac{\partial\phi_2}{\partial t} &= \left[-\frac{\hbar^2}{2m_2}\nabla^2 + V_2 - \mu_2\right]\phi_2 + U_{22}\left[n_{2c} + 2\tilde{n}_2\right]\phi_2 + U_{22}\tilde{m}_2\phi_2^* \\ &+ U_{12}\left[n_{1c} + \tilde{n}_1\right]\phi_2 + \langle\tilde{\psi}_2^\dagger\tilde{\psi}_2\tilde{\psi}_2\rangle + \langle\tilde{\psi}_1^\dagger\tilde{\psi}_1\tilde{\psi}_2\rangle, \end{aligned} \tag{2.59}$$

where we have introduced the local densities: $n_{kc} \equiv |\phi_k|^2$, $\tilde{n}_k \equiv \langle\tilde{\psi}_k^\dagger\tilde{\psi}_k\rangle$, $\tilde{m}_k \equiv \langle\tilde{\psi}_k\tilde{\psi}_k\rangle$ as the condensate, non-condensate, and anomalous densities, respectively. Proceeding, like in single-species BEC, the equation of motion for the non-condensate density of the first species is

$$i\hbar\frac{\partial\tilde{\psi}_1}{\partial t} = i\hbar\frac{\partial}{\partial t}(\hat{\psi}_1 - \phi_1). \tag{2.60}$$

Using Eq. (2.55) and Eq. (2.58) the equation can be expanded as,

$$\begin{aligned} i\hbar\frac{\partial\tilde{\psi}_1}{\partial t} &= \left(-\frac{\hbar^2}{2m_1}\nabla^2\tilde{\psi}_1 + V_1\tilde{\psi}_1 + 2U_{11}|\phi_1|^2\tilde{\psi}_1 + U_{12}|\phi_2|^2\tilde{\psi}_1 + 2U_{11}\tilde{n}_1\tilde{\psi}_1 - \mu_1\tilde{\psi}_1\right) \\ &+ U_{11}\phi_1^2\tilde{\psi}_1^\dagger + U_{12}\left(\phi_2^*\tilde{\psi}_2\tilde{\psi}_1 + \phi_1\phi_2^*\tilde{\psi}_2 + \phi_1\phi_2\tilde{\psi}_2^\dagger + \phi_2\tilde{\psi}_2^\dagger\tilde{\psi}_1\right) \\ &+ 2U_{11}\phi_1\left(\tilde{\psi}_1^\dagger\tilde{\psi}_1 - \tilde{n}_1\right) + U_{12}\phi_1\left(\tilde{\psi}_2^\dagger\tilde{\psi}_2 - \tilde{n}_2\right) + U_{11}\phi_1^*\left(\tilde{\psi}_1\tilde{\psi}_1 - \tilde{m}_1\right) \\ &- 2U_{11}\tilde{n}_1\tilde{\psi}_1 + U_{11}\left(\tilde{\psi}_1^\dagger\tilde{\psi}_1\tilde{\psi}_1 - \langle\tilde{\psi}_1^\dagger\tilde{\psi}_1\tilde{\psi}_1\rangle\right) + U_{12}\left(\tilde{\psi}_2^\dagger\tilde{\psi}_2\tilde{\psi}_1 - \langle\tilde{\psi}_2^\dagger\tilde{\psi}_2\tilde{\psi}_1\rangle\right). \end{aligned} \tag{2.61}$$

Applying mean-field approximation, $\tilde{\psi}_k^\dagger\tilde{\psi}_j \simeq \langle\tilde{\psi}_k^\dagger\tilde{\psi}_j\rangle$, $\tilde{\psi}_k\tilde{\psi}_j \simeq \langle\tilde{\psi}_k\tilde{\psi}_j\rangle$, $\tilde{\psi}_1^\dagger\tilde{\psi}_1\tilde{\psi}_1 \simeq 2\langle\tilde{\psi}_1^\dagger\tilde{\psi}_1\rangle\tilde{\psi}_1 + \langle\tilde{\psi}_1\tilde{\psi}_1\rangle\tilde{\psi}_1^\dagger$, $\tilde{\psi}_2^\dagger\tilde{\psi}_2\tilde{\psi}_1 \simeq \langle\,\tilde{\psi}_2^\dagger\tilde{\psi}_2\rangle\tilde{\psi}_1$. For fluctuation operators of the same species $k = j$, like in single-species, $\langle\tilde{\psi}_k^\dagger\tilde{\psi}_k\rangle = \tilde{n}_k$, and $\langle\tilde{\psi}_k\tilde{\psi}_k\rangle = \tilde{m}_k$. However, when the fluctuation operators are of different species $k \neq j$, we use the approximation $\langle\tilde{\psi}_k^\dagger\tilde{\psi}_j\rangle = \langle\tilde{\psi}_k\tilde{\psi}_j\rangle = 0$. Using these definitions and neglecting the three-field correlation term, the equation of motion of the fluctuation operator for the first species is

$$\begin{aligned} i\hbar\frac{\partial\tilde{\psi}_1}{\partial t} &= \left(-\frac{\hbar^2}{2m_1}\nabla^2 + V_1 + 2U_{11}(n_{1c} + \tilde{n}_1) - \mu_1 + U_{12}|\phi_2|^2 + U_{12}\tilde{n}_2\right)\tilde{\psi}_1 \\ &+ U_{11}\left(\phi_1^2 + \tilde{m}_1\right)\tilde{\psi}_1^\dagger + U_{12}\phi_1\phi_2^*\tilde{\psi}_2 + U_{12}\phi_1\phi_2\tilde{\psi}_2^\dagger. \end{aligned} \tag{2.62}$$

Similarly, the equation of motion of the fluctuation operator of the second species is,

$$\begin{aligned} i\hbar\frac{\partial\tilde{\psi}_2}{\partial t} &= \left(-\frac{\hbar^2}{2m_2}\nabla^2 + V_2 + 2U_{22}(n_{2c} + \tilde{n}_2) - \mu_2 + U_{21}|\phi_1|^2 + U_{21}\tilde{n}_1\right)\tilde{\psi}_2 \\ &+ U_{22}\left(\phi_2^2 + \tilde{m}_2\right)\tilde{\psi}_2^\dagger + U_{21}\phi_1^*\phi_2\tilde{\psi}_1 + U_{21}\phi_1\phi_2\tilde{\psi}_1^\dagger. \end{aligned} \tag{2.63}$$

For compact notation, we have used the definitions $n_k = n_{kc} + \tilde{n}_k$, $m_k = \phi_k^2 + \tilde{m}_k$. The next step is to diagonalize the Hamiltonian matrix and obtain the quasiparticle amplitude functions us and vs. After which, like in single-component BEC, under Bogoliubov transformation the fluctuation operators are

$$\tilde{\psi}_k = \sum_j \left[u_{kj}\hat{\alpha}_j e^{-iE_jt/\hbar} - v_{kj}^*\hat{\alpha}_j^\dagger e^{iE_jt/\hbar}\right], \tag{2.64a}$$

$$\tilde{\psi}_k^\dagger = \sum_j \left[u_{kj}^*\hat{\alpha}_j^\dagger e^{iE_jt/\hbar} - v_{kj}\hat{\alpha}_j e^{-iE_jt/\hbar}\right]. \tag{2.64b}$$

To recall, here k represents the species index, and the remaining symbols are as defined earlier. We take the operators α and $\alpha^\dagger$ as common to both the species, this is natural and consistent representation as the dynamics of the species are coupled. Furthermore,

this reproduces the standard coupled Bogoliubov-de Gennes equations at $T = 0$ and in the limit $a_{12} \to 0$, noninteracting TBEC, the quasiparticle spectra separates into two distinct sets: one set for each of the condensates. On substituting Eq. (2.64) in Eqns. (2.62) and (2.63) we obtain the following Bogoliubov-de Gennes equations for binary condensate mixtures

$$\left(-\frac{\hbar^2}{2m_1}\nabla^2 + V_1 + 2U_{11}n_1 + U_{12}n_{2c} + U_{12}\tilde{n}_2 - \mu_1\right) u_{1j} - U_{11}m_1 v_{1j} + U_{12}\phi_1\phi_2^* u_{2j} - U_{12}\phi_1\phi_2 v_{2j} = E u_{1j}, \quad (2.65a)$$

$$-\left(-\frac{\hbar^2}{2m_1}\nabla^2 + V_1 + 2U_{11}n_1^* + U_{12}n_{2c} + U_{12}\tilde{n}_2^* - \mu_1\right) v_{1j} + U_{11}m_1^* u_{1j} - U_{12}\phi_1^*\phi_2 v_{2j} + U_{12}\phi_1^*\phi_2^* u_{2j} = E_j v_{1j}, \quad (2.65b)$$

$$\left(-\frac{\hbar^2}{2m_2}\nabla^2 + V_2 + 2U_{22}n_2 + U_{12}n_{1c} + U_{12}\tilde{n}_1 - \mu_2\right) u_{2j} - U_{22}m_2 v_{2j} + U_{12}\phi_1^*\phi_2 u_{1j} - U_{12}\phi_1\phi_2 v_{1j} = E_j u_{2j}, \quad (2.65c)$$

$$-\left(-\frac{\hbar^2}{2m_2}\nabla^2 + V_2 + 2U_{22}n_2^* + U_{12}n_{1c} + U_{12}\tilde{n}_1^* - \mu_2\right) v_{2j} + U_{22}m_2^* u_{2j} - U_{12}\phi_1\phi_2^* v_{1j} + U_{12}\phi_1^*\phi_2^* u_{1j} = E_j v_2. \quad (2.65d)$$

The quasiparticle amplitudes are normalized as

$$\int dz\ \left(|u_1|^2 - |v_1|^2 + |u_2|^2 - |v_2|^2\right) = 1. \quad (2.66)$$

This normalization procedure for binary condensates follows from the fact that $\langle\tilde{\Psi}|\tilde{\Psi}\rangle = 1$, where $|\tilde{\Psi}\rangle$ is the two component representation of the fluctuations or non-condensate atoms. Such a representation is described earlier in Eq. (2.53) for the field operators, as for the components $\langle\tilde{\psi}_k|\tilde{\psi}_k\rangle = 1$. This gives consistent results in the limit $a_{12} \to 0$, the Bogoliubov-de Gennes equations of the two species are then decoupled and obtain two sets of normalized quasiparticle amplitudes corresponding to two independent single-species BEC.

Under time-independent HFB-Popov approximation, for a TBEC, ϕ_ks are thus the static solutions of the coupled generalized GP equations

$$\hat{h}_1\phi_1 + U_{11}\left[n_{c1} + 2\tilde{n}_1\right]\phi_1 + U_{12}n_2\phi_1 = 0, \quad (2.67a)$$

$$\hat{h}_2\phi_2 + U_{22}\left[n_{c2} + 2\tilde{n}_2\right]\phi_2 + U_{12}n_1\phi_2 = 0. \quad (2.67b)$$

The scaled Bogoliubov-de Gennes equations are

$$\hat{\mathcal{L}}_1 u_{1j} - U_{11}\phi_1^2 v_{1j} + U_{12}\phi_1\left(\phi_2^* u_{2j} - \phi_2 v_{2j}\right) = E_j u_{1j}, \tag{2.68a}$$

$$\underline{\hat{\mathcal{L}}}_1 v_{1j} + U_{11}\phi_1^{*2} u_{1j} - U_{12}\phi_1^*\left(\phi_2 v_{2j} - \phi_2^* u_{2j}\right) = E_j v_{1j}, \tag{2.68b}$$

$$\hat{\mathcal{L}}_2 u_{2j} - U_{22}\phi_2^2 v_{2j} + U_{12}\phi_2\left(\phi_1^* u_{1j} - \phi_1 v_{1j}\right) = E_j u_{2j}, \tag{2.68c}$$

$$\underline{\hat{\mathcal{L}}}_2 v_{2j} + U_{22}\phi_2^{*2} u_{2j} - U_{12}\phi_2^*\left(\phi_1 v_{1j} - \phi_1^* u_{1j}\right) = E_j v_{2j}, \tag{2.68d}$$

where $\hat{\mathcal{L}}_1 = \left(\hat{h}_1 + 2U_{11}n_1 + U_{12}n_2\right)$, $\hat{\mathcal{L}}_2 = \left(\hat{h}_2 + 2U_{22}n_2 + U_{12}n_1\right)$ and $\underline{\hat{\mathcal{L}}}_k = -\hat{\mathcal{L}}_k$ [136, 137]. To solve Eq. (2.68) we define, similar to the single-species case discussed in Section 2.1.4, u_k and v_k's as linear combination of N_b harmonic oscillator eigenstates,

$$\begin{aligned} u_{1j} &= \sum_{i=0}^{N_b} p_{ij}\varphi_i, \quad v_{1j} = \sum_{i=0}^{N_b} q_{ij}\varphi_i, \\ u_{2j} &= \sum_{i=0}^{N_b} r_{ij}\varphi_i, \quad v_{2j} = \sum_{i=0}^{N_b} s_{ij}\varphi_i, \end{aligned} \tag{2.69}$$

where φ_i is the ith harmonic oscillator eigenstate and p_{ij}, q_{ij}, r_{ij} and s_{ij} are the coefficients of linear combination. Using this expansion the Eq. (2.68) is then reduced to a matrix eigenvalue equation and solved using standard matrix diagonalization algorithms. The matrix has a dimension of $4(N_b+1) \times 4(N_b+1)$ and is non-Hermitian, non-symmetric and may have complex eigenvalues. The eigenvalue spectrum obtained from the diagonalization of the matrix has an equal number of positive and negative eigenvalues E_j's. Using the quasiparticle amplitudes obtained, the number density $\tilde{n}_k$ of the non-condensate atoms is

$$\tilde{n}_k = \sum_j \{[|u_{kj}|^2 + |v_{kj}|^2]N_0(E_j) + |v_{kj}|^2\}, \tag{2.70}$$

where $\langle \hat{\alpha}_j^\dagger \hat{\alpha}_j \rangle = (e^{\beta E_j} - 1)^{-1} \equiv N_0(E_j)$ is the Bose factor of the quasiparticle state with real and positive energy E_j. The coupled Eqns. (2.67) and (2.68) are solved iteratively till the solutions converge to desired accuracy. We use this theory to investigate the evolution of Goldstone modes and mode energies as a function of the interaction strengths and temperature. The results are discussed in the subsequent chapters. Although, HFB-Popov does have the advantage vis-a-vis calculation of the modes, it is nontrivial to get converged solutions.

Chapter 3

Evolution of Goldstone mode in binary BECs

The phenomenon of *spontaneous symmetry breaking* (SSB) is ubiquitous in nature, it appears at all energy scales ranging from the low-energy phase transition in ferromagnetism to unification of fundamental forces in high energy physics. It plays a pivotal role in critical phenomena for example, the paramagnetic to ferromagnetic transition [138], the exotic behaviour of superfluids and superconductors, etc. The same mechanism of SSB, explains the origin of mass in the elementary particles through the scalar field of *Higgs boson*, which was observed using Large Hadron Collider located at CERN in 2012 [139, 140]. A milestone experimental work which culminated in honoring François Englert and Peter W. Higgs with 2013 Nobel Physics Prize for their theoretical prediction of the Higgs boson [141–146].

To elucidate further, according to Goldstone's theorem when continuum symmetries of a system are spontaneously broken, then there exist gapless modes known as Nambu-Goldstone (NG) modes in the long-wavelength limit [147–149] for which the 2008 Nobel Physics Prize was awarded to Y. Nambu, M. Kobayashi, and T. Maskawa [150]. In relativistic or Lorenz-invariant systems the number of NG ($n_{\rm NG}$) modes coincides with the number of broken symmetries ($n_{\rm SSB}$), and the energy ϵ is linear in momentum p. That is, the dispersion relation in such systems is $\epsilon \propto p$ [75]. However, for systems lacking Lorentz invariance that is either non-relativistic systems or relativistic systems at nonzero density, this prescription of counting NG modes fails [151].

NG theorem has limitations for systems with spontaneously broken space-time symmetry, and further assumptions are required to guarantee the validity of this theorem. The intricacies, and right approach to count NG modes in non-relativistic systems, and generalization of NG theorem has been reviewed in Refs. [152–157].

For the current work, we consider scalar BECs which is accompanied by the appearance of a complex order parameter. This is a result of SSB of the global $U(1)$ symmetry, and the accompanying NG mode is a phonon. In addition, if the spatial symmetry of the system is also spontaneously broken the NG theorem for these systems becomes non-trivial and is a topic of active research in the current years. To cite an example in which $n_{\rm NG} \neq n_{\rm SSB}$, let us consider a BEC with a vortex line along the axial direction z. The translational symmetries in the radial directions x and y are explicitly broken, hence $n_{\rm SSB} = 3$. However, the system has $n_{\rm NG} = 2$; the Kelvin mode with a quadratic and the varicose mode with a linear dispersion relation [158–161].

Another relevant but rather non-trivial example is a system consisting of two-component Bose-Einstein condensates (TBECs). The system is characterized by two complex order parameters belonging to the constituent species and the low-lying excitation spectrum has two NG modes associated with two broken $U(1)$ symmetries. The TBECs may be miscible or immiscible (phase-separated) depending on the intra- and the interspecies interaction strengths. Depending on the phase of TBEC, more Goldstone modes may appear in the excitation spectrum. In this chapter, we use HFB-Popov approximation to investigate the evolution of Goldstone modes and mode energies as a function of the interspecies interaction in TBECs, more specifically phase-separated TBECs. Recent work [74] reported the existence of an additional Goldstone mode at phase-separation in the symmetry-broken density profiles, which we refer to as the *side-by-side* density profiles. In Ref. [75], it has been shown that in side-by-side density profiles where domain walls are formed at the interface, the translational symmetry normal to the wall is broken and zero energy is required for transverse shift of the wall. Thus, despite $n_{\rm SSB} = 3$ the system has $n_{\rm NG} = 2$ namely a ripplon and phonon. We, however, demonstrate that in the other type of density profile where one of the species is surrounded on both sides by the other, which we refer to as the *sandwich* type, the mode evolves very differently.

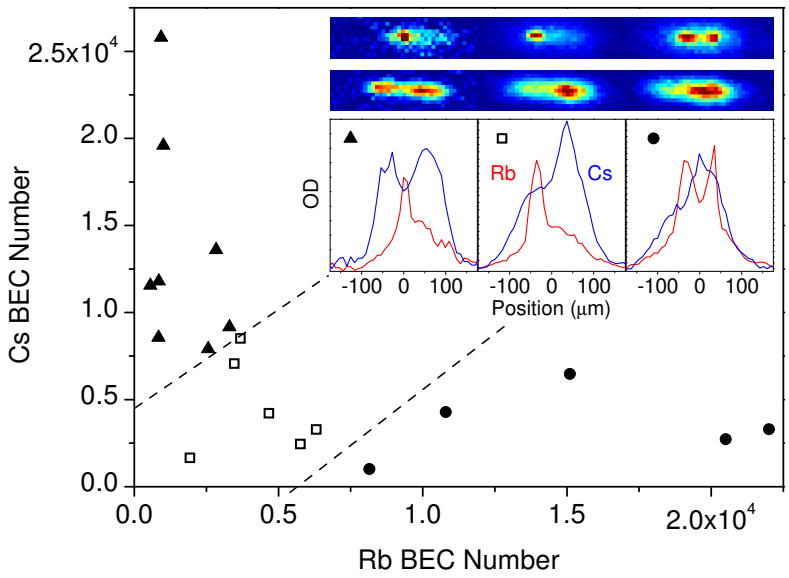

Figure 3.1: False color coded experimental images of ^{87}Rb- ^{133}Cs TBEC taken by the method of absorption imaging. These images show three distinct structures of the TBEC correlated with the number of atoms in each condensate. Reprinted figure from [McCarron *et al.*, *Phys. Rev. A* **84**, 011603(R) (2011).] Copyright © 2011 by the American Physical Society.

In the first part of the work, we consider the trapped TBEC of ^{87}Rb-^{133}Cs [48, 49], with coincident trap centers at $T = 0$. The images of density distribution, and plots of density profiles in one of the experimental realizations of ^{87}Rb-^{133}Cs TBEC [49] are shown in Fig. 3.1. It is evident that the TBEC exhibit different structures for varied combination of number of atoms from each species. This mixture has widely differing s-wave scattering lengths and masses. This choice does add to the severity of the convergence issues but this also makes it a good test for the methods we use. We choose the parameter domain where the system is quasi-1D and a mean-field description like HFB-Popov is applicable. The quasi-1D trapped bosons exhibit a rich phase structure as a function of density and interaction strengths [162]. For comparison with the experimental results we also consider the parameters as in the experiment [49]. We find that, like in Ref. [163], the quasi-1D descriptions are in good agreement with the condensate density profiles of 3D calculations [164]. We also discuss the evolution of Goldstone modes in trapped TBECs with separated trap centers. In the latter part of the work, we further examine the softening of higher excited modes to Goldstone

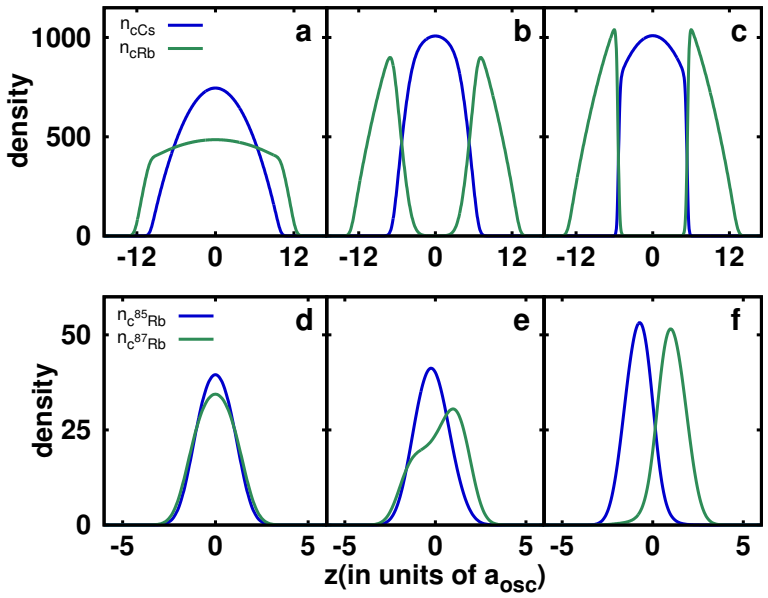

Figure 3.2: Transition to phase-separation and structure of the density profiles in TBEC. (a-c) show the transition from miscible to sandwich type density profile with the change in interspecies scattering length a_{CsRb} for a Cs-Rb TBEC and correspond to $a_{\mathrm{CsRb}} = \{200a_0, 310a_0, 420a_0\}$ respectively. The density profiles in (c) is referred to as the sandwich type. (d-f) show the transition from miscible to side-by-side density profile with the change in $a_{^{85}\mathrm{Rb}^{87}\mathrm{Rb}}$ for a ^{85}Rb $-^{87}$ Rb TBEC and correspond to $a_{^{85}\mathrm{Rb}^{87}\mathrm{Rb}} = \{100a_0, 290a_0, 400a_0\}$ respectively. The density profile in (f) is referred to as the side-by-side type. In the plots density is measured in units of a_{osc}^{-1}.

modes in TBECs with a dark soliton. We show that the presence of soliton induces instability in single and binary condensates.

3.1 Mode evolution of trapped TBEC at $T = 0$

In TBECs, when the TF approximation is applicable phase-separation occurs when the interactions satisfy the condition $U_{12} > \sqrt{U_{11}U_{22}}$ [43, 44, 165–167]. For the present work, we consider Cs and Rb as the first and second species, respectively. With this identification $a_{11} = a_{\mathrm{CsCs}} = 280a_0$ and $a_{22} = a_{\mathrm{RbRb}} = 100a_0$, where a_0 is the Bohr radius, and arrive at the condition for phase separation $a_{12} = a_{\mathrm{CsRb}} > 261a_0$ using TF approximation, which is smaller than the background value of $a_{\mathrm{CsRb}} \approx 650a_0$ [48]. To examine the nature of modes in the neighbourhood of phase-separation, we com-

pute the mode energies and functions at $T = 0$ and vary $a_{\rm CsRb}$, which is experimentally possible with the Cs-Rb magnetic Feshbach resonance [168]. The evolution of the low-lying modes in the domain $0 \leqslant a_{\rm CsRb} \leqslant 450a_0$ with $N_{\rm Cs} = N_{\rm Rb} = 10^4$ are computed with $\omega_{z({\rm Rb})} = 2\pi \times 3.89$ Hz and $\omega_{z({\rm Cs})} = 2\pi \times 4.55$ Hz as in Refs. [49, 164]. However, to satisfy the basic condition of $\omega_\perp \gg \omega_z$ for a quasi-1D system we take $\omega_\perp = 50\omega_z$, so that $\hbar\omega_\perp \gg \mu_k$. In addition, there are two relevant quasi-1D parameters, namely α and γ. The former is the ratio between the interaction strength and the trap frequency ω_z, and latter is the ratio of interaction to kinetic energy is represented. Depending on the values of α, γ and the total number of atoms, the quasi-1D system can either be in TF, or Gaussian or Tonks-Girardeau regime. For the parameters considered here $\alpha = 2a_{\rm CsCs}\sqrt{(\omega_\perp/\omega_z)(m\omega_\perp/\hbar)} \approx 0.36$ and $\gamma = 2(a_{\rm CsCs}/n_{\rm Cs})(m\omega_\perp/\hbar) \approx 10^{-5}$, so the system is in the weakly interacting TF regime [162] and mean field description through GP equation is valid. For this set of parameters the ground state is of sandwich geometry, in which the species with the heavier mass is at the center and flanked by the species with lighter mass at the edges. An example of the sandwich profile corresponding to the experimentally relevant [49, 164] parameters is shown in Fig. 3.2(c). On the other hand for TBEC with species of equal or near equal masses and low number of atoms, in general, the ground state geometry is side-by-side. As an example the side-by-side ground state density profile of ^{85}Rb-^{87}Rb TBEC is shown in Fig. 3.2(f). One important aspect which deserves due attention, considering we have chosen equal and specific number of atoms in each species, is the precise control of atom numbers in cold atom experiments. Achieving TBECs of equal atom numbers in experiments is a challenging task, and in general, the observed number of atoms of each species has $10 - 20\%$ uncertainties. However, for this typical uncertainty range, the change in the mode evolution in our present calculations is small when compared to the mixtures of equal atom numbers. But, the key point is, the overall the trend is remains unchanged. For instance, with the transition from miscible to phase-separated domain, there is $\approx 2\%$ change in the value of U_{12} at phase-separation.

From here on we consider the same set of ω_z ($\omega_{z({\rm Rb})} = 2\pi \times 3.89$ Hz and $\omega_{z({\rm Cs})} = 2\pi \times 4.55$ Hz), as mentioned earlier, for the results of calculations reported in this chapter. In the computations we scale the spatial and temporal variables as $z/a_{\rm osc(Cs)}$

and $\omega_{z(\mathrm{Cs})}t$ which render the equations dimensionless. Moreover all the $T = 0$ computations are performed ignoring the quantum fluctuations. That is, we solve the usual Bogoliubov-de-Gennes equations to examine the mode evolution at $T = 0$. We have observed that the mode energies computed with the inclusion of quantum fluctuations, using HFB-Popov approximation, are lower than what is predicted by the standard Hartree-Fock-Bogoliubov approach. Ranging from the miscible to completely immiscible regimes, the contribution from the quantum fluctuations varies and amounts to $\approx 0.1\% < \Delta\omega < 3\%$. So, in qualitative terms, the quantum fluctuations do not render any significant changes to the trend in the mode evolution. When $a_{\mathrm{CsRb}} = 0$, the U_{CsRb} dependent terms in Eq. (2.68) are zero and the spectrum of the two species are independent as the two condensates are decoupled. The system has two Goldstone modes, one each for the two species. The two lowest modes with nonzero excitation energies are the Kohn modes of the two species, and these occur at $\hbar\omega_{z(\mathrm{Cs})}$ and $0.85\hbar\omega_{z(\mathrm{Cs})}$ for Cs and Rb species, respectively. The existence of these Kohn modes follow from the Kohn's theorem [169]. It states that, there is a mode in which the center of mass of any trapped condensate oscillates with the frequency of the harmonic trapping potential [170]. This mode frequency is independent of the interaction strength or the type of interaction. This is similar to the cyclotron resonance frequency of electrons in a 3D electron gas in the presence of an uniform magnetic field, which remains unchanged inspite of the electron-electron Coloumbic interactions [169]. However, in a magnetic trap, in the vicinity of a Feshbach resonance Kohn's theorem has been shown to break down [171].

3.1.1 Third Goldstone mode

The neat separation between the modes of the two species is lost and mode mixing occurs when $a_{\mathrm{CsRb}} > 0$. For example, the Kohn modes of the two species intermix when $a_{\mathrm{CsRb}} > 0$, however, there is a difference in the evolution of the mode energies. The energy of the Rb Kohn mode decreases, but the one corresponding to Cs remains steady at $\hbar\omega_{z(\mathrm{Cs})}$. At higher a_{CsRb} the energy of the Rb Kohn mode decreases further and goes soft, or its energy tends to zero at phase-separation ($U_{\mathrm{CsRb}} > \sqrt{U_{\mathrm{CsCs}}U_{\mathrm{RbRb}}}$) when $a_{\mathrm{CsRb}} \approx 310a_0$. It is to be noted that the value of a_{CsRb} at which phase-separation

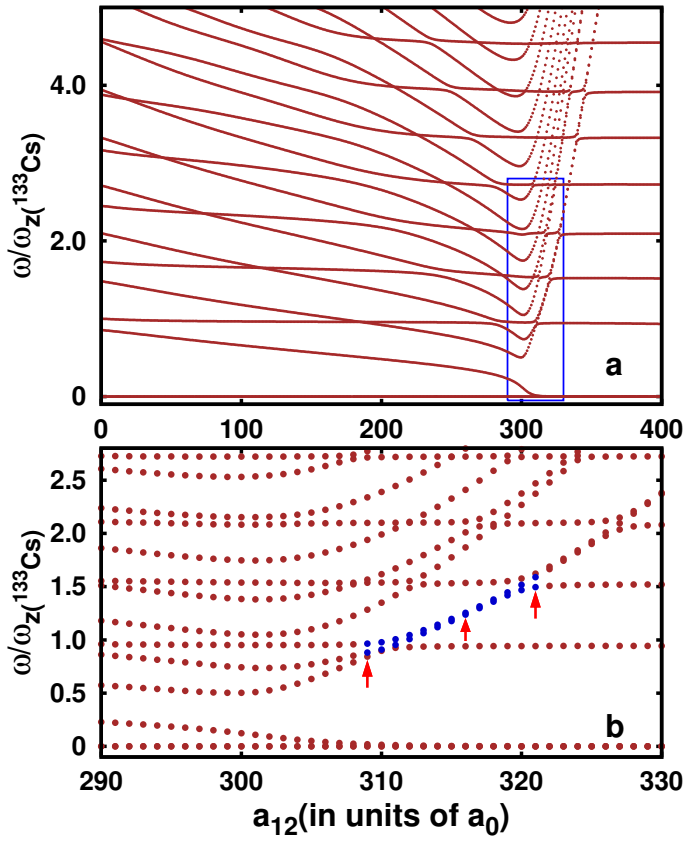

Figure 3.3: The evolution of the modes as a function of the interspecies scattering length a_{CsRb} in Cs-Rb TBEC. (a) shows the evolution of the low-lying modes in the domain $0 \leqslant a_{\mathrm{CsRb}} \leqslant 400a_0$ for $N_{^{87}\mathrm{Rb}} = N_{^{133}\mathrm{Cs}} = 10^4$. (b) is the enlarged view of the region enclosed within the blue colored rectangular box in figure (a) to resolve the avoided crossing and quasidegeneracy of modes (highlighted with dark-blue points). The points marked with red arrows correspond to interspecies scattering length $a_{\mathrm{CsRb}} = \{309a_0, 316a_0, 321a_0\}$ respectively.

occurs is higher with the numerical solution of GP equation than the value obtained from the TF approximation. This introduces a new Goldstone mode of the Rb BEC to the excitation spectrum. The reason is, for the parameters chosen, the density profiles at phase-separation assume sandwich geometry with Cs BEC at the center and Rb BEC at the edges. So, the Rb BEC clouds at the edges are effectively two topologically distinct BECs, and two Goldstone modes with the same $|u_{\mathrm{Rb}}|$ and $|v_{\mathrm{Rb}}|$ but different phases occur in the spectrum, and the global phase symmetry of the Rb condensate is broken. A similar result of the Kohn mode going soft was observed for single-species BEC confined in a double well potential [172]. Although, the two systems are very different,

the genesis of Kohn mode going soft is common: partition of one condensate cloud into two distinct ones. This could be, in our case by another condensate or by a potential barrier as in Ref. [172]. However, the phenomenon of diminishing energy difference between the Goldstone and the Kohn modes at phase-separation is unique, and different from the case of energy level splitting due to tunneling in a double-well potential. To start with, the two states are degenerate with zero barrier height in the conventional double-well potential with an adjustable barrier, and is exponentially suppressed in the asymptotic limit [173]. In the present case, the energy difference between the two relevant modes, Kohn and Goldstone modes, is finite for TBECs with parameter set analogous ($a_{\rm CsRb} = 0$) to the zero barrier height in the double-well potential. The separation is reduced when $a_{\rm CsRb}$ is increased, and the structure of the density profiles gets modified. In the domain where $a_{\rm CsRb} > 0$, but prior to phase separation, TBEC does not have an analogous counter part with the case of double-well potential. At higher values of $a_{\rm CsRb}$, when phase-separation sets in, one of the Kohn mode goes soft and the mode function has structural similarities to the exponentially suppressed state in the double-well potential. However, the similarity between the systems is only that, and it is not possible to extend beyond it. The interpretation of tunneling of Rb atoms through Cs atoms would lead to instabilities across the interface separating the two TBECs which, in the present case is not noticeable in the excitation spectra. It is an example of phase-transition with the appearance of level-crossings in the excitation spectrum [174].

To examine the mode evolution with the experimentally realized parameters [49], we repeat the computations with $\omega_{\perp({\rm Cs})} = 2\pi \times 40.2$ Hz and $\omega_{\perp({\rm Rb})} = 2\pi \times 32.2$ Hz. With these parameters the system is not strictly quasi-1D as $\hbar\omega_{\perp k} \approx \mu_k$ for $N_{\rm Cs} = N_{\rm Rb} = 10^4$, however, as $\omega_{zk} \ll \omega_{\perp k}$ there are qualitative similarities to a quasi-1D system [163]. Indeed, with the variation of $a_{\rm CsRb}$ the modes evolve similar to the case of $\omega_{\perp k} = 50\omega_{zk}$ and low-energy modes are shown in Fig. 3.3(a). The evolution of the Rb Kohn mode functions ($u_{\rm Rb}$ and $v_{\rm Rb}$) with $a_{\rm CsRb}$ are shown in Fig. 3.4. It is evident from Fig. 3.4(a) that when $a_{\rm CsRb} = 0$, there is no admixture from the Cs Kohn mode ($u_{\rm Cs} = v_{\rm Cs} = 0$). However, when $0 < a_{\rm CsRb} \lesssim 310a_0$ the admixture from the Cs Kohn mode increases initially and then goes to zero as we approach $U_{\rm CsRb} > \sqrt{U_{\rm CsCs}U_{\rm RbRb}}$

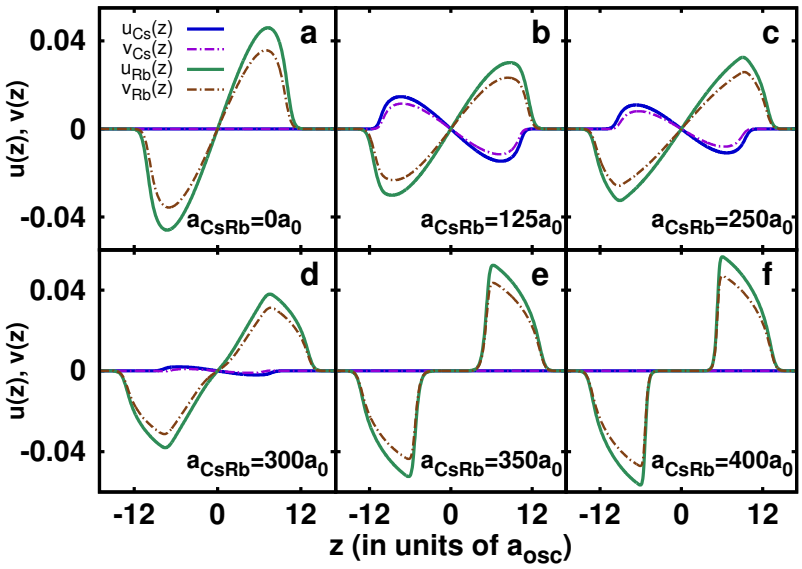

Figure 3.4: Evolution of quasiparticle amplitude corresponding to the Rb Kohn mode as $a_{\rm CsRb}$ is increased from 0 to $400a_0$. For better visibility $u_{\rm cs}$ and $u_{\rm Rb}$ are scaled by a factor of 1.2. (a) When $a_{\rm CsRb} = 0$, it is a Kohn mode of the Rb condensate. (b-d) In the domain $0 < a_{\rm CsRb} \lesssim 310a_0$ the mode acquires admixtures from the Cs Kohn mode (nonzero $u_{\rm Cs}$ and $v_{\rm Cs}$). (e-f) At phase-separation $310a_0 \lesssim a_{\rm CsRb}$ the mode transforms to a Goldstone mode: $u_{\rm Rb}$ and $v_{\rm Rb}$ have same profile as the $n_{\rm Rb} = |\phi_{\rm Rb}|^2$ but with a phase difference. In the plots u's and v's are in units of $a_{\rm osc}^{-1/2}$.

(Fig. 3.4(b-f)).

One striking result is, the Rb Kohn mode after going soft at $a_{\rm CsRb} \approx 310a_0$, as shown in Fig. 3.3(a), continues as the third Goldstone mode for $310a_0 < a_{\rm CsRb}$. This is different from the evolution of the zero energy mode in TBEC with side-by-side density profiles. In this case after phase separation, z-parity symmetry of the system is broken and the zero energy mode regains energy. So, there are only two Goldstone modes in the system. This is evident from Fig. 3.5, where we show the mode evolution of ^{85}Rb-^{87}Rb mixture with side-by-side density profiles at phase-separation. The parameters of the system considered are $N_{^{85}\rm Rb} = N_{^{87}\rm Rb} = 10^2$ with the same ω_{zk} and $\omega_{\perp k}$ as in the Cs-Rb mixture. Here, we use intraspecies scattering lengths as $99a_0$ and $100a_0$ for ^{85}Rb and ^{87}Rb, respectively and tune the interspecies interaction for better comparison with the Cs-Rb results. This is, however, different from the experimental realization [53], where the intraspecies interaction of ^{85}Rb is varied. A similar result was reported in an earlier work on quasi-2D system of TBEC [74].

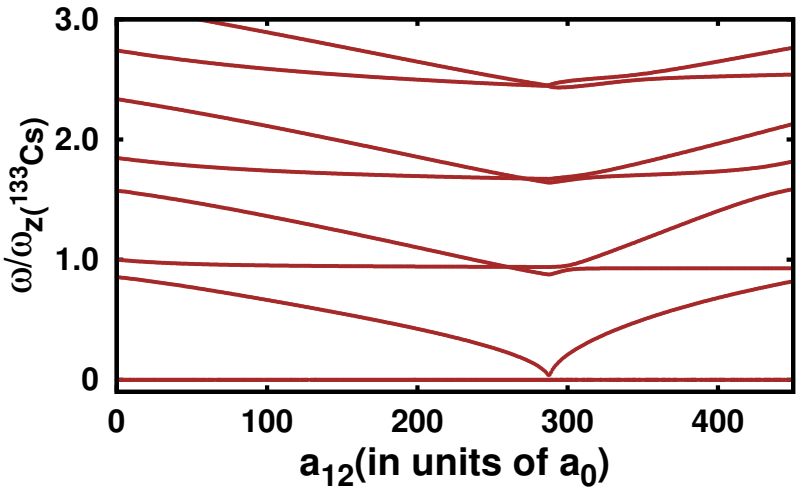

Figure 3.5: Low-lying modes of ^{85}Rb-^{87}Rb for $N_{^{87}\mathrm{Rb}} = N_{^{85}\mathrm{Rb}} = 10^2$ as a function of $a_{^{85}\mathrm{Rb}^{87}\mathrm{Rb}}$. At phase-separation the structure of the density profiles is side-by-side and one of the modes goes soft.

3.1.2 Avoided crossings and quasidegeneracy

Avoided crossings or level repulsion are generic to Hamiltonians which have coupling or interaction terms. With tunable coupling parameter, two neighbouring energy levels can undergo a close encounter and avoided crossings happen between levels having the same symmetries. Otherwise, they just cross each other and level mixing does not occur. The effect of perturbation through the coupling parameter is manifested through the phenomenon of level repulsion. This phenomenon is quantum-mechanical in nature and contributes to emergence of quantum chaos [175].

From Fig. 3.3(a), it is evident that there are several instances of avoided level crossings as a_{CsRb} is varied to higher values. These arise from the changes in the profile of $n_{ck}(z)$, the condensate densities, as the u_k and v_k depend on $n_{ck}(z)$ through the BdG equations. For this reason, the density of avoided crossings is higher around the critical value of a_{CsRb}, where there is a significant change in the structure of density profiles $n_{ck}(z)$ due to phase separation. Another remarkable feature which emerges when $a_{\mathrm{CsRb}} > 310a_0$ are the avoided crossings involving three modes. As an example, the mode evolution around one such case involving the Kohn mode is shown in Fig. 3.3(b). Let us, in particular, examine the 5th and 6th modes, the corresponding mode energies in the domain of interest ($309a_0 \leqslant a_{\mathrm{CsRb}} \leqslant 321a_0$) are represented by blue colored

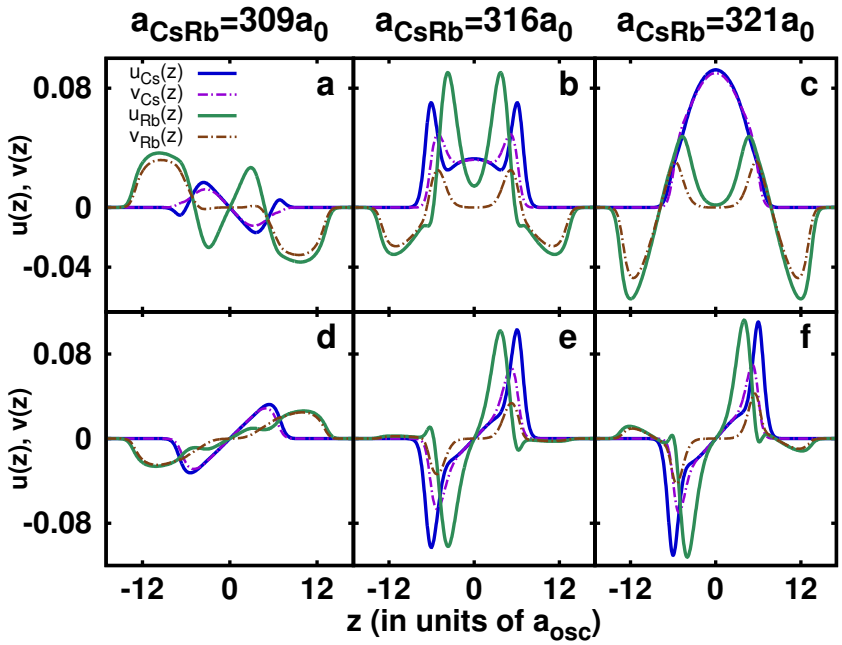

Figure 3.6: The quasiparticle amplitudes of the 5th and 6th modes at quasidegeneracy. (a-c) The quasiparticle amplitudes u_k's and v_k's of the 5^{th} mode for 3 values of a_{CsRb} represented and marked by blue points and red arrows, respectively, in Fig. 3.3. (d-f) The quasiparticle amplitudes u_k's and v_k's corresponding to the 6^{th} mode for the same values of a_{CsRb}. In the plots u_k's and v_k's are in the units of $a_{\text{osc}}^{-1/2}$.

points in Fig. 3.3(b). At $a_{\text{CsRb}} = 309a_0$, the 6th mode is the Kohn mode, which is evident from the dipolar structure of the u_k and v_k as shown in Fig. 3.6(d). The closest approach of the three modes, 4th, 5th and 6th, occurs when $a_{\text{CsRb}} \approx 311a_0$, at this point the 4th mode is transformed into Kohn mode. For $a_{\text{CsRb}} > 311a_0$, the 5th and 6th mode energies are quasidegenerate and pushed to higher values. For example, at $a_{\text{CsRb}} = 316a_0$ the energies of the 5th and 6th modes are $1.24\hbar\omega_{z(\text{Cs})}$ and $1.25\hbar\omega_{z(\text{Cs})}$, respectively. However, as shown in Fig. 3.6(b) and (e), the structure of the corresponding u_k and v_k show significant difference. It is evident that for the 5th mode u_{Cs} and u_{Rb} correspond to principal quantum number n equal to 0 and 2, respectively. On the other hand, for the 6th mode both u_{Cs} and u_{Rb} have n equal to 1. At $a_{\text{CsRb}} \approx 320a_0$, the two modes (5th and 6th) undergo their second avoided crossing with a third mode, the 7th mode. Afterwards, for $a_{\text{CsRb}} > 320a_0$, the 5th mode remains steady at $1.50\hbar\omega_{z(\text{Cs})}$, and the 6th and 7th are quasidegenerate. To show the transformation of the 5th and 6th modes beyond the second avoided crossing, the u_k and v_k of the modes are shown in

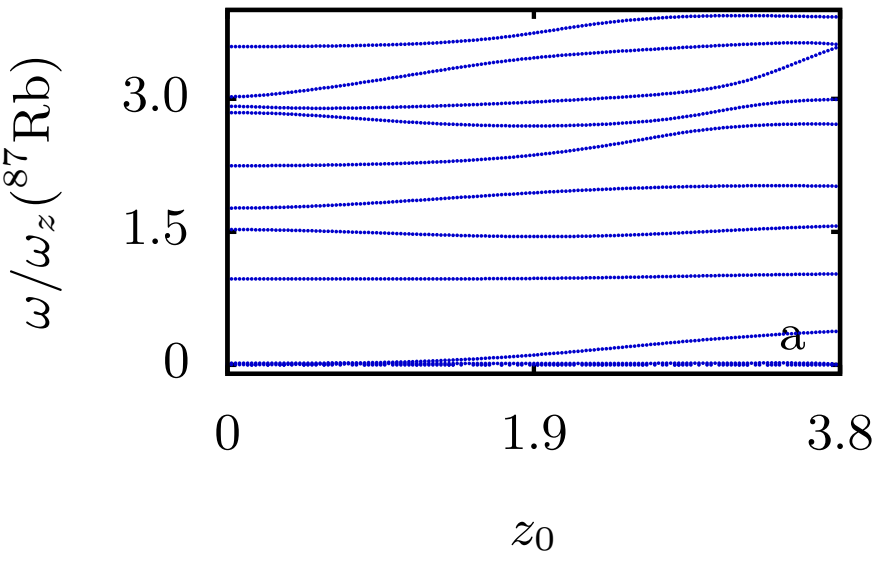

Figure 3.7: The evolution of the low-lying quasiparticle eigenfrequencies in the Rb-Na TBEC; $N_{^{23}\mathrm{Na}} = N_{^{87}\mathrm{Rb}} = 10^4$. (a) Shows the evolution of the low-lying quasiparticle excitations as a function of z_0, trap center separation, in the domain $0 \leqslant z_0 \leqslant 3.8a_{\mathrm{osc(Rb)}}$ for $a_{\mathrm{NaRb}} = 100a_0$.

Fig. 3.6(c) and (f) for $a_{\mathrm{CsRb}} = 321a_0$. It is evident from the figures that the u_{Cs} and v_{Cs} of the 5th mode undergo a significant change in the structure: the central dip around $a_{\mathrm{CsRb}} = 321a_0$, visible in Fig. 3.6(b), is modified to a maxima.

3.1.3 Mode hardening in displaced trap centers

The configuration of the trapping potential considered so far, coincident centres, are difficult to realize in experiments. The centers never coincide due to gravitational sagging, and deviations of the trapping potentials from perfect alignment. In this configuration, non-coincident trapping potential centers, we find that the third Goldstone mode in the phase-separated domain hardens with the increase in the separation of the trap centers. To probe the mode evolution, the trapping potentials are replaced by the following effective potentials

$$V_k(z, z_0) = \frac{1}{2} m_k \omega_{zk}^2 \left[z + (-1)^k z_0\right]^2, \tag{3.1}$$

where $2z_0$ is the separation between two trap centers, and the other symbols have their usual meaning. For the present study, we consider a quasi-1D Rb-Na mixture

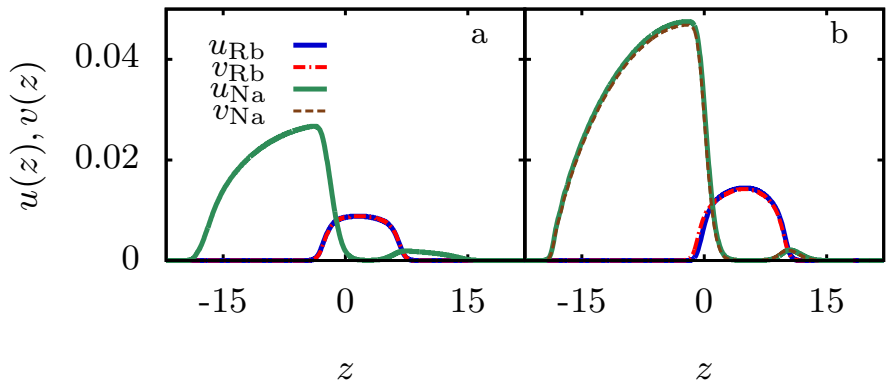

Figure 3.8: The evolution of the low-lying quasiparticle eigenfunctions as a function of z_0 in the Rb-Na TBEC in the domain $0 \leqslant z_0 \leqslant 3.8a_{\mathrm{osc(Rb)}}$ for (a) $z_0 = 1.5a_{\mathrm{osc(Rb)}}$, (b) $z_0 = 2.5a_{\mathrm{osc(Rb)}}$.

in the immiscible regime with $\omega_{z(\mathrm{Rb})} = 2\pi \times 4.55$ Hz, $\omega_{z(\mathrm{Na})} = 2\pi \times 3.89$ Hz and $\omega_{\perp(\mathrm{Rb})} = 2\pi \times 40.2$ Hz, $\omega_{\perp(\mathrm{Na})} = 2\pi \times 32.2$ Hz and $N_{\mathrm{Na}} = N_{\mathrm{Rb}} = 10^4$. Let Rb and Na be the first and second species, respectively with $a_{11} = a_{\mathrm{RbRb}} = 100a_0$, $a_{22} = a_{\mathrm{NaNa}} = 50a_0$, and $a_{12} = a_{\mathrm{NaRb}} = 100a_0$ where a_0 is the Bohr radius. With these parameters, $U_{\mathrm{NaRb}} > \sqrt{U_{\mathrm{RbRb}}U_{\mathrm{NaNa}}}$ and hence, the TBEC is in the phase separated domain. When the trap centers are coincident, that is, $z_0 = 0$, the spectra is characterized by three Goldstone modes. The condensate density profile assumes a sandwich geometry, in which Rb condensate is at the center and flanked by Na condensate at the edges. For the Rb-Na TBEC, experimentally, it is possible to steer the system from miscible to immiscible domain through the Rb-Na Feshbach resonance [176]. Phase-separation in Rb-Na TBEC has also been experimentally observed [51].

For $z_0 > 0$, separated trap centers, with the breaking of the z-parity of the system, the energy of the second Goldstone mode of the Na condensate gradually increases and gets hardened at a critical value of $z_0 \approx 1.8a_{\mathrm{osc(Rb)}}$. The Na Kohn mode which is transformed into the third Goldstone mode of the system, second for the Na condensate, at phase-separation with $z = 0$, regains energy when $z_0 > 0$ to emerge as the second Kohn mode of the system. This is evident from the mode evolution as shown as a function of z_0 in Fig. 3.7(a), and the profile of the hardened mode is shown in Fig. 3.8. The energy of the Rb Kohn mode, on the other hand, remains unchanged even in a separated trap setting. Furthermore, with the change from coincident to non

coincident trap center, the sandwich type density profile gradually changes into a side-by-side density profile. The excitation spectra of the system is now identified by two Goldstone modes and two Kohn modes. It must, however, be emphasized that the evolution of the Goldstone mode when the TBEC undergoes a transition from miscible to immiscible with $z_0 = 0$, discussed in Sec. 3.1.1, is different from the current case [177]. Other recent studies related to the Goldstone modes in condensates are: the Goldstone mode is predicted to harden in spinor condensates(three-component condensates) due to quantum fluctuations [178]; and for TBECs in optical lattices quantum fluctuations modify the ground sate geometry, and hence the structure of the Goldstone modes [179].

3.2 Mode evolution in TBEC with dark soliton at $T = 0$

The experimental realization of single- and multi-component Bose-Einstein condensates (BECs) in atomic gases have opened up the possibility of exploring topological defects. Due to the ubiquitous presence of topological defects in nature, study of matter-wave excitations such as vortices and solitons in atomic BECs has been a topic of extensive research both experimentally and theoretically over the last few years. In fact, these have attracted much attention as they are created spontaneously during BEC phase transition through Kibble-Zurek mechanism [180–183]. Other novel phenomena have inspired numerous experiments [184, 185] and theoretical studies [76, 186–191] with dark and bright solitons in atomic BECs in a wide range of settings under different scenarios. The experimental observation shows that the notch of the dark soliton gets filled up with thermal atoms over time and the soliton becomes grey, hence starts oscillating which are either short- or long-lived depending upon the system of interest [77, 192, 193].

Most of the theoretical studies on the statics and the dynamics of dark solitons have been carried out in quasi-1D setting at zero temperature where thermal fluctuations can be ignored [194]. Stability of multiple solitons in quasi-1D trap has been examined [195, 196]. Quantum depletion in BECs with soliton at $T = 0$ in weakly interacting

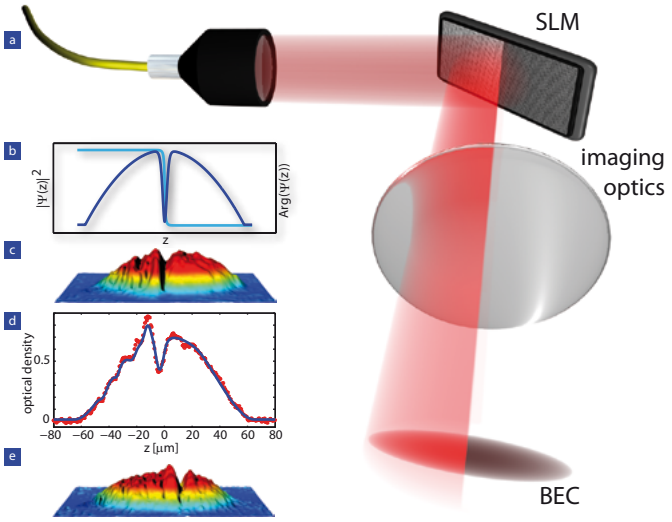

Figure 3.9: Experimental technique to imprint a dark soliton in a BEC. In particular, a spatial light modulator (SLM) is used to imprint a π phase jump by exposing part of the condensate to a far-detuned laser beam. Frame (c) shows an absorption image of the condensate, taken directly after preparation of the soliton followed by a subsequent free expansion. Frame (d) shows integrated column density, and Frame (e) shows an image of the soliton after evolution. Reprinted by permission from Macmillan Publishers Ltd: [Becker *et al.*, *Nat. Phys.* **4**, 496 (2008).] Copyright © 2008.

Bose gases has also been studied using approximate models [197–203]. This motivated us to reexamine the role of quantum fluctuations in BECs, whether it is with or without soliton. We show that quantum fluctuation in BECs with soliton is higher than without it. This is due to the presence of the anomalous mode, and we demonstrate that quantum fluctuations can make the dark soliton grey, which as a result becomes dynamically unstable.

Furthermore, repulsive TBECs support coupled dark-bright solitons which makes it richer and more interesting than single-component BECs [76]. The bright soliton, on the other hand, cannot survive in single-component BECs with repulsive interaction. This has prompted us to study the evolution of Goldstone modes and mode energies for TBEC with soliton as a function of interspecies scattering length. As the scattering length is varied, the TBEC undergoes a phase transition from miscible to immiscible phase. Here we show that the presence of the soliton introduces an additional Goldstone mode to the system. Even at zero temperature without considering any quantum

fluctuation, for certain range of interspecies scattering length, the TBEC becomes dynamically unstable. The difference in the mass of the two species also plays a significant role in mode evolution and topology of density profiles.

3.2.1 The Dark Soliton

Solitons are localized disturbances which propagate without change of form. They exist and preserve their shape because non-linearity of the medium nullifies the effect of dispersion in the medium. Soliton solutions exist for several non-linear equations; for example, the Korteweg-de Vries equation which describes the properties of shallow water waves. Solitons may either correspond to density depressions known as dark solitons, or density elevation referred to as bright soliton. Dark soliton can be further divided into black ones whose minimum density is zero, and grey ones, for which it is non-zero [27].

For repulsively interacting homogeneous BECs, the GP equation bears one dimensional soliton solution. Here the density is a function of spatial coordinate z, time t, and depends explicitly on $z - ut$; where u is the velocity of the soliton. Furthermore, we take $n \to n_0$ as $z \to \pm\infty$. Using solution of the form

$$\phi(z,t) = f(z-ut)e^{-i\mu t/\hbar}, \tag{3.2}$$

in the time-dependent GP equation, one arrives at the following soliton wave function

$$\phi = \sqrt{n_0}\left[i\frac{u}{s} + \sqrt{\left(1-\frac{u^2}{s^2}\right)}\tanh\left(\frac{z-ut}{\sqrt{2}\xi_u}\right)\right]e^{-i\mu t/\hbar}, \tag{3.3}$$

and the density $n = |\phi|^2$ is [27]

$$n = n_0 - (n_0 - n_{\min})\frac{1}{\cosh^2[(z-ut)/\sqrt{2}\xi_u]}. \tag{3.4}$$

Here $\sqrt{n_0}$ denotes the amplitude of the wave function for $z \to \pm\infty$ and s is the speed of acoustic waves in the medium. The width of the soliton, ξ_u, is given by

$$\xi_u = \frac{\xi}{[1-(u/s)^2]^{1/2}}, \tag{3.5}$$

and the minimum density $n_{\min} = n_0\dfrac{u^2}{s^2}$. In the above equation, ξ is the value of the healing length at position z_0. The location of a dark soliton is a place in a quasi-1D condensate where the condensate wave function $\phi(z)$ changes sign.

The wave function of condensate with a soliton at $z_0 = 0$ is antisymmetric and the phase of the wave function jumps discontinuously by π as ϕ passes through the origin. The experimental images of condensates with dark and grey solitons, along with the schematics of soliton generation with phase imprinting technique from Ref. [77] are shown in Fig. 3.9. In a homogeneous condensate as $s = \sqrt{n_0 U/m}$, the soliton velocity $u = (n_{\min} U/m)^{1/2}$ [27, 204]. Thus, when $u = 0$, $n_{\min} = 0$, and the density profile is reduced to

$$\phi(z) = \phi_0 \tanh\left(\frac{z}{\sqrt{2}\xi}\right). \tag{3.6}$$

The soliton energy is given by

$$E_{\text{sol}} = \frac{4}{3} n_0 \hbar s \left(1 - \frac{u^2}{s^2}\right)^{3/2}. \tag{3.7}$$

This shows decrease in soliton energy with increasing u due to a negative effective mass arising from the depletion of particles associated with the soliton.

The presence of an external confining potential affects the dynamics of a soliton. Most importantly, the energy of the soliton is modified to

$$E_{\text{sol}} = \frac{4}{3\sqrt{m}U}[\mu - V(z_s) - m u^2(z_s)]^{3/2}, \tag{3.8}$$

where z_s denotes the position of the soliton centre. Subject to the constraint that the total energy is conserved, it turns out that the motion of a soliton in a trapped BEC is the same as that of a particle of mass $2m$ in the same potential. For a potential having a global minima, the period of motion of a soliton is $\sqrt{2}\omega_z$. Thus one can say that dark solitons behave like particles in slowly varying external potentials [186]. In addition, the soliton accelerates due to the external potential emitting sound waves. The acoustic radiation from the soliton is similar to the Larmor radiation from an accelerating charged particle [205]. The energy dissipated tends to make the soliton less dark, making it grey [206].

3.2.2 Fluctuation induced instability in single-species BEC

The low-lying excitation spectrum of a quasi-1D BEC with a soliton is characterized by the presence of an anomalous mode, which indicates that the BEC is in an energetically excited state. This is in addition to the Goldstone and the Kohn modes, which

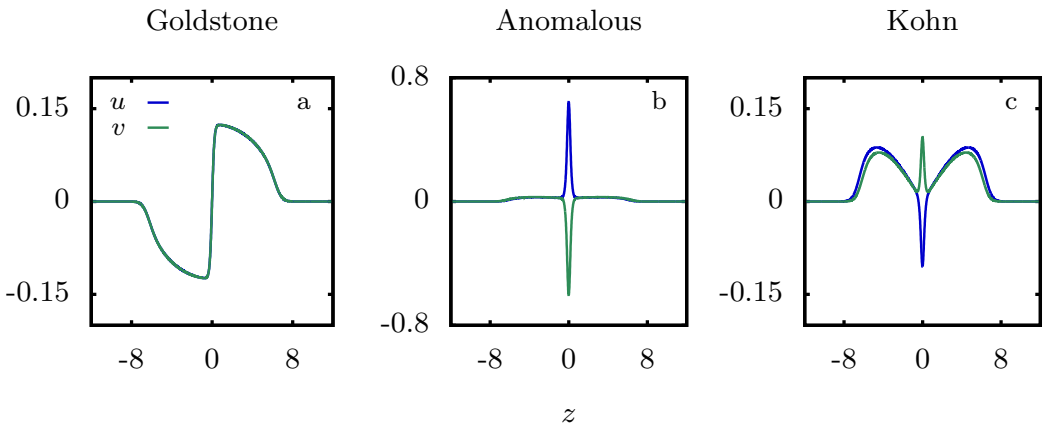

Figure 3.10: Quasiparticle amplitudes corresponding to the first two excited modes of a single-species BEC with a dark soliton. In the plots u's and v's are in units of $a_{\rm osc}^{-1/2}$.

are also present in the excitation spectrum of a quasi-1D BEC without soliton. The quasiparticle amplitudes corresponding to the first two excited modes are shown in Fig. 3.10.

For further analysis we introduce Δ_j, the amount of energy carried by the jth eigenmode in a single-species BEC. It is defined as

$$\Delta_j = \int dz(|u_j|^2 - |v_j|^2)E_j. \tag{3.9}$$

The sign of the quantity Δ_j is known as *Krein sign*. If this sign turns out to be negative for the jth mode, then the mode is referred to as an *anomalous mode* [197, 207–210]. It signifies the energetic instability which may be present due to a topological defect in the system. If such a mode is resonant with another mode with a positive *Krein sign*, then complex frequencies appear in the excitation spectrum. In general, the anomalous, and Kohn mode energies are real, and the energy of the anomalous mode $E_{\rm an} \approx \hbar\omega_z/\sqrt{2}$. The appearance of the anomalous mode signifies that the solitonic solution of the stationary quasi-1D GP equation is dynamically stable, however, the system is in a metastable state. So, when the solution is evolved in imaginary time, with the inclusion of $\tilde{n}$ at $T = 0$, the anomalous mode is transformed into an imaginary energy eigenmode. This is an unambiguous signature of quantum depletion induced instability of the solitonic solution. In other words, the non-zero $\tilde{n}$ arising from the quantum fluctuations within the notch of the soliton turns it grey, and renders the system dynamically unstable. Furthermore, the low-lying energy spectrum is devoid of

any negative *Krein sign* eigenmodes. The anomalous mode, however, reappears in the spectrum on evolving the system over imaginary time.

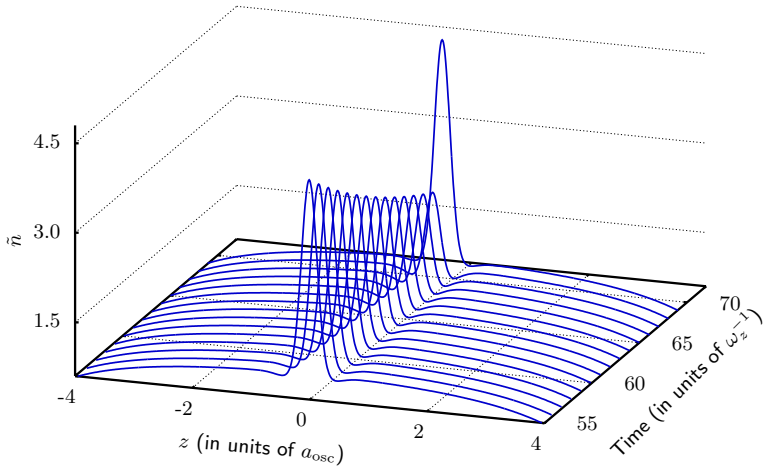

Figure 3.11: The temporal evolution in the profile of the non-condensate atom density $\tilde{n}$ at $T = 0$ measured in units of $a_{\rm osc}^{-1}$, where $a_{\rm osc} = \sqrt{\hbar/(m\omega_z)}$. The plots show a steady drop in the number of non-condensate atoms till it reaches a threshold value, and then, the anomalous mode reappears in the spectrum. The latter is reflected in the profile of $\tilde{n}$ at $t = 69\omega_z^{-1}$, where it has maximal distribution.

To study the trend in the evolution of $E_{\rm an}$ we examine the temporal variation of $\tilde{n}$. For this, we consider condensate of ^{87}Rb with a soliton at the center of the trap consisting of $N = 2000$ atoms whose s-wave scattering length is $a_{11} = a_{\rm RbRb} = 100a_0$, where a_0 is the Bohr radius. The evolution of the low-lying modes are computed for the above-mentioned $a_{\rm RbRb}$ with ω_z = $2\pi \times 4.55$ Hz, and $\omega_\perp = 20\omega_z$. This choice of parameters are consistent with the experimental setting and satisfies the condition of quasi-1D approximation [164, 192, 211]. The contribution from the anomalous mode fills up the notch of the soliton and $\tilde{n}(0)$ has the largest possible value at the initial state of evolution. At later times, $E_{\rm an}$ is imaginary and $\tilde{n}(0)$ decreases, the trend is as shown in Fig. 3.11. However, when $\tilde{n}(0)$ reaches a critical value, which in the present work is $\approx 2.312\ a_{\rm osc}^{-1}$, it is no longer large enough to render the solitonic solution dynamically unstable and the anomalous mode reappears. This confirms $\tilde{n}(0)$ has a threshold value below which the solitonic solution may be stable. Apart from this criterion, the observed long lifetime of dark soliton in experiments with quasi-1D condensates is attributed to an optimum choice of radial trapping frequency, and the strength of the

repulsive inter-atomic interactions [77].

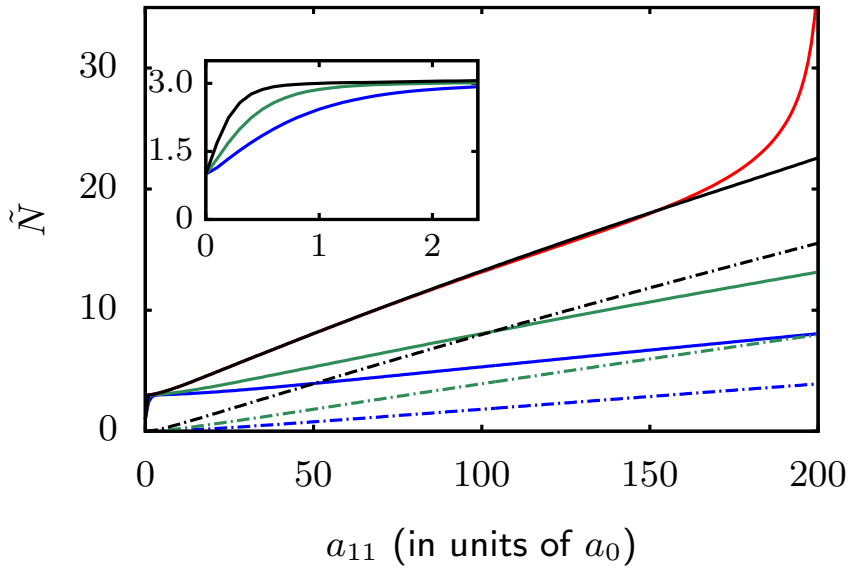

Figure 3.12: Variation in the total number of non-condensate atoms $\tilde{N}$ at $T = 0$ as a function of the scattering length a_{11}. The solid (dashed) blue, green, and black lines represent $\tilde{N}$ in the presence (absence) of soliton with total number of atoms N = 500, 1000, and 2000, respectively. The solid red line represents $\tilde{N}$ in the presence of soliton for $N = 2000$, with the number of basis $N_b = 170$, it is shown to indicate lack of accuracy at higher a_{11} with lower number of basis functions. The inset plots show the trend of $\tilde{N}$ in the neighbourhood of $a_{11} \approx 0$, where there is a sharp increase.

For the limiting case of $a_{\mathrm{RbRb}} \to 0$, or the non-interacting limit the Bogoliubov modes are, to a very good approximation, the eigenstates of the trapping potential. In this limit too, the condensate with the soliton has higher $\tilde{n}$ than the condensate without soliton. An exponential increase in the total number of non-condensate atoms

$$\tilde{N} = \int_{-\infty}^{\infty} \tilde{n}\, dz, \tag{3.10}$$

is observed as a_{RbRb} is increased from near-zero to $a_{\mathrm{RbRb}} \approx a_0$, this is evident from the inset plot in Fig. 3.12. However, $\tilde{N}$ increases linearly with further increase of a_{RbRb} and this is shown in the main plot of Fig. 3.12. An important observation is that, $d\tilde{N}/da_{\mathrm{RbRb}} \propto N$ (total number of atoms), which is due to higher repulsive interaction energy with increasing N. This is visible in the family of curves given for different values of N in Fig. 3.12. It should be emphasized here that an optimal choice of basis size N_b is necessary in all the computations to obtain accurate mode functions and

energies. For weakly interacting condensates with soliton, a basis set consisting of 170 basis functions give converged and reliable results. But, for the strongly interacting case $1 \ll NU$, the energy eigenvalues E_js do not converge and $\tilde{N}$ diverges as shown by the red solid line in Fig. 3.12 for $N = 2000$. However, we get converged and reliable results when the basis size is increased to 240 basis functions.

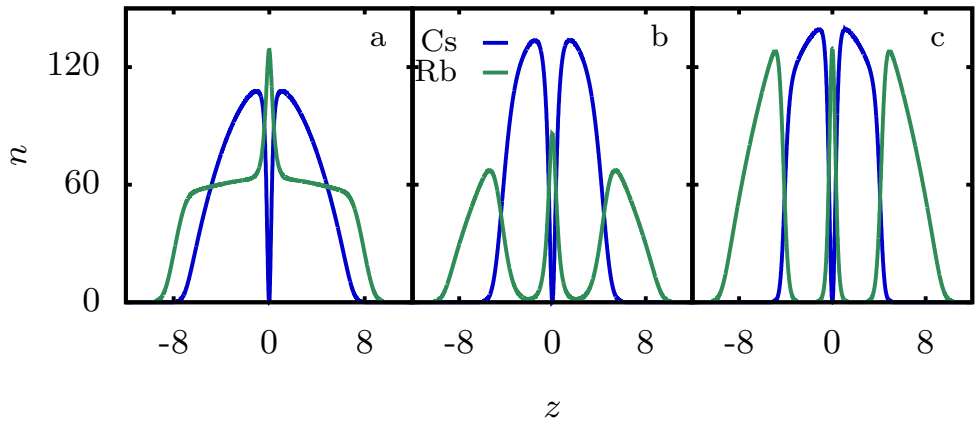

Figure 3.13: Transition to phase-separation and structure of the density profiles in TBEC with soliton. (a-c) show the transition from miscible to sandwich type density profile with the change in interspecies scattering length a_{CsRb} for a Cs-Rb TBEC and correspond to $a_{\mathrm{CsRb}} = \{200a_0, 320a_0, 400a_0\}$ respectively. In the plots density is measured in units of a_{osc}^{-1}.

3.2.3 Interaction induced instability in TBEC with soliton

Dark solitons in one of the component in quasi-1D TBECs, like in single-species are dynamically unstable at $T = 0$ due to the quantum fluctuations. There is, however, another type of instability associated with dark solitons, and unique to TBECs. It arises from the interspecies interactions, and occurs when an anomalous mode collides with a higher energy mode. The collision transforms the two modes into degenerate complex energy modes, and renders the dark solitonic state unstable. In this thesis, we examine the collision of the modes as a function of the interspecies scattering length, and study in detail the nature of these modes, and their evolution. Mode collisions of similar nature, giving rise to *oscillatory unstable* states, have been investigated in the context of a single-species cigar-shaped BEC with dark solitons in double-well potentials [208].

In TBECs, as mentioned earlier, phase-separation occurs when $U_{12} > \sqrt{U_{11}U_{22}}$. To study the stability of dark solitons in TBECs, like in Section. 3.1 we consider Cs and Rb as the first and second species, respectively. To investigate the mode evolution with solitons, we imprint a soliton onto the first species (Cs condensate) at $z = 0$. We, then, vary $a_{\rm CsRb}$ from miscible to immiscible regime, which is experimentally possible with the Cs-Rb Feshbach resonance [168]. The mode energies, E_j, are computed at $T = 0$ in steps of increasing $a_{\rm CsRb}$ in the domain $[0, 420a_0]$ with $N_{\rm Rb} = N_{\rm Cs} = 10^3$, $\omega_{z({\rm Rb})} = 2\pi \times 3.89$ Hz and $\omega_{z({\rm Cs})} = 2\pi \times 4.55$ Hz as in Ref. [49, 164]. To make the system quasi-1D we take $\omega_\perp = 30\omega_z$, and Fig. 3.13 shows the density profiles of the TBEC with a dark soliton imprinted in the central component undergoing transition from the miscible to immiscible phases on tuning $a_{\rm CsRb}$. The low-lying excitation spectrum is characterized by the presence of an anomalous mode signifying the presence of soliton. The other two significant low-lying modes, which are also present in quasi-1D TBECs without soliton, are the Goldstone and Kohn modes of the two species.

When $a_{\rm CsRb} = 0$, the $U_{\rm CsRb}$ dependent terms in Eq. (2.68) are zero and the spectrum of the two species are independent as the two condensates are decoupled. The clear separation between the modes of the two species is lost and mode mixing occurs when $a_{\rm CsRb} > 0$. For instance, the energy of the Cs anomalous mode increases with increasing $a_{\rm CsRb}$, and collides with the other modes resulting in the generation of a quartet of degenerate complex mode energies. This occurs when $a_{\rm CsRb}$ is in the domains $[157a_0, 162a_0]$, $[281a_0, 317a_0]$, and $[318a_0, 327a_0]$ marked by red dots in Fig. 3.14. In these domains, the low-lying energy spectrum has no anomalous mode and the system is *oscillatory unstable*. For $162a_0 < a_{\rm CsRb} < 281a_0$, the anomalous mode reappears and crosses the fourth excited state at $a_{\rm CsRb} \approx 264a_0$. Continuing further, as evident from Fig. 3.14(b), at $a_{\rm CsRb} \approx 327a_0$ there is a bifurcation after which the anomalous mode ceases to undergo mode collisions.

It should be emphasized here that, with the transition from miscible to immiscible regime the Kohn mode and the fourth excited modes go soft. This introduces two new Goldstone modes, including which, there are four Goldstone modes in the excitation spectrum. These features deserve detailed discussion and are given in the following sections.

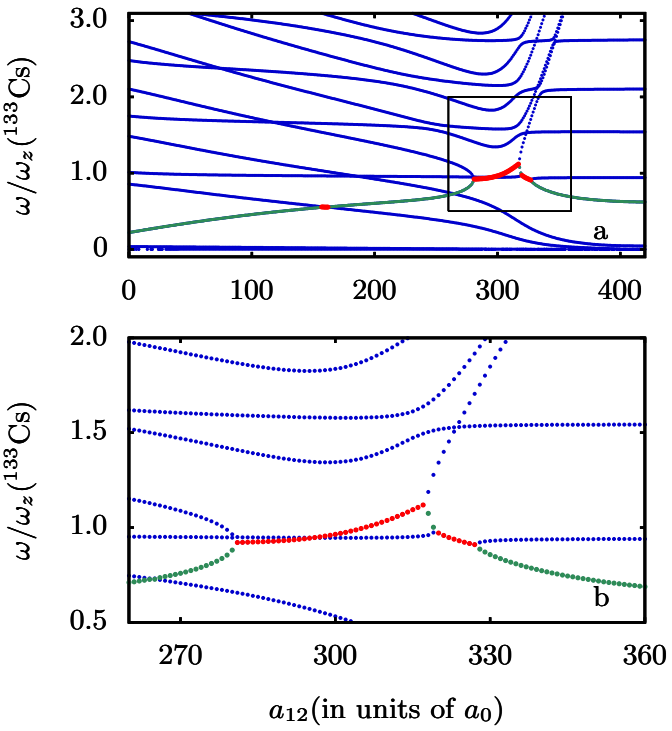

Figure 3.14: The evolution of the modes as a function of the interspecies scattering length a_{CsRb} in the Cs-Rb TBEC with soliton. (a)The evolution of the low-lying modes in the domain $0 \leqslant a_{\mathrm{CsRb}} \leqslant 420a_0$ for $N_{\mathrm{Rb}} = N_{\mathrm{Cs}} = 10^3$. (b) The enlarged view of the region enclosed within the black colored rectangular box in (a) to resolve the mode collisions and bifurcations. The plots show only the real part of mode energies ω/ω_z.

3.2.4 Mode collisions

From Fig. 3.14, it is evident that there are several instances of avoided crossings and *mode collisions* when two modes meet as a_{CsRb} is varied to higher values. We have used the latter term (mode collision) to identify the case when one of the two modes is the anomalous mode and when mode collisions do happen, the evolution of the mode energies is different from the avoided crossings. In mode collisions, there are two possible scenarios: either the two modes cross each other or undergo bifurcation. These occur due to the changes in the spatial profile of the mode functions (u_{Rb}, v_{Rb}, u_{Cs} and v_{Cs}), which in turn depend on the condensate densities $n_{ck}(z)$.

To examine the case of two modes crossing each other during mode collision, consider the anomalous and fourth excited mode in the neighborhood of $a_{\mathrm{CsRb}} = 261a_0$. At values of a_{CsRb} slightly below $261a_0$, the anomalous and the fourth excited mode

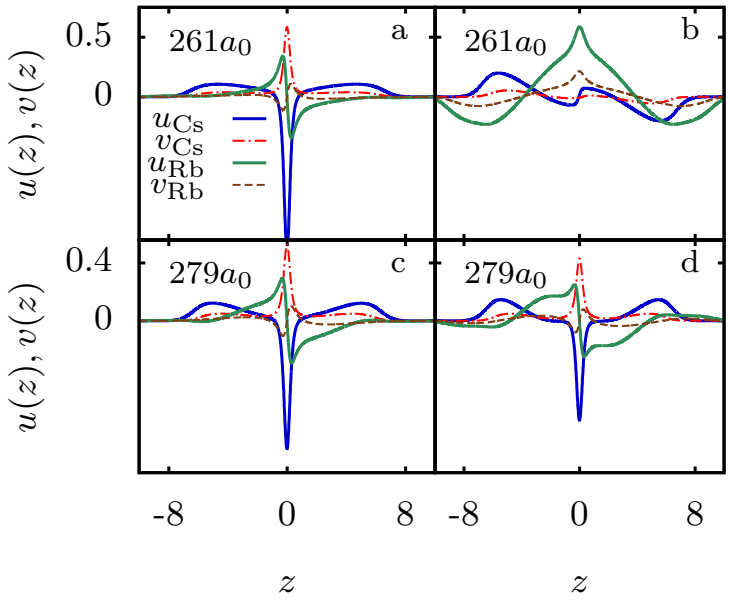

Figure 3.15: Variation in the nature of mode evolution near mode crossing and collision. (a-b) Quasiparticle amplitudes corresponding to the anomalous and fourth excited mode, respectively, at $a_{\mathrm{CsRb}} = 261a_0$ when the modes cross each other. (c-d) Quasiparticle amplitudes corresponding to the anomalous and sixth excited mode, respectively, at $a_{\mathrm{CsRb}} = 279a_0$ when the modes collide. For better visibility u_{Cs} and u_{Rb} are scaled by a factor of 2.5. In the plots u's and v's are in units of $a_{\mathrm{osc}}^{-1/2}$.

approach and cross each other at $a_{\mathrm{CsRb}} \approx 261a_0$. In this case, there are no mode mixing pre and post mode collision. As shown in Fig. 3.15(a), the mode functions u_{Rb} and v_{Rb} corresponding to the anomalous mode are zero at $z = 0$, whereas the mode functions u_{Cs} and v_{Cs}, have maxima at $z = 0$. In contrast, the fourth excited mode has u_{Cs} and v_{Cs} which are zero at $z = 0$, while u_{Rb} and v_{Rb} have maxima at $z = 0$ as shown in Fig. 3.15(b). The mode functions, thus, have very different profiles at $z = 0$ and mode mixing does not occur, instead they just cross through.

Now, let us consider the case of bifurcation at $a_{\mathrm{CsRb}} \approx 279a_0$. For this value of a_{CsRb} the mode functions corresponding to the anomalous mode and the sixth mode have similar profiles with both u_{Cs}, $v_{\mathrm{Cs}} \neq 0$ at $z = 0$ as shown in Fig. 3.15(c-d). These two modes collide and give rise to complex mode energies. A similar trend is also observed at $a_{\mathrm{CsRb}} \approx 157a_0$, when the Cs anomalous mode collides with the Rb Kohn mode. In the domain $157a_0 \leqslant a_{\mathrm{CsRb}} \leqslant 162a_0$, the profile of the Rb Kohn mode resembles the structure of the Cs anomalous mode. So that after mode collision, they

give rise to complex eigenfrequencies and makes the states *oscillatory unstable*.

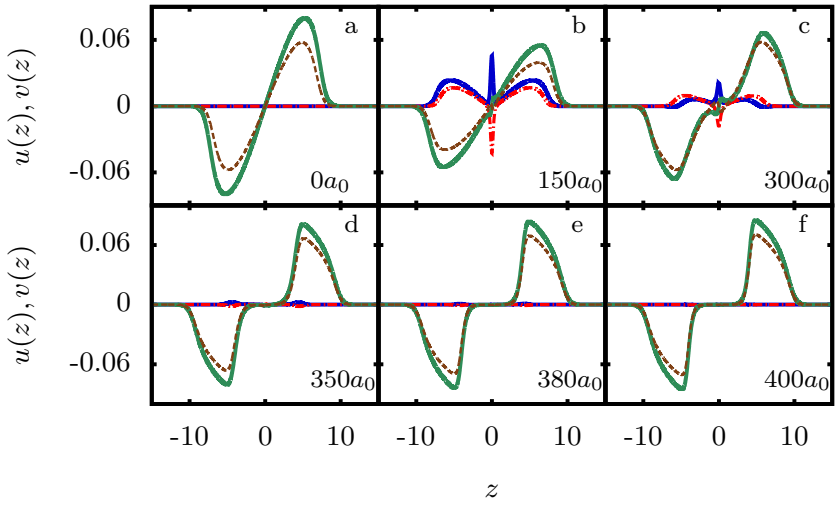

Figure 3.16: Evolution of quasiparticle amplitudes corresponding to the Rb Kohn mode as a_{CsRb} is increased from 0 to $400a_0$. (a) At $a_{\mathrm{CsRb}} = 0$, it is a Kohn mode of the Rb condensate. (b-d) In the domain $0 < a_{\mathrm{CsRb}} \lesssim 350a_0$ the mode acquires admixtures from the Cs Kohn mode (nonzero u_{Cs} and v_{Cs}). (e-f) At phase-separation $310a_0 \lesssim a_{\mathrm{CsRb}}$ the mode transforms to a Goldstone mode: u_{Rb} and v_{Rb} resemble the profile of $n_{\mathrm{Rb}} = |\phi_{\mathrm{Rb}}|^2$ but with a phase difference. In the plots u's and v's are in units of $a_{\mathrm{osc}}^{-1/2}$.

3.2.5 Third and fourth Goldstone modes

The third Goldstone mode emerges in the excitation spectrum as a_{CsRb} is increased, and the Rb Kohn mode goes soft at phase separation when $a_{\mathrm{CsRb}} \approx 350a_0$. This is consistent with the results discussed in Section. 3.1.1 and reported in our work [136]. The evolution of the Rb Kohn mode functions (u_{Rb} and v_{Rb}) with increasing a_{CsRb} is shown in Fig. 3.16. It is evident that when $a_{\mathrm{CsRb}} = 0$ (Fig. 3.16(a)), there is no admixture from the Cs Kohn mode ($u_{\mathrm{Cs}} = v_{\mathrm{Cs}} = 0$). However, when $0 < a_{\mathrm{CsRb}} \lesssim 400a_0$ the admixture from the Cs Kohn mode increases initially, and decreases to zero as we approach $U_{\mathrm{CsRb}} > \sqrt{U_{\mathrm{CsCs}}U_{\mathrm{RbRb}}}$ (Fig. 3.16(b-f)). So, the third Goldstone mode is present in the system when $a_{\mathrm{CsRb}} \gtrsim 350a_0$. As mentioned earlier, two of the Goldstone modes have identical $|u_{\mathrm{Rb}}|$ and $|v_{\mathrm{Rb}}|$ but with different phases, and thus, the global phase symmetry of the Rb condensate is broken.

The fourth excited mode, unlike in the case of quasi-1D TBECs without a soliton

also goes soft at $a_{\mathrm{CsRb}} \approx 380a_0$. The evolution of the mode functions (u_{Rb} and v_{Rb}) corresponding to the fourth excited mode with a_{CsRb} are shown in Fig. 3.17. It is noticeable that when $a_{\mathrm{CsRb}} = 0$ (Fig. 3.17(a)), there is no contribution from higher energy modes of Cs. However, when $a_{\mathrm{CsRb}} > 0$ the admixture from the third excited mode of the Cs condensate is discernible in the lower values of a_{CsRb} and are shown in Fig. 3.17(b-c). At higher values of a_{CsRb}, $261a_0 \lesssim a_{\mathrm{CsRb}} \lesssim 400a_0$, the spatial profile of the mode functions are different from those of the lower values of a_{CsRb}, and are shown in Fig. 3.16(d-f). At around $a_{\mathrm{CsRb}} \approx 300a_0$, the mode functions begin to resemble the structure of ϕ_{Rb}, and the transformation is complete at $a_{\mathrm{CsRb}} \approx 380a_0$ when the mode goes soft. Moreover, $|u_{\mathrm{Rb}}|$ and $|v_{\mathrm{Rb}}|$ resemble the structure of the bright soliton in ϕ_{Rb} and has a different phase from $|u_{\mathrm{Rb}}|$ and $|v_{\mathrm{Rb}}|$ at the edges which softened at $a_{\mathrm{CsRb}} \gtrsim 350a_0$. Thus, at phase separation the Rb BEC at the edges, the bright soliton in ϕ_{Rb}, and Cs BEC at the center are four topologically distinct BECs leading to four fragments, hence four Goldstone modes. Here too, the underlying principle behind the appearance of an additional Goldstone modes is not due to tunnel splitting as discussed earlier.

3.2.6 Different mass ratios

To gain insight on the complex nature of the mode evolution in the Cs-Rb TBEC, we study the interplay of mass difference and intraspecies scattering lengths. For the set of aforementioned parameters the ground state of TBEC, after phase-separation is of sandwich geometry, in which the species with the heavier mass (Cs) is at the center and flanked by the species with lighter mass (Rb) at the edges [49], albeit $a_{\mathrm{CsCs}} \gg a_{\mathrm{RbRb}}$. This geometry minimizes the trapping potential energy, and hence the total energy of the system. In contrast, for TBECs with $m_1 \approx m_2$, at phase-separation, the species with the smaller intraspecies scattering length is surrounded by the other species. In this case the mode evolution in the presence of soliton is devoid of any *mode collisions*. Thus, we attribute the pattern of mode collisions in Cs-Rb TBEC binary condensate with soliton to the interplay between mass difference and intraspecies scattering lengths.

To understand the transition in the mode evolution from $m_1 \approx m_2$ to a case similar

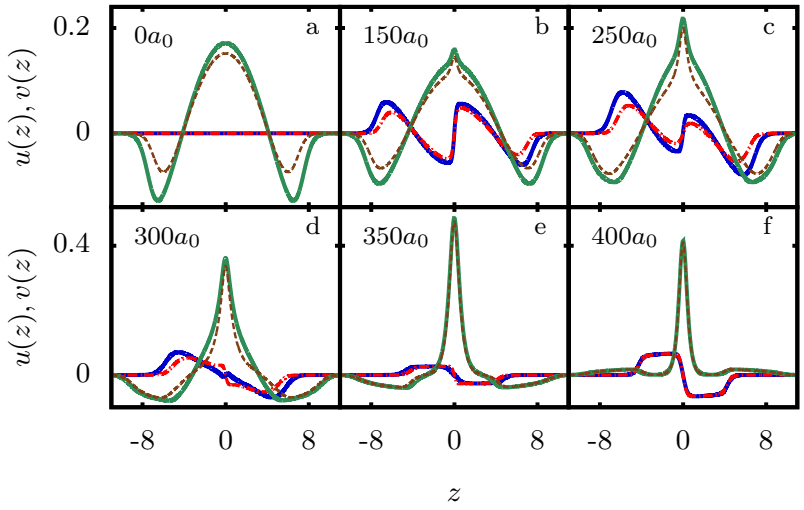

Figure 3.17: Evolution of the quasiparticle amplitudes corresponding to the fourth excited mode as a_{CsRb} is increased from 0 to $420a_0$. (a) At $a_{\mathrm{CsRb}} = 0$, it is the second excited mode of the Rb condensate. (b-d) In the domain $0 < a_{\mathrm{CsRb}} \lesssim 300a_0$ the mode acquires admixtures from the Cs Kohn mode (nonzero u_{Cs} and v_{Cs}). (e-f) At phase-separation $380a_0 \lesssim a_{\mathrm{CsRb}}$ the mode transforms to a Goldstone mode: u_{Rb}, v_{Rb} and u_{Cs}, v_{Cs} resemble the profile of $n_{\mathrm{Rb}} = |\phi_{\mathrm{Rb}}|^2$ and $n_{\mathrm{Cs}} = |\phi_{\mathrm{Cs}}|^2$ but with a phase difference. In the plots u's and v's are in units of $a_{\mathrm{osc}}^{-1/2}$.

to Cs-Rb TBEC, we consider a test case where $87\,\mathrm{amu} \leqslant m_1 \leqslant 125\,\mathrm{amu}$ and fix $m_2 = m_{\mathrm{Rb}}$. We then compute the evolution of the modes as a function of the interspecies scattering length as we increase m_1 from 87 amu to 125 amu in steps of 2 amu. For example, the mode evolution for three different values of m_1 (95 amu, 100 amu, and 105 amu) are shown in Fig. 3.18. From Fig. 3.18(a) it is evident that at $m_1 = 95$ amu the anomalous mode goes soft at phase-separation and becomes the third Goldstone mode of the system without any mode collisions. At $a_{12} \approx 300a_0$, the two species are partially miscible and the notch of n_1 at $z = 0$ due to the soliton is filled with the second species.

For higher values of $a_{12} \approx 340a_0$, the energetically favorable state is of a sandwich geometry where the species with the heavier mass ($m_1 = 95$ amu) is at the edge of the trap and the species with lower mass ($m_2 = 87$ amu) occupies the center. It should, however be recalled here that $a_{11} > a_{22}$.

There is a major change in the nature of mode evolution, as shown in Fig. 3.18(b) for $m_1 = 100$: the anomalous mode collides with the second excited mode twice at

$a_{12} \approx 180a_0$ and $320a_0$. The emergence of a bifurcation is evident in the second mode collision at $a_{12} \approx 320a_0$. On further increase of m_1, as shown in Fig. 3.18(c) for $m_1 = 105$, the trend of the mode collision begins to resemble that of the Cs-Rb mixture. In this case, the bifurcation arising from the collision between the anomalous and sixth excited mode is quite evident. Coming to the topology of the density profiles, prior to phase-separation ($a_{12} \approx 300a_0$) n_1 and n_2 overlap with each other and the notch of the soliton is filled by the second species. At still higher values of a_{12}, n_2 from the edges migrates towards the notch of the soliton and the soliton gets topologically deformed. This is the energetically favorable density configuration. At $a_{12} \approx 380a_0$, the migration is complete and n_2 occupies the center of the trap and is surrounded by n_1 and the system is then phase-separated. Here, it must be mentioned that without soliton the density profile would be opposite: condensates with masses m_1 and m_2 occupy the center and edges, respectively. Thus, the presence of the soliton induces a change in the topology of the density profiles in TBECs. On further increase of m_1, the energy of the anomalous mode increases with increasing a_{12} and the collision with the sixth mode occurs at higher energies.

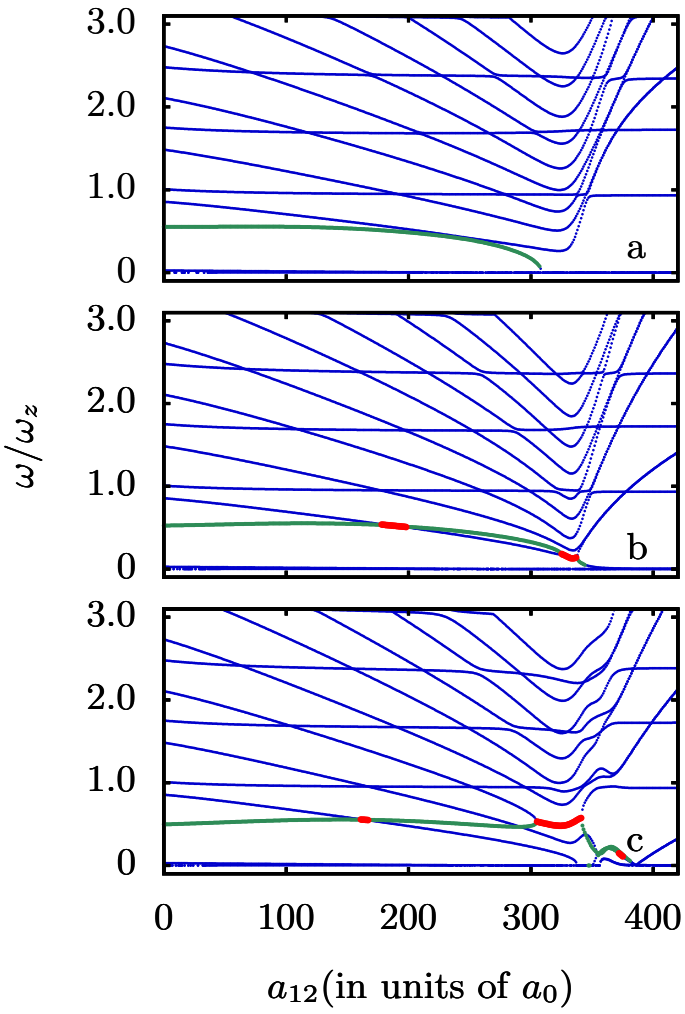

Figure 3.18: The evolution of the low-lying modes of the TBEC with soliton for different mass ratios as a function of the interspecies scattering length a_{12} in the domain $0 \leqslant a_{12} \leqslant 420a_0$. The masses of the first and second species in each of the panels correspond to (a) 95 and 87, (b) 100 and 87, and (c) 105 and 87 amu, respectively. The number of atoms in each species is 10^3. The intraspecies scattering lengths of the first and second species are $a_{11} = 280a_0$ and $a_{22} = 100a_0$, respectively. The plots show only the real part of mode energies ω/ω_z.

3.3 Summary of the Chapter

TBECs with strong interspecies repulsion with the sandwich density profile at phase-separation are equivalent to three coupled condensate fragments devoid of any node and satisfies Feynman's no-node theorem. The Rb condensate gets redistributed and

occupies the edges with its central density ≈ 0. On the contrary the Cs condensate occupies the center of the trap. Because of this we observe three Goldstone modes in the system after phase-separation. At higher interspecies interactions, we predict avoided crossings involving three modes and followed with the coalescence or quasidegeneracy of two of the participating modes. The third Goldstone mode in TBECs with sandwich profile at phase separation gets hardened when the trap centers are separated by a critical distance. This is accompanied by the topological change from sandwich to side-by-side condensate density profiles. This result has important experimental implications, and demonstrates why it is a major challenge to obtain sandwich type density profiles in TBEC experiments.

Furthermore we have examined the stability of solitons in single and two-component BEC. We have predicted that at zero temperature presence of soliton enhances the quantum depletion and fills up the notch of the soliton which makes it oscillatory unstable. In TBECs having a dark soliton with strong interspecies interaction, four Goldstone modes emerge in the excitation spectrum. We have also predicted that the TBECs with soliton in one of the components oscillate while interacting even at zero temperature. This is due to the non-zero density of the other species within the notch of the dark soliton. We have also shown a soliton induced change in the density profiles when the atomic masses of the two species differ widely. We also find an enhancement in the mass ratio at which the heavier species, with higher scattering length, occupies the central position at phase-separation. The results and discussion that have been described here in this chapter are at $T = 0$.

Our next task is to consider the effect of the thermal cloud on the condensates which will be discussed in the subsequent chapters.

Chapter 4

Finite temperature effects in condensate mixtures

Phase-separation in two-component fluids is ubiquitous in nature, and the transition from miscible to immiscible phase is a quintessential example of critical phenomena. One classic example is the temperature driven phase-separation in the cyclohexane-aniline mixture [138]. It is then natural to ask what are the similarities and differences in binary mixtures of quantum fluids ? The criterion for phase-separation, derived from Thomas-Fermi (TF) approximation at zero temperature [27], is that the intra-(U_{11}, U_{22}) and interspecies interaction (U_{12}) strengths, must satisfy the inequality $U_{12}^2 > U_{11}U_{22}$. This criterion is based on TF approximation at zero temperature, however, experiments are performed at finite temperatures. Therefore, deviations from the criterion are to be expected.

In this thesis, we study the role of thermal fluctuations in the phenomenon of phase-separation in trapped TBECs using HFB-Popov approximation, and as example, self-energy Feynman diagrams subsumed in this approximation are shown in Fig. 4.1. Our studies reveal that at $T \neq 0$, the constituent species in the TBEC undergo phase-separation at a higher U_{12} than the value predicted based on the TF-approximation at $T = 0$. Consistent with experimental observations of dual species condensate of ^{87}Rb and ^{133}Cs [49], our theoretical investigations show that even when the TF phase-separation condition is met, there is a sizable overlap between the two species. We attribute this to the presence of the thermal clouds, which have profound effect on the

miscibility-immiscibility transition. At $T = 0$, the TBECs are coherent throughout the spatial extent of the condensate, however, when $T \neq 0$ coherence decays and is reflected in the correlation function. This implies that at $T = 0$, the miscible and the immiscible phases are indistinguishable from the trends in the correlation function. But, for $T \neq 0$ the miscible-immiscible transition and the associated changes in the density profiles have a characteristic signature in the correlation functions. There is a smooth cross-over between the correlation functions when the transition occurs. Furthermore, we examine the mode evolution at $T \neq 0$ and demonstrate the existence of mode bifurcation near the critical temperature. The Kohn mode, however, exhibits deviation from the natural frequency at finite temperatures after the phase-separation. This is due to the exclusion of the non-condensate atoms in the dynamics. We choose the parameter domain where the system is quasi-1D and a mean-field description like HFB-Popov is applicable. The quasi-1D trapped bosons exhibit a rich phase structure as a function of density and interaction strengths [162]. For comparison with the experimental results we also consider the parameters as in the experiment [49]. We find that, like in Ref. [163], the quasi-1D description is in good agreement with the condensate density profiles of 3D calculations [164].

4.1 Overlap measure and correlation function

To examine the role of temperature in phase-separation of TBECs, we introduce overlap integral Λ as a measure of phase separation. It is defined as

$$\Lambda = \frac{\left[\int n_1(z) n_2(z) dz\right]^2}{\left[\int n_1^2(z) dz\right]\left[\int n_2^2(z) dz\right]}, \tag{4.1}$$

where n_k is the density of the kth species, including condensate and non-condensate atoms. In the expression, the integral in the numerator is a measure of the overlap between the two species, and normalized to the densities so that $0 \leqslant \Lambda \leqslant 1$. The two limits $\Lambda = 0$ and 1 signify complete phase-separation and miscible phase with maximal density overlaps [213]. To distinguish the two phases, we consider the TBEC is phase separated and miscible when $0 < \Lambda \leqslant 0.5$ and $0.5 < \Lambda \leqslant 1$, respectively.

Another important measure, which describes the coherence of the species in a TBEC, is the field-field correlation. In terms of the Bose field operator $\hat{\Psi}_k$, the nor-

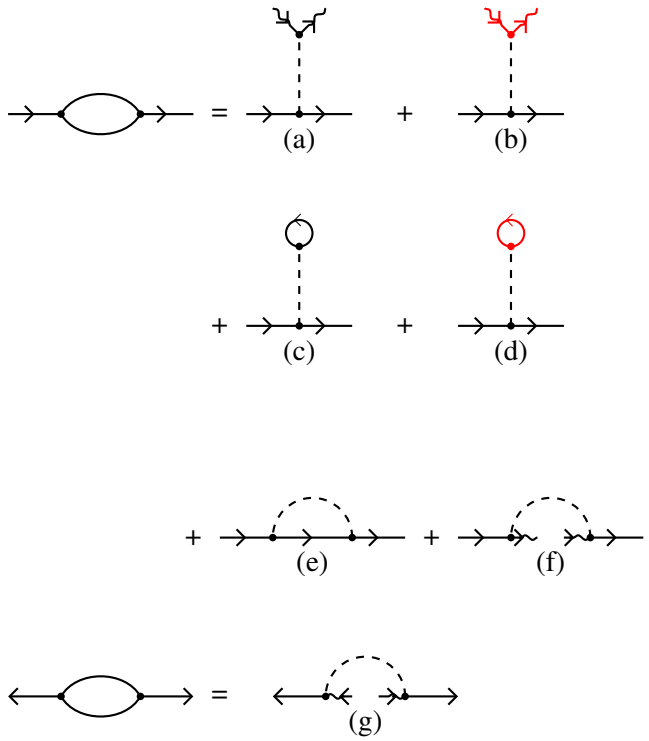

Figure 4.1: Self-energy diagrams for TBEC in the HFB-Popov approximation. The black and red wiggly lines represent propagator for ϕ_1 and ϕ_2, respectively. The smooth solid lines denote propagator for $\tilde{n}_1$. The broken lines represent interatomic interaction [98, 212].

malized first order or the off-diagonal correlation function, which is also a measure of the phase fluctuations, is

$$g_k^{(1)}(z,z') = \frac{\langle \hat{\Psi}_k^\dagger(z)\hat{\Psi}_k(z')\rangle}{\sqrt{\langle \hat{\Psi}_k^\dagger(z)\hat{\Psi}_k(z)\rangle\langle \hat{\Psi}_k^\dagger(z')\hat{\Psi}_k(z')\rangle}}. \tag{4.2}$$

It can also be expressed in terms of off-diagonal condensate and non-condensate densities as

$$g_k^{(1)}(z,z') = \frac{n_{ck}(z,z') + \tilde{n}_k(z,z')}{\sqrt{n_k(z)n_k(z')}}, \tag{4.3}$$

where,

$$\begin{aligned} n_{ck}(z,z') &= \phi_k^*(z)\phi_k(z') \\ \tilde{n}_k(z,z') &= \sum_j \{[u_{kj}^*(z)u_{kj}(z') + v_{kj}^*(z)v_{kj}(z')]N_0(E_j) \\ &\quad + v_{kj}^*(z)v_{kj}(z')\}. \end{aligned}$$

At $T = 0$, when the entire system is coherent and characterized by the presence of condensate only, then $g_k^{(1)} = 1$ within the extent of the condensate, whether it is in

the miscible or in the immiscible regime. So, one cannot distinguish between the two phases from the trends in the correlation functions of the individual species. However, at $T \neq 0$, a clear signature of miscible-immiscible transition of the density profiles is reflected in the form of the correlation functions. The correlation undergoes power law decay of $g_k^{(1)}$ in the neighbourhood of $z = 0$, and exponential decay at the edges of the TBEC.

4.2 Mode evolution of trapped TBEC at $T \neq 0$

For the $T \neq 0$ calculations, as mentioned earlier, we solve the coupled Eq. (2.67) and (2.68) iteratively till convergence. After each iteration, $\phi_k(z)$ are renormalized so that

$$\int_{-\infty}^{\infty} \left[|\phi_k(z)|^2 + \tilde{n}_k(z)\right] dz = N_k, \tag{4.4}$$

where k is the species index. To improve convergence, we use successive over relaxation, but at higher T we encounter serious convergence solutions and require careful choice of the relaxation parameters. For computations, we again consider the Cs-Rb TBEC with trap parameters $\omega_{\perp(\mathrm{Cs})} = 2\pi \times 40.2$ Hz, $\omega_{\perp(\mathrm{Rb})} = 2\pi \times 32.2$ Hz, $\omega_{z(\mathrm{Rb})} = 2\pi \times 3.89$ Hz and $\omega_{z(\mathrm{Cs})} = 2\pi \times 4.55$ Hz with coinciding trap centers, the number of atoms as $N_{\mathrm{Rb}} = N_{\mathrm{Cs}} = 10^3$ and $a_{\mathrm{CsRb}} = 650a_0$. The evolution of ω (mode frequency) with T is shown in Fig. 4.2, where the T is in units of T_c, the critical temperature of ideal bosons in quasi-1D harmonic traps defined through the relation $N = (k_{\mathrm{B}}T_c/\hbar\omega_z)\ln(2k_{\mathrm{B}}T_c/\hbar\omega_z)$ [214], where N is the number of atoms. Considering that $\omega_{z(\mathrm{Rb})} < \omega_{z(\mathrm{Cs})}$, the critical temperature of Rb is lower than that of Cs. So, for better description we scale the temperature with respect to the T_c of Rb atoms, and here after by T_c we mean the critical temperature of Rb atoms. From Fig. 4.2, when $T/T_c \geqslant 0.2$ the Kohn mode energy increases with T/T_c. Based on this observation, for the present work, the HFB-Popov theory produces reliable results in the temperature range $T < 0.2T_c$. This is consistent with an earlier work on HFB-Popov studies in single-species condensate [107], but different from the trend observed in Ref. [105, 106]. The increase in Kohn mode energy could arise from an important factor associated with the thermal atoms. In the HFB-Popov formalism the collective modes oscillate in a static thermal cloud background and dynamics of $\tilde{n}_k$ are not taken

into account. In TBECs the effects of dynamics of $\tilde{n}_k$ may be larger as $\tilde{n}_k$ is large at the interface. An inclusion of the full dynamics of the thermal cloud in the theory would ensure the Kohn mode energy to be constant at all temperatures [132]. The Goldstone modes, on the other hand, remain steady [107].

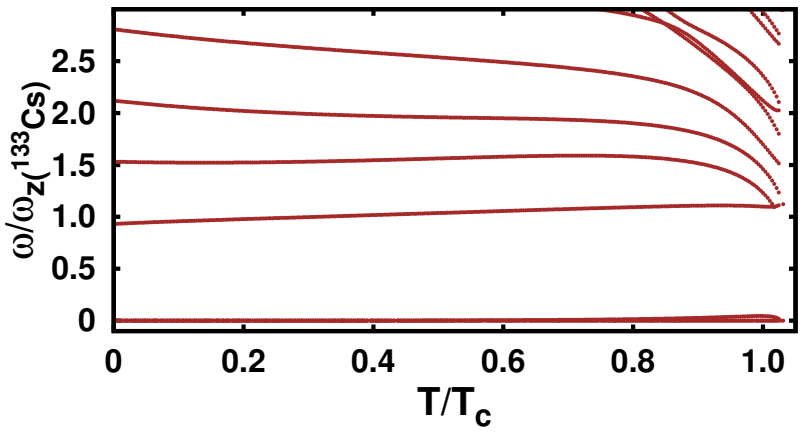

Figure 4.2: Frequencies (ω_j) of the low-lying modes at $T/T_c \neq 0$. The filled circles (brown) are the excitation energies from the HFB-Popov theory with $N_{\rm Rb} = N_{\rm Cs} = 10^3$.

The trend in the evolution of the modes indicates bifurcations at $T/T_c \approx 1$ and is consistent with the theoretical observations in single-species condensates [105–107]. At this temperature, as evident from Fig. 4.2, the Kohn mode and the mode above it (which has principal quantum no $n = 2$ for both the species) merge. This is one of the bifurcations emerging from the Rb atoms crossing the critical temperature, above this temperature there is no Rb condensate. At $T > T_c$ the Cs condensate density is still non-zero as Cs has higher critical temperature. So, there may be another mode-bifurcation at the critical temperature of Cs. A reliable calculation for this would, however, require treating the interaction between thermal Rb atoms and Cs condensate more precisely. For this reason in the present work we do not explore temperature much higher than the T_c of Rb atoms and the possibility of the second mode bifurcation shall be examined in future works. In the case of single-species calculations, at $T/T_c > 1$, the mode frequencies coalesce to the mode frequencies of the trapping potential. In the present work we limit the calculations to $0 \leqslant T/T_c \leqslant 1.1$, so that $T/T_c \ll T_d/T_c$. Here, $T_d \approx (N_{\rm Rb}+N_{\rm Cs})\hbar\omega_z/k_{\rm B}$ is the degeneracy temperature of the system and in the present case $T_d \approx 437$ nK. For a single-species BEC in 3D, the results for $T/T_c > 0.65$ may have significant errors as extensive numerical studies have shown that the HFB-

Popov theory gives accurate results at $T/T_c \leqslant 0.65$ [106]. We have, however, extended the computations in the present work to $T/T_c > 0.2$ like in Ref. [105] to study the general trends and properties of mode bifurcations at the critical temperature.

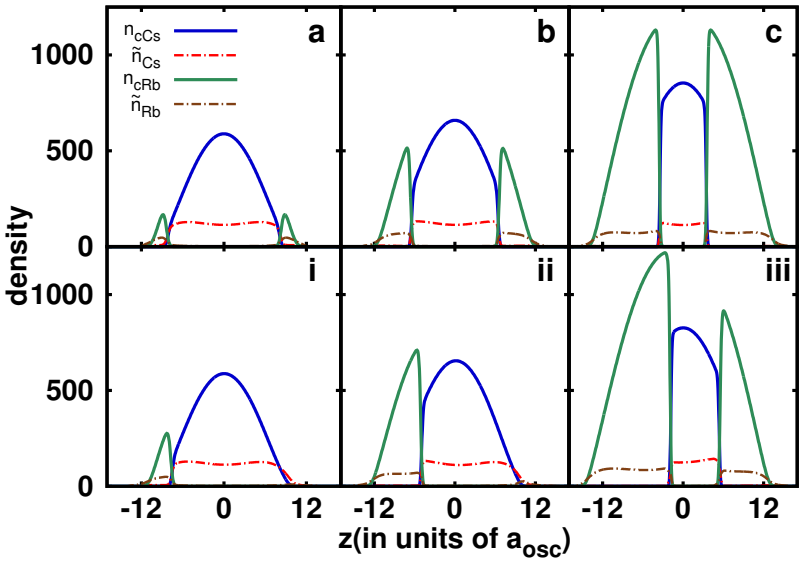

Figure 4.3: Density profile of n_c and $\tilde{n}$ at 25 nK. (a), (b) and (c) correspond to $N_{\rm Rb} = 840(N_{\rm Cs} = 8570)$, $N_{\rm Rb} = 3680(N_{\rm Cs} = 8510)$, and $N_{\rm Rb} = 15100(N_{\rm Cs} = 6470)$, respectively, with coincident trap centers. (i), (ii) and (iii) correspond to same atom numbers as the previous sequence, however, the trap centers are shifted relatively by $0.8a_{\rm osc(Cs)}$. In the plots density is measured in units of $a_{\rm osc}^{-1}$.

To examine the profiles of n_{ck} and $\tilde{n}_k$, we compute the densities at 25 nK for three cases, these are $N_{\rm Rb} = 840(N_{\rm Cs} = 8570)$, $N_{\rm Rb} = 3680(N_{\rm Cs} = 8510)$, and $N_{\rm Rb} = 15100(N_{\rm Cs} = 6470)$. The same set was used in the previous work of Pattinson *et al.* at $T = 0$ [164] and correspond to three regimes considered ($N_{\rm Cs} > N_{\rm Rb}$, $N_{\rm Cs} \approx N_{\rm Rb}$, and $N_{\rm Cs} < N_{\rm Rb}$) in the experimental work of McCarron *et al.* [49]. The actual experimental images for these cases from Ref. [49] are shown in Fig. 3.1. Consider the trap centers, along z-axis, are coincident, then $\tilde{n}_k$ and n_{ck} are symmetric about $z = 0$, and are shown in Fig. 4.3(a-c). In all the cases, Cs condensate occupies the central position. This configuration is energetically preferred as heavier atomic species at the center has lower trapping potential energy and minimizes the total energy. In the experiments, the trap centers are not exactly coincident. So, to replicate the experimental situation we shift the trap centers, along z-axis, by $0.8a_{\rm osc(Cs)}$ and the corresponding density profiles are shown in Fig. 4.3(i-iii). For $N_{\rm Rb} = 840(N_{\rm Cs} = 8570)$

and $N_{\rm Rb} = 3680 (N_{\rm Cs} = 8510)$, Fig. 4.3(i-ii), the n_{ck} and $\tilde{n}_k$ are located sideways. So, there are only two Goldstone modes in the excitation spectrum. But, for $N_{\rm Rb} = 15100 (N_{\rm Cs} = 6470)$, Fig. 4.3(iii), $n_{\rm Cs}$ is at the center with $n_{\rm Rb}$ at the edges forming *sandwich* geometry and hence has three Goldstone modes. In all the cases $\tilde{n}_k$ have maxima in the neighbourhood of the interface and the respective n_{ck}s are not negligible. So, we can expect larger n_{ck}-$\tilde{n}_k$ coupling in TBECs than single-species condensates. For the $N_{\rm Rb} = 3680 (N_{\rm Cs} = 8510)$ and $N_{\rm Rb} = 15100 (N_{\rm Cs} = 6470)$ cases, n_{ck} are very similar to the results of 3D calculations at $T = 0$ [164]. However, it requires a 3D calculation to reproduce the experimental profiles of n_{ck} for $N_{\rm Rb} = 840 (N_{\rm Cs} = 8570)$ as the relative shift δx is crucial in this case.

4.3 Suppression of phase segregation

The thermal suppression of phase-separation is generic to any binary condensate mixture. For comparison with experimental realizations we, however, consider the Cs-Rb BEC mixture. The interspecies scattering length is chosen here to be $a_{12} = a_{\rm CsRb} = 295 a_0$ with $N_{\rm Cs} = N_{\rm Rb} = 5 \times 10^3$. With these parameters, the TBEC is in the phase separated domain and has sandwich profile: Cs condensate occupying the central region surrounded by Rb condensate at the edges . To form a quasi-1D trap we take $\omega_{z({\rm Cs})} = 2\pi \times 4.55$ Hz, $\omega_{z({\rm Rb})} = 2\pi \times 3.89$ Hz, $\omega_{\perp({\rm Cs})} = 50 \omega_{z({\rm Cs})}$ and $\omega_{\perp({\rm Rb})} = 50 \omega_{z({\rm Rb})}$. For these values of $\omega_\perp$, the temperature along the radial direction is $\hbar\omega_\perp / k_{\rm B} \approx 11$ nK, and the tight confinement condition is valid as $\mu_k / \hbar\omega_\perp \approx 10^{-2}$. In addition to this, the healing length $\xi_k \gg 1/n_k$. Thus the system is in the weakly interacting TF regime [162] and mean field description through GP equation is valid. This choice of parameters is consistent with the experimental parameters of a recent work on quasi-1D TBEC of different hyperfine states of ^{87}Rb [215], in which dynamical evolution of mixtures of quantum gases has been observed. It should be emphasized here that sandwich type density profiles are applicable only to trapped systems. In uniform systems, at phase-separation, the energetically preferred states are the symmetry-broken density profiles where one species is entirely to the left and the other is entirely to the right. We refer to this configuration of density profiles as *side-by-side* type. In

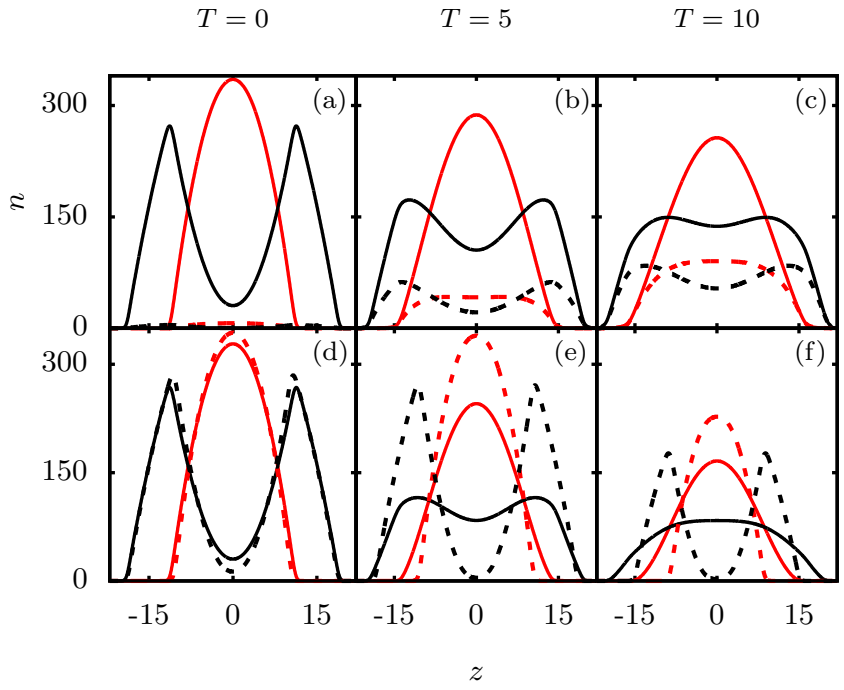

Figure 4.4: The suppression of phase-separation in ^{87}Rb-^{133}Cs TBEC at $a_{12} = 295a_0$. (a)-(c) The solid and dashed red (black) lines represent $n_{\rm Cs}(n_{\rm Rb})$ and $\tilde{n}_{\rm Cs}(\tilde{n}_{\rm Rb})$, respectively, at $T = 0, 5, 10$ nK. (d)-(f) The solid red (black) lines represent $n_{c\rm Cs}(n_{c\rm Rb})$ at $T = 0, 5, 10$ nK respectively. The dashed red (black) lines $n_{c\rm Cs}(n_{c\rm Rb})$ at $T = 0$ with the same number of condensate atoms at $T = 0, 5, 10$ nK respectively. Here, n and z are measured in units of $a_{\rm osc}^{-1}$ and $a_{\rm osc}$, respectively.

the present work, we demonstrate the role of thermal cloud in sandwich type density profiles since these are unique to trapped systems and experimentally pertinent. For the homogeneous binary condensates, using periodic boundary condition with $\omega_z = 0$ in our computations, we do get side-by-side density profiles at phase-separation and these are consistent with the results reported in previous works [216].

At $T = 0$, in TBECs, as mentioned earlier, the criterion for phase-separation is $U_{12} > \sqrt{U_{11}U_{22}}$. With the parameters of Cs-Rb TBEC, consider keeping $a_{\rm Cs}$ and $a_{\rm Rb}$ fixed, but varying $a_{12} = a_{\rm CsRb}$ through a magnetic Feshbach resonance [168]. The condition for phase-separation, using TF-approximation, is then $a_{12} > 261a_0$. When $a_{12} = 0$, the TBEC is non-interacting and the two species are completely miscible, in which case $\Lambda = 1$. On increasing a_{12}, the extent of overlap between the two-species decreases, and hence Λ decreases. For instance, at $a_{12} = 50a_0$, $\Lambda = 0.97$ and it decreases monotonically with $\Lambda \to 0$ at complete phase-separation. At $a_{12} = 295a_0$,

just at the onset of phase-separation, $\Lambda = 0.14$. As shown in Fig. 4.4(a), the density profiles corresponding to the two-species have interfacial overlap, and the interaction parameters satisfy the phase-separation condition. Furthermore, at phase-separation, $n_{c\mathrm{Cs}}(0)$ is maximum, whereas $n_{c\mathrm{Rb}}(0) \approx 0$ and the species do not have significant overlap. In other words, Cs at the center of the trap is flanked by Rb at the edges and $\Lambda \approx 10^{-1}$. It is to be emphasized that the value of a_{12} at which phase-separation occurs is higher with the numerical solution of GP equation than the value obtained from the TF approximation. This can be attributed to the large condensate density gradients around the interface region at phase-separation, which are ignored in the TF-approximation.

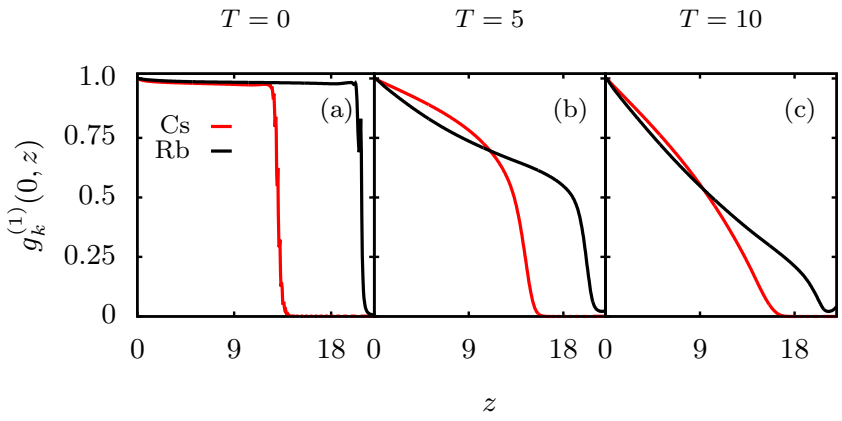

Figure 4.5: (a)-(c) The first order spatial correlation function, $g^{(1)}_{\mathrm{Cs/Rb}}(0,z)$ with $z \geqslant 0$, of ^{87}Rb-^{133}Cs TBEC at equilibrium for $a_{12} = 295a_0$ at $T = 0, 5, 10$ nK respectively. Here z is measured in units of a_{osc}.

For $T \neq 0$ the Bose factor $N_0(E_j) \neq 0$, so in addition to the quantum fluctuations, the non-condensate densities $\tilde{n}_k$ have contributions from the thermal cloud as well. The condensate atoms n_{ck} then interact with $\tilde{n}_k$ of both the species, and modify n_{ck}. For illustration, at $T = 5$ nK and $a_{12} = 295a_0$, the total and non-condensate density profiles are shown in Fig. 4.4(b). Compared to the density profiles in Fig. 4.4(a), there is a remarkable change in $n_{c\mathrm{Rb}}$ as a result of the finite temperature: $n_{c\mathrm{Rb}}(0) > 0$. Thus, keeping all the parameters same, but taking $T = 5$ nK, the two species have substantial overlap as shown in Fig. 4.4(b), and the value of Λ changes from $\approx 10^{-1}$ at zero temperature to ≈ 0.55 at 5 nK. In other words, the finite temperature transforms the phase separated TBEC at $T = 0$ to a partially miscible phase. The degree of overlap

increases with temperature and at $T = 10$ nK, the TBEC is miscible as $\Lambda \approx 0.77$. Thus, with the increase in temperature, the density of thermal cloud increases and the *phase-separation is suppressed*. This is evident from Fig. 4.4(c), which shows the plots of corresponding total and non-condensate density profiles. Thus, a_{12} has to be greater than $295a_0$ at $T \neq 0$ for phase-separation to occur. To confirm that the suppression is a consequence of non-zero temperature, we identify and compute the number of condensate atoms in each species, and use these numbers for $T = 0$ computations. Despite the difference in the numbers of atoms, as shown in Figs. 4.4(d-f), the TBEC retains the immiscible profiles at zero temperature. This implies that without the thermal cloud, there are no deviations from the usual phase-separation condition.

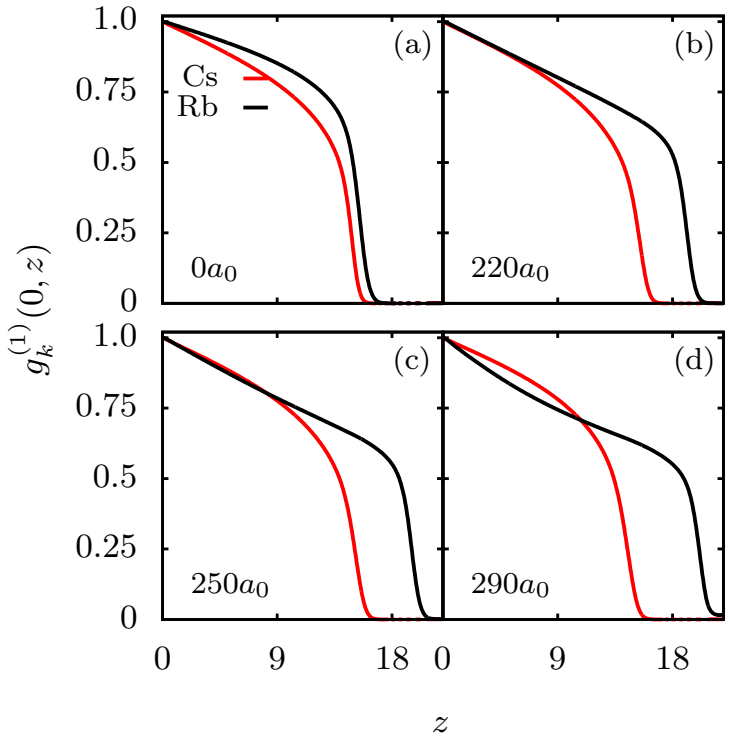

Figure 4.6: (a)-(d) The first order spatial correlation function, $g^{(1)}_{\mathrm{Cs/Rb}}(0,z)$ with $z \geqslant 0$, of ^{87}Rb-^{133}Cs TBEC at equilibrium at $T = 5$ nK for $a_{12} = 0, 220, 250, 290a_0$, respectively. Here z is measured in units of a_{osc}.

To investigate the spatial coherence at equilibrium, we examine the nature of the first order correlation function $g_k^{(1)}(z,z')$ as defined in Eq. (4.3). As to be expected, profile of $g_k^{(1)}(z,z')$ depends on the interaction strength and temperature. This is independent of whether the TBEC is in miscible or immiscible regime.

As stated earlier, in the quasi-1D regime at $T = 0$, there is coherence in the Cs-Rb TBEC and $g^{(1)}_{\mathrm{Cs/Rb}}(0, z) \approx 1$ within the spatial extent of the condensates. The decay as seen in Fig. 4.5(a) is due to the finite size of the system. For homogeneous case the decay would be absent, however, it must be mentioned here that a Bose gas cannot condense in a homogeneous 1D system at $T = 0$ and $T \neq 0$. This is due to Hohenberg-Mermin-Wagner theorem [217,218], and a consequence of large quantum fluctuations. For simplicity and based on the symmetry of the system we consider $g^{(1)}_{\mathrm{Cs/Rb}}(0, z)$ with $z \geqslant 0$, and plots at different temperatures are shown in Fig. 4.5. At $T = 0$ the form of the $g^{(1)}_{\mathrm{Cs/Rb}}(0, z)$ remains unchanged as the system undergoes the dramatic transition from miscible to immiscible phase. This is evident from the plot in Fig. 4.5(a). However, when $T \neq 0$, unlike the zero temperature case, $g^{(1)}_{\mathrm{Cs/Rb}}(0, z)$ is maximum at $z = 0$ and decays to zero with z. This is due to the non-condensate atoms, which modify the nature of coherence in the system. The rate of decay of the $g^{(1)}_{\mathrm{Cs/Rb}}(0, z)$ increases with temperature, and this is evident from the plots of $g^{(1)}_{\mathrm{Cs/Rb}}(0, z)$ at $T = 5$ nK and $T = 10$ nK shown in Figs. 4.5(b-c) for $a_{12} = 295a_0$. We also observe a dramatic variation in $g^{(1)}_{\mathrm{Cs/Rb}}(0, z)$ as the value of a_{12} is steered from miscible to immiscible regime at fixed temperature. At the outset, when the TBEC is miscible at $a_{12} = 0$, $g^{(1)}_{\mathrm{Rb}}(0, z)$ decays to 0 at a larger distance than $g^{(1)}_{\mathrm{Cs}}(0, z)$ as shown in Fig. 4.6(a). This is because n_{Rb} has a larger spatial extent than n_{Cs}. As a_{12} is increased, the TBEC undergoes a phase-transition from miscible to sandwich type density profiles. Along with this, the distance at which $g^{(1)}_{\mathrm{Rb}}(0, z)$ falls off to zero increases with increase in a_{12}. On the contrary, the distance at which $g^{(1)}_{\mathrm{Cs}}(0, z)$ falls off to zero decreases with increase in a_{12}. This causes the $g^{(1)}_{k}(0, z)$ of the individual species to cross each other at a certain distance z_0 from the origin. At z_0, the two species have equal $g^{(1)}_{\mathrm{Cs/Rb}}(0, z_0)$ and this is a characteristic signature of immiscible phase. These features are shown in Figs. 4.6(b-d). It deserves to be mentioned here that z_0 increases, and $g^{(1)}_{\mathrm{Cs/Rb}}(0, z_0)$ decreases with increase in a_{12}. In addition, there is a dramatic difference in the decay rates of $g^{(1)}_{\mathrm{Cs/Rb}}(0, z_0)$; it is much faster in Cs. This is attributed to the fact that both $n_{c\mathrm{Rb}}$ and $\tilde{n}_{\mathrm{Rb}}$ increase along z within the bulk of Cs-Rb TBEC. Where as in Cs, around the origin $n_{c\mathrm{Cs}}$ decreases but $\tilde{n}_{\mathrm{Cs}}$ increases. This trend is similar with a single-species Cs condensate. The presence of Rb does not affect the nature of $g^{(1)}_{\mathrm{Cs}}(0, z)$ in Cs-Rb

TBEC. Around the point of phase-separation $n_{c\mathrm{Rb}}(0)$ in a Cs-Rb TBEC is distinctly different from single-species Rb condensate, so is the nature of $g^{(1)}_{\mathrm{Rb}}(0,z)$.

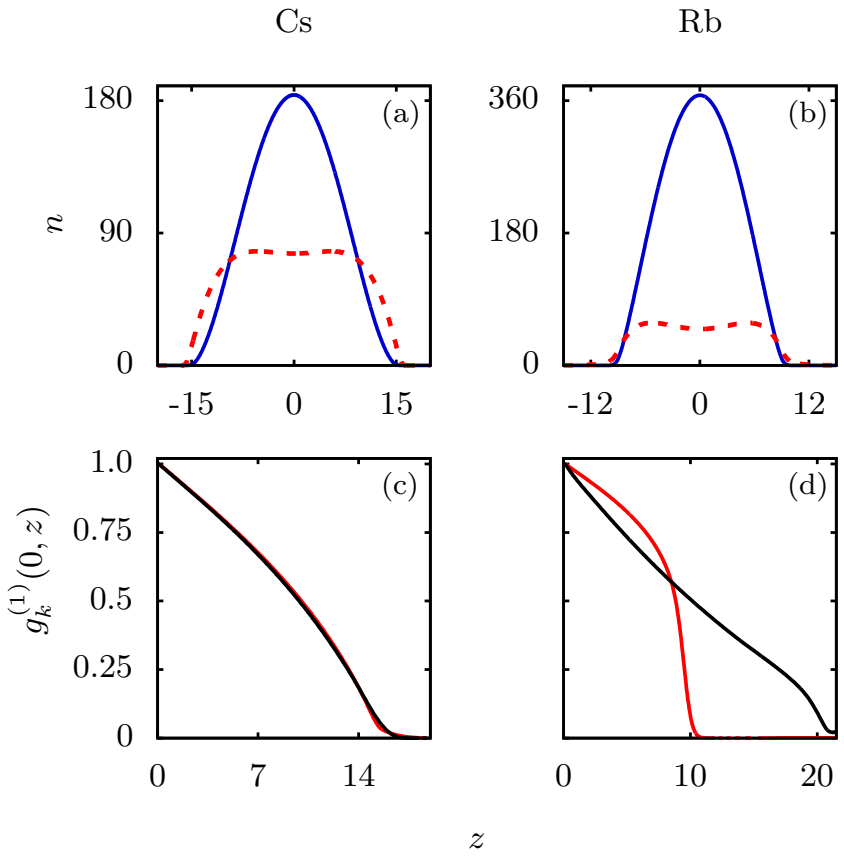

Figure 4.7: The equilibrium density profiles and first order spatial correlation function $g^{(1)}(0,z)$ with $z \geqslant 0$ of Cs and Rb BEC respectively at $T = 10$ nK. (a) The solid blue and dashed red lines represent $n_{c\mathrm{Cs}}$ and $\tilde{n}_{\mathrm{Cs}}$, respectively. (b) The solid blue and dashed red lines represent $n_{c\mathrm{Rb}}$ and $\tilde{n}_{\mathrm{Rb}}$, respectively. (c) The solid red (black) line represents $g^{(1)}_{\mathrm{Cs}}(0,z)$ in Cs BEC (Cs-Rb TBEC) at $T = 10$ nK. (d) The solid red (black) line represents $g^{(1)}_{\mathrm{Rb}}(0,z)$ in Rb BEC (Cs-Rb TBEC) at $T = 10$ nK. Here, n and z are measured in units of a_{osc}^{-1} and a_{osc}, respectively.

To show the dramatic transformation of $g^{(1)}(0,z)$ in TBEC, the $g^{(1)}(0,z)$s of single-species condensates of ^{87}Rb and ^{133}Cs are shown in Fig. 4.7. From the figure we see there is no significant change in $g^{(1)}_{\mathrm{cs}}(0,z)$ of the ^{133}Cs in a single-species condensate and Cs-Rb TBEC. In the latter, ^{133}Cs condensate occupies the central region at phase-separation. But, there is a major deviation in $g^{(1)}_{\mathrm{Rb}}(0,z)$ from the single-species case when it occupies the outer edges in a TBEC.

To examine the provenance of the thermal suppression, we identify the quasiparti-

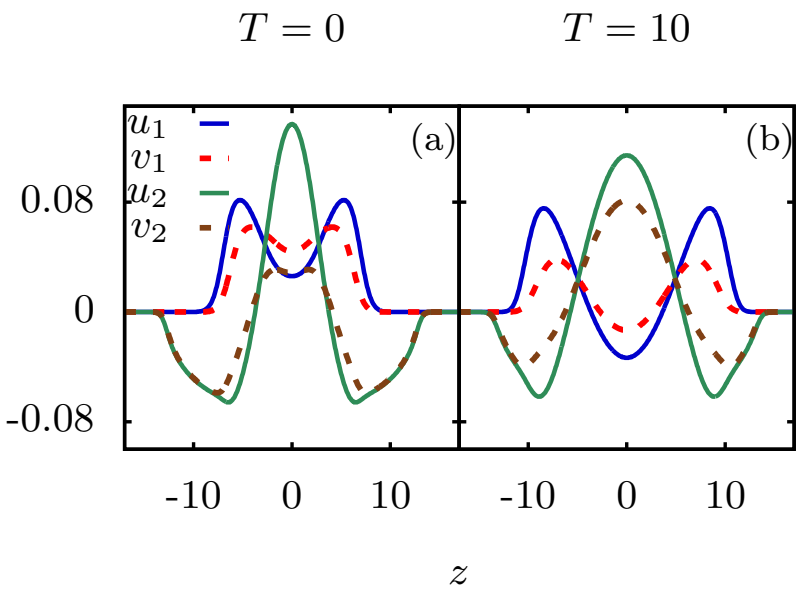

Figure 4.8: Quasiparticle amplitudes corresponding to the fourth excited mode in ^{85}Rb-^{87}Rb TBEC at $T = 0, 10$ nK respectively. In the plots u's and v's are in units of $a_{\rm osc}^{-1/2}$.

cle mode which has maximum contribution to the thermal cloud. From the solutions of the coupled BdG equations, it is the fourth excited mode which has the largest contribution to the thermal density. From Fig. 4.8(a), it is clear that at $T = 0$, $u_2(0)$ is maximum whereas $v_2(0) \approx 0$. Thus $\tilde{n}_2(0)$ is finite but small, and the condensates are phase-separated. The quasiparticle amplitudes u_1 and v_1 belonging to species 1 and have very little contribution towards $\tilde{n}_1$ as they get repelled from $\phi_2(0)$ and $\tilde{n}_2(0)$. However, at finite temperatures there are few notable changes in the spatial structure of this quasiparticle amplitude. For example, consider the case of $T = 10$ nK, $u_2(0)$ and $v_2(0)$ both being maxima, has larger contribution to $\tilde{n}_2(0)$ as shown in Fig. 4.8(b). Similar to the $T = 0$ case, $u_1(0)$ and $v_1(0)$ are still small. The emergence of higher $\tilde{n}_2(0)$ modifies $\phi_2(0)$ and the TBEC becomes partially miscible.

4.4 Segregation independent of temperature

In the domain of large $a_{12}, U_{12} \gg \sqrt{U_{11}U_{22}}$, $\Lambda \approx 0$, and the phase-segregation is more prominent. However, due to the geometry of the TBEC mean-field approximation is still valid. In this domain the interfacial overlap is minimal and the TBECs assume sandwich type density profile. The system is then equivalent to three coupled conden-

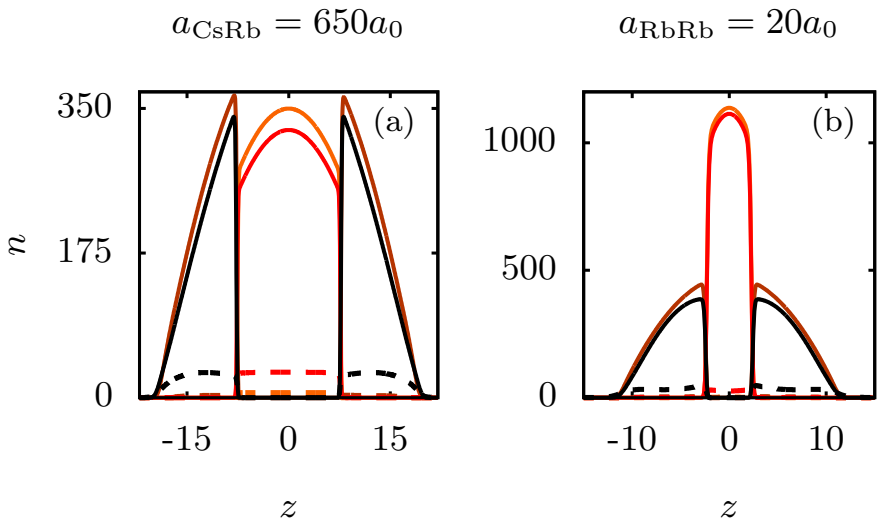

Figure 4.9: Density profiles showing complete phase-separation at $T = 0$ and $T = 10$ nK. (a) Phase-separation in ^{87}Rb-^{133}Cs TBEC for $a_{12} = 650a_0$. The solid and dashed orange (brown) lines represent $n_{c\mathrm{Cs}}(n_{c\mathrm{Rb}})$ and $\tilde{n}_{c\mathrm{Cs}}(\tilde{n}_{c\mathrm{Rb}})$, respectively at $T = 0$. The solid and dashed red (black) lines represent $n_{c\mathrm{Cs}}(n_{c\mathrm{Rb}})$ and $\tilde{n}_{c\mathrm{Cs}}(\tilde{n}_{c\mathrm{Rb}})$, respectively at $T = 10$ nK. (b) Phase-separation in ^{85}Rb-^{87}Rb TBEC for $a_{12} = 20a_0$. The solid and dashed orange (brown) lines represent n_c and $\tilde{n}$ of ^{85}Rb (^{87}Rb), respectively at $T = 0$. The solid and dashed red (black) lines represent n_c and $\tilde{n}$ of ^{85}Rb (^{87}Rb), respectively at $T = 10$ nK. Here, n and z are measured in units of a_{osc}^{-1} and a_{osc}, respectively.

sate fragments, and as discussed earlier the Bogoliubov analysis shows the presence of three Goldstone modes [136]. For the Cs-Rb TBEC considered here, the background interspecies scattering length $a_{\mathrm{CsRb}} = 650a_0$ satisfies the above condition. With this value of a_{12}, at $T = 0$ as shown in Fig. 4.9(a), Cs condensate lies at the center of the trap and Rb condensate at the edges. So, at the center $n_{\mathrm{Rb}}(0) = 0$ and $n_{\mathrm{Cs}}(0)$ is maximum. With the increase in a_{12}, there is a decrease in the number of non-condensate atoms arising from quantum fluctuations. This is a manifestation of smaller overlap between the condensates at the interfaces. On the contrary, for a single-species BEC, with the increase in intraspecies interaction strength, the number of non-condensate atoms due to quantum fluctuations increases [137]. When $T \neq 0$, the thermal densities $\tilde{n}_k$ interact with the condensate clouds through the intra- and interspecies interactions. But, due to the large a_{12}, the interspecies interaction energy is much larger than the intraspecies interaction energy. This makes $n_{\mathrm{Rb}}(0) \approx 0$, and there is little overlap of the thermal cloud of one species with the condensate of the other species, such that

$\Lambda < 0.1$. Thus, there is *no thermal suppression* in the domain of large a_{12} [219]. We observe similar results in the case of ^{85}Rb-^{87}Rb TBEC as well, where the intraspecies interaction of ^{85}Rb is decreased to obtain completely phase-separated density profiles. These are shown in Fig. 4.9(b).

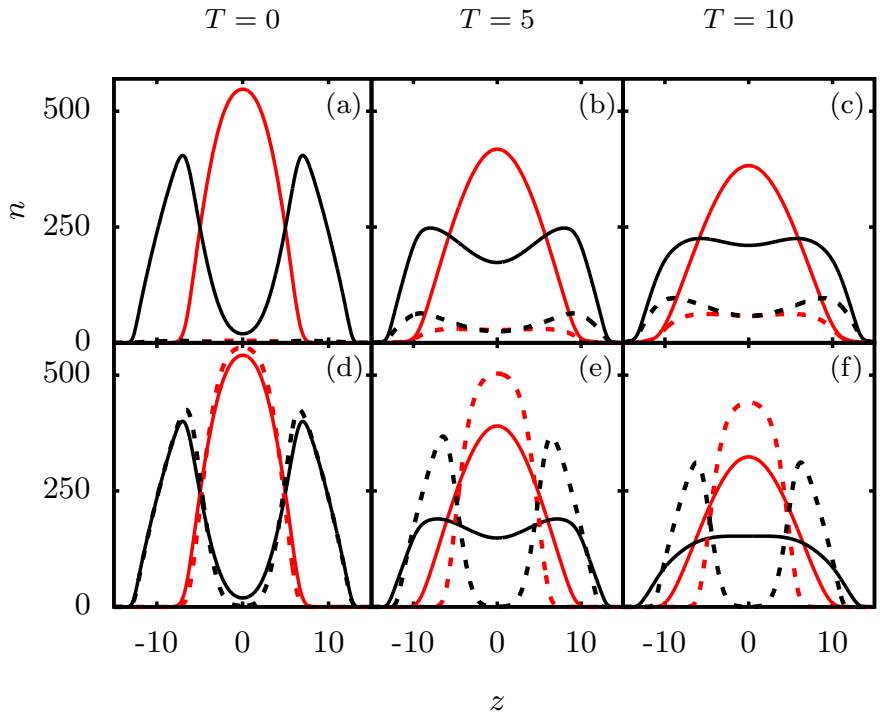

Figure 4.10: The suppression of phase-separation in ^{85}Rb-^{87}Rb TBEC at $a_{11} = 120a_0$. (a)-(c) The solid and dashed red (black) lines represent $n_1(n_2)$ and $\tilde{n}_1(\tilde{n}_2)$ at $T = 0, 5, 10$ nK respectively. (d)-(f) The solid red (black) lines represent $n_{c1}(n_{c2})$ at $T = 0, 5, 10$ nK respectively. The dashed red (black) lines $n_{c1}(n_{c2})$ at $T = 0$ with the same number of condensate atoms at $T = 0, 5, 10$ nK respectively. Here, n and z are measured in units of $a_{\rm osc}^{-1}$ and $a_{\rm osc}$, respectively.

4.5 Thermal suppression in ^{85}Rb-^{87}Rb BEC

Consider the ^{85}Rb-^{87}Rb BEC mixture at phase-separation [53, 64] as an example of binary condensates with different isotopes of the same element, take ^{85}Rb and ^{87}Rb as the first and second species, respectively. To navigate the TBEC through the miscible-immiscible transition, in experiments as well, the intraspecies scattering length of ^{85}Rb is varied using magnetic Feshbach resonance [220]. We, then, consider a set of param-

eters in the immiscible domain and examine the finite temperature effects to phase-separation. The parameters are: the intraspecies scattering lengths $a_{11} = a_{^{85}\mathrm{Rb}} = 120a_0$, $a_{22} = a_{^{87}\mathrm{Rb}} = 100a_0$, the interspecies scattering length $a_{12} = a_{^{85}\mathrm{Rb}^{87}\mathrm{Rb}} = 214a_0$ with $N_{^{85}\mathrm{Rb}} = N_{^{87}\mathrm{Rb}} = 5 \times 10^3$. To examine the TBEC in quasi-1D trap we take $\omega_{z(^{85}\mathrm{Rb})} = 2\pi \times 4.55$ Hz and $\omega_{z(^{87}\mathrm{Rb})} = 2\pi \times 3.89$ Hz; $\omega_{\perp(^{85}\mathrm{Rb})} = 50\omega_{z(^{85}\mathrm{Rb})}$ and $\omega_{\perp(^{87}\mathrm{Rb})} = 50\omega_{z(^{87}\mathrm{Rb})}$. For this parameter set, the ground state is sandwich type with the ^{85}Rb condensate at the centre and surrounded by the ^{87}Rb condensate at the edges.

As mentioned earlier thermal suppression of phase-separation is universal to any binary condensate mixture. For illustration, the total and non-condensate density profiles are shown in Fig. 4.10(b),(c) for $T = 10, 25$ nK and $a_{11} = 115a_0$. Here too, the finite temperature transforms the phase separated TBEC at $T = 0$ to a partially miscible phase. As expected, we find that with increase in temperature the *phase-separation is suppressed* due to the increase in the density of the thermal clouds.

4.6 Summary of the Chapter

At finite temperatures, to examine the properties of binary condensates in the neighbourhood of phase-separation, it is essential to incorporate the thermal component. At $T \neq 0$ there are mode bifurcations close to the $T/T_c \approx 1$. In general, there is a delay or suppression of phase-separation due to the thermal component, and we have examined this in detail with the Cs-Rb binary condensate as an example. In this system the transition is driven by tuning the interspecies interaction, and similar results are obtained in ^{85}Rb-^{87}Rb binary condensate, where tuning the intraspecies interaction of ^{85}Rb induces the transition. The binary condensate mixtures of dilute atomic gases are different from the classical binary fluids which undergo miscible-immiscible transition with temperature as control parameter. First, the variation of temperature in TBECs is applicable only below the lower of the two critical temperatures. Second, each species has two sub-components, the condensate and non-condensate atoms. The condensate or the superfluid components are coherent, but the non-condensate components are incoherent and like the normal gas. Third, there are spatial density variations of all the components due to the nature of the confining potential and diluteness of the atomic

gas. Fourth, beyond a certain critical value of interaction strength or in the strongly phase separated domain, temperature does not alter the density profiles. Finally, the transition to the phase separated domain at finite temperatures is associated with a distinct change in the profile of the correlation functions.

Chapter 5

Fluctuations in quasi-2D condensates

The remarkable advances in cooling and trapping techniques of dilute atomic gases have accelerated research in the field of quantum gases in the last two decades. Central to such achievements are the experimental realizations of optical lattices [221, 222], double-well potentials [223–225], elongated [211] or pancake shaped traps, quasi-homogeneous potential [226], and random potentials [227]. The phenomenon of Anderson localization which was originally predicted in the context of electron transport in crystals [228] has also been observed in BEC of dilute atomic gases using random disordered potential [229, 230]. A collection of ultracold atoms with repulsive binary interactions exhibits diverse properties depending on the geometry of the potential and provides an ideal testbed to explore fundamental topics in many-body physics. One of the topics of particular interest is the physics of toroidal BECs, which has attracted much attention since these are multiply connected systems and topologically distinct from conventional harmonically trapped BECs. The superfluidity of an interacting dilute atomic gas in such a ring geometry is elucidated through the presence of persistent current. Experiments with cold atoms in toroidal traps [231, 232] provide an opportunity to validate the cosmological scenario for string formation in the early Universe through the Kibble-Zurek mechanism [180, 233].

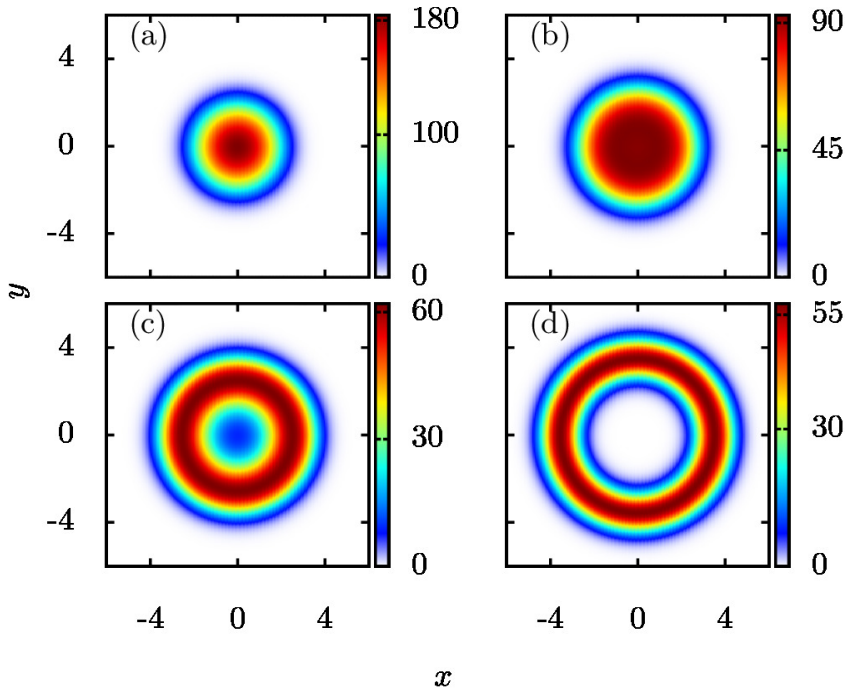

Figure 5.1: Transformation of condensate density distribution as harmonic trapping potential is modified to a toroidal one. (a) - (d) Show the ^{23}Na condensate density profiles corresponding to $U_0 = 0, 5, 10, 20\hbar\omega_x$ respectively with $N_{\rm Na} = 2 \times 10^3$, $\alpha = 1$, $\lambda = 39.5$, and $\omega_\perp = 20.0$ Hz. Density is measured in units of $a_{\rm osc}^{-2}$.

5.1 Quasi-2D BEC : Theory

In a quasi-2D system, the trapping frequencies of the harmonic oscillator potential $V = (1/2)m\omega_x^2(x^2 + \alpha^2 y^2 + \lambda^2 z^2)$ should satisfy the condition $\omega_x, \omega_y \ll \omega_z$, and $\hbar\omega_z \gg \mu$. Here, $\alpha = \omega_y/\omega_x$ and $\lambda = \omega_z/\omega_x$ are the anisotropy parameters along the transverse and axial directions. For $\lambda \gg 1$, the axial degrees of freedom can be integrated out and only the transverse excitations contribute to the dynamics. Under mean field approximation, in Cartesian coordinate system, the second quantized form of the grand-canonical Hamiltonian describing an interacting BEC is

$$\begin{aligned}\hat{H} &= \iint dxdy\hat{\Psi}^\dagger(x,y,t)\Big[-\frac{\hbar^2}{2m}\left(\frac{\partial^2}{\partial x^2}+\frac{\partial^2}{\partial y^2}\right)+V(x,y)\\ &\quad -\mu+\frac{U}{2}\hat{\Psi}^\dagger(x,y,t)\hat{\Psi}(x,y,t)\Big]\hat{\Psi}(x,y,t). \qquad (5.1)\end{aligned}$$

Here, $\hat{\Psi}$ and μ are the Bose field operator of the single-species BEC, and the chemical potential, respectively. The strength of the repulsive interaction between two atoms in

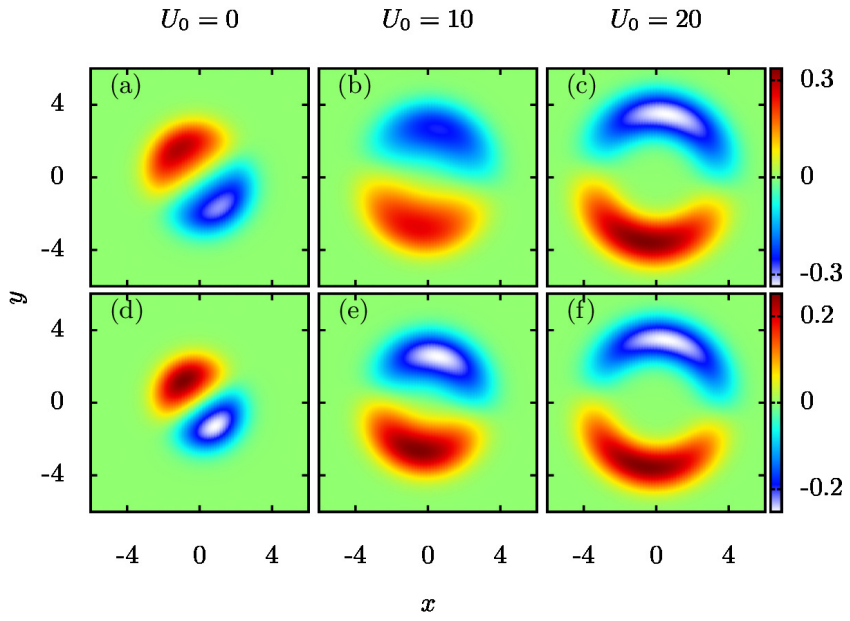

Figure 5.2: Evolution of quasiparticle amplitude corresponding to the Kohn mode as U_0 is increased from 0 to $20\hbar\omega_x$ for $\alpha = 1$. (a) - (c) Show the $u_{\rm Na}$ corresponding to $U_0 = 0, 10, 20\hbar\omega_x$, respectively. Harmonic trapping potential is applicable when $U_0 = 0$, otherwise, it is a Mexican hat potential. At $U_0 = 20$, a toroidal shaped BEC is formed and the Kohn modes get deformed. (d) - (f) Show the $v_{\rm Na}$ corresponding to $U_0 = 0, 10, 20\hbar\omega_x$, respectively. In the plots u and v are in units of $a_{\rm osc}^{-1}$. Here x and y are measured in units of $a_{\rm osc}$.

a quasi-2D condensate is given by $U = 2g\sqrt{2\pi\lambda}$, where $\lambda = (\omega_z/\omega_\perp) \gg 1$. Based on this Hamiltonian, the equation of motion of the Bose field operator is

$$i\hbar\frac{\partial}{\partial t}\hat{\Psi} = \hat{h}\hat{\Psi} + U\hat{\Psi}^\dagger\hat{\Psi}\hat{\Psi}, \tag{5.2}$$

where $\hat{h} = (-\hbar^2/2m)\left(\partial^2/\partial x^2 + \partial^2/\partial y^2\right) + V(x,y) - \mu$. In this thesis, to study toroidal condensates we superimpose a 2D-Gaussian potential to the harmonic oscillator potential. Thus, the confining potential is

$$V_{\rm net}(x,y) = V(x,y) + U_0 e^{-(x^2+\alpha^2y^2)/2\sigma^2}, \tag{5.3}$$

with U_0 as the strength of the Gaussian potential, and σ is the width of the Gaussian potential along the x and y directions. With $U_0 = 0$, when $\alpha = 1$, $V_{\rm net}$ is rotationally symmetric and hence, is rotationally invariant. But, when $\alpha < 1$ the rotational symmetry of the potential $V_{\rm net}$ is broken and the circle is transformed to an ellipse

with the major axis oriented along the y-axis. Furthermore, when $U_0 \gg 0$, $V_{\rm net}$ is modified, and at higher values of U_0 the potential assumes the form of a doughnut or a toroid. Such a trapping potential configuration was realized in an experiment with Na condensate [234]. This transformation is reflected in the geometry of the condensate density distribution, which is evident from the density plots in Fig. 5.1. The possibilities of a toroidal potential were first examined in theoretical works with Laguerre-Gaussian (LG_p^l) laser beams [235,236] of radial and azimuthal orders, $p \geqslant 0$ and l, respectively. Following which, in experiments, toroidal condensates of atomic ^{23}Na [237], and ^{87}Rb [238] have been achieved using LG_0^l beams [239]. Furthermore, toroidal trapping potentials for ^{87}Rb condensates have been realized by combining an RF-dressed magnetic trap with an optical potential [232] or by the intersection of three light beams as elucidated in Ref. [240]. In the present case, like in the previous cases, the spatial and temporal variables are scaled as $x/a_{\rm osc}$, $y/a_{\rm osc}$ and $\omega_x t$ respectively, where $a_{\rm osc} = \sqrt{\hbar/m\omega_x}$. To study the dependence of the collective excitations of the system on U_0 and α, and to examine the density distribution at finite temperatures we employ HFB-Popov approximation. In this formalism, the Bose field operator $\hat{\Psi}$ is decomposed into two parts; the c-field or the condensate part represented by $\phi(x,y,t)$ and the non-condensate or the fluctuation part denoted by $\tilde{\psi}(x,y,t)$. Thus, $\hat{\Psi}$ is written as,

$$\hat{\Psi} = \phi + \tilde{\psi}. \tag{5.4}$$

The generalized GP equation with the time-independent HFB-Popov approximation is then given by

$$\hat{h}\phi + U\left[n_c + 2\tilde{n}\right]\phi = 0, \tag{5.5}$$

where, $n_c(x,y) \equiv |\phi(x,y)|^2$, $\tilde{n}(x,y) \equiv \langle\tilde{\psi}^\dagger(x,y,t)\tilde{\psi}(x,y,t)\rangle$, and $n(x,y) = n_c(x,y) + \tilde{n}(x,y)$ are the local condensate, non-condensate, and total density, respectively. Applying Bogoliubov transformation, the fluctuations operators in terms of the quasiparticle modes are

$$\begin{aligned}
\tilde{\psi}(x,y,t) &= \sum_j \left[u_j(x,y)\hat{\alpha}_j(x,y)e^{-iE_jt/\hbar} - v_j^*(x,y)\hat{\alpha}_j^\dagger(x,y)e^{iE_jt/\hbar}\right], \\
\tilde{\psi}^\dagger(x,y,t) &= \sum_j \left[u_j^*(x,y)\hat{\alpha}_j^\dagger(x,y)e^{iE_jt/\hbar} - v_j(x,y)\hat{\alpha}_j(x,y)e^{-iE_jt/\hbar}\right].
\end{aligned}$$

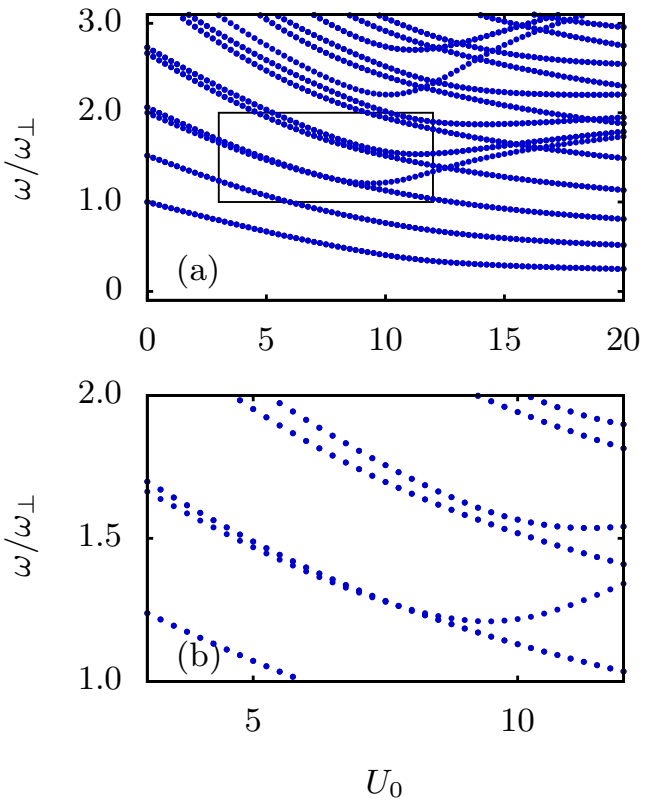

Figure 5.3: The evolution of the mode energies as a function of U_0 for $\alpha = 1$ at $T = 0$. (a) Shows the evolution of the low-lying mode energies in the domain $0 \leqslant U_0 \leqslant 20\hbar\omega_x$ for $N_{\rm Na} = 2 \times 10^3$. (b) The enlarged view of the region enclosed within the black rectangular box in (a) to resolve the avoided crossing and quasidegeneracy of modes.

Here, $\hat{\alpha}_j$ ($\hat{\alpha}_j^\dagger$) are the quasiparticle annihilation (creation) operators and satisfy the usual Bose commutation relations, and the subscript j represents the energy eigenvalue index. The Bogoliubov-de Gennes (BdG) equations, discussed in previous chapters, are

$$(\hat{h} + 2Un)u_j - U\phi^2 v_j = E_j u_j, \tag{5.6a}$$

$$-(\hat{h} + 2Un)v_j + U\phi^{*2} u_j = E_j v_j. \tag{5.6b}$$

The number density $\tilde{n}$ of the thermal or non-condensate particles is given by

$$\tilde{n} = \sum_j \{[|u_j|^2 + |v_j|^2]N_0(E_j) + |v_j|^2\}, \tag{5.7}$$

where $\langle \hat{\alpha}_j^\dagger \hat{\alpha}_j \rangle = (e^{\beta E_j} - 1)^{-1} \equiv N_0(E_j)$ with $\beta = 1/k_{\rm B}T$, is the Bose factor of the quasiparticle state with energy E_j at temperature T. However, it should be emphasized

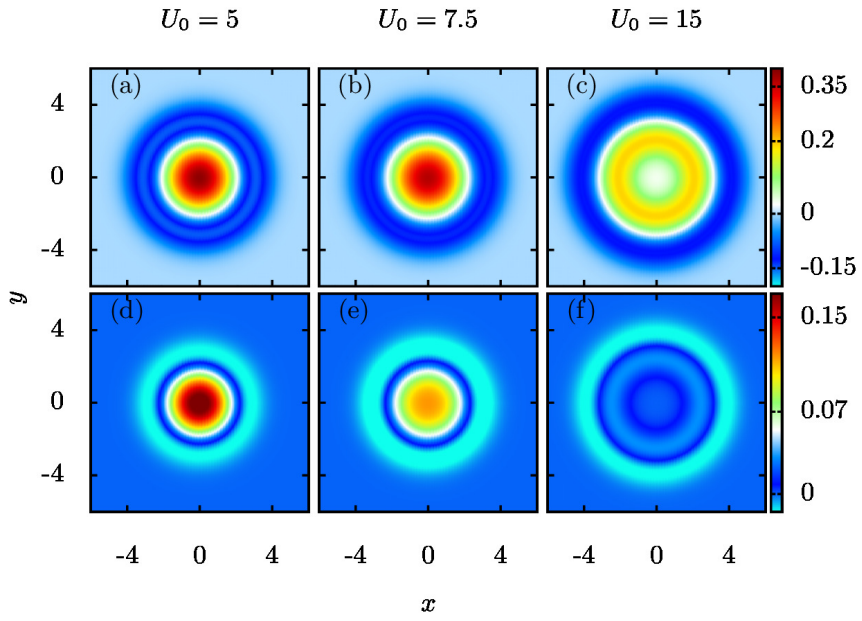

Figure 5.4: Evolution of quasiparticle amplitude corresponding to the $l = 0$ mode as U_0 is increased from 0 to $15\hbar\omega_x$ for $\alpha = 1$. (a) - (c) Show the $u_{\rm Na}$ corresponding to $U_0 = 5, 7.5, 15\hbar\omega_x$, respectively. (d) - (f) Show the $v_{\rm Na}$ corresponding to $U_0 = 5, 7.5, 15\hbar\omega_x$, respectively. In the plots u and v are in units of $a_{\rm osc}^{-1}$. Here x and y are measured in units of $a_{\rm osc}$.

that, when $T \to 0$, $N_0(E_j)$'s in Eq. (5.7) vanish. The non-condensate density is then reduced to

$$\tilde{n} = \sum_j |v_j|^2. \tag{5.8}$$

Thus, at zero temperature we need to solve the equations self-consistently as the quantum depletion term $|v_j|^2$ in the above equation is non-zero.

5.2 Mode evolution at $T = 0$

To examine the properties of a quasi-2D condensate with a Gaussian potential, as a test case, we consider a ^{23}Na BEC with $a = 53.3a_0$ [2, 57]. The evolution of the quasiparticle modes is computed for $N_{\rm Na} = 2 \times 10^3$ with $\lambda = 39.5$, and $\omega_x = \omega_y = \omega_\perp = 20.0$ Hz. We, then, study mode evolution in two different ways: varying U_0, but keeping $\alpha = 1$; and varying α, but keeping U_0 constant. For this set of parameters, $\hbar\omega_z \gg \mu$ such that the system can be assumed to be in the harmonic oscillator ground state along the axial direction z. All the degrees of the freedom along z are frozen.

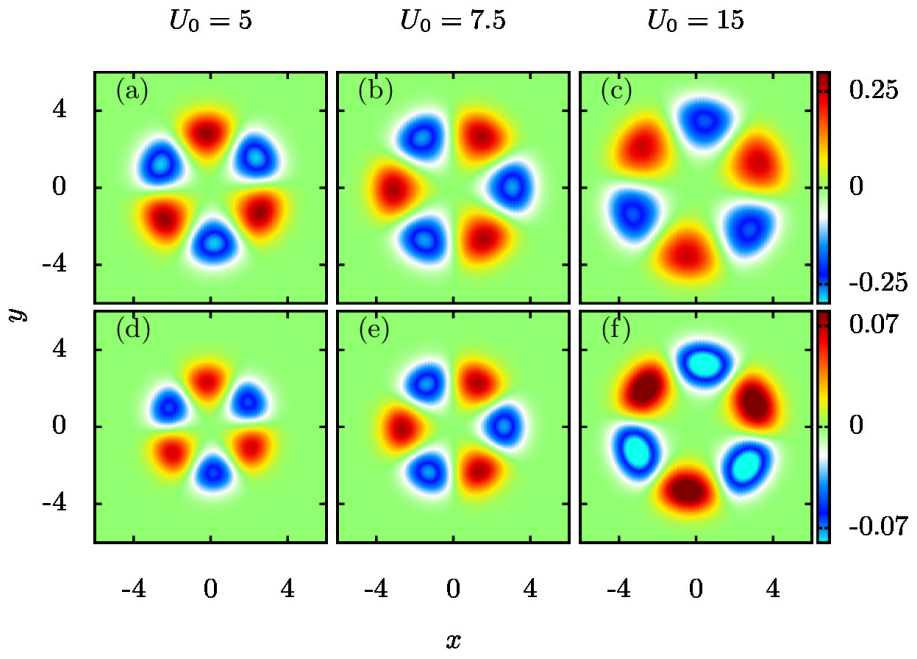

Figure 5.5: Evolution of quasiparticle amplitude corresponding to the hexapole mode which goes soft as U_0 is increased from 0 to $15\hbar\omega_x$ for $\alpha = 1$. (a) - (c) Show the $u_{\rm Na}$ corresponding to $U_0 = 5, 7.5, 15\hbar\omega_x$, respectively. (d) - (f) Show the $v_{\rm Na}$ corresponding to $U_0 = 5, 7.5, 15\hbar\omega_x$, respectively. In the plots u and v are in units of $a_{\rm osc}^{-1}$. Here x and y are measured in units of $a_{\rm osc}$.

5.2.1 Variation in U_0

To examine the mode spectrum with variation in U_0, we consider the value in the range $0 \leqslant U_0 \leqslant 20\hbar\omega_\perp$. At the starting point when $U_0 = 0$, the density profile has rotational symmetry with $n_c(0,0)$ as the maximum and decreases to zero with $r > 0$. The corresponding excitation spectrum is identified by the presence of a Goldstone mode, and doubly degenerate Kohn modes with $\omega/\omega_\perp = 1$. The quasiparticle amplitudes corresponding to one of the degenerate Kohn modes is shown in Fig. 5.2(a).

For $U_0 \neq 0$, the condensate density at the central region of the trap gets depleted. So, the general trend is, as to be expected, an increase in U_0 is associated with a decrease in $n_c(0,0)$, and the radial extent of the condensate increases. When $15\hbar\omega_\perp \lessapprox U_0$, the effective potential assumes the form of a Mexican hat, and the condensate cloud lies along the toroid with $n_c(0,0) \to 0$. For instance, when $U_0 = 0, 5, 10, 15, 20\hbar\omega_x$, $n_c(0,0) \approx 200, 92, 9, 0.04, 0 a_{\rm osc}^{-2}$, respectively. In addition, as shown in Fig. 5.1, the

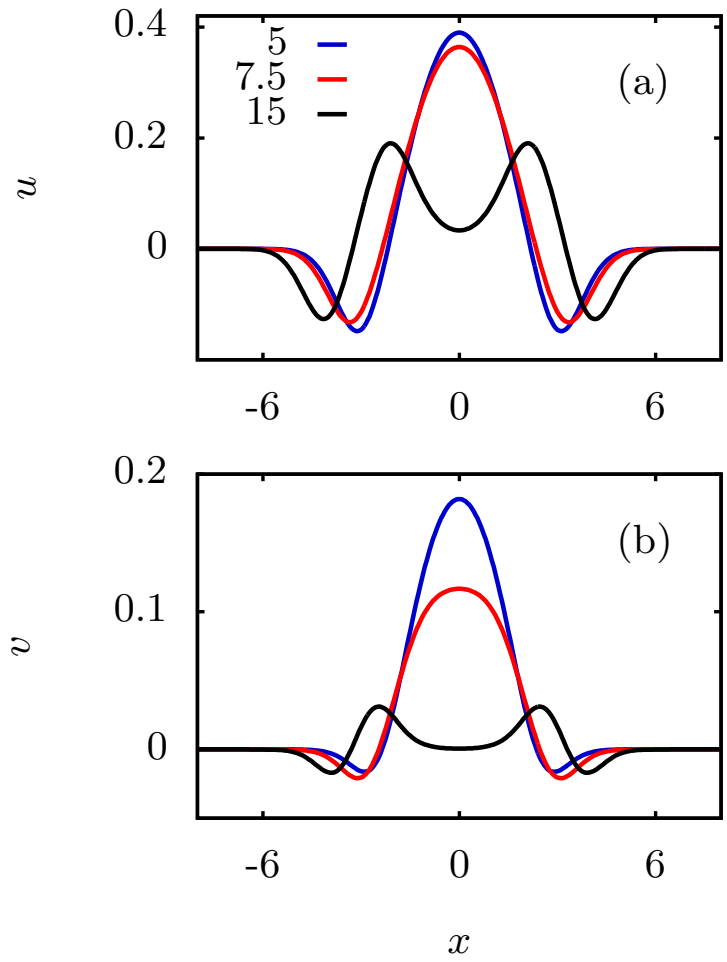

Figure 5.6: The plots show the variation in the profile of (a) $u_{\rm Na}$, and (b) $v_{\rm Na}$ along x-axis at $y = 0$ corresponding to the $l = 0$ mode at $T = 0$ and $\alpha = 1$. These represent one of the transformations in the mode function as harmonic to toroidal trap geometry occurs. The plots correspond to $U_0 = 5, 7.5, 15\hbar\omega_x$, and in the plots u and v are in units of $a_{\rm osc}^{-1}$. Here x is measured in units of $a_{\rm osc}$.

maximum value of the condensate density decreases with increasing U_0. The change in the topology of the density profiles brings about a change in the nature of the excitation spectrum and the structure of the Bogoliubov quasiparticle amplitudes. With the transformation from a harmonic to a toroidal BEC, the wavelength of excitations becomes longer as they now lie along the circumference of the toroid. This decreases the energy of the quasiparticle excitations. For the present study, the evolution of mode energies as a function of U_0 is shown in Fig. 5.3. In the lower part of the plot, the Kohn mode getting soft with increase in U_0 is discernible. The metamorphosis of the Kohn mode from harmonic to toroidal configuration of the BEC is shown in Figs. 5.2. At

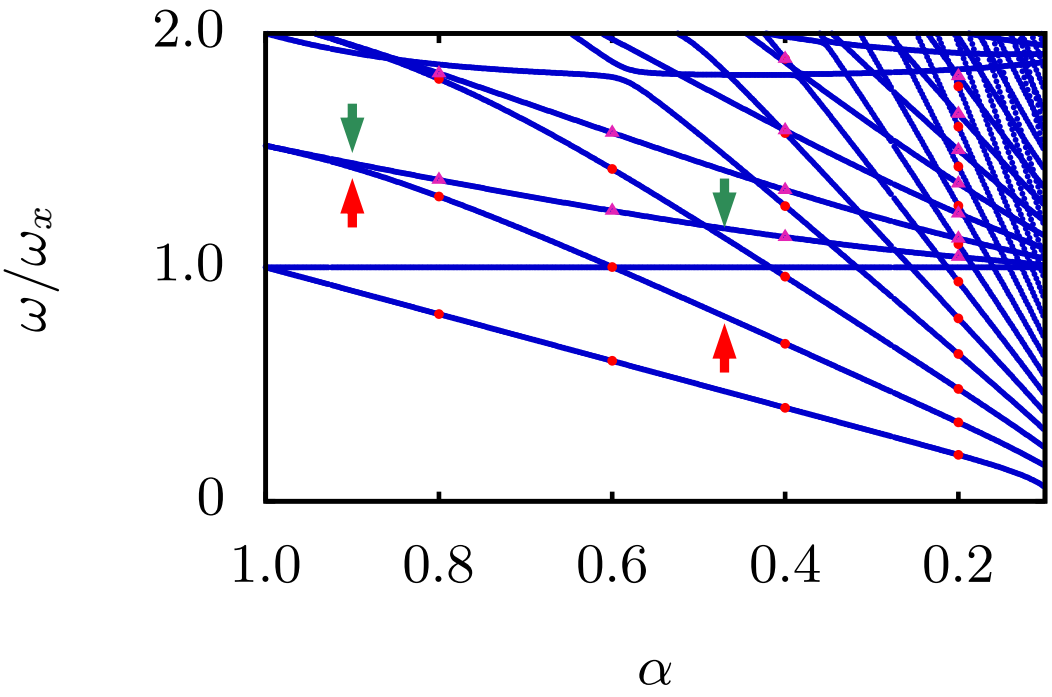

Figure 5.7: The evolution of the quasiparticle mode energies as a function of α for $U_0 = 0$ at $T = 0$. Two distinct family of curves, marked by solid red dots (●) and purple triangles (▲), are discernible as α is decreased from 1 to 0.1. In each of the families, each member differs from the other by the principal quantum number n. As an example, the degeneracy of the 3^{rd} and the 4^{th} eigenvalues is lifted to give rise to two branches traced by the red and the green arrows.

$U_0 = 20\hbar\omega_x$, the lobes of the degenerate Kohn mode get distorted and become horse-shoe shaped. In particular, the ratio of the wavelength of the Kohn mode of $U_0 = 20$ to $U_0 = 0$ is ≈ 4.0 and agrees well with the corresponding ratio of their energies as provided in Fig. 5.3. It deserves to be mentioned here that for $15 < U_0 < 20\hbar\omega_x$, the energy of the Kohn mode gets saturated. This is because the variation in the circumference of the condensate is small, and the change in the wavelength of excitations is negligible.

The other striking feature that deserves discussion is the softening and hardening of $l = 0$ mode and the subsequent bifurcations. At $U_0 = 0$, the mode with $\omega/\omega_\perp = 2.0$ is nondegenerate and corresponds to the $l = 0$ mode. The mode is rotationally symmetric. Close to this mode are the doubly degenerate modes with $\omega/\omega_\perp = 2.06$ which are hexapole in structure. With the increase in U_0, say at $U_0 = 5\hbar\omega_x$, the energy of the $l = 0$ mode is lowered to $\omega/\omega_\perp = 1.47$. The same trend is observed with

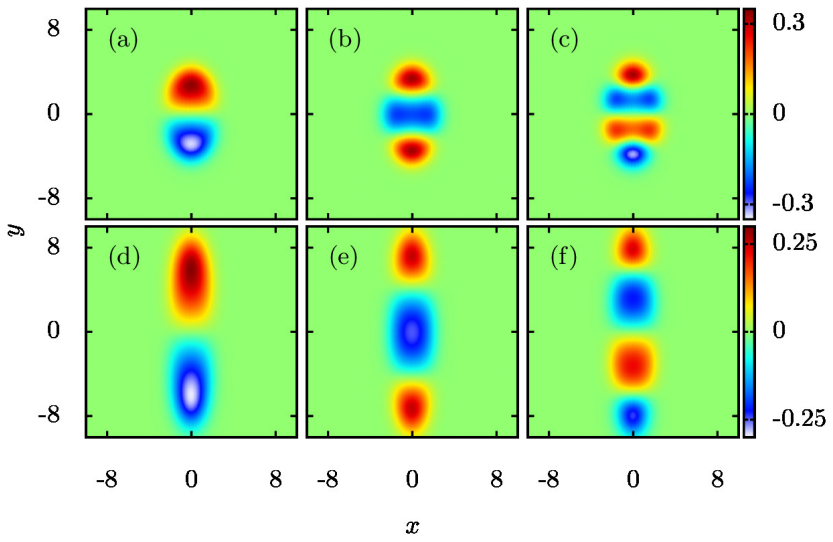

Figure 5.8: Evolution of Bogoliubov quasiparticle amplitudes for the family of curves connected by solid red dots (●) as shown in Fig. 5.7. (a) - (c) Show $u_{\rm Na}$ corresponding to the first three eigenvalues for $\alpha = 0.6$ with principal quantum number $n = 1, 2, 3$, respectively. (d) - (f) Show $u_{\rm Na}$ corresponding to the first three eigenvalues for $\alpha = 0.2$ with principal quantum number $n = 1, 2, 3$, respectively. In the plots us are in units of $a_{\rm osc}^{-1}$. Here x and y are measured in units of $a_{\rm osc}$.

the hexapole modes, and the mode energy decreases to $\omega/\omega_\perp = 1.49$. The closest approach of these two modes occurs at $U_0 \approx 7.5\hbar\omega_x$. At this point the hexapole modes are lower in energy than the $l = 0$ mode and avoided level crossing occurs. At $U_0 \approx 10\hbar\omega_x$, we observe a bifurcation and the $l = 0$ mode hardens due to the increase in the number of nodes at higher values of U_0, the energy of the hexapole modes continues to be lower than the $l = 0$ mode. The evolution of the quasiparticle amplitudes corresponding to the $l = 0$ and hexapole mode for $0 < U_0 \leq 15$ are shown in Figs. 5.4, and 5.5. The changes in the node structure is visible from the variation of $u_{\rm Na}$ and $v_{\rm Na}$ along x at $y = 0$, which are shown in Figs. 5.6.

As evident from the Fig. 5.6, the radial extent of the mode function corresponding to the $l = 0$ mode increases for $0 < U_0 < 10$, which lowers the excitation energy. However, when $U_0 \geq 10$ the mode develops a dip at the center and the condensate atoms are repelled from the central region. This hardens the $l = 0$ mode. The other noticeable feature of this excitation spectrum is the evolution of the doubly degenerate modes at $\omega/\omega_\perp \approx 2.67, 2.73$ when $U_0 = 0$. As U_0 is increased, these two modes

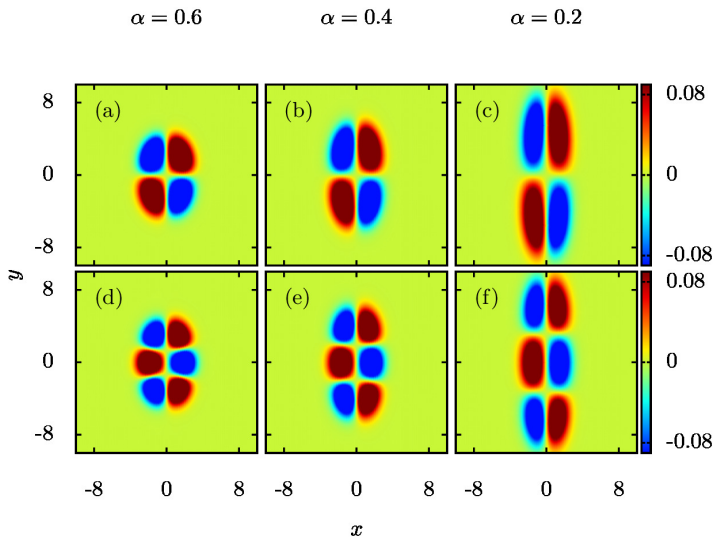

Figure 5.9: Evolution of Bogoliubov quasiparticle amplitudes for the family of curves connected by solid purple triangles (▲) as shown in Fig. 5.7. (a) - (c) Show $u_{\rm Na}$ corresponding to the first eigenvalue marked by (▲) for $\alpha = 0.6, 0.4, 0.2$ with principal quantum number $n = 1$, respectively. (d) - (f) Show $u_{\rm Na}$ corresponding to the second eigenvalue marked by (▲) for $\alpha = 0.6, 0.4, 0.2$ with principal quantum number $n = 2$, respectively. In the plots us are in units of $a_{\rm osc}^{-1}$. Here x and y are measured in units of $a_{\rm osc}$.

initially soften, then at a critical value of $U_0 \approx 10.5\hbar\omega_x$ start hardening, and crosses other modes of opposite parity. So, no avoided crossing occur, and unlike the previous case, at every U_0 the higher excited mode continues to be higher in energy than the other. For illustration, the mode with $\omega/\omega_\perp \approx 2.67, 2.73$ at U_0 gets transformed to a mode with lower in energy with $\omega/\omega_\perp \approx 1.13, 1.79$ at $U_0 = 20\hbar\omega_x$.

One may recall that, as mentioned earlier, LG beams are used in experiments [237, 238] to produce toroidal optical dipole traps. In cylindrical coordinates the intensity profile of a LG beam at its focus ($z = 0$) is given by [235]

$$I_{p,l}(r) = \frac{2p!}{(p+|l|)!}\frac{P_0}{\pi w_{p,l}^2}\left(\frac{2r^2}{w_{p,l}^2}\right)^{|l|} e^{-2r^2/w_{p,l}^2}\left[L_p^{|l|}\left(\frac{2r^2}{w_{p,l}^2}\right)\right]^2, \tag{5.9}$$

where, P_0 is the power of laser beam, and l is the azimuthal mode index. The number of radial intensity maxima is given by radial mode index p. The mode spot size is given by $w_{p,l}$ and $L_p^{|l|}$ is the generalized Laguerre polynomial. To create a single-ringed toroidal trap, a red-detuned laser field ($\Delta < 0$) is used with $p = 0$ and $l > 0$. The optical dipole

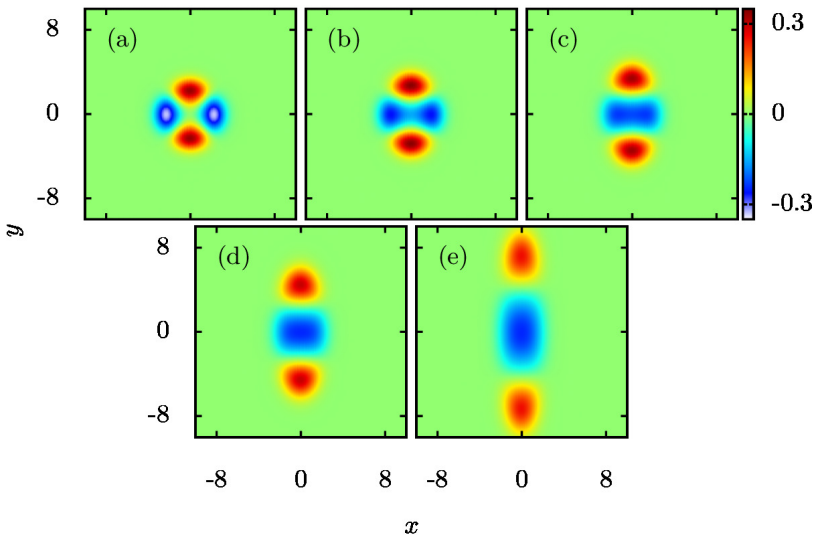

Figure 5.10: Evolution of the quasiparticle amplitudes corresponding to the eigenvalues traced by the red arrows in Fig. 5.7. (a) Shows the quadrupole mode corresponding to the 3^{rd} eigenvalue for $\alpha = 1.0$. (b) - (d) Show the deformation of the quadrupole mode with the wavelength of the quasiparticle excitation increasing along the y direction corresponding to $\alpha = 0.8, 0.6, 0.4$ respectively. (e) Shows the three lobed mode corresponding to $\alpha = 0.2$. In the plots us are in units of a_{osc}^{-1}. Here x and y are measured in units of a_{osc}.

potential in order to produce a toroid of radius r_T is given by

$$U_l(r) = U_l \left(\frac{r}{r_T}\right)^{2l} e^{-l(r^2/r_T^2-1)}, \tag{5.10}$$

where,

$$U_1 = \frac{\hbar\Gamma^2}{8\Delta}\left(\frac{e^{-1}P_0}{\pi r_T^2 I_{\text{Sat}}}\right), U_l \approx U_1\sqrt{l}. \tag{5.11}$$

Here U_1 is the optical dipole potential well depth for $l = 1$ with the radius fixed at r_T. The natural linewidth of the optical transition is denoted by Γ, Δ is the laser detuning parameter from the optical transition frequency, and I_{Sat} is the resonant saturation intensity. The toroidal trap becomes more deeper and tighter with increasing l, which is similar to the configuration we have used (combination of harmonic and Gaussian trapping potentials) when $U_0 = 0$. However, it is to be noted that, at $r = 0$ and $r \to \pm\infty$, $U_l = 0$ for any $l > 0$. So, the LG beams do not have a counterpart of $U_0 = 0$ or low values of U_0, and cannot be adopted to examine the evolution of the fluctuations as a pancake shaped condensate is transformed to a toroidal one.

On examining the number of non-condensate atoms due to quantum fluctuations

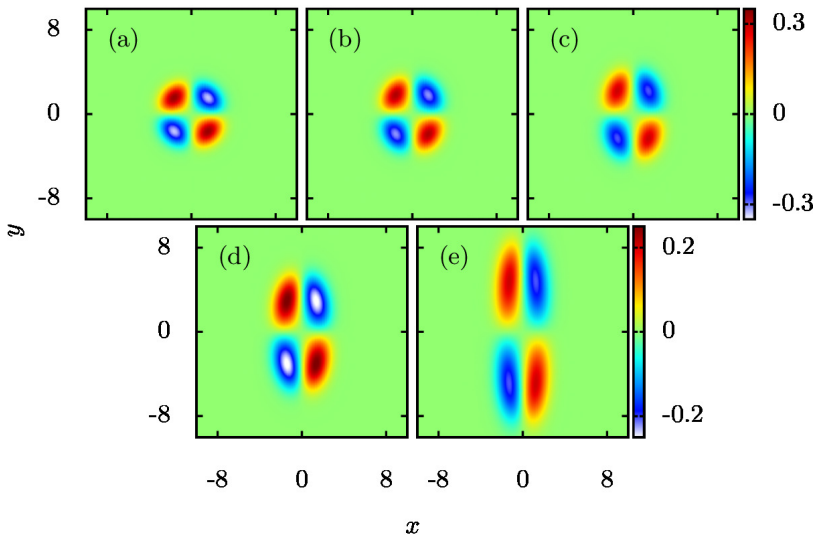

Figure 5.11: Evolution of the quasiparticle amplitudes corresponding to the eigenvalues traced by the green arrows in Fig. 5.7. (a) Shows the quadrupole mode corresponding to the 4^{th} eigenvalue for $\alpha = 1.0$. (b) - (e) Show the evolution of the quadrupole mode for $\alpha = 0.8, 0.6, 0.4, 0.2$ respectively. In the plots us are in units of a_{osc}^{-1}. Here x and y are measured in units of a_{osc}.

at $T = 0$, we observe an increase in the number of non-condensate atoms with the increase U_0. A closer inspection reveals that the dominant contribution to the number of non-condensate atoms $\tilde{N} = \int \tilde{n}(x, y)\, dxdy$ arises from the $|v|^2$ corresponding to the doubly degenerate Kohn modes. This contribution is the least for $U_0 = 0$, and rises as U_0 is increased from 0 to $20\hbar\omega_x$. It must be mentioned here that the genesis of higher quantum fluctuations in quasi-1D BEC with a dark soliton is very different: anomalous mode and interactions play a vital role.

5.2.2 Variation in α

We now study the mode evolution of the system with variation in the anisotropy parameter α, but keeping U_0 fixed. As α is decreased or ω_y is decreased, the rotational symmetry of the condensate is broken and transformed to an ellipse with the semi-major axis along the y direction. With this transformation, the excitations along the y direction are lower in energy than the excitations along the x direction. For $U_0 = 0$, the Kohn mode is doubly degenerate when $\alpha = 1$. The degeneracy is lifted when $\alpha < 1$, and the excitations along the x and y directions differ in energy. The Kohn

mode with $\omega/\omega_x = 1$ remains steady, whereas the other Kohn mode decreases on lowering α. The evolution of the mode energies with variation in α is shown in Fig. 5.7. It is evident from the figure that as α is varied from 1 to 0.1, the condensate density profiles transform from a quasi-2D to an effectively quasi-1D regime. With this the quasiparticle modes form a families of curves with similar slopes, and two such families are discernible in the figure, which are marked with solid red dots and purple triangles. The curve represented by red dots and purple triangles differ in the nature of

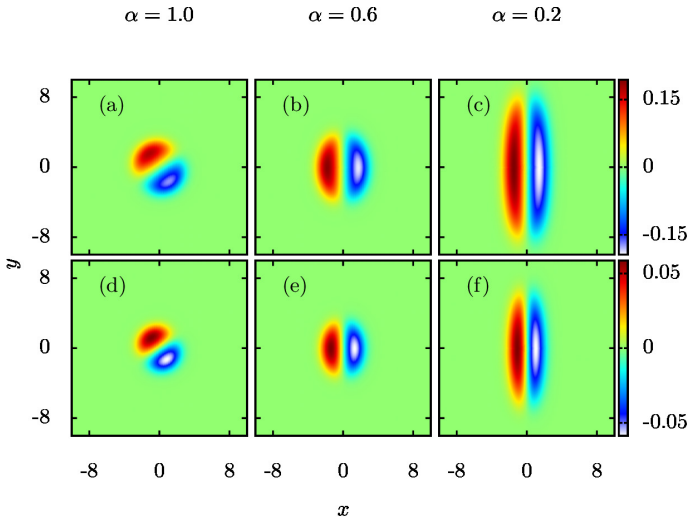

Figure 5.12: Evolution of the Bogoliubov quasiparticle amplitude corresponding to the Kohn mode which remains steady as α is decreased from 1 to 0.1 when $U_0 = 0$. Show the (a) - (c) $u_{\rm Na}$, and (d) - (f) $v_{\rm Na}$ corresponding to $\alpha = 1.0, 0.6, 0.2$, respectively. The mode excitation is effectively along the x-direction and the wavelength of excitation along this direction remains unchanged with decrease in α. In the plots us and vs are in units of $a_{\rm osc}^{-1}$. Here x and y are measured in units of $a_{\rm osc}$.

excitation which is elucidated through the quasiparticle amplitudes. However, in each of the families, the curves differ from the other by the principal quantum number n. In particular, with varying α, each member of the family has the same n, but l differs from each other. This trend in the nature of the curves is shown in Figs. 5.8, and 5.9. In Fig. 5.8 we show the quasiparticle amplitudes corresponding to the modes shown by red dots in Fig. 5.7. Each member constituting the family is distinct from the other by the number of nodes. The first member of the family corresponds to a dipole or Kohn mode for any value of α. For the quasiparticle amplitudes corresponding to the modes connected by purple triangles, a similar trend is observed with the first member, which

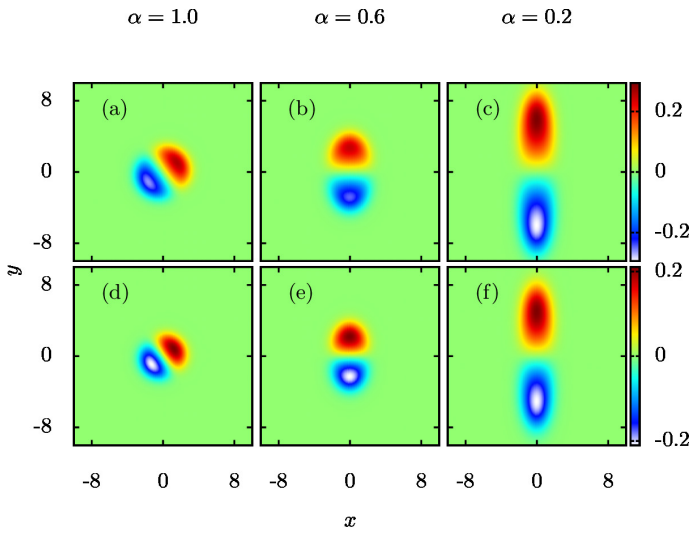

Figure 5.13: Evolution of the Bogoliubov quasiparticle amplitude corresponding to the Kohn mode which goes soft as α is varied from 1 to 0.1 when $U_0 = 0$. Show the (a) - (c) $u_{\rm Na}$, and (d) - (f) $v_{\rm Na}$ corresponding to $\alpha = 1.0, 0.6, 0.2$, respectively. The mode excitation is effectively along the y-direction and the wavelength of excitation along this direction increases with decrease in α. In the plots us and vs are in units of $a_{\rm osc}^{-1}$. Here x and y are measured in units of $a_{\rm osc}$.

is a quadrupole mode as shown in Fig. 5.9.

The other interesting feature is the bifurcation due to the lifting of degeneracy as α is varied from 1.0 to 0.1. At the outset when $\alpha = 1.0$, the $3^{\rm rd}$ and the $4^{\rm th}$ eigenvalues are ≈ 1.52. As the rotational symmetry of the condensate is broken for $\alpha < 1$, these modes bifurcate to give rise to two branches. The first branch, traced by the red arrows in Fig. 5.7, softens with decrease in α. For $\alpha = 1.0$, the quasiparticle amplitude corresponding to $\omega/\omega_x = 1.52$ is a quadrupole mode as shown in Fig. 5.10(a). As α is decreased, the condensate gets elongated along the y direction with contraction along the x-axis. This makes the lobes along the x-axis coalesce, and the quadrupole mode is transformed to a three lobed structure at $\alpha = 0.2$ as shown in Fig. 5.10(e). The intermediate stages of deformation are also shown in Fig. 5.10.

The other degenerate mode at $\alpha = 1.0$ which can be thought of an excitation along the x-axis forms the second branch traced by the green arrows in Fig. 5.7. The wavelength of the quadrupole mode (at $\alpha = 1.0$) decreases with the variation in α, which is the reflected by a decrease in the energy as shown in Fig. 5.7. As evident from

the figure the decrease in the energy of this branch is less than the other branch. With the decrease in α this mode retains it structure as shown in Fig. 5.11.

Furthermore, the quasiparticle amplitude corresponding to the steady and softened Kohn mode is also shown in Fig. 5.12 and 5.13 respectively.

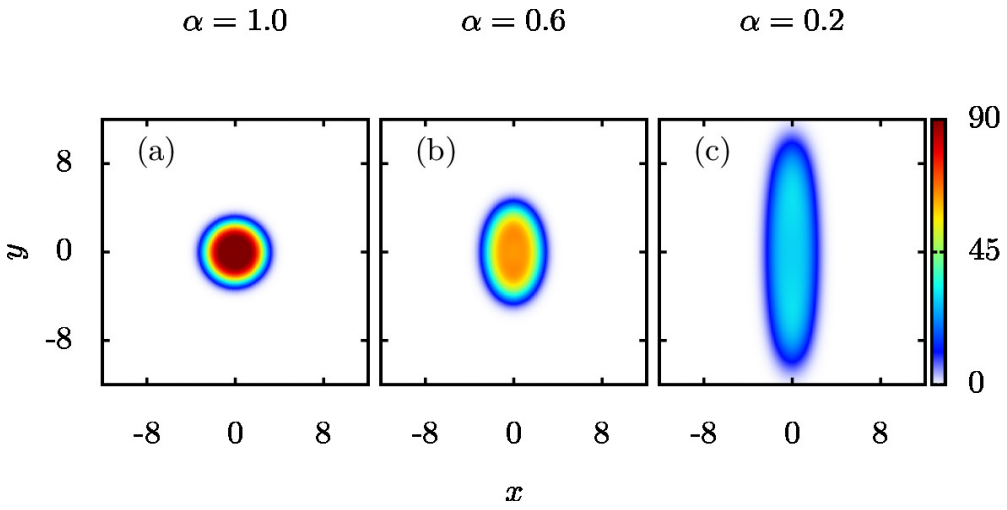

Figure 5.14: Transformation of a rotationally symmetric to an ellipsoidal BEC for $U_0 = 5$. (a) - (c) Show the ^{23}Na condensate density profiles corresponding to $\alpha = 1.0, 0.6, 0.2$ respectively with $N_{\rm Na} = 2 \times 10^3$, $\alpha = 1$, $\lambda = 39.5$, and $\omega_\perp = 20.0$ Hz. Density is measured in units of $a_{\rm osc}^{-2}$.

With $U_0 \neq 0$, the radial extent of n_c increases when $\alpha = 1$, and for $\alpha < 1$ the condensate becomes elongated along the y direction as shown in Fig. 5.14. The doubly degenerate Kohn modes becomes nondegenerate and its energy decreases further with lowering of α as shown in Fig. 5.15. Of these two modes, one corresponds to the excitation along the x direction and the other along the y direction. The decrease in the energy of the Kohn mode is enhanced for $U_0 \neq 0$. For example, when $U_0 = 5$ the mode identified along y direction softens and gets transformed into a Goldstone mode as shown in Fig. 5.15. At $\alpha = 0.2$, spontaneous symmetry breaking occurs and a new Goldstone mode emerges in the excitation spectrum. To examine the further, consider the condensate density in TF-approximation, where the equipotential curves of the trapping potential coincides with isodensity curves. The same is applicable for $\alpha \neq 1$, so, the condensate density profiles matches the equipotential curves of the trapping potential. However, at lower α or higher U_0, the condensate density profile along semi-minor axis has large gradients, and TF approximation is not valid. In other

words, the equipotential curves are no longer coincident with the isodensity curves. This mismatch is the root of symmetry breaking and the appearance of the Goldstone mode. For higher values of U_0, symmetry breaking and the subsequent appearance of an additional Goldstone mode occurs at lower values of α. The mode along x does not remain steady and gets reduced unlike when $U_0 = 0$, and like in $U_0 = 0$, we observe bifurcations and the appearance of a family of curves identified by the principal quantum number n.

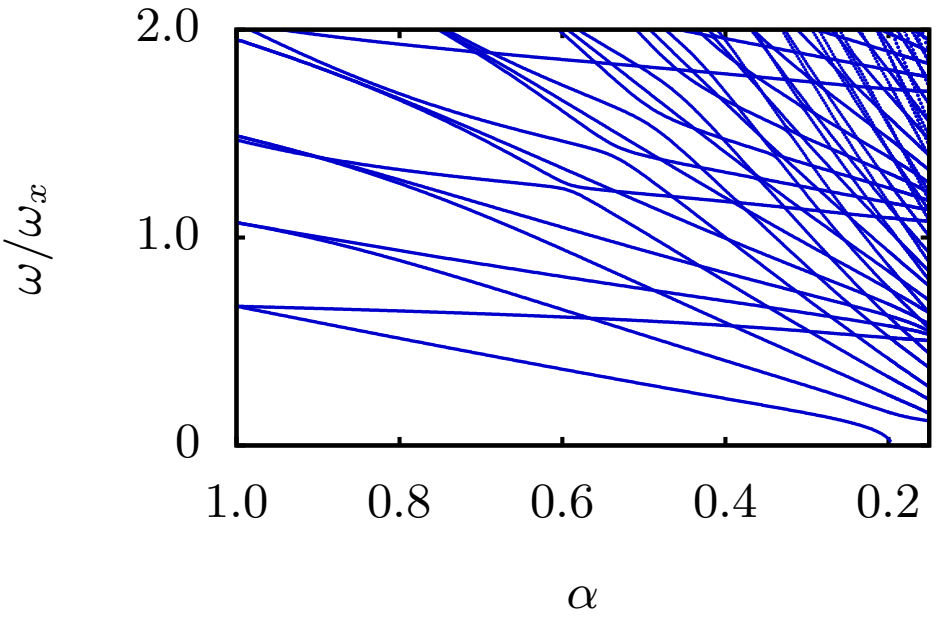

Figure 5.15: The evolution of the quasiparticle modes as a function of α for $U_0 = 5$ at $T = 0$. One prominent feature, which distinguishes the plot from $U_0 = 0$, is the softening of the Kohn mode.

5.3 $T \neq 0$ results

Consider $U_0 = 0$ and $\alpha = 1$ as the starting choice of parameters to probe the finite temperature effects. When $T \neq 0$ the Bose factor $N_0 \neq 0$, so in addition to the quantum fluctuations, the non-condensate densities $\tilde{n}$ have contributions from the thermal fluctuations as well. The condensate atoms n_c then interact with $\tilde{n}$, and this in turn modifies n_c. Due to the repulsive interaction energy between the condensate and non-condensate atoms, the profile of $\tilde{n}$ develops a dip at the center of the trap, where n_c is maximum. In general, due to higher kinetic energy, the spatial extent of the thermal

cloud is larger than the condensate cloud, this is evident from the density plots shown in Fig. 5.16.

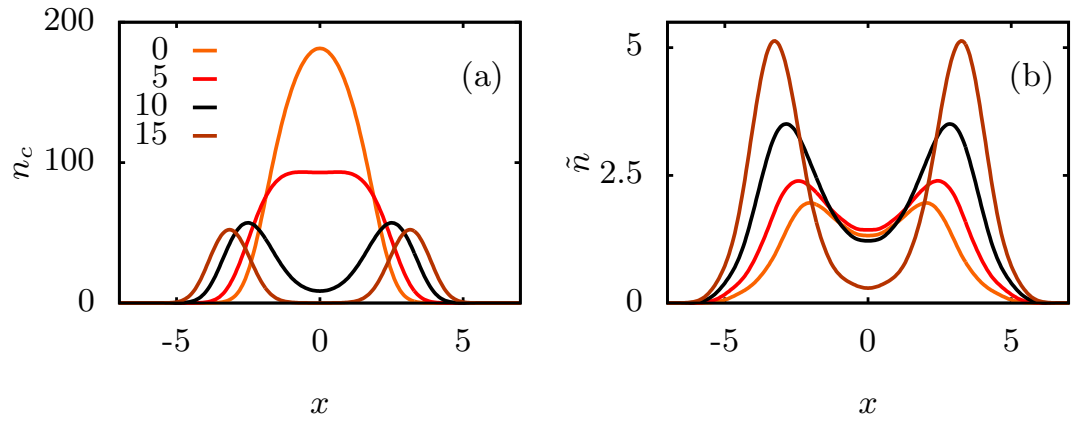

Figure 5.16: The plots along x-axis at $y = 0$ showing the variation in (a) condensate and (b) non-condensate density profiles at $T = 10$ nK for different values of U_0. In the plots n_c and $\tilde{n}$ are in units of $a_{\rm osc}^{-2}$. Here x is measured in units of $a_{\rm osc}$.

With higher U_0, n_c gets modified developing a dip at the center, and ultimately gets transformed to a toroidal condensate which is shown in Fig. 5.16. Subsequently, the non-condensate density distribution also gets modified. At $U_0 = 15$, both n_c and $\tilde{n}$ are low at the central region, and with $\tilde{n} > n_c$. The low n_c reduces the repulsive interaction energy between the thermal and condensate atoms. This renders energetically favourable for the non-condensate atoms to reside in the central region of the trap even when $n_c \to 0$ as shown in Fig. 5.17 (d), (h). With higher U_0, the maxima of n_c decreases, whereas the maxima of the non-condensate density increases; the position of the maxima of the condensate as well as the non-condensate densities shift radially outward. Initially, these two maxima do not coincide and the separation is $\approx 2.0 a_{\rm osc}$. When $U_0 = 15$, the separation reduces to $\approx 0.1 a_{\rm osc}$ and the Kohn modes resemble the structure of the condensate density profiles. The trend in the shifting of the maxima is shown through a radial cut along $y = 0$ in Fig. 5.16. The density plots are also shown in Fig. 5.17. The number of thermal atoms increases with increasing the strength of U_0.

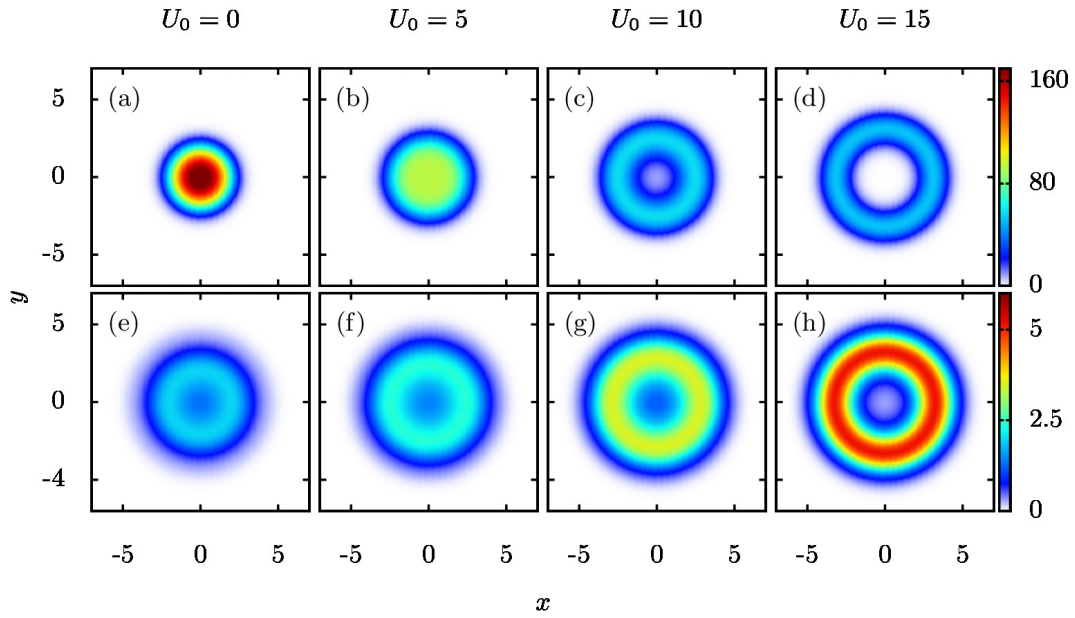

Figure 5.17: Condensate and non-condensate density plots at $T = 10$ nK for different values of U_0. (a) - (d) plots of condensate, and (e) - (f) non-condensate density distribution for $U_0 = 0, 5, 10, 15$, respectively. Here x and y are measured in units of a_{osc}.

5.4 Summary of the Chapter

At $T = 0$, with the changeover from a rotationally symmetric harmonic to a toroidal trapping potential, the Kohn mode is transformed from a radial to a circular mode. This decreases the energy of the Kohn mode. The degeneracy of the modes is lifted when $\alpha < 1$. The nondegenerate quasiparticle modes form distinct group of curves as α is varied from 1 to 0.1. Each branch forming the group is distinguished from the other by the principal quantum number. With finite strength of U_0 and varying α, an additional Goldstone mode appears in the system at a critical value of α. On increase of U_0, the Goldstone mode appears at a higher value of α. That is, higher U_0 enhances the phenomenon of SSB. At $T \neq 0$, for $\alpha = 1$ with increase in U_0, the maxima of equilibrium condensate and non-condensate density profiles tends to coincide. This is not the case with $U_0 = 0$, where the non-condensate density is depleted in the central region, but in the same region the condensate density has a maximum.

Chapter 6

Scope for Future Work

We have used the self-consistent HFB-Popov approximation, which is best suited to examine the quasiparticle spectrum and mode functions, to study the equilibrium solutions of TBEC. Using this formalism, we have examined in detail the equilibrium density profiles of a trapped TBEC at $T = 0$ and $T \neq 0$. We have also examined the evolution of quasiparticle modes of the stationary TBEC as a function of the interaction strengths and temperature. The role of thermal cloud in the suppression of phase-separation in TBEC has also been demonstrated. In the HFB-Popov approximation the dynamics of the non-condensate part is not included which may be the dominant reason for damping of Kohn mode at finite temperatures. However, in our future works we plan to study the dynamics of Bose gases with the inclusion of finite temperature effects using Zaremba-Nikuni-Griffin (ZNG) formalism [98]. In this method, a dissipative GP equation describes the dynamics of the condensate cloud. The non-condensate evolution is represented by a quantum Boltzmann equation which includes collisions between condensate and non-condensate parts resulting in transfer of atoms.

Using the ZNG formalism, the growth dynamics of a TBEC can be a topic of future study [241, 242]. One can also look at the dynamics of vortex dipole, multiple vortices of like or different charge in a BEC at finite temperatures. Melting of vortex lattices at $T \neq 0$ in a BEC or a TBEC is again a topic of further investigation. Motivated by the recent study of finite temperature dynamical structure factor of a 1D Bose gas [243], the ZNG formalism can be employed to perform a similar investigation for TBEC. As

pointed in Ref. [243], the dynamical structure factor has a typical width which bears a close connection to the Kardar-Parisi-Zhang (KPZ) universality class of dynamical critical phenomena. "Is this applicable to TBEC ?", is a question that needs to be answered in the future investigations.

Appendix A

Numerical Details

For the $T = 0$ studies we solve the pair of coupled Eqns. (2.67) by neglecting the non-condensate density ($\tilde{n}_k = 0$) using finite-difference methods and in particular, we use the split-step Crank-Nicholson method [244] adapted for binary condensates. The method when implemented with imaginary time propagation is appropriate to obtain the stationary ground state wave function of the TBEC. Using this solution, and based on Eq. (2.69), we cast the Eq. (2.68) as a matrix eigenvalue equation in the basis of the trapping potential. The matrix is then diagonalized using the LAPACK routine `zgeev` [245] to find the quasiparticle energies and amplitudes, E_j, and u_k's and v_k's, respectively. This step is the beginning of the first iteration for $T \neq 0$ calculations. In which case, the u_k's and v_k's along with E_j are used to get the initial estimate of $\tilde{n}_k$ through Eq. (2.70). For this we consider only the positive energy modes. Using this updated value of $\tilde{n}_k$, the ground state wave function of TBEC ϕ_k and chemical potential μ_k are again re-calculated from Eq. (2.67). This procedure is repeated till the solutions reach desired convergence. In the present work the convergence criteria is that the change in μ_k between iterations should be less than 10^{-4}. In general, the convergence is not smooth and we encounter severe oscillations very frequently. To damp the oscillations and accelerate convergence we employ successive over (under) relaxation technique for updating the condensate (non-condensate) densities [246]. The new solutions after IC iteration cycle are

$$\begin{aligned} \phi_{\rm IC}^{\rm new}(z) &= s^{\rm ov}\phi_{\rm IC}(z) + (1 - s^{\rm ov})\phi_{\rm IC-1}(z), \\ \tilde{n}_{\rm IC}^{\rm new}(z) &= s^{\rm un}\tilde{n}_{\rm IC}(z) + (1 - s^{\rm un})\tilde{n}_{\rm IC-1}(z), \end{aligned} \tag{A.1}$$

where $s^{\rm ov} > 1$ ($s^{\rm un} < 1$) is the over (under) relaxation parameter. During the calculation of the u_k and v_k, we choose an optimal number of the harmonic oscillator basis functions. The conditions based on which we decide the optimal size are: obtaining reliable Goldstone modes; and all eigenvalues must be real for stable equilibrium solutions.

Bibliography

[1] M. H. Anderson, J. R. Ensher, M. R. Matthews, C. E. Wieman, and E. A. Cornell, Science **269**, 198 (1995).

[2] K. B. Davis, M. O. Mewes, M. R. Andrews, N. J. van Druten, D. S. Durfee, D. M. Kurn, and W. Ketterle, Phys. Rev. Lett. **75**, 3969 (1995).

[3] C. C. Bradley, C. A. Sackett, J. J. Tollett, and R. G. Hulet, Phys. Rev. Lett. **75**, 1687 (1995).

[4] "The Nobel Prize in Physics 2001" Nobelprize.org (The Royal Swedish Academy of Sciences, 2001).

[5] M.-O. Mewes, M. R. Andrews, N. J. van Druten, D. M. Kurn, D. S. Durfee, and W. Ketterle, Phys. Rev. Lett. **77**, 416 (1996).

[6] D. G. Fried, T. C. Killian, L. Willmann, D. Landhuis, S. C. Moss, D. Kleppner, and T. J. Greytak, Phys. Rev. Lett. **81**, 3811 (1998).

[7] S. L. Cornish, N. R. Claussen, J. L. Roberts, E. A. Cornell, and C. E. Wieman, Phys. Rev. Lett. **85**, 1795 (2000).

[8] A. Robert, O. Sirjean, A. Browaeys, J. Poupard, S. Nowak, D. Boiron, C. I. Westbrook, and A. Aspect, Science **292**, 461 (2001).

[9] G. Modugno, G. Ferrari, G. Roati, R. J. Brecha, A. Simoni, and M. Inguscio, Science **294**, 1320 (2001).

[10] T. Weber, J. Herbig, M. Mark, H.-C. Nägerl, and R. Grimm, Science **299**, 232 (2003).

[11] Y. Takasu, K. Maki, K. Komori, T. Takano, K. Honda, M. Kumakura, T. Yabuzaki, and Y. Takahashi, Phys. Rev. Lett. **91**, 040404 (2003).

[12] A. Griesmaier, J. Werner, S. Hensler, J. Stuhler, and T. Pfau, Phys. Rev. Lett. **94**, 160401 (2005).

[13] S. Kraft, F. Vogt, O. Appel, F. Riehle, and U. Sterr, Phys. Rev. Lett. **103**, 130401 (2009).

[14] Y. N. M. de Escobar, P. G. Mickelson, M. Yan, B. J. DeSalvo, S. B. Nagel, and T. C. Killian, Phys. Rev. Lett. **103**, 200402 (2009).

[15] S. Stellmer, M. K. Tey, B. Huang, R. Grimm, and F. Schreck, Phys. Rev. Lett. **103**, 200401 (2009).

[16] S. Stellmer, M. K. Tey, R. Grimm, and F. Schreck, Phys. Rev. A **82**, 041602(R) (2010).

[17] P. G. Mickelson, Y. N. Martinez de Escobar, M. Yan, B. J. DeSalvo, and T. C. Killian, Phys. Rev. A **81**, 051601(R) (2010).

[18] M. Lu, N. Q. Burdick, S. H. Youn, and B. L. Lev, Phys. Rev. Lett. **107**, 190401 (2011).

[19] S. Sugawa, R. Yamazaki, S. Taie, and Y. Takahashi, Phys. Rev. A **84**, 011610(R) (2011).

[20] K. Aikawa, A. Frisch, M. Mark, S. Baier, A. Rietzler, R. Grimm, and F. Ferlaino, Phys. Rev. Lett. **108**, 210401 (2012).

[21] W. Ketterle, Rev. Mod. Phys. **74**, 1131 (2002).

[22] W. Muessel, H. Strobel, D. Linnemann, D. B. Hume, and M. K. Oberthaler, Phys. Rev. Lett. **113**, 103004 (2014).

[23] T. Kovachy, J. M. Hogan, A. Sugarbaker, S. M. Dickerson, C. A. Donnelly, C. Overstreet, and M. A. Kasevich, Phys. Rev. Lett. **114**, 143004 (2015).

[24] T. Byrnes, K. Wen, and Y. Yamamoto, Phys. Rev. A **85**, 040306(R) (2012).

[25] M. Ueda, *Fundamentals and New Frontiers of Bose-Einstein Condensation* (World Scientific, Singapore, 2010).

[26] N. P. Proukakis and B. Jackson, J. Phys. B **41**, 203002 (2008).

[27] C. Pethick and H. Smith, *Bose-Einstein Condensation in Dilute Gases* (Cambridge University Press, New York, 2008).

[28] S. N. Bose, Z. Phys. **26**, 178 (1924).

[29] A. Einstein, Sitzber. Kgl. Preuss. Akad. Wiss. **22**, 261 (1924).

[30] A. Einstein, Sitzber. Kgl. Preuss. Akad. Wiss. **23**, 3 (1925).

[31] O. Penrose and L. Onsager, Phys. Rev. **104**, 576 (1956).

[32] F. Dalfovo, S. Giorgini, L. P. Pitaevskii, and S. Stringari, Rev. Mod. Phys. **71**, 463 (1999).

[33] K. E. O'Hara, L. Ó Súilleabháin, and J. P. Wolfe, Phys. Rev. B **60**, 10565 (1999).

[34] A. Griffin, D. Snoke, and S. Stringari, *Bose-Einstein Condensation* (Cambridge University Press, New York, 1996).

[35] Y. Yamamoto, Nature (London) **405**, 629 (2000).

[36] M. Saba, C. Ciuti, J. Bloch, V. Thierry-Mieg, R. Andre, L. S. Dang, S. Kundermann, A. Mura, G. Bongiovanni, J. L. Staehli, and B. Deveaud, Nature (London) **414**, 731 (2001).

[37] J. Kasprzak, M. Richard, S. Kundermann, A. Baas, P. Jeambrun, J. M. J. Keeling, F. M. Marchetti, M. H. Szymanska, R. Andre, J. L. Staehli, V. Savona, P. B. Littlewood, B. Deveaud, and L. S. Dang, Nature (London) **443**, 409 (2006).

[38] H. Deng, H. Haug, and Y. Yamamoto, Rev. Mod. Phys. **82**, 1489 (2010).

[39] T. Byrnes and N. Y. Kim, Nat. Phys. **10**, 803 (2014).

[40] S. O. Demokritov, V. E. Demidov, O. Dzyapko, G. A. Melkov, A. A. Serga, B. Hillebrands, and A. N. Slavin, Nature (London) **443**, 430 (2006).

[41] J. Klaers, J. Schmitt, F. Vewinger, and M. Weitz, Nature (London) **468**, 545 (2010).

[42] J. Marelic and R. A. Nyman, Phys. Rev. A **91**, 033813 (2015).

[43] T.-L. Ho and V. B. Shenoy, Phys. Rev. Lett. **77**, 3276 (1996).

[44] M. Trippenbach, K. Góral, K. Rzazewski, B. Malomed, and Y. B. Band, J. Phys. B **33**, 4017 (2000).

[45] S. Inouye, M. R. Andrews, J. Stenger, H.-J. Miesner, D. M. Stamper-Kurn, and W. Ketterle, Nature (London) **392**, 151 (1998).

[46] C. Chin, R. Grimm, P. Julienne, and E. Tiesinga, Rev. Mod. Phys. **82**, 1225 (2010).

[47] G. Modugno, M. Modugno, F. Riboli, G. Roati, and M. Inguscio, Phys. Rev. Lett. **89**, 190404 (2002).

[48] A. Lercher, T. Takekoshi, M. Debatin, B. Schuster, R. Rameshan, F. Ferlaino, R. Grimm, and H.-C. Nägerl, Eur. Phys. J. D **65**, 3 (2011).

[49] D. J. McCarron, H. W. Cho, D. L. Jenkin, M. P. Köppinger, and S. L. Cornish, Phys. Rev. A **84**, 011603(R) (2011).

[50] B. Pasquiou, A. Bayerle, S. M. Tzanova, S. Stellmer, J. Szczepkowski, M. Parigger, R. Grimm, and F. Schreck, Phys. Rev. A **88**, 023601 (2013).

[51] D. Xiong, X. Li, F. Wang, and D. Wang, arXiv: 1305.7091 (2013).

[52] L. Wacker, N. B. Jørgensen, D. Birkmose, R. Horchani, W. Ertmer, C. Klempt, N. Winter, J. Sherson, and J. J. Arlt, arXiv: 1505.07975 (2015).

[53] S. B. Papp, J. M. Pino, and C. E. Wieman, Phys. Rev. Lett. **101**, 040402 (2008).

[54] S. Händel, T. P. Wiles, A. L. Marchant, S. A. Hopkins, C. S. Adams, and S. L. Cornish, Phys. Rev. A **83**, 053633 (2011).

[55] C. J. Myatt, E. A. Burt, R. W. Ghrist, E. A. Cornell, and C. E. Wieman, Phys. Rev. Lett. **78**, 586 (1997).

[56] D. S. Hall, M. R. Matthews, J. R. Ensher, C. E. Wieman, and E. A. Cornell, Phys. Rev. Lett. **81**, 1539 (1998).

[57] D. M. Stamper-Kurn, M. R. Andrews, A. P. Chikkatur, S. Inouye, H.-J. Miesner, J. Stenger, and W. Ketterle, Phys. Rev. Lett. **80**, 2027 (1998).

[58] J. Stenger, S. Inouye, D. M. Stamper-Kurn, H.-J. Miesner, A. P. Chikkatur, and W. Ketterle, Nature (London) **396**, 345 (1998).

[59] P. Maddaloni, M. Modugno, C. Fort, F. Minardi, and M. Inguscio, Phys. Rev. Lett. **85**, 2413 (2000).

[60] G. Delannoy, S. G. Murdoch, V. Boyer, V. Josse, P. Bouyer, and A. Aspect, Phys. Rev. A **63**, 051602(R) (2001).

[61] L. E. Sadler, J. M. Higbie, S. R. Leslie, M. Vengalattore, and D. M. Stamper-Kurn, Nature (London) **443**, 312 (2006).

[62] K. M. Mertes, J. W. Merrill, R. Carretero-González, D. J. Frantzeskakis, P. G. Kevrekidis, and D. S. Hall, Phys. Rev. Lett. **99**, 190402 (2007).

[63] R. P. Anderson, C. Ticknor, A. I. Sidorov, and B. V. Hall, Phys. Rev. A **80**, 023603 (2009).

[64] S. Tojo, Y. Taguchi, Y. Masuyama, T. Hayashi, H. Saito, and T. Hirano, Phys. Rev. A **82**, 033609 (2010).

[65] S. Gautam and D. Angom, J. Phys. B **44**, 025302 (2011).

[66] K. Sasaki, N. Suzuki, D. Akamatsu, and H. Saito, Phys. Rev. A **80**, 063611 (2009).

[67] S. Gautam and D. Angom, Phys. Rev. A **81**, 053616 (2010).

[68] T. Kadokura, T. Aioi, K. Sasaki, T. Kishimoto, and H. Saito, Phys. Rev. A **85**, 013602 (2012).

[69] S. Stringari, Phys. Rev. Lett. **77**, 2360 (1996).

[70] H. Pu and N. P. Bigelow, Phys. Rev. Lett. **80**, 1134 (1998).

[71] R. Graham and D. Walls, Phys. Rev. A **57**, 484 (1998).

[72] D. Gordon and C. M. Savage, Phys. Rev. A **58**, 1440 (1998).

[73] P. Kuopanportti, J. A. M. Huhtamäki, and M. Möttönen, Phys. Rev. A **85**, 043613 (2012).

[74] C. Ticknor, Phys. Rev. A **88**, 013623 (2013).

[75] H. Takeuchi and K. Kasamatsu, Phys. Rev. A **88**, 043612 (2013).

[76] T. Busch and J. R. Anglin, Phys. Rev. Lett. **87**, 010401 (2001).

[77] C. Becker, S. Stellmer, P. Soltan-Panahi, S. Dorscher, M. Baumert, E.-M. Richter, J. Kronjager, K. Bongs, and K. Sengstock, Nat. Phys. **4**, 496 (2008).

[78] C. Hamner, J. J. Chang, P. Engels, and M. A. Hoefer, Phys. Rev. Lett. **106**, 065302 (2011).

[79] P. Öhberg and L. Santos, J. Phys. B **34**, 4721 (2001).

[80] P. Öhberg and L. Santos, Phys. Rev. Lett. **86**, 2918 (2001).

[81] P. G. Kevrekidis, H. E. Nistazakis, D. J. Frantzeskakis, B. A. Malomed, and R. Carretero-González, Eur. Phys. J. D **28**, 181 (2004).

[82] D. Schumayer and B. Apagyi, Phys. Rev. A **69**, 043620 (2004).

[83] F. London, Nature (London) **141**, 643 (1938).

[84] F. London, Phys. Rev. **54**, 947 (1938).

[85] L. Tisza, Nature (London) **141**, 913 (1938).

[86] C. E. Hecht, Physica **25**, 1159 (1959).

[87] W. C. Stwalley and L. H. Nosanow, Phys. Rev. Lett. **36**, 910 (1976).

[88] I. F. Silvera and J. T. M. Walraven, Phys. Rev. Lett. **44**, 164 (1980).

[89] R. W. Cline, D. A. Smith, T. J. Greytak, and D. Kleppner, Phys. Rev. Lett. **45**, 2117 (1980).

[90] H. F. Hess, Phys. Rev. B **34**, 3476 (1986).

[91] W. Petrich, M. H. Anderson, J. R. Ensher, and E. A. Cornell, Phys. Rev. Lett. **74**, 3352 (1995).

[92] K. B. Davis, M.-O. Mewes, M. A. Joffe, M. R. Andrews, and W. Ketterle, Phys. Rev. Lett. **74**, 5202 (1995).

[93] A. I. Safonov, S. A. Vasilyev, I. S. Yasnikov, I. I. Lukashevich, and S. Jaakkola, Phys. Rev. Lett. **81**, 4545 (1998).

[94] M. Naraschewski and D. M. Stamper-Kurn, Phys. Rev. A **58**, 2423 (1998).

[95] M. J. Bijlsma, E. Zaremba, and H. T. C. Stoof, Phys. Rev. A **62**, 063609 (2000).

[96] R. Walser, J. Williams, J. Cooper, and M. Holland, Phys. Rev. A **59**, 3878 (1999).

[97] P. Blakie, A. Bradley, M. Davis, R. Ballagh, and C. Gardiner, Advances in Physics **57**, 363 (2008).

[98] A. Griffin, T. Nikuni, and E. Zaremba, *Bose-Condensed Gases at Finite Temperatures* (Cambridge University Press, New York, 2009).

[99] L. P. Kadanoff and P. C. Martin, Ann. Phys. **24**, 419 (1963).

[100] L. Kadanoff, G. Baym, and D. Pines, *Quantum Statistical Mechanics* (Addison-Wesley, New York, 1994).

[101] E. Zaremba, T. Nikuni, and A. Griffin, J. Low Temp. Phys. **116**, 277 (1999).

[102] A. J. Allen, *Non-Equilibrium and Finite Temperature Trapped Bose Gases: Interactions and Decay of Macroscopic Excitations,* Ph.D. thesis, Newcastle University (2012).

[103] N. Proukakis, S. Gardiner, M. Davis, and M. Szymanska, *Quantum Gases: Finite Temperatures and Non-equilibrium Dynamics* (Imperial College Press, U. K., 2013).

[104] A. Griffin, Phys. Rev. B **53**, 9341 (1996).

[105] D. A. W. Hutchinson, E. Zaremba, and A. Griffin, Phys. Rev. Lett. **78**, 1842 (1997).

[106] R. J. Dodd, M. Edwards, C. W. Clark, and K. Burnett, Phys. Rev. A **57**, R32 (1998).

[107] C. Gies, B. P. van Zyl, S. A. Morgan, and D. A. W. Hutchinson, Phys. Rev. A **69**, 023616 (2004).

[108] D. S. Jin, M. R. Matthews, J. R. Ensher, C. E. Wieman, and E. A. Cornell, Phys. Rev. Lett. **78**, 764 (1997).

[109] M. O. C. Pires and E. J. V. de Passos, Phys. Rev. A **77**, 033606 (2008).

[110] P. Öhberg and S. Stenholm, Phys. Rev. A **57**, 1272 (1998).

[111] C.-H. Zhang and H. A. Fertig, Phys. Rev. A **75**, 013601 (2007).

[112] P. Öhberg, Phys. Rev. A **61**, 013601 (1999).

[113] E. Gross, Il Nuovo Cimento Series 10 **20**, 454 (1961).

[114] E. P. Gross, J. Math. Phys. **4**, 195 (1963).

[115] L. P. Pitaevskii, J. Exptl. Theoret. Phys. (U.S.S.R.) p. 451 (1961).

[116] L. Pitaevskii and S. Stringari, *Bose-Einstein Condensation*, International Series of Monographs on Physics (Clarendon Press, U. K., 2003).

[117] A. M. Mateo and V. Delgado, Phys. Rev. A **77**, 013617 (2008).

[118] A. M. Mateo and V. Delgado, Ann. Phys. **324**, 709 (2009).

[119] N. Bogoliubov, J. Phys. **11**, 23 (1947).

[120] N. Bogoljubov, Il Nuovo Cimento **7**, 794 (1958).

[121] W. Greiner, D. Bromley, and J. Reinhardt, *Field Quantization* (Springer Berlin Heidelberg, 2013).

[122] C. Gies and D. A. W. Hutchinson, Phys. Rev. A **70**, 043606 (2004).

[123] B. G. Wild, *The Hartree-Fock-Bogoliubov theory of Bose-Einstein Condensates,* Ph.D. thesis, University of Otago, Dunedin, New Zealand (2011).

[124] C. W. Gardiner, *Quantum Noise* (Springer Berlin Heidelberg, 1991).

[125] N. M. Hugenholtz and D. Pines, Phys. Rev. **116**, 489 (1959).

[126] N. P. Proukakis, S. A. Morgan, S. Choi, and K. Burnett, Phys. Rev. A **58**, 2435 (1998).

[127] N. P. Proukakis, K. Burnett, and H. T. C. Stoof, Phys. Rev. A **57**, 1230 (1998).

[128] N. P. Proukakis, *Microscopic mean field theories of trapped Bose-Einstein Condensates,* Ph.D. thesis, University of Oxford (1998).

[129] D. A. W. Hutchinson, Int. J. Mod. Phys. B **15**, 1651 (2001).

[130] S. A. Morgan, J. Phys. B **33**, 3847 (2000).

[131] D. A. W. Hutchinson, R. J. Dodd, and K. Burnett, Phys. Rev. Lett. **81**, 2198 (1998).

[132] D. A. W. Hutchinson, K. Burnett, R. J. Dodd, S. A. Morgan, M. Rusch, E. Zaremba, N. P. Proukakis, M. Edwards, and C. W. Clark, J. Phys. B **33**, 3825 (2000).

[133] S. Giorgini, L. P. Pitaevskii, and S. Stringari, Phys. Rev. A **54**, R4633 (1996).

[134] F. Dalfovo, S. Giorgini, M. Guilleumas, L. Pitaevskii, and S. Stringari, Phys. Rev. A **56**, 3840 (1997).

[135] J. Reidl, A. Csordás, R. Graham, and P. Szépfalusy, Phys. Rev. A **59**, 3816 (1999).

[136] A. Roy, S. Gautam, and D. Angom, Phys. Rev. A **89**, 013617 (2014).

[137] A. Roy and D. Angom, Phys. Rev. A **90**, 023612 (2014).

[138] H. Stanley, *Introduction to Phase Transitions and Critical Phenomena*, International Series of Monographs on Physics (Oxford University Press, Oxford, U. K., 1971).

[139] G. Aad *et al.*, Phys. Lett. B **716**, 1 (2012).

[140] S. Chatrchyan *et al.*, Phys. Lett. B **716**, 30 (2012).

[141] P. W. Higgs, Phys. Rev. Lett. **13**, 508 (1964).

[142] P. Higgs, Phys. Lett. **12**, 132 (1964).

[143] F. Englert and R. Brout, Phys. Rev. Lett. **13**, 321 (1964).

[144] G. S. Guralnik, C. R. Hagen, and T. W. B. Kibble, Phys. Rev. Lett. **13**, 585 (1964).

[145] P. W. Higgs, Phys. Rev. **145**, 1156 (1966).

[146] T. W. B. Kibble, Phys. Rev. **155**, 1554 (1967).

[147] Y. Nambu and G. Jona-Lasinio, Phys. Rev. **122**, 345 (1961).

[148] J. Goldstone, Il Nuovo Cimento **19**, 154 (1961).

[149] J. Goldstone, A. Salam, and S. Weinberg, Phys. Rev. **127**, 965 (1962).

[150] "The Nobel Prize in Physics 2008" Nobelprize.org (The Royal Swedish Academy of Sciences, 2008).

[151] T. Brauner, Symmetry **2**, 609 (2010).

[152] H. Nielsen and S. Chadha, Nucl. Phys. B **105**, 445 (1976).

[153] I. Low and A. V. Manohar, Phys. Rev. Lett. **88**, 101602 (2002).

[154] Y. Nambu, J. Stat. Phys. **115**, 7 (2004).

[155] H. Watanabe and T. Brauner, Phys. Rev. D **84**, 125013 (2011).

[156] H. Watanabe and H. Murayama, Phys. Rev. Lett. **108**, 251602 (2012).

[157] Y. Hidaka, Phys. Rev. Lett. **110**, 091601 (2013).

[158] R. Donnelly, *Quantized Vortices in Helium II*, Cambridge Studies in American Literature and Culture (Cambridge University Press, New York, 1991).

[159] H. Takeuchi, K. Kasamatsu, and M. Tsubota, Phys. Rev. A **79**, 033619 (2009).

[160] T. P. Simula, T. Mizushima, and K. Machida, Phys. Rev. A **78**, 053604 (2008).

[161] T. P. Simula and K. Machida, Phys. Rev. A **82**, 063627 (2010).

[162] D. S. Petrov, G. V. Shlyapnikov, and J. T. M. Walraven, Phys. Rev. Lett. **85**, 3745 (2000).

[163] M. Egorov, B. Opanchuk, P. Drummond, B. V. Hall, P. Hannaford, and A. I. Sidorov, Phys. Rev. A **87**, 053614 (2013).

[164] R. W. Pattinson, T. P. Billam, S. A. Gardiner, D. J. McCarron, H. W. Cho, S. L. Cornish, N. G. Parker, and N. P. Proukakis, Phys. Rev. A **87**, 013625 (2013).

[165] P. Ao and S. T. Chui, Phys. Rev. A **58**, 4836 (1998).

[166] E. Timmermans, Phys. Rev. Lett. **81**, 5718 (1998).

[167] V. I. Yukalov and E. P. Yukalova, Laser Phys. Lett. **1**, 50 (2004).

[168] K. Pilch, A. D. Lange, A. Prantner, G. Kerner, F. Ferlaino, H.-C. Nägerl, and R. Grimm, Phys. Rev. A **79**, 042718 (2009).

[169] W. Kohn, Phys. Rev. **123**, 1242 (1961).

[170] J. F. Dobson, Phys. Rev. Lett. **73**, 2244 (1994).

[171] H. Al-Jibbouri and A. Pelster, Phys. Rev. A **88**, 033621 (2013).

[172] L. Salasnich, A. Parola, and L. Reatto, Phys. Rev. A **60**, 4171 (1999).

[173] Y. Hao, J.-Q. Liang, and Y. Zhang, Eur. Phys. J. D **36**, 33 (2005).

[174] S. Sachdev, *Quantum Phase Transitions* (Cambridge University Press, New York, 2011).

[175] F. Haake, *Quantum Signatures of Chaos* (Springer Heidelberg, 2010).

[176] F. Wang, D. Xiong, X. Li, D. Wang, and E. Tiemann, Phys. Rev. A **87**, 050702(R) (2013).

[177] A. Roy, S. Gautam, and D. Angom, Eur. Phys. J. Sp. Topics **224**, 571 (2015).

[178] N. T. Phuc, Y. Kawaguchi, and M. Ueda, Phys. Rev. Lett. **113**, 230401 (2014).

[179] K. Suthar, A. Roy, and D. Angom, Phys. Rev. A **91**, 043615 (2015).

[180] W. H. Zurek, Nature (London) **317**, 505 (1985).

[181] W. H. Zurek, Phys. Rev. Lett. **102**, 105702 (2009).

[182] B. Damski and W. H. Zurek, Phys. Rev. Lett. **104**, 160404 (2010).

[183] G. Lamporesi, S. Donadello, S. Serafini, F. Dalfovo, and G. Ferrari, Nat. Phys. **9**, 656 (2013).

[184] S. Burger, K. Bongs, S. Dettmer, W. Ertmer, K. Sengstock, A. Sanpera, G. V. Shlyapnikov, and M. Lewenstein, Phys. Rev. Lett. **83**, 5198 (1999).

[185] J. Denschlag, J. E. Simsarian, D. L. Feder, C. W. Clark, L. A. Collins, J. Cubizolles, L. Deng, E. W. Hagley, K. Helmerson, W. P. Reinhardt, S. L. Rolston, B. I. Schneider, and W. D. Phillips, Science **287**, 97 (2000).

[186] T. Busch and J. R. Anglin, Phys. Rev. Lett. **84**, 2298 (2000).

[187] S. Middelkamp, J. Chang, C. Hamner, R. Carretero-González, P. Kevrekidis, V. Achilleos, D. Frantzeskakis, P. Schmelcher, and P. Engels, Phys. Lett. A **375**, 642 (2011).

[188] M. A. Hoefer, J. J. Chang, C. Hamner, and P. Engels, Phys. Rev. A **84**, 041605(R) (2011).

[189] K. Kasamatsu and M. Tsubota, Phys. Rev. A **74**, 013617 (2006).

[190] S. Rajendran, P. Muruganandam, and M. Lakshmanan, J. Phys. B **42**, 145307 (2009).

[191] V. Achilleos, D. Yan, P. G. Kevrekidis, and D. J. Frantzeskakis, New J. Phys. **14**, 055006 (2012).

[192] A. Weller, J. P. Ronzheimer, C. Gross, J. Esteve, M. K. Oberthaler, D. J. Frantzeskakis, G. Theocharis, and P. G. Kevrekidis, Phys. Rev. Lett. **101**, 130401 (2008).

[193] S. Stellmer, C. Becker, P. Soltan-Panahi, E.-M. Richter, S. Dörscher, M. Baumert, J. Kronjäger, K. Bongs, and K. Sengstock, Phys. Rev. Lett. **101**, 120406 (2008).

[194] A. E. Muryshev, H. B. van Linden van den Heuvell, and G. V. Shlyapnikov, Phys. Rev. A **60**, R2665 (1999).

[195] R. Atre, P. K. Panigrahi, and G. S. Agarwal, Phys. Rev. E **73**, 056611 (2006).

[196] G. Theocharis, A. Weller, J. P. Ronzheimer, C. Gross, M. K. Oberthaler, P. G. Kevrekidis, and D. J. Frantzeskakis, Phys. Rev. A **81**, 063604 (2010).

[197] J. Dziarmaga and K. Sacha, Phys. Rev. A **66**, 043620 (2002).

[198] J. Dziarmaga, Z. P. Karkuszewski, and K. Sacha, Phys. Rev. A **66**, 043615 (2002).

[199] J. Dziarmaga and K. Sacha, Phys. Rev. A **67**, 033608 (2003).

[200] J. Dziarmaga, Z. P. Karkuszewski, and K. Sacha, J. Phys. B **36**, 1217 (2003).

[201] C. K. Law, P. T. Leung, and M.-C. Chu, J. Phys. B **35**, 3583 (2002).

[202] C. K. Law, Phys. Rev. A **68**, 015602 (2003).

[203] D. M. Gangardt and A. Kamenev, Phys. Rev. Lett. **104**, 190402 (2010).

[204] T. Tsuzuki, J. Low Temp. Phys. **4**, 441 (1971).

[205] T. Kambe, J. Fluid Mech. **173**, 643 (1986).

[206] P. O. Fedichev, A. E. Muryshev, and G. V. Shlyapnikov, Phys. Rev. A **60**, 3220 (1999).

[207] T. Kapitula, P. G. Kevrekidis, and B. Sandstede, Physica D **195**, 263 (2004).

[208] S. Middelkamp, G. Theocharis, P. G. Kevrekidis, D. J. Frantzeskakis, and P. Schmelcher, Phys. Rev. A **81**, 053618 (2010).

[209] D. V. Skryabin, Phys. Rev. A **63**, 013602 (2000).

[210] D. V. Skryabin, Phys. Rev. E **64**, 055601(R) (2001).

[211] A. Görlitz, J. M. Vogels, A. E. Leanhardt, C. Raman, T. L. Gustavson, J. R. Abo-Shaeer, A. P. Chikkatur, S. Gupta, S. Inouye, T. Rosenband, and W. Ketterle, Phys. Rev. Lett. **87**, 130402 (2001).

[212] A. Fetter and J. Walecka, *Quantum Theory of Many-particle Systems*, Dover Books on Physics (Dover Publications, New York, 2003).

[213] P. Jain and M. Boninsegni, Phys. Rev. A **83**, 023602 (2011).

[214] W. Ketterle and N. J. van Druten, Phys. Rev. A **54**, 656 (1996).

[215] S. De, D. L. Campbell, R. M. Price, A. Putra, B. M. Anderson, and I. B. Spielman, Phys. Rev. A **89**, 033631 (2014).

[216] B. Van Schaeybroeck, Phys. Rev. A **78**, 023624 (2008).

[217] P. Hohenberg and P. Martin, Annals of Physics **34**, 291 (1965).

[218] N. D. Mermin and H. Wagner, Phys. Rev. Lett. **17**, 1133 (1966).

[219] A. Roy and D. Angom, Phys. Rev. A **92**, 011601(R) (2015).

[220] J. L. Roberts, N. R. Claussen, J. P. Burke, C. H. Greene, E. A. Cornell, and C. E. Wieman, Phys. Rev. Lett. **81**, 5109 (1998).

[221] M. Greiner, O. Mandel, T. Esslinger, T. W. Hansch, and I. Bloch, Nature (London) **415**, 39 (2002).

[222] I. Bloch, Nat. Phys. **1**, 23 (2005).

[223] Y. Shin, M. Saba, T. A. Pasquini, W. Ketterle, D. E. Pritchard, and A. E. Leanhardt, Phys. Rev. Lett. **92**, 050405 (2004).

[224] M. Albiez, R. Gati, J. Fölling, S. Hunsmann, M. Cristiani, and M. K. Oberthaler, Phys. Rev. Lett. **95**, 010402 (2005).

[225] M. Saba, T. A. Pasquini, C. Sanner, Y. Shin, W. Ketterle, and D. E. Pritchard, Science **307**, 1945 (2005).

[226] A. L. Gaunt, T. F. Schmidutz, I. Gotlibovych, R. P. Smith, and Z. Hadzibabic, Phys. Rev. Lett. **110**, 200406 (2013).

[227] J. E. Lye, L. Fallani, M. Modugno, D. S. Wiersma, C. Fort, and M. Inguscio, Phys. Rev. Lett. **95**, 070401 (2005).

[228] P. W. Anderson, Phys. Rev. **109**, 1492 (1958).

[229] J. Billy, V. Josse, Z. Zuo, A. Bernard, B. Hambrecht, P. Lugan, D. Clement, L. Sanchez-Palencia, P. Bouyer, and A. Aspect, Nature (London) **453**, 891 (2008).

[230] G. Roati, C. D'Errico, L. Fallani, M. Fattori, C. Fort, M. Zaccanti, G. Modugno, M. Modugno, and M. Inguscio, Nature (London) **453**, 895 (2008).

[231] S. Gupta, K. W. Murch, K. L. Moore, T. P. Purdy, and D. M. Stamper-Kurn, Phys. Rev. Lett. **95**, 143201 (2005).

[232] W. H. Heathcote, E. Nugent, B. T. Sheard, and C. J. Foot, New J. Phys. **10**, 043012 (2008).

[233] T. W. B. Kibble, J. Phys. A **9**, 1387 (1976).

[234] C. Ryu, M. F. Andersen, P. Cladé, V. Natarajan, K. Helmerson, and W. D. Phillips, Phys. Rev. Lett. **99**, 260401 (2007).

[235] E. M. Wright, J. Arlt, and K. Dholakia, Phys. Rev. A **63**, 013608 (2000).

[236] J. Courtial, K. Dholakia, L. Allen, and M. J. Padgett, Phys. Rev. A **56**, 4193 (1997).

[237] A. Ramanathan, K. C. Wright, S. R. Muniz, M. Zelan, W. T. Hill, C. J. Lobb, K. Helmerson, W. D. Phillips, and G. K. Campbell, Phys. Rev. Lett. **106**, 130401 (2011).

[238] S. Moulder, S. Beattie, R. P. Smith, N. Tammuz, and Z. Hadzibabic, Phys. Rev. A **86**, 013629 (2012).

[239] J. E. Curtis and D. G. Grier, Phys. Rev. Lett. **90**, 133901 (2003).

[240] G. E. Marti, R. Olf, and D. M. Stamper-Kurn, Phys. Rev. A **91**, 013602 (2015).

[241] M. J. Edmonds, K. L. Lee, and N. P. Proukakis, Phys. Rev. A **91**, 011602(R) (2015).

[242] M. J. Edmonds, K. L. Lee, and N. P. Proukakis, Phys. Rev. A **92**, 063607 (2015).

[243] M. Kulkarni and A. Lamacraft, Phys. Rev. A **88**, 021603(R) (2013).

[244] P. Muruganandam and S. K. Adhikari, Comp. Phys. Comm. **180**, 1888 (2009).

[245] E. Anderson, Z. Bai, C. Bischof, S. Blackford, J. Demmel, J. Dongarra, J. D. Croz, A. Greenbaum, S. Hammarling, A. McKenney, and D. Sorensen, *LAPACK Users' Guide* (Society for Industrial and Applied Mathematics, Philadelphia, PA, 1999), 3rd ed.

[246] T. Simula, S. Virtanen, and M. Salomaa, Comp. Phys. Comm. **142**, 396 (2001).

List of Publications

International journals

1. **Arko Roy**, D. Angom:
   Thermal suppression of phase separation in condensate mixtures,
   Phys. Rev. A **92**, 011601(R) (2015). 5pp, arXiv:1502.00473.

2. K. Suthar, **Arko Roy**, and D. Angom:
   Fluctuation-driven topological transition of binary condensates in optical lattices, Phys. Rev. A **91**, 043615 (2015). 9pp, arXiv:1412.0405.

3. **Arko Roy**, S. Gautam, and D. Angom:
   Evolution of Goldstone mode in binary condensate mixtures,
   Eur. Phys. J. Sp. Topics **224**, 571 (2015). 5pp, arXiv:1501.03590.

4. **Arko Roy**, D. Angom:
   Fluctuation- and interaction-induced instability of dark solitons in single and binary condensates, Phys. Rev. A **90**, 023612 (2014). 9pp, arXiv:1405.6459.

5. K. Suthar, **Arko Roy**, and D. Angom:
   Acoustic radiation from vortex-barrier interaction in atomic Bose-Einstein condensate, J. Phys. B **47**, 135301 (2014). 9pp, arXiv:1312.7811.

6. **Arko Roy**, S. Gautam, and D. Angom:
   Goldstone modes and bifurcations in phase-separated binary condensates at finite temperature, Phys. Rev. A **89**, 013617 (2014). 7pp, arXiv:1307.5716.

7. S. Gautam, **Arko Roy**, and Subroto Mukerjee:
   Finite-temperature dynamics of vortices in Bose-Einstein condensates,
   Phys. Rev. A **89**, 013612 (2014). 8pp, arXiv:1309.6205.

Preprints

1. **Arko Roy**, D. Angom:
   Reorganization of Kohn mode from harmonic to toroidal trap,
   arXiv:1512.08655 (under review).

2. **Arko Roy**, S. Gautam, and D. Angom:
   Mode bifurcation in the Rayleigh-Taylor instability of binary condensates,
   arXiv:1210.0381 (under review).

Publications attached with thesis

1. **Arko Roy**, S. Gautam, and D. Angom:
   Goldstone modes and bifurcations in phase-separated binary condensates at finite temperature, Phys. Rev. A **89**, 013617 (2014). 7pp,
   doi: 10.1103/PhysRevA.89.013617

2. **Arko Roy**, D. Angom:
   Fluctuation- and interaction-induced instability of dark solitons in single and binary condensates, Phys. Rev. A **90**, 023612 (2014). 9pp,
   doi: 10.1103/PhysRevA.90.023612

3. **Arko Roy**, D. Angom:
   Thermal suppression of phase separation in condensate mixtures,
   Phys. Rev. A **92**, 011601(R) (2015). 5pp,
   doi: 10.1103/PhysRevA.92.011601

Goldstone modes and bifurcations in phase-separated binary condensates at finite temperature

Arko Roy,[1] S. Gautam,[2] and D. Angom[1]
[1]*Physical Research Laboratory, Navrangpura, Ahmedabad-380009, Gujarat, India*
[2]*Department of Physics, Indian Institute of Science, Bangalore-560012, India*
(Received 25 July 2013; revised manuscript received 14 November 2013; published 21 January 2014)

We show that the third Goldstone mode, which emerges in binary condensates at phase separation, persists to higher interspecies interaction for density profiles where one component is surrounded on both sides by the other component. This is not the case with symmetry-broken density profiles where one species is entirely to the left and the other is entirely to the right. We, then, use Hartree-Fock-Bogoliubov theory with Popov approximation to examine the mode evolution at $T \neq 0$ and demonstrate the existence of mode bifurcation near the critical temperature. The Kohn mode, however, exhibits deviation from the natural frequency at finite temperatures after the phase separation. This is due to the exclusion of the noncondensate atoms in the dynamics.

DOI: 10.1103/PhysRevA.89.013617 PACS number(s): 67.85.Bc, 03.75.Hh, 03.75.Mn

I. INTRODUCTION

The remarkable feature of binary condensates or two-species Bose-Einstein condensates (TBECs) is the phenomenon of phase separation [1,2]. This relates the system to novel phenomena in nonlinear dynamics and pattern formation, nonequilibrium statistical mechanics, optical systems, and phase transitions in condensed matter systems. Experimentally, TBECs have been realized in the mixture of two different alkali-metal atoms [3–5], and in two different isotopes [6] and hyperfine states [7,8] of an atom. Most importantly, in experiments, the TBEC can be steered from miscible to phase-separated domain or vice versa [9,10] through a Feshbach resonance. These have motivated theoretical investigations on stationary states [1,11], dynamical instabilities [12–14], and collective excitations [15–21] of TBECs.

In this paper, we report the development of Hartree-Fock-Bogoliubov theory with Popov (HFB-Popov) approximation [22] for TBECs. We use it to investigate the evolution of Goldstone modes and mode energies as a function of the interspecies interaction and temperature, respectively. Recent works [20,21] reported the existence of an additional Goldstone mode at phase separation in the symmetry-broken density profiles, which we refer to as the *side-by-side* density profiles. We, however, demonstrate that in the other type of density profile where one of the species is surrounded on both sides by the other, which we refer to as the *sandwich* type, the mode evolves very differently. To include the finite temperature effects, besides HFB-Popov approximation, there are other different approaches. These include projected Gross-Pitaevskii (GP) equation [23], stochastic GP equation (SGPE) [24], and Zaremba-Nikuni-Griffin (ZNG) formalism [25]. For the present work we have chosen the HFB-Popov approximation, which is a gapless theory and satisfies the Hugenholtz-Pines theorem [26]. The method is particularly well suited to examine the evolution of the low-lying modes. It has been used extensively in single-species BEC to study finite temperature effects to mode energies [22,27–29] and agrees well with the experimental results [30] at low temperatures. In TBECs, the HFB-Popov approximation has been used in the miscible domain [31] and in this paper, we describe the results for the phase-separated domain. Other works which have examined the finite temperature effects in TBECs use the Hartree-Fock treatment with or without trapping potential [32,33] and the semiclassical approach [34]. Although, HFB-Popov does have the advantage vis-a-vis calculation of the modes, it is nontrivial to get converged solutions. In the present work, we consider the TBEC of ^{87}Rb-^{133}Cs [4,5], which have widely differing s-wave scattering lengths and masses. This choice does add to the severity of the convergence issues but this also makes it a good test for the methods we use. We choose the parameter domain where the system is quasi-one-dimensional (quasi-1D) and a mean-field description like HFB-Popov is applicable. The quasi-1D trapped bosons exhibit a rich phase structure as a function of density and interaction strengths [35]. For comparison with the experimental results we also consider the parameters as in the experiment [5]. We find that, like in Ref. [36], the quasi-1D descriptions are in good agreement with the condensate density profiles of three-dimensional (3D) calculations [37].

II. THEORY

For a highly anisotropic cigar-shaped harmonic trapping potential $V = (1/2)m(\omega_x^2 x^2 + \omega_y^2 y^2 + \omega_z^2 z^2)$, the trapping frequencies should satisfy the condition $\omega_x = \omega_y = \omega_\perp \gg \omega_z$. In this case, we can integrate out the condensate wave function along xy and reduce it to a quasi-1D system. The transverse degrees of freedom are then frozen and the system is confined in the harmonic oscillator ground state along the transverse direction for which $\hbar\omega_\perp \gg \mu_k$. We thus consider excitations present only in the axial direction z [38,39]. The grand-canonical Hamiltonian, in the second quantized form, describing the mixture of two interacting BECs is then

$$H = \sum_{k=1,2} \int dz \hat{\Psi}_k^\dagger(z,t) \left[-\frac{\hbar^2}{2m_k}\frac{\partial^2}{\partial z^2} + V_k(z) - \mu_k + \frac{U_{kk}}{2}\hat{\Psi}_k^\dagger(z,t)\hat{\Psi}_k(z,t) \right] \hat{\Psi}_k(z,t) + U_{12}\int dz \hat{\Psi}_1^\dagger(z,t)\hat{\Psi}_2^\dagger(z,t)\hat{\Psi}_1(z,t)\hat{\Psi}_2(z,t), \quad (1)$$

where $k = 1,2$ is the species index, $\hat{\Psi}_k$'s are the Bose field operators of the two different species, and μ_k's are the chemical

potentials. The strength of intra- and interspecies interactions are $U_{kk} = (a_{kk}\lambda)/m_k$ and $U_{12} = (a_{12}\lambda)/(2m_{12})$, respectively, where $\lambda = (\omega_\perp/\omega_z) \gg 1$ is the anisotropy parameter, a_{kk} is the s-wave scattering length, m_k's are the atomic masses of the species, and $m_{12} = m_1m_2/(m_1 + m_2)$. In the present work we consider all the interactions are repulsive, that is, a_{kk},$a_{12} > 0$. The equation of motion of the Bose field operators is

$$i\hbar\frac{\partial}{\partial t}\begin{pmatrix}\hat{\Psi}_1\\ \hat{\Psi}_2\end{pmatrix} = \begin{pmatrix}\hat{h}_1 + U_{11}\hat{\Psi}_1^\dagger\hat{\Psi}_1 & U_{12}\hat{\Psi}_2^\dagger\hat{\Psi}_1\\ U_{12}\hat{\Psi}_1^\dagger\hat{\Psi}_2 & \hat{h}_2 + U_{22}\hat{\Psi}_2^\dagger\hat{\Psi}_2\end{pmatrix}\begin{pmatrix}\hat{\Psi}_1\\ \hat{\Psi}_2\end{pmatrix},$$

where $\hat{h}_k = (-\hbar^2/2m_k)\partial^2/\partial z^2 + V_k(z) - \mu_k$. For compact notations, we refrain from writing the explicit dependence of $\hat{\Psi}_k$ on z and t. Since a majority of the atoms reside in the ground state for the temperature regime relevant to the experiments ($T \leq 0.65T_c$) [28], the condensate part can be separated out from the Bose field operator $\hat{\Psi}(\mathbf{r},t)$. The noncondensed or the thermal cloud of atoms are then the fluctuations of the condensate field. Here, T_c is the critical temperature of ideal gas in a harmonic confining potential. Accordingly, we define [22], $\hat{\Psi}(z,t) = \Phi(z) + \tilde{\Psi}(z,t)$, where $\Phi(z)$ is a c-field and represents the condensate, and $\tilde{\Psi}(z,t)$ is the fluctuation part. In two-component representation,

$$\begin{pmatrix}\hat{\Psi}_1\\ \hat{\Psi}_2\end{pmatrix} = \begin{pmatrix}\phi_1\\ \phi_2\end{pmatrix} + \begin{pmatrix}\tilde{\psi}_1\\ \tilde{\psi}_2\end{pmatrix}, \tag{2}$$

where $\phi_k(z)$ and $\tilde{\psi}_k(z)$ are the condensate and fluctuation part of the kth species. Thus for a TBEC, ϕ_ks are the stationary solutions of the coupled generalized GP equations, with time-independent HFB-Popov approximation, given by

$$\hat{h}_1\phi_1 + U_{11}[n_{c1} + 2\tilde{n}_1]\phi_1 + U_{12}n_2\phi_1 = 0, \tag{3a}$$

$$\hat{h}_2\phi_2 + U_{22}[n_{c2} + 2\tilde{n}_2]\phi_2 + U_{12}n_1\phi_2 = 0, \tag{3b}$$

where $n_{ck}(z) \equiv |\phi_k(z)|^2$, $\tilde{n}_k(z) \equiv \langle\tilde{\psi}_k^\dagger(z,t)\tilde{\psi}_k(z,t)\rangle$, and $n_k(z) = n_{ck}(z) + \tilde{n}_k(z)$ are the local condensate, noncondensate, and total density, respectively. Using Bogoliubov transformation,

$$\tilde{\psi}_k(z,t) = \sum_j[u_{kj}(z)\hat{\alpha}_j(z)e^{-iE_jt} - v_{kj}^*(z)\hat{\alpha}_j^\dagger(z)e^{iE_jt}],$$

where $\hat{\alpha}_j$ ($\hat{\alpha}_j^\dagger$) are the quasiparticle annihilation (creation) operators and satisfy Bose commutation relations, u_k and v_k are the quasiparticle amplitudes, and j is the energy eigenvalue index. We define the operators as common to both the species, which is natural and consistent as the dynamics of the species are coupled. Furthermore, this reproduces the standard coupled Bogoliubov-de Gennes equations at $T = 0$ [20] and in the limit $a_{12} \to 0$, noninteracting TBEC, the quasiparticle spectra separates into two distinct sets: one set for each of the condensates. From the above definitions, we get the following Bogoliubov-de Gennes equations,

$$\hat{\mathcal{L}}_1u_{1j} - U_{11}\phi_1^2v_{1j} + U_{12}\phi_1(\phi_2^*u_{2j} - \phi_2v_{2j}) = E_ju_{1j}, \tag{4a}$$

$$\hat{\underline{\mathcal{L}}}_1v_{1j} + U_{11}\phi_1^{*2}u_{1j} - U_{12}\phi_1^*(\phi_2v_{2j} - \phi_2^*u_{2j}) = E_jv_{1j}, \tag{4b}$$

$$\hat{\mathcal{L}}_2u_{2j} - U_{22}\phi_2^2v_{2j} + U_{12}\phi_2(\phi_1^*u_{1j} - \phi_1v_{1j}) = E_ju_{2j}, \tag{4c}$$

$$\hat{\underline{\mathcal{L}}}_2v_{2j} + U_{22}\phi_2^{*2}u_{2j} - U_{12}\phi_2^*(\phi_1v_{1j} - \phi_1^*u_{1j}) = E_jv_{2j}, \tag{4d}$$

where $\hat{\mathcal{L}}_1 = \big(\hat{h}_1 + 2U_{11}n_1 + U_{12}n_2\big)$, $\hat{\mathcal{L}}_2 = \big(\hat{h}_2 + 2U_{22}n_2 + U_{12}n_1\big)$, and $\hat{\underline{\mathcal{L}}}_k = -\hat{\mathcal{L}}_k$. To solve Eq. (4) we define u_k and v_k's as the linear combination of N harmonic oscillator eigenstates.

$$u_{1j} = \sum_{i=0}^{N} p_{ij}\xi_i, \quad v_{1j} = \sum_{i=0}^{N} q_{ij}\xi_i,$$
$$u_{2j} = \sum_{i=0}^{N} r_{ij}\xi_i, \quad v_{2j} = \sum_{i=0}^{N} s_{ij}\xi_i, \tag{5}$$

where ξ_i is the ith harmonic oscillator eigenstate and p_{ij}, q_{ij}, r_{ij}, and s_{ij} are the coefficients of linear combination. Using this expansion Eq. (4) is then reduced to a matrix eigenvalue equation and solved using standard matrix diagonalization algorithms. The matrix has a dimension of $4N \times 4N$ and is non-Hermitian, nonsymmetric, and may have complex eigenvalues. In the present work, to avoid metastable states, we ensure that E_j's are real during the iteration. The eigenvalue spectrum obtained from the diagonalization of the matrix has an equal number of positive and negative eigenvalues E_j's. The number density $\tilde{n}_k$ of the noncondensate atoms is then

$$\tilde{n}_k = \sum_j\{[|u_{kj}|^2 + |v_{kj}|^2]N_0(E_j) + |v_{kj}|^2\}, \tag{6}$$

where $\langle\hat{\alpha}_j^\dagger\hat{\alpha}_j\rangle = (e^{\beta E_j} - 1)^{-1} \equiv N_0(E_j)$ is the Bose factor of the quasiparticle state with real and positive energy E_j. The coupled Eqs. (3) and (4) are solved iteratively until the solutions converge to desired accuracy. However, it should be emphasized that, when $T \to 0$, $N_0(E_j)$'s in Eq. (6) vanish. The noncondensate density is then reduced to

$$\tilde{n}_k = \sum_j |v_{kj}|^2. \tag{7}$$

Thus, at zero temperature we need to solve the equations self-consistently as the quantum depletion term $|v_{kj}|^2$ in the above equation is nonzero. The contribution from the quantum depletion to the noncondensate is very small; it is $\approx$0.1% for the set of parameters used in our calculations. In addition, the solutions to the equations converge in less than five iterations.

III. RESULTS AND DISCUSSIONS

A. Numerical details

For the $T = 0$ studies we solve the pair of coupled equations [Eq. (3)] by neglecting the noncondensate density ($\tilde{n}_k = 0$) using finite-difference methods and in particular, we use the split-step Crank-Nicholson method [41] adapted for binary condensates. The method when implemented with imaginary time propagation is appropriate to obtain the stationary ground-state wave function of the TBEC. Using this solution, and based on Eq. (5), we cast the Eq. (4) as a matrix eigenvalue equation in the basis of the trapping potential. The matrix is then diagonalized using the LAPACK routine ZGEEV [40] to find the quasiparticle energies and amplitudes, E_j, and u_k's and v_k's, respectively. This step is the beginning of the first iteration for $T \neq 0$ calculations. In which case, the u_k's and v_k's along with E_j are used to get the initial estimate of $\tilde{n}_k$

through Eq. (6). For this we consider only the positive energy modes. Using this updated value of $\tilde{n}_k$, the ground-state wave function of TBEC ϕ_k and chemical potential μ_k are again recalculated from Eq. (3). This procedure is repeated until the solutions reach desired convergence. In the present work the convergence criteria is that the change in μ_k between iterations should be less than 10^{-4}. In general, the convergence is not smooth and we encounter severe oscillations very frequently. To damp the oscillations and accelerate convergence we employ a successive over- (under-) relaxation technique for updating the condensate (noncondensate) densities [42]. The new solutions after the IC iteration cycle are

$$\begin{aligned}\phi_{\rm IC}^{\rm new}(z) &= s^{\rm ov}\phi_{\rm IC}(z) + (1-s^{\rm ov})\phi_{\rm IC-1}(z),\\ \tilde{n}_{\rm IC}^{\rm new}(z) &= s^{\rm un}\tilde{n}_{\rm IC}(z) + (1-s^{\rm un})\tilde{n}_{\rm IC-1}(z),\end{aligned} \tag{8}$$

where $s^{\rm ov} > 1$ ($s^{\rm un} < 1$) is the over- (under-) relaxation parameter. During the calculation of the u_k and v_k, we choose an optimal number of the harmonic oscillator basis functions. The conditions based on which we decide the optimal size are as follows: obtaining reliable Goldstone modes; all eigenvalues must be real. For the $T = 0$ studies we find that a basis set consisting of 130 harmonic oscillator eigenstates is an optimal choice. We observe the Goldstone mode eigenenergies becoming complex, with a small imaginary component, in the eigenspectrum when the basis set is very large. So, in the present studies, we ensure that there are no complex eigenvalues with an appropriate choice of the basis set size.

B. Mode evolution of trapped TBEC at $T = 0$

In TBECs, phase separation occurs when $U_{12} > \sqrt{U_{11}U_{22}}$. For the present work, we consider Cs and Rb as the first and second species, respectively. With this identification $a_{11} = a_{\rm CsCs} = 280a_0$ and $a_{22} = a_{\rm RbRb} = 100a_0$, where a_0 is the Bohr radius, and arrive at the condition for phase separation $a_{12} = a_{\rm CsRb} > 261a_0$, which is smaller than the background value of $a_{\rm CsRb} \approx 650a_0$ [4]. To examine the nature of modes in the neighbourhood of phase separation, we compute E_j at $T = 0$ and vary $a_{\rm CsRb}$, which is experimentally possible with the Rb-Cs Feshbach resonance [43]. The evolution of the low-lying modes in the domain $0 \le a_{\rm CsRb} \le 450a_0$ with $N_{\rm Rb} = N_{\rm Cs} = 10^4$ are computed with $\omega_{z({\rm Rb})} = 2\pi \times 3.89$ Hz and $\omega_{z({\rm Cs})} = 2\pi \times 4.55$ Hz as in Refs. [5,37]. However, to form a quasi-1D system we take $\omega_\perp = 50\omega_z$, so that $\hbar\omega_\perp \gg \mu_k$. For these values, the relevant quasi-1D parameters $\alpha = 2a_{\rm CsCs}\sqrt{(\omega_\perp/\omega_z)}(m\omega_\perp/\hbar) \approx 0.36$ and $\gamma = 2(a_{\rm CsCs}/n_{\rm Cs})(m\omega_\perp/\hbar) \approx 10^{-5}$, so the system is in the weakly interacting TF regime [35] and mean-field description through the GP equation is valid. For this set of parameters the ground state is of *sandwich* geometry, in which the species with the heavier mass is at the center and flanked by the species with lighter mass at the edges. An example of the *sandwich* profile corresponding to the experimentally relevant parameters is shown in Fig. 1(c). On the other hand for TBEC with species of equal or near equal masses and a low number of atoms, in general, the ground-state geometry is *side by side*. As an example the *side-by-side* ground-state density profile of ^{85}Rb-^{87}Rb TBEC is shown in Fig. 1(f).

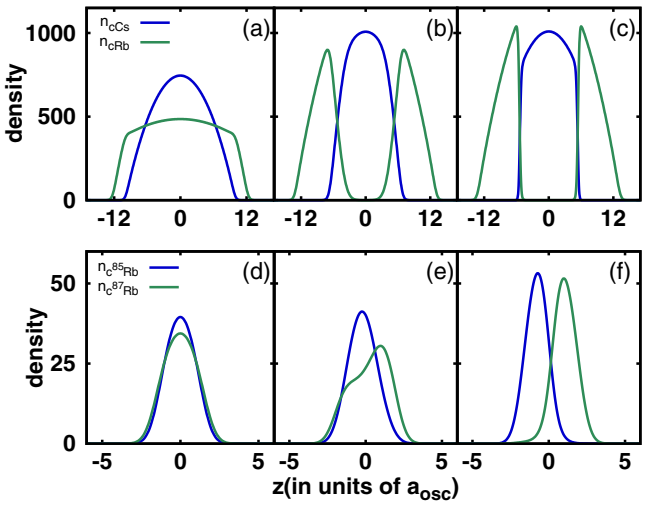

FIG. 1. (Color online) Transition to phase separation and structure of the density profiles in TBEC. (a)–(c) Show the transition from miscible to *sandwich*-type density profile with the change in interspecies scattering length $a_{\rm CsRb}$ for a Cs-Rb TBEC and correspond to $a_{\rm CsRb} = \{200a_0, 310a_0, 420a_0\}$, respectively. The density profiles in (c) is referred to as the *sandwich* type. (d)–(f) Show the transition from miscible to *side-by-side* density profile with the change in $a_{^{85}{\rm Rb}^{87}{\rm Rb}}$ for a ^{85}Rb $-^{87}$ Rb TBEC and correspond to $a_{^{85}{\rm Rb}^{87}{\rm Rb}} = \{100a_0, 290a_0, 400a_0\}$, respectively. The density profile in (f) is referred to as the *side-by-side* type. In the plots density is measured in units of $a_{\rm osc}^{-1}$.

From here on we consider the same set of ω_z ($\omega_{z({\rm Rb})} = 2\pi \times 3.89$ Hz and $\omega_{z({\rm Cs})} = 2\pi \times 4.55$ Hz), as mentioned earlier, in the rest of the calculations reported in the manuscript. In the computations we scale the spatial and temporal variables as $z/a_{\rm osc(Cs)}$ and $\omega_{z({\rm Cs})}t$ which render the equations dimensionless. When $a_{\rm CsRb} = 0$, the $U_{\rm CsRb}$-dependent terms in Eq. (4) are zero and the spectrum of the two species are independent as the two condensates are decoupled. The system has two Goldstone modes, one each for the two species. The two lowest modes with nonzero excitation energies are the Kohn modes of the two species, and these occur at $\hbar\omega_{z({\rm Cs})}$ and $0.85\hbar\omega_{z({\rm Cs})}$ for Cs and Rb species, respectively.

1. Third Goldstone mode

The clear separation between the modes of the two species is lost and mode mixing occurs when $a_{\rm CsRb} > 0$. For example, the Kohn modes of the two species intermix when $a_{\rm CsRb} > 0$, however, there is a difference in the evolution of the mode energies. The energy of the Rb Kohn mode decreases, but the one corresponding to Cs remains steady at $\hbar\omega_{z({\rm Cs})}$. At higher $a_{\rm CsRb}$ the energy of the Rb Kohn mode decreases further and goes soft at phase separation ($U_{\rm CsRb} > \sqrt{U_{\rm CsCs}U_{\rm RbRb}}$) when $a_{\rm CsRb} \approx 310a_0$. This introduces a new Goldstone mode of the Rb BEC to the excitation spectrum. The reason is, for the parameters chosen, the density profiles at phase separation assume *sandwich* geometry with Cs BEC at the center and Rb BEC at the edges. So, the Rb BECs at the edges are effectively two topologically distinct BECs and there are two Goldstone modes with the same $|u_{\rm Rb}|$ and $|v_{\rm Rb}|$ but different phases. A similar result of the Kohn mode going soft was observed for

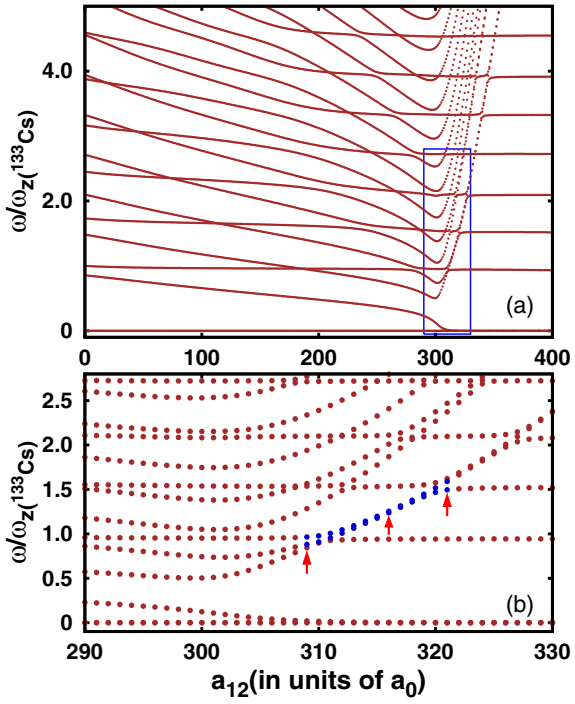

FIG. 2. (Color online) The evolution of the modes as a function of the interspecies scattering length a_{CsRb} in Cs-Rb TBEC. (a) Shows the evolution of the low-lying modes in the domain $0 \leq a_{\mathrm{CsRb}} \leq 400a_0$ for $N_{^{87}\mathrm{Rb}} = N_{^{133}\mathrm{Cs}} = 10^4$. (b) The enlarged view of the region enclosed within the blue colored rectangular box in (a) to resolve the avoided crossing and quasidegeneracy of modes (highlighted with dark-blue points). The points marked with red arrows correspond to interspecies scattering length $a_{\mathrm{CsRb}} = \{309a_0, 316a_0, 321a_0\}$, respectively.

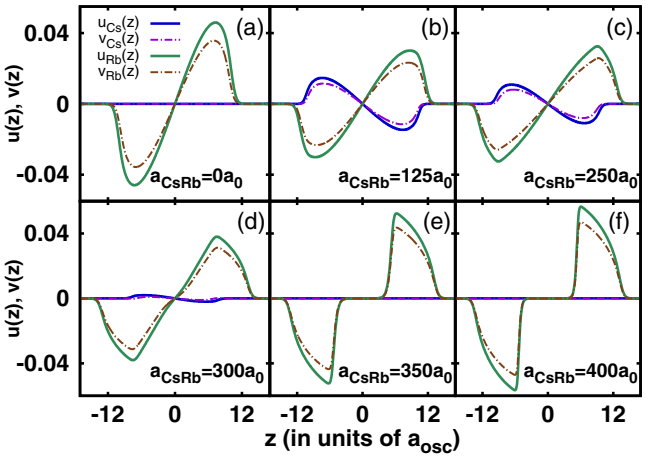

FIG. 3. (Color online) Evolution of quasiparticle amplitude corresponding to the Rb Kohn mode as a_{CsRb} is increased from 0 to $400a_0$. For better visibility u_{Cs} and u_{Rb} are scaled by a factor of 1.2. (a) When $a_{\mathrm{CsRb}} = 0$, it is a Kohn mode of the Rb condensate. (b)–(d) In the domain $0 < a_{\mathrm{CsRb}} \lesssim 310a_0$ the mode acquires admixtures from the Cs Kohn mode (nonzero u_{Cs} and v_{Cs}). (e)–(f) At phase separation $310a_0 \lesssim a_{\mathrm{CsRb}}$ the mode transforms to a Goldstone mode: u_{Rb} and v_{Rb} have the same profile as the $n_{\mathrm{Rb}} = |\phi_{\mathrm{Rb}}|^2$ but with a phase difference. In the plots u's and v's are in units of $a_{\mathrm{osc}}^{-1/2}$.

single-species BEC confined in a double-well potential [44]. Although the the two systems are widely different, there is a common genesis to the softening of the Kohn mode, and that is the partition of the one condensate cloud into two distinct ones. This could be, in our case, by another condensate or by a potential barrier as in Ref. [44].

To examine the mode evolution with the experimentally realized parameters [5], we repeat the computations with $\omega_{\perp(\mathrm{Cs})} = 2\pi \times 40.2$ Hz and $\omega_{\perp(\mathrm{Rb})} = 2\pi \times 32.2$ Hz. With these parameters the system is not strictly quasi-1D as $\hbar\omega_{\perp k} \approx \mu_k$ for $N_{\mathrm{Cs}} = N_{\mathrm{Rb}} = 10^4$, however, as $\omega_{zk} \ll \omega_{\perp k}$ there must be qualitative similarities to a quasi-1D system [36]. Indeed, with the variation of a_{CsRb} the modes evolve similar to the case of $\omega_{\perp k} = 50\omega_{zk}$ and low-lying ωs are shown in Fig. 2(a). The evolution of the Rb Kohn mode functions (u_{Rb} and v_{Rb}) with a_{CsRb} are shown in Fig. 3. It is evident that when $a_{\mathrm{CsRb}} = 0$ [Fig. 3(a)], there is no admixture from the Cs Kohn mode ($u_{\mathrm{Cs}} = v_{\mathrm{Cs}} = 0$). However, when $0 < a_{\mathrm{CsRb}} \lesssim 310a_0$ the admixture from the Cs Kohn mode increases initially and then goes to zero as we approach $U_{\mathrm{CsRb}} > \sqrt{U_{\mathrm{CsCs}}U_{\mathrm{RbRb}}}$ [Figs. 3(b)–3(f)].

One striking result is the Rb Kohn mode after going soft at $a_{\mathrm{CsRb}} \approx 310a_0$, as shown in Fig. 2(a), continues as the third Goldstone mode for $310a_0 < a_{\mathrm{CsRb}}$. This is different from the evolution of the zero energy mode in TBEC with *side-by-side* density profiles. In this case after phase separation, z-parity symmetry of the system is broken and the zero energy mode regains energy. So, there are only two Goldstone modes in the system. This is evident from Fig. 4, where we show the mode evolution of ^{85}Rb-^{87}Rb mixture with *side-by-side* density profiles at phase separation. The parameters of the system considered are $N_{^{85}\mathrm{Rb}} = N_{^{87}\mathrm{Rb}} = 10^2$ with the same ω_{zk} and $\omega_{\perp k}$ as in the Rb-Cs mixture. Here, we use intraspecies scattering lengths as $99a_0$ and $100a_0$ for ^{85}Rb and ^{87}Rb, respectively, and tune the interspecies interaction for better comparison with the Rb-Cs results. This is, however, different from the experimental realization [9], where the intraspecies interaction of ^{85}Rb is varied. A similar result was reported in an earlier work on the quasi-2D system of TBEC [20].

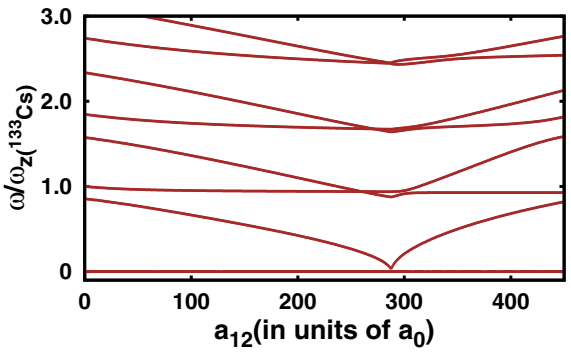

FIG. 4. (Color online) Low-lying modes of ^{85}Rb-^{87}Rb for $N_{^{87}\mathrm{Rb}} = N_{^{85}\mathrm{Rb}} = 10^2$ as a function of $a_{^{85}\mathrm{Rb}^{87}\mathrm{Rb}}$. At phase separation the structure of the density profiles is *side by side* and one of the modes goes soft.

2. *Avoided crossings and quasidegeneracy*

From Fig. 2(a), it is evident that there are several instances of avoided level crossings as a_{CsRb} is varied to higher values. These arise from the changes in the profile of $n_{ck}(z)$, the condensate densities, as the u_k and v_k depend on $n_{ck}(z)$ through the BdG equations. For this reason, the number of avoided crossings is high around the critical value of a_{CsRb}, where there is a significant change in the structure of $n_{ck}(z)$ due to phase separation. Another remarkable feature which emerges when $a_{\text{CsRb}} > 310a_0$ are the avoided crossings involving three modes. As an example, the mode evolution around one such case involving the Kohn mode is shown in Fig. 2(b). Let us, in particular, examine the fifth and sixth modes; the corresponding mode energies in the domain of interest ($309a_0 \leq a_{\text{CsRb}} \leq 321a_0$) are represented by blue colored points in Fig. 2(b). At $a_{\text{CsRb}} = 309a_0$, the sixth mode is the Kohn mode, which is evident from the dipolar structure of the u_k and v_k as shown in Fig. 5(d). The closest approach of the three modes, fourth, fifth, and sixth, occurs when $a_{\text{CsRb}} \approx 311a_0$; at this point the fourth mode is transformed into the Kohn mode. For $a_{\text{CsRb}} > 311a_0$, the fifth and sixth mode energies are quasidegenerate and pushed to higher values. For example, at $a_{\text{CsRb}} = 316a_0$ the energies of the fifth and sixth modes are $1.24\hbar\omega_{z(\text{Cs})}$ and $1.25\hbar\omega_{z(\text{Cs})}$, respectively. However, as shown in Figs. 5(b) and 5(e), the structure of the corresponding u_k and v_k show significant difference. It is evident that for the fifth mode u_{Cs} and u_{Rb} correspond to principal quantum number n equal to 0 and 2, respectively. On the other hand, for the sixth mode both u_{Cs} and u_{Rb} have n equal to 1. At $a_{\text{CsRb}} \approx 320a_0$, the two modes (fifth and sixth) undergo their second avoided crossing with a third mode, the seventh mode. After wards, for $a_{\text{CsRb}} > 320a_0$, the fifth mode remains steady at $1.50\hbar\omega_{z(\text{Cs})}$, and the sixth and seventh are quasidegenerate. To show the transformation of the fifth and sixth modes beyond the second avoided crossing, the u_k and v_k of the modes are shown in Figs. 5(c) and 5(f) for $a_{\text{CsRb}} = 321a_0$. It is evident from the figures that the u_{Cs} and v_{Cs} of the fifth mode undergoes a significant change in the structure: The central dip at $a_{\text{CsRb}} < 321a_0$, visible in Fig. 5(b), is modified to a maxima.

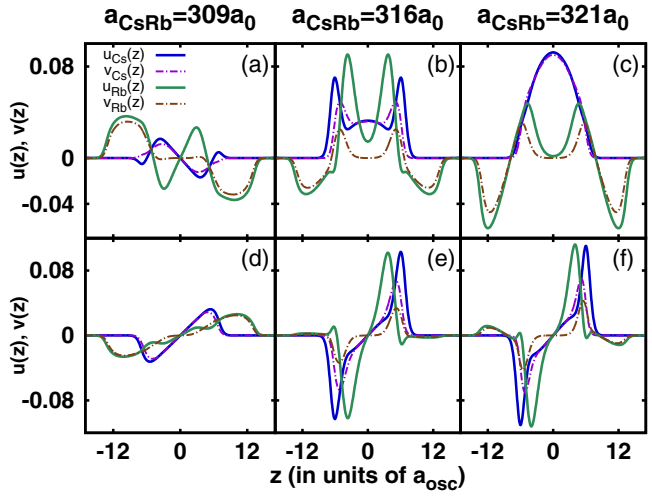

FIG. 5. (Color online) The quasiparticle amplitudes of the fifth and sixth modes at quasidegeneracy. (a)–(c) The quasiparticle amplitudes u_k's and v_k's of the fifth mode for three values of a_{CsRb} represented and marked by blue points and red arrows, respectively, in Fig. 2. (d)–(f) The quasiparticle amplitudes u_k's and v_k's corresponding to the sixth mode for the same values of a_{CsRb}. In the plots u_k's and v_k's are in the units of $a_{\text{osc}}^{-1/2}$.

C. Mode evolution of trapped TBEC at $T \neq 0$

For the $T \neq 0$ calculations, as mentioned earlier, we solve the coupled Eqs. (3) and (4) iteratively until convergence. After each iteration, $\phi_k(z)$'s are renormalized so that

$$\int_{-\infty}^{\infty} \left[|\phi_k(z)|^2 + \tilde{n}_k(z)\right] dz = N_k, \tag{9}$$

where k is either Rb or Cs. To improve convergence, we use successive over-relaxation, but at higher T we face difficulties and require careful choice of the relaxation parameters. For computations, we again consider the trap parameters $\omega_{\perp(\text{Cs})} = 2\pi \times 40.2$ Hz and $\omega_{\perp(\text{Rb})} = 2\pi \times 32.2$ Hz with coinciding trap centers, the number of atoms as $N_{\text{Rb}} = N_{\text{Cs}} = 10^3$ and $a_{\text{CsRb}} = 650a_0$. The evolution of ω (mode frequency) with T is shown in Fig. 6, where the T is in units of T_c, the critical temperature of ideal bosons in quasi-1D harmonic traps defined through the relation $N = (k_{\text{B}}T_c/\hbar\omega_z)\ln(2k_{\text{B}}T_c/\hbar\omega_z)$ [45], where N is the number of atoms. Considering that $\omega_{z(\text{Rb})} < \omega_{z(\text{Cs})}$, the critical temperature of Rb is lower than that of Cs. So, for better description we scale the temperature with respect to the T_c of Rb atoms, and hereafter by T_c we mean the critical temperature of Rb atoms. From the figure, when $T/T_c \geq 0.2$ the Kohn mode energy increases with T/T_c. This is consistent with an earlier work on HFB-Popov studies in a single-species condensate [29], but different from the trend observed in Refs. [27,28]. The increase in Kohn mode energy could arise from an important factor associated with the thermal atoms. In the HFB-Popov formalism the collective modes oscillate in a static thermal cloud background and dynamics of $\tilde{n}_k$ is not taken into account. In TBECs the effects of dynamics of $\tilde{n}_k$ may be larger as $\tilde{n}_k$ is large at the interface. An inclusion of the full dynamics of the thermal cloud in the theory would ensure the Kohn mode energy to be constant at all temperatures [46]. The Goldstone modes, on the other hand, remain steady [29].

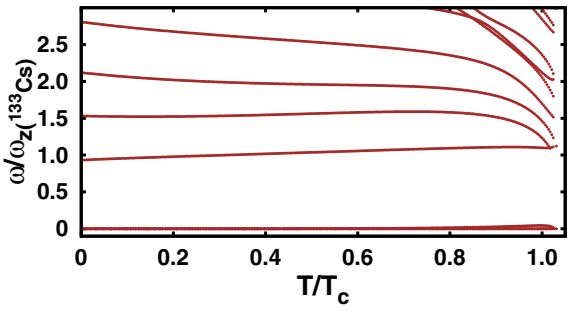

FIG. 6. (Color online) Frequencies (ω_j) of the low-lying modes at $T/T_c \neq 0$. The solid circles (brown) are the excitation energies from the HFB-Popov theory with $N_{\text{Rb}} = N_{\text{Cs}} = 10^3$.

The trend in the evolution of the modes indicates bifurcations at $T/T_c \approx 1$ and is consistent with the theoretical observations in single-species condensates [27–29]. At this temperature, as evident from Fig. 6, the Kohn mode and the mode above it (which has principal quantum number $n = 2$ for both the species) merges. This is one of the bifurcations emerging from the Rb atoms crossing the critical temperature; above this temperature there are no Rb condensates atoms. At $T > T_c$ the Cs condensate density is still nonzero as Cs has higher critical temperature. So, there may be another mode bifurcation at the critical temperature of Cs. A reliable calculation for this would, however, require treating the interaction between thermal Rb atoms and Cs condensate more precisely. For this reason in the present work we do not explore temperature much higher than the T_c of Rb atoms and the possibility of the second mode bifurcation shall be examined in our future works. In the case of single-species calculations, at $T/T_c > 1$ the mode frequencies coalesce to the mode frequencies of the trapping potential. In the present work we limit the calculations to $0 \leq T/T_c \leq 1.1$, so that $T/T_c \ll T_d/T_c$. Here, $T_d \approx (N_{\rm Rb} + N_{\rm Cs})\hbar\omega_z/k_{\rm B}$ is the degeneracy temperature of the system and in the present case $T_d \approx 437$nK. The results for $T/T_c > 0.65$ may have significant errors as the HFB-Popov theory gives accurate results at $T/T_c \leq 0.65$ [28]. We have, however, extended the calculations to $T/T_c > 0.65$ like in Ref. [27] to study the mode bifurcation.

To examine the profiles of n_{ck} and $\tilde{n}_k$, we compute the densities at 25 nK for three cases; these are $N_{\rm Rb} = 840(N_{\rm Cs} = 8570)$, $N_{\rm Rb} = 3680(N_{\rm Cs} = 8510)$, and $N_{\rm Rb} = 15100(N_{\rm Cs} = 6470)$. The same set was used in the previous work of Pattinson *et al.* at $T = 0$ [37] and corresponds to three regimes considered ($N_{\rm Cs} > N_{\rm Rb}$, $N_{\rm Cs} \approx N_{\rm Rb}$, and $N_{\rm Cs} < N_{\rm Rb}$) in the experimental work of McCarron *et al.* [5]. Consider the trap centers, along the z axis, are coincident, then $\tilde{n}_k$ and n_{ck} are symmetric about $z = 0$, and are shown in Figs. 7(a)–7(c). In all the cases, $n_{\rm Cs}$ is at the center. This configuration is energetically preferred as the heavier atomic species at the center has smaller trapping potential energy and lowers the total energy. In the experiments, the trap centers are not exactly coincident. So, to replicate the experimental situation we shift the trap centers, along the z axis, by $0.8a_{\rm osc(Cs)}$ and n are shown in Figs. 7(i)–7(iii). For $N_{\rm Rb} = 840(N_{\rm Cs} = 8570)$ and $N_{\rm Rb} = 3680(N_{\rm Cs} = 8510)$, Figs. 7(i) and 7(ii), the n_{ck} and $\tilde{n}_k$ are located sideways. So, there are only two Goldstone modes in the excitation spectrum. But, for $N_{\rm Rb} = 15100(N_{\rm Cs} = 6470)$, Fig. 7(iii), $n_{\rm Cs}$ is at the center with $n_{\rm Rb}$ at the edges forming *sandwich* geometry and hence has three Goldstone modes. In all the cases $\tilde{n}_k$ have maxima in the neighborhood of the interface and the respective n_{ck}s are not negligible. So, we can expect larger n_{ck}-$\tilde{n}_k$ coupling in TBECs than single-species condensates. For the $N_{\rm Rb} = 3680(N_{\rm Cs} = 8510)$ and $N_{\rm Rb} = 15100(N_{\rm Cs} = 6470)$ cases, n_{ck} are very similar to the results of 3D calculations at $T = 0$ [37]. However, it requires a 3D calculation to reproduce n_{ck} for $N_{\rm Rb} = 840(N_{\rm Cs} = 8570)$ as the relative shift δx is crucial in this case.

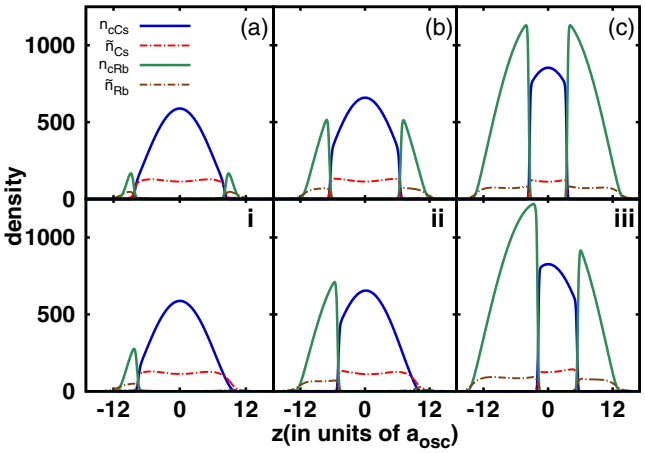

FIG. 7. (Color online) Density profile of n_c and $\tilde{n}$ at 25 nK. (a)–(c) Correspond to $N_{\rm Rb} = 840(N_{\rm Cs} = 8570)$, $N_{\rm Rb} = 3680(N_{\rm Cs} = 8510)$, and $N_{\rm Rb} = 15100(N_{\rm Cs} = 6470)$, respectively, with coincident trap centers. (i)–(iii) Correspond to the same atom numbers as the previous sequence, however, the trap centers are shifted relatively by $0.8a_{\rm osc(Cs)}$. In the plots density is measured in units of $a_{\rm osc}^{-1}$.

IV. CONCLUSIONS

TBECs with strong interspecies repulsion with the *sandwich* density profile at phase separation are equivalent to three coupled condensate fragments. Because of this we observe three Goldstone modes in the system after phase separation. At higher interspecies interactions, we predict avoided crossings involving three modes and followed with the coalescence or quasidegeneracy of two of the participating modes. At $T \neq 0$ there are mode bifurcations close to the $T/T_c \approx 1$.

ACKNOWLEDGMENTS

We thank K. Suthar and S. Chattopadhyay for useful discussions. The results presented in the paper are based on the computations using the 3TFLOP HPC Cluster at Physical Research Laboratory, Ahmedabad, India. We also thank the anonymous referees for their thorough review and valuable comments, which contributed to improving the quality of the manuscript.

[1] T.-L. Ho and V. B. Shenoy, Phys. Rev. Lett. **77**, 3276 (1996).
[2] M. Trippenbach, K. Góral, K. Rzazewski, B. Malomed, and Y. B. Band, J. Phys. B **33**, 4017 (2000).
[3] G. Modugno, M. Modugno, F. Riboli, G. Roati, and M. Inguscio, Phys. Rev. Lett. **89**, 190404 (2002).
[4] A. D. Lercher, T. Takekoshi, M. Debatin, B. Schuster, R. Rameshan, F. Ferlaino, R. Grimm, and H.-C. Nägerl, Europhys. J. D **65**, 3 (2011).
[5] D. J. McCarron, H. W. Cho, D. L. Jenkin, M. P. Köppinger, and S. L. Cornish, Phys. Rev. A **84**, 011603 (2011).

[6] S. Inouye, M. R. Andrews, J. Stenger, H.-J. Miesner, D. M. Stamper-Kurn, and W. Ketterle, Nature (London) **392**, 151 (1998).
[7] D. M. Stamper-Kurn, M. R. Andrews, A. P. Chikkatur, S. Inouye, H.-J. Miesner, J. Stenger, and W. Ketterle, Phys. Rev. Lett. **80**, 2027 (1998).
[8] C. J. Myatt, E. A. Burt, R. W. Ghrist, E. A. Cornell, and C. E. Wieman, Phys. Rev. Lett. **78**, 586 (1997).
[9] S. B. Papp, J. M. Pino, and C. E. Wieman, Phys. Rev. Lett. **101**, 040402 (2008).
[10] S. Tojo, Y. Taguchi, Y. Masuyama, T. Hayashi, H. Saito, and T. Hirano, Phys. Rev. A **82**, 033609 (2010).
[11] S. Gautam and D. Angom, J. Phys. B **44**, 025302 (2011).
[12] K. Sasaki, N. Suzuki, D. Akamatsu, and H. Saito, Phys. Rev. A **80**, 063611 (2009).
[13] S. Gautam and D. Angom, Phys. Rev. A **81**, 053616 (2010).
[14] T. Kadokura, T. Aioi, K. Sasaki, T. Kishimoto, and H. Saito, Phys. Rev. A **85**, 013602 (2012).
[15] S. Stringari, Phys. Rev. Lett. **77**, 2360 (1996).
[16] H. Pu and N. P. Bigelow, Phys. Rev. Lett. **80**, 1134 (1998).
[17] R. Graham and D. Walls, Phys. Rev. A **57**, 484 (1998).
[18] D. Gordon and C. M. Savage, Phys. Rev. A **58**, 1440 (1998).
[19] P. Kuopanportti, J. A. M. Huhtamäki, and M. Möttönen, Phys. Rev. A **85**, 043613 (2012).
[20] C. Ticknor, Phys. Rev. A **88**, 013623 (2013).
[21] H. Takeuchi and K. Kasamatsu, Phys. Rev. A **88**, 043612 (2013).
[22] A. Griffin, Phys. Rev. B **53**, 9341 (1996).
[23] P. Blakie, A. Bradley, M. Davis, R. Ballagh, and C. Gardiner, Adv. Phys. **57**, 363 (2008).
[24] N. P. Proukakis and B. Jackson, J. Phys. B **41**, 203002 (2008).
[25] E. Zaremba, T. Nikuni, and A. Griffin, J. Low Temp. Phys. **116**, 277 (1999).
[26] N. M. Hugenholtz and D. Pines, Phys. Rev. **116**, 489 (1959).
[27] D. A. W. Hutchinson, E. Zaremba, and A. Griffin, Phys. Rev. Lett. **78**, 1842 (1997).
[28] R. J. Dodd, M. Edwards, C. W. Clark, and K. Burnett, Phys. Rev. A **57**, R32 (1998).
[29] C. Gies, B. P. van Zyl, S. A. Morgan, and D. A. W. Hutchinson, Phys. Rev. A **69**, 023616 (2004).
[30] D. S. Jin, M. R. Matthews, J. R. Ensher, C. E. Wieman, and E. A. Cornell, Phys. Rev. Lett. **78**, 764 (1997).
[31] M. O. C. Pires and E. J. V. de Passos, Phys. Rev. A **77**, 033606 (2008).
[32] P. Öhberg and S. Stenholm, Phys. Rev. A **57**, 1272 (1998).
[33] C.-H. Zhang and H. A. Fertig, Phys. Rev. A **75**, 013601 (2007).
[34] P. Öhberg, Phys. Rev. A **61**, 013601 (1999).
[35] D. S. Petrov, G. V. Shlyapnikov, and J. T. M. Walraven, Phys. Rev. Lett. **85**, 3745 (2000).
[36] M. Egorov, B. Opanchuk, P. Drummond, B. V. Hall, P. Hannaford, and A. I. Sidorov, Phys. Rev. A **87**, 053614 (2013).
[37] R. W. Pattinson, T. P. Billam, S. A. Gardiner, D. J. McCarron, H. W. Cho, S. L. Cornish, N. G. Parker, and N. P. Proukakis, Phys. Rev. A **87**, 013625 (2013).
[38] A. Muñoz Mateo and V. Delgado, Phys. Rev. A **77**, 013617 (2008).
[39] A. Muñoz Mateo and V. Delgado, Ann. Phys. **324**, 709 (2009).
[40] E. Anderson, Z. Bai, C. Bischof, S. Blackford, J. Demmel, J. Dongarra, J. D. Croz, A. Greenbaum, S. Hammarling, A. McKenney, and D. Sorensen, LAPACK *Users' Guide*, 3rd ed. (Society for Industrial and Applied Mathematics, Philadelphia, 1999).
[41] P. Muruganandam and S. K. Adhikari, Comput. Phys. Commun. **180**, 1888 (2009).
[42] T. Simula, S. Virtanen, and M. Salomaa, Comput. Phys. Commun. **142**, 396 (2001).
[43] K. Pilch, A. D. Lange, A. Prantner, G. Kerner, F. Ferlaino, H.-C. Nägerl, and R. Grimm, Phys. Rev. A **79**, 042718 (2009).
[44] L. Salasnich, A. Parola, and L. Reatto, Phys. Rev. A **60**, 4171 (1999).
[45] W. Ketterle and N. J. van Druten, Phys. Rev. A **54**, 656 (1996).
[46] D. A. W. Hutchinson, K. Burnett, R. J. Dodd, S. A. Morgan, M. Rusch, E. Zaremba, N. P. Proukakis, M. Edwards, and C. W. Clark, J. Phys. B **33**, 3825 (2000).

Fluctuation- and interaction-induced instability of dark solitons in single and binary condensates

Arko Roy and D. Angom
Physical Research Laboratory, Navrangpura, Ahmedabad-380009, Gujarat, India
(Received 6 June 2014; revised manuscript received 15 July 2014; published 8 August 2014)

We show that the presence of a soliton in a single-species condensate, at zero temperature, enhances the quantum depletion sufficiently enough to induce dynamical instability of the system. We also predict that for two-species condensates, two Goldstone modes emerge in the excitation spectrum at phase separation. Of these, one is due to the presence of the soliton. We use Hartree-Fock-Bogoliubov theory with Popov approximation to examine the mode evolution, and demonstrate that when the anomalous mode collides with a higher energy mode it renders the solitonic state oscillatory unstable. We also report a soliton-induced change in the topology of the density profiles of the two-species condensates at phase separation.

DOI: 10.1103/PhysRevA.90.023612 PACS number(s): 03.75.Mn, 03.75.Hh, 67.85.Bc

I. INTRODUCTION

The experimental realization of single and multicomponent Bose-Einstein condensates (BECs) in atomic gases has opened up the possibility of exploring topological defects. Due to the ubiquitous presence of topological defects in nature, the study of matter-wave excitations such as vortices and solitons in atomic BECs has been a topic of extensive research both experimentally and theoretically over the last few years. In fact, these have attracted much attention as they are created spontaneously during BEC phase transition through the Kibble-Zurek mechanism [1–4]. A soliton, for instance, can be used to probe the phase of the image acquired in a BEC interferometer as proposed by Negretti *et al.* [5,6]. These and other novel phenomena have inspired numerous experiments [7,8] and theoretical studies [9–15] with dark and bright solitons in atomic BECs in a wide range of settings under different scenarios. The experimental observation shows that the notch of the dark soliton gets filled up with thermal atoms over time and the soliton becomes gray, and hence starts oscillating which is either short- or long-lived depending upon the system of interest [16–18].

On the theoretical front, most of the studies on the statics and the dynamics of dark solitons have been carried out in a quasi-one-dimensional (1D) setting at zero temperature where thermal fluctuations can be ignored [19]. There have been several works on the stability of solitons in cigar-shaped double-well potential [20], disordered potential [21], and optical lattice [22–25]. The stability of multiple solitons in a quasi-1D trap has also been examined [26,27]. Quantum depletion in BECs with a soliton at $T = 0$ in weakly interacting Bose gases has also been studied using approximate models [28–34]. This motivated us to reexamine the role of quantum fluctuations in BECs, whether it be with or without solitons. We show that quantum fluctuation in BECs with a soliton is higher than without it. This is due to the presence of the anomalous mode, and we demonstrate that quantum fluctuations can make the dark soliton gray, which as a result becomes dynamically unstable.

The two-component BECs (TBECs), on the other hand, have different ground states depending on the interactions, as compared to a single-component BEC. The most unique aspect of TBECs is the phenomenon of phase separation. Most importantly, in experiments, the TBECs can be steered from a miscible to a phase-separated domain or vice versa through a Feshbach resonance [35,36]. This has motivated numerous theoretical investigations on stationary states [37–39], dynamical instabilities [40–42], and collective excitations [43–47] of TBECs. Furthermore, repulsive TBECs support coupled dark-bright solitons which makes them richer and more interesting than single-component BECs [10]. The bright soliton, on the other hand, cannot survive in single-component BECs with repulsive interaction. It may be mentioned here that, solitons in BECs and TBECs have been experimentally achieved either by a phase-imprinting method [16] or in two counterflowing miscible TBECs above a critical velocity [48]. For miscible TBECs, the creation and interaction of dark solitons has been theoretically examined in Refs. [49,50]. Families of stable solitonic solutions from coupled Gross-Pitaevskii (GP) equations in quasi-1D TBECs at zero temperature have been obtained [51,52].

In the present work, we describe the development of Hartree-Fock-Bogoliubov theory with Popov (HFB-Popov) approximation for trapped TBECs. We use it to examine the evolution of Goldstone modes and mode energies for TBECs with a soliton as a function of interspecies scattering length. Recent works [43–46] have reported the existence of an additional Goldstone mode at phase separation in the symmetry-broken density profiles. We have demonstrated in our earlier work [45] that in the *sandwich-type* density profiles where one of the species is surrounded on both sides by the other, the mode evolves very differently with the appearance of a third Goldstone mode. In the present work, we show that the presence of the soliton introduces an additional Goldstone mode to the system. Even at zero temperature without considering any quantum fluctuation, for a certain range of interspecies scattering length, the TBEC becomes dynamically unstable. The difference in the mass of the two species also plays a significant role in the mode evolution and topology of density profiles.

II. THEORY

A. Single-component BEC

For a quasi-1D system, the trapping frequencies in $V = (1/2)m(\omega_x^2 x^2 + \omega_y^2 y^2 + \omega_z^2 z^2)$ should satisfy the condition $\omega_x = \omega_y = \omega_\perp \gg \omega_z$. The condensate wave function in such a

potential can be integrated out along the xy direction to reduce it to a quasi-1D system. The grand-canonical Hamiltonian, in second quantized form, describing an interacting BEC is then

$$H = \int dz\, \hat{\Psi}^\dagger(z,t)\Big[-\frac{\hbar^2}{2m}\frac{\partial^2}{\partial z^2} + V(z) - \mu + \frac{U}{2}\hat{\Psi}^\dagger(z,t)\hat{\Psi}(z,t)\Big]\hat{\Psi}(z,t), \tag{1}$$

where $\hat{\Psi}$ is the Bose field operator of the single-species BEC, and μ is the chemical potential. The strength of the intraspecies repulsive interactions is $U = (a\lambda)/m$, where $\lambda = (\omega_\perp/\omega_z) \gg 1$ is the anisotropy parameter, a is the s-wave scattering length, and m is the atomic mass of the species. Starting with this Hamiltonian, the equation of motion of the Bose field operator is

$$i\hbar\frac{\partial}{\partial t}\hat{\Psi} = \hat{h}\hat{\Psi} + U\hat{\Psi}^\dagger\hat{\Psi}\hat{\Psi}, \tag{2}$$

where $\hat{h} = (-\hbar^2/2m)\partial^2/\partial z^2 + V(z) - \mu$. For the sake of simplicity of notation, we will refrain from writing the explicit dependence of $\hat{\Psi}$ on z and t. Since a majority of the atoms populate the ground state for the temperature domain pertinent to the experiments ($T \leq 0.65T_c$) [53], the condensate part can be separated out from the Bose field operator $\hat{\Psi}(z,t)$. The noncondensed or the thermal cloud of atoms are then the fluctuations of the condensate field. Here, T_c is the critical temperature of an ideal gas in a harmonic confining potential. Accordingly, we define [54] $\hat{\Psi}(z,t) = \phi(z,t) + \tilde{\psi}(z,t)$, where $\phi(z,t)$ is a c field and represents the condensate, and $\tilde{\psi}(z,t)$ is the fluctuation part. For a single-component BEC, $\hat{\Psi}$ can then be written as

$$\hat{\Psi} = \phi + \tilde{\psi}. \tag{3}$$

Thus for a single species BEC, ϕ is the stationary solution of the generalized GP equation, within the time-independent HFB-Popov approximation, given by

$$\hat{h}\phi + U\,[n_c + 2\tilde{n}]\,\phi = 0. \tag{4}$$

In the above equation, $n_c(z) \equiv |\phi(z)|^2$, $\tilde{n}(z) \equiv \langle\tilde{\psi}^\dagger(z,t)\tilde{\psi}(z,t)\rangle$, and $n(z) = n_c(z) + \tilde{n}(z)$ are the local condensate, noncondensate, and total density, respectively. Using Bogoliubov transformation, the fluctuations are

$$\tilde{\psi}(z,t) = \sum_j [u_j(z)\hat{\alpha}_j(z)e^{-iE_jt} - v_j^*(z)\hat{\alpha}_j^\dagger(z)e^{iE_jt}],$$

$$\tilde{\psi}^\dagger(z,t) = \sum_j [u_j^*(z)\hat{\alpha}_j^\dagger(z)e^{iE_jt} - v_j(z)\hat{\alpha}_j(z)e^{-iE_jt}].$$

Here, $\hat{\alpha}_j$ ($\hat{\alpha}_j^\dagger$) are the quasiparticle annihilation (creation) operators and satisfy the usual Bose commutation relations, and the subscript j represents the energy eigenvalue index. From the above definitions, we get the following Bogoliubov–de Gennes (BdG) equations:

$$(\hat{h} + 2Un)u_j - U\phi^2 v_j = E_j u_j, \tag{5a}$$

$$-(\hat{h} + 2Un)v_j + U\phi^{*2}u_j = E_j v_j. \tag{5b}$$

The number density $\tilde{n}$ of noncondensate particles is then

$$\tilde{n} = \sum_j \{[|u_j|^2 + |v_j|^2]N_0(E_j) + |v_j|^2\}, \tag{6}$$

where $\langle\hat{\alpha}_j^\dagger\hat{\alpha}_j\rangle = (e^{\beta E_j} - 1)^{-1} \equiv N_0(E_j)$ with $\beta = 1/k_BT$ is the Bose factor of the quasiparticle state with energy E_j at temperature T. However, it should be emphasized that, when $T \to 0$, the $N_0(E_j)$'s in Eq. (6) vanish. The noncondensate density is then reduced to

$$\tilde{n} = \sum_j |v_j|^2. \tag{7}$$

Thus, at zero temperature we need to solve the equations self-consistently as the quantum depletion term $|v_j|^2$ in the above equation is nonzero.

B. Harmonic oscillator basis

We solve the quasiparticle amplitudes u_j and v_j in the basis of the harmonic oscillator trapping potential.

$$u_j = \sum_{i=0}^{N_b} p_{ij}\xi_i, \quad v_j = \sum_{i=0}^{N_b} q_{ij}\xi_i, \tag{8}$$

where ξ_i is the ith harmonic oscillator eigenstate and N_b is the number of the basis that is considered. Using this expansion, Eq. (5) is then reduced to a matrix eigenvalue equation and solved using standard matrix diagonalization algorithms. The matrix has a dimension of $2N_b \times 2N_b$, and is non-Hermitian, nonsymmetric, and may have complex eigenvalues. The eigenvalue spectrum obtained from the diagonalization of the matrix has an equal number of positive and negative eigenvalues E_j. In addition, the amount of energy that is carried by the eigenmode j is given by

$$\Delta_j = \int dz(|u_j|^2 - |v_j|^2)E_j. \tag{9}$$

The sign of the quantity Δ_j is known as the *Krein sign*. If this sign turns out to be negative for a mode j, then the corresponding mode is called the *anomalous mode*. It signifies the energetic instability which may be present due to a topological defect in the system.

C. Hartree-Fock basis

To incorporate the interactions present in the system while calculating the Bogoliubov quasiparticle amplitudes u_j and v_j more efficiently, in terms of basis size, we resort to the Hartree-Fock basis. Thus, to solve Eq. (5), we define u_j's and v_j's as a linear combination of *Hartree-Fock basis* functions ζ_k,

$$u_j = \sum_k c_k^j\zeta_k, \quad v_j = \sum_k d_k^j\zeta_k, \tag{10}$$

where c_k and d_k are the coefficients of linear combination. In principle, the GP equation has an infinite number of eigenvalues ϵ_k and eigenvectors ζ_k. In general, Eq. (4) can then be recast into a matrix eigenvalue equation

$$\mathcal{H}\zeta_k = \epsilon_k\zeta_k, \tag{11}$$

where $\mathcal{H} = \hat{h} + U[n_c + 2\tilde{n}]$, and k stands for the eigenvalue index. The eigensolution with the lowest eigenvalue ϵ_0 is referred to as the condensate ground state with the condensate wave function $\phi \equiv \zeta_0$. To calculate the quasiparticle amplitudes u_j and v_j we again expand the eigensolutions ζ_k in terms of ξ_i, then

$$\zeta_k = \sum_i a_i^k \xi_i. \tag{12}$$

Taking the orthogonality and linear independence of ξ_i's into account and plugging Eq. (12) into Eq. (11), one can obtain the expansion coefficients a_k used in decomposing the above equation. This yields a set of basis functions $\{\zeta_k\}$, which is generally referred to as the *Hartree-Fock basis*. The choice of ζ_k reduces the number of basis functions required in the calculation of u_j's and v_j's as ζ_k subsumes the effect of interactions in the system.

D. Two-component BEC

Similarly, for a TBEC in a quasi-1D trapped system,

$$H = \sum_{k=1,2} \int dz\, \hat{\Psi}_k^\dagger(z,t)\Big[-\frac{\hbar^2}{2m_k}\frac{\partial^2}{\partial z^2} + V_k(z) - \mu_k + \frac{U_{kk}}{2}\hat{\Psi}_k^\dagger(z,t)\hat{\Psi}_k(z,t)\Big]\hat{\Psi}_k(z,t) + U_{12}\int dz\, \hat{\Psi}_1^\dagger(z,t)\hat{\Psi}_2^\dagger(z,t)\hat{\Psi}_1(z,t)\hat{\Psi}_2(z,t), \tag{13}$$

where $k = 1,2$ is the species index, $\hat{\Psi}_k$'s are the Bose field operators of the two different species, and μ_k's are the chemical potentials. The strengths of the intra- and interspecies repulsive interactions are $U_{kk} = (a_{kk}\lambda)/m_k$ and $U_{12} = (a_{12}\lambda)/(2m_{12})$, respectively, where $\lambda = (\omega_\perp/\omega_z) \gg 1$ is the anisotropy parameter, a_{kk} is the s-wave scattering length, m_k's are the atomic masses of the species, and $m_{12} = m_1 m_2/(m_1 + m_2)$. Starting with this Hamiltonian, the equation of motion of the Bose field operators is

$$i\hbar\frac{\partial}{\partial t}\begin{pmatrix}\hat{\Psi}_1\\ \hat{\Psi}_2\end{pmatrix} = \begin{pmatrix}\hat{h}_1 + U_{11}\hat{\Psi}_1^\dagger\hat{\Psi}_1 & U_{12}\hat{\Psi}_2^\dagger\hat{\Psi}_1\\ U_{12}\hat{\Psi}_1^\dagger\hat{\Psi}_2 & \hat{h}_2 + U_{22}\hat{\Psi}_2^\dagger\hat{\Psi}_2\end{pmatrix}\begin{pmatrix}\hat{\Psi}_1\\ \hat{\Psi}_2\end{pmatrix},$$

where $\hat{h}_k = (-\hbar^2/2m_k)\partial^2/\partial z^2 + V_k(z) - \mu_k$. In the same way as in the single-species case, we define [54] $\hat{\Psi}(z,t) = \Phi(z) + \tilde{\Psi}(z,t)$, where $\Phi(z)$ is a c field and represents the condensate, and $\tilde{\Psi}(z,t)$ is the fluctuation part. In the two-component representation

$$\begin{pmatrix}\hat{\Psi}_1\\ \hat{\Psi}_2\end{pmatrix} = \begin{pmatrix}\phi_1\\ \phi_2\end{pmatrix} + \begin{pmatrix}\tilde{\psi}_1\\ \tilde{\psi}_2\end{pmatrix}, \tag{14}$$

where $\phi_k(z)$ and $\tilde{\psi}_k(z)$ are the condensate and fluctuation parts of the kth species. Thus for a TBEC, ϕ_k's are the stationary solutions of the coupled generalized GP equations, with time-independent HFB-Popov approximation, given by

$$\hat{h}_1\phi_1 + U_{11}\left[n_{c1} + 2\tilde{n}_1\right]\phi_1 + U_{12}n_2\phi_1 = 0, \tag{15a}$$

$$\hat{h}_2\phi_2 + U_{22}\left[n_{c2} + 2\tilde{n}_2\right]\phi_2 + U_{12}n_1\phi_2 = 0. \tag{15b}$$

In the above equation, $n_{ck}(z) \equiv |\phi_k(z)|^2$, $\tilde{n}_k(z) \equiv \langle\tilde{\psi}_k^\dagger(z,t)\tilde{\psi}_k(z,t)\rangle$, and $n_k(z) = n_{ck}(z) + \tilde{n}_k(z)$ are the local condensate, noncondensate, and total density, respectively. Using Bogoliubov transformation, the fluctuations are

$$\tilde{\psi}_k(z,t) = \sum_j\left[u_{kj}(z)\hat{\alpha}_j(z)e^{-iE_jt} - v_{kj}^*(z)\hat{\alpha}_j^\dagger(z)e^{iE_jt}\right],$$

$$\tilde{\psi}_k^\dagger(z,t) = \sum_j\left[u_{kj}^*(z)\hat{\alpha}_j^\dagger(z)e^{iE_jt} - v_{kj}(z)\hat{\alpha}_j(z)e^{-iE_jt}\right].$$

From this formalism we obtain the following BdG equations:

$$\hat{\mathcal{L}}_1 u_{1j} - U_{11}\phi_1^2 v_{1j} + U_{12}\phi_1(\phi_2^* u_{2j} - \phi_2 v_{2j}) = E_j u_{1j}, \tag{16a}$$

$$\hat{\underline{\mathcal{L}}}_1 v_{1j} + U_{11}\phi_1^{*2}u_{1j} - U_{12}\phi_1^*(\phi_2 v_{2j} - \phi_2^* u_{2j}) = E_j v_{1j}, \tag{16b}$$

$$\hat{\mathcal{L}}_2 u_{2j} - U_{22}\phi_2^2 v_{2j} + U_{12}\phi_2(\phi_1^* u_{1j} - \phi_1 v_{1j}) = E_j u_{2j}, \tag{16c}$$

$$\hat{\underline{\mathcal{L}}}_2 v_{2j} + U_{22}\phi_2^{*2}u_{2j} - U_{12}\phi_2^*(\phi_1 v_{1j} - \phi_1^* u_{1j}) = E_j v_{2j}, \tag{16d}$$

where $\hat{\mathcal{L}}_1 = (\hat{h}_1 + 2U_{11}n_1 + U_{12}n_2)$, $\hat{\mathcal{L}}_2 = (\hat{h}_2 + 2U_{22}n_2 + U_{12}n_1)$, and $\hat{\underline{\mathcal{L}}}_k = -\hat{\mathcal{L}}_k$. The number density $\tilde{n}_k$ of noncondensate particles is then

$$\tilde{n}_k = \sum_j\{[|u_{kj}|^2 + |v_{kj}|^2]N_0(E_j) + |v_{kj}|^2\}. \tag{17}$$

To solve Eq. (16) we define u's and v's as a linear combination of ξ_i's. The equation is then reduced to a matrix eigenvalue equation and solved using standard matrix diagonalization algorithms.

III. THE DARK SOLITON

The location of a dark soliton is a place in a quasi-1D condensate where the condensate wave function $\phi(z)$ changes sign. The condensate wave function then has a kink where the density is zero. Typically, a wave function of the dark soliton is simply proportional to $\tanh[(z - z_0)/\xi]$, where ξ is a local value of the healing length at position z_0 of the soliton. Hereafter, it is to be noted that the symbol ξ without any subscript refers to the healing length. The condensate with a soliton at $z_0 = 0$ is an antisymmetric wave function of z and the phase of the wave function jumps discontinuously by π as z passes through zero. Even at $T = 0$, quantum depletion from the condensate leads to graying of the dark soliton. The kink of the soliton gets filled up with incoherent atoms quantum depleted from the condensate. The soliton is created by employing a phase-imprinting method [16]. We assume that before phase imprinting all the atoms of the system are in symmetric ground state. Right after this operation one gets a condensate with an antisymmetric wave function.

IV. RESULTS AND DISCUSSIONS

A. Numerical details

For studies of single-component BECs at $T = 0$ we solve Eq. (4) neglecting the noncondensate density ($\tilde{n} = 0$) using finite-difference methods, and in particular, we use the split-step Crank-Nicholson method [55]. For TBECs, we proceed in a similar way by solving the pair of coupled Eqs. (15) and setting $\tilde{n}_k = 0$. The method when implemented with imaginary time propagation is appropriate to obtain the stationary ground state wave function of the single-component BEC or TBEC. Furthermore, we use numerical implementation of the phase-imprinting method to generate a dark soliton in the (T)BEC. For this, we begin the simulation with imaginary time propagation of the GP equation and imprint π phase jump corresponding to a soliton at $z_0 = 0$ by using $\phi = |\phi| \exp(i\pi)$. Using this solution of the GPE, and based on Eq. (8), we cast Eq. (5) as a matrix eigenvalue equation in the basis of the trapping potential. The matrix is then diagonalized using the LAPACK routine ZGEEV [56] to find the quasiparticle energies and amplitudes E_j, and u_j's and v_j's, respectively. We begin our $T = 0$ calculations to account for quantum fluctuations with this step. This sets the starting point of the first iteration where the u_j's and v_j's along with positive energy modes E_j are used to get the initial estimate of $\tilde{n}$ through Eq. (6). The ground state wave function ϕ of the BEC and chemical potential μ are again redetermined from Eq. (4), using this updated value of $\tilde{n}$. For calculation of eigenmodes of the TBEC with a soliton, we again cast Eq. (16) as a matrix and diagonalize it [45]. During the calculation of the u_k and v_k, we choose an optimal number of the harmonic oscillator basis functions.

B. Single-species BEC

The low-lying excitation spectrum of a quasi-1D BEC with a soliton is characterized by the presence of an anomalous mode, which indicates that the BEC is in an energetically excited state. This is in addition to the Goldstone and the Kohn modes, which are also present in the excitation spectrum of a quasi-1D BEC without the soliton. The anomalous and Kohn mode energies are real, and the energy of the anomalous mode is $\approx \hbar\omega_z/\sqrt{2}$. A unique feature of the anomalous mode is the negative Krein sign [20,28]. This shows that the solitonic solution of the stationary quasi-1D GP equation is stable. However, when the solution is evolved in imaginary time, with the inclusion of $\tilde{n}$ in the $T = 0$ GP equation, the anomalous mode is transformed into an imaginary energy eigenmode. This is an unambiguous signature of quantum depletion induced instability of the solitonic solution. In other words, the nonzero $\tilde{n}$ arising from the quantum fluctuations within the notch of the soliton turns it gray, and renders the system dynamically unstable. Furthermore, the low-lying energy spectrum is devoid of any negative Krein sign eigenmodes. The anomalous mode, however, reappears in the excitation spectrum on further evolving the system over imaginary time.

To further examine the trend in the evolution of $E_{\rm an}$, the energy of the anomalous mode, or the first excited state, we study the variation of $\tilde{n}$ with time as shown in Fig. 1. The contribution from the anomalous mode fills up the notch of

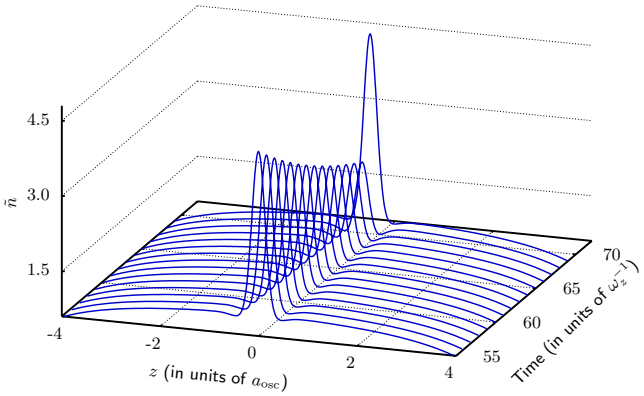

FIG. 1. (Color online) The temporal evolution in the profile of the noncondensate atom density $\tilde{n}$ at $T = 0$ measured in units of $a_{\rm osc}^{-1}$, where $a_{\rm osc} = \sqrt{\hbar/(m\omega_z)}$. The plots show a steady drop in the number of noncondensate atoms until it reaches a threshold value, and then, the anomalous mode reappears in the spectrum. The latter is reflected in the profile of $\tilde{n}$ at $t = 69\omega_z^{-1}$, where it has maximal distribution.

the soliton and $\tilde{n}(0)$ has the largest possible value at the initial state of evolution. At later times, $E_{\rm an}$ is imaginary and $\tilde{n}(0)$ decreases; the trend is as shown in Fig. 1. However, when $\tilde{n}(0)$ reaches a critical value, which in the present work is $\approx 2.312 a_{\rm osc}^{-1}$, it is no longer large enough to render the solitonic solution unstable and the anomalous mode reappears. This confirms $\tilde{n}(0)$ has a threshold value below which the solitonic solution may be stable.

For the limiting case of $a_{\rm RbRb} \to 0$, or the noninteracting limit, the Bogoliubov modes are, to a very good approximation, the eigenstates of the trapping potential. In this limit too, the condensate with the soliton has higher $\tilde{n}$ than the condensate without the soliton. An exponential increase in the total number of noncondensate atoms,

$$\tilde{N} = \int_{-\infty}^{\infty} \tilde{n}\, dz, \tag{18}$$

is observed as $a_{\rm RbRb}$ is increased from near zero to $a_{\rm RbRb} \approx a_0$; this is evident from the inset plot in Fig. 2. However, $\tilde{N}$ increases linearly with a further increase of $a_{\rm RbRb}$ and this is shown in the main plot of Fig. 2. An important observation is that $d\tilde{N}/da_{\rm RbRb} \propto N$ (total number of atoms), which is due to higher repulsive interaction energy with increasing N. This is visible in the family of curves given for different values of N in Fig. 2. It should be emphasized here that an optimal choice of basis size N_b is necessary in all the computations to obtain accurate mode functions and energies. For weakly interacting condensates with a soliton, a basis set consisting of 170 basis functions gives converged and reliable results. But, for the strongly interacting case $1 \ll NU$, the energy eigenvalues E_j do not converge and $\tilde{N}$ diverges as shown by the red solid line in Fig. 2 for $N = 2000$. However, we get converged and reliable results when the basis size is increased to 240 basis functions.

The results that we have presented in this section correspond to a condensate with a soliton at the center of the trap consisting of $N = 2000$ ^{87}Rb atoms whose s-wave scattering length is $a_{11} = a_{\rm RbRb} = 100a_0$, where a_0 is the Bohr radius. The

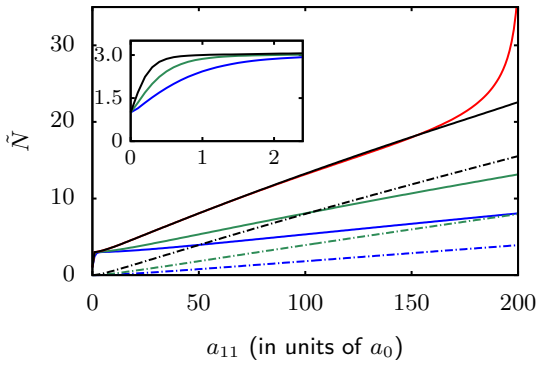

FIG. 2. (Color online) Variation in the total number of noncondensate atoms $\tilde{N}$ at $T = 0$ as a function of the scattering length a_{11}. The solid (dashed) blue, green, and black lines represent $\tilde{N}$ in the presence (absence) of a soliton with a total number of atoms $N =$ 500, 1000, and 2000, respectively. The solid red line represents $\tilde{N}$ in the presence of a soliton for $N = 2000$, with the number of basis $N_b = 170$; it is shown to indicate a lack of accuracy at higher a_{11} with a lower number of basis functions. The inset plots show the trend of $\tilde{N}$ in the neighborhood of $a_{11} \approx 0$, where there is a sharp increase.

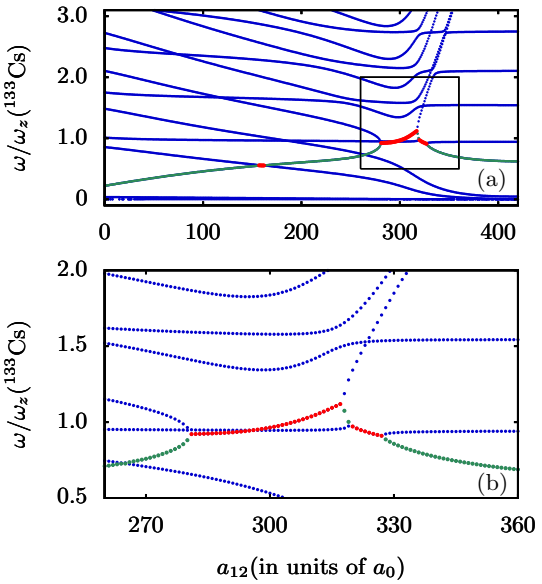

FIG. 3. (Color online) The evolution of the modes as a function of the interspecies scattering length a_{CsRb} in the Rb-Cs TBEC with a soliton. (a) The evolution of the low-lying modes in the domain $0 \le a_{\mathrm{CsRb}} \le 420a_0$ for $N_{\mathrm{Rb}} = N_{\mathrm{Cs}} = 10^3$. (b) The enlarged view of the region enclosed within the black-colored rectangular box in (a) to resolve the mode collisions and bifurcations. The plots show only the real part of mode energies ω/ω_z.

evolution of the low-lying modes is computed for the above-mentioned a_{RbRb} with $\omega_z = 2\pi \times 4.55$ Hz and $\omega_\perp = 20\omega_z$. This choice of parameters is consistent with the experimental setting and satisfies the condition of quasi-1D approximation [17,57,58]. It must be mentioned here that we get almost identical results using either the harmonic oscillator basis or the Hartree-Fock basis. With the latter, in general, we require a smaller basis size. However, for the present work on quasi-1D condensates, the dimension of the BdG matrix is within manageable limits even with the harmonic oscillator basis.

C. Interaction induced instability in TBEC

Dark solitons in one of the components in quasi-1D TBECs, like in single species, are also dynamically unstable at $T = 0$ due to the quantum fluctuations. There is, however, another type of instability associated with dark solitons, and unique to TBECs. It arises from the interspecies interactions, and occurs when an anomalous mode collides with a higher energy mode. The collision transforms the two modes into degenerate complex energy modes, and renders the dark solitonic state unstable. In the present work, we examine the collision of the modes as a function of the interspecies scattering length, and study in detail the nature of these modes and their evolution. Mode collisions of similar nature, giving rise to *oscillatory unstable* states, have been investigated in the context of a single-species cigar-shaped BEC with dark solitons in double-well potentials [20].

In TBECs, phase separation occurs when $U_{12} > \sqrt{U_{11}U_{22}}$. For the present study, we consider Cs and Rb as the first and second species, respectively. With this identification $a_{11} = a_{\mathrm{CsCs}} = 280a_0$ and $a_{22} = a_{\mathrm{RbRb}} = 100a_0$, and arrive at the condition for phase separation $a_{12} = a_{\mathrm{CsRb}} > 261a_0$, which is smaller than the background value of $a_{\mathrm{CsRb}} \approx 650a_0$ [59]. To investigate the mode evolution with solitons, we imprint a soliton onto the first species (Cs condensate) at $z = 0$. We then vary a_{CsRb} from a miscible to an immiscible regime, which is experimentally possible with the Rb-Cs Feshbach resonance [60]. The mode energies E_j are computed at $T = 0$ in steps of increasing a_{CsRb} in the domain $[0,420a_0]$ with $N_{\mathrm{Rb}} = N_{\mathrm{Cs}} = 10^3$, $\omega_{z(\mathrm{Rb})} = 2\pi \times 3.89$ Hz, and $\omega_{z(\mathrm{Cs})} = 2\pi \times 4.55$ Hz as in Refs. [58,61]. To make the system quasi-1D we take $\omega_\perp = 30\omega_z$. The low-lying excitation spectrum is characterized by the presence of an anomalous mode signifying the presence of a soliton. The other two significant low-lying modes, which are also present in quasi-1D TBECs without solitons, are the Goldstone and Kohn modes of the two species.

When $a_{\mathrm{CsRb}} = 0$, the U_{CsRb}-dependent terms in Eq. (16) are zero and the spectrums of the two species are independent as the two condensates are decoupled. The clear separation between the modes of the two species is lost and mode mixing occurs when $a_{\mathrm{CsRb}} > 0$. For instance, the energy of the Cs anomalous mode increases with increasing a_{CsRb}, and collides with the other modes resulting in the generation of a quartet of degenerate complex mode energies. This occurs when a_{CsRb} is in the domains $[157a_0,162a_0]$, $[281a_0,317a_0]$, and $[318a_0,327a_0]$ marked by red dots in Fig. 3. In these domains, the low-lying energy spectrum has no anomalous mode and the system is oscillatory unstable. For $162a_0 < a_{\mathrm{CsRb}} < 281a_0$, the anomalous mode reappears and crosses the fourth excited state at $a_{\mathrm{CsRb}} \approx 264a_0$. Continuing further, as evident from Fig. 3(b), at $a_{\mathrm{CsRb}} \approx 327a_0$ there is a bifurcation after which the anomalous mode ceases to undergo mode collisions.

It should be emphasized here that, with the transition from a miscible to an immiscible regime the Kohn mode and the fourth excited mode go soft. This introduces two new Goldstone modes, including which, there are four Goldstone modes

in the excitation spectrum. These features deserve detailed discussion and are given in the following sections.

1. Mode collisions

From Fig. 3, it is evident that there are several instances of avoided crossings and *mode collisions* when two modes meet as a_{CsRb} is varied to higher values. We have used the latter term (mode collision) to identify the case when one of the two modes is the anomalous mode and when mode collisions do happen, the evolution of the mode energies is different from the avoided crossings. In mode collisions, there are two possible scenarios: either the two modes cross each other or undergo bifurcation. These occur due to the changes in the spatial profile of the mode functions (u_{Rb}, v_{Rb}, u_{Cs}, and v_{Cs}), which in turn depend on the condensate densities $n_{ck}(z)$.

To examine the case of two modes crossing each other during mode collision, consider the anomalous and fourth excited mode in the neighborhood of $a_{\mathrm{CsRb}} = 261a_0$. At values of a_{CsRb} slightly below $261a_0$, the anomalous and the fourth excited modes approach and cross each other at $a_{\mathrm{CsRb}} \approx 261a_0$. In this case, there are no mode mixing pre- and postmode collisions. As shown in Fig. 4(a), the mode functions u_{Rb} and v_{Rb} corresponding to the anomalous mode are zero at $z = 0$, whereas the mode functions u_{Cs} and v_{Cs} have maxima at $z = 0$. In contrast, the fourth excited mode has u_{Cs} and v_{Cs} which are zero at $z = 0$, while u_{Rb} and v_{Rb} have maxima at $z = 0$ as shown in Fig. 4(b). The mode functions thus have very different profiles at $z = 0$ and mode mixing does not occur; instead they just cross through.

Now, let us consider the case of bifurcation at $a_{\mathrm{CsRb}} \approx 279a_0$. For this value of a_{CsRb} the mode functions corresponding to the anomalous mode and the sixth mode have similar profiles with both $u_{\mathrm{Cs}}, v_{\mathrm{Cs}} \neq 0$ at $z = 0$ as shown in Figs. 4(c) and 4(d). These two modes collide and give rise to complex mode energies. A similar trend is also observed at $a_{\mathrm{CsRb}} \approx 157a_0$, when the Cs anomalous mode collides with the Rb Kohn mode. In the domain $157a_0 \leq a_{\mathrm{CsRb}} \leq 162a_0$, the profile of the Rb Kohn mode resembles the structure of the Cs anomalous mode. So that after mode collision, they give rise to complex eigenfrequencies and make the states oscillatory unstable.

2. Third and fourth Goldstone modes

The third Goldstone mode emerges in the excitation spectrum as a_{CsRb} is increased, and the Rb Kohn mode goes soft at phase separation when $a_{\mathrm{CsRb}} \approx 350a_0$. This is consistent with the results reported in our earlier work [45]. The evolution of the Rb Kohn mode functions (u_{Rb} and v_{Rb}) with a_{CsRb} are shown in Fig. 5. It is evident that when $a_{\mathrm{CsRb}} = 0$ [Fig. 5(a)], there is no admixture from the Cs Kohn mode ($u_{\mathrm{Cs}} = v_{\mathrm{Cs}} = 0$). However, when $0 < a_{\mathrm{CsRb}} \lesssim 400a_0$ the admixture from the Cs Kohn mode increases initially, and decreases to zero as we approach $U_{\mathrm{CsRb}} > \sqrt{U_{\mathrm{CsCs}} U_{\mathrm{RbRb}}}$ [Figs. 5(b)–5(f)]. So, the third Goldstone mode is present in the system when $a_{\mathrm{CsRb}} \gtrsim 350a_0$.

The fourth excited mode, unlike in the case of quasi-1D TBECs without a soliton, also goes soft at $a_{\mathrm{CsRb}} \approx 380a_0$. The evolution of the mode functions (u_{Rb} and v_{Rb}) corresponding to the fourth excited mode with a_{CsRb} are shown in Fig. 6. It is noticeable that when $a_{\mathrm{CsRb}} = 0$ [Fig. 6(a)], there is no contribution from the higher energy modes of Cs. However, when $0 < a_{\mathrm{CsRb}}$ the admixture from the third excited mode of the Cs condensate is discernible in the lower values of a_{CsRb} and is shown in Figs. 6(b) and 6(c). At higher values of a_{CsRb}, $261a_0 \lesssim a_{\mathrm{CsRb}} \lesssim 400a_0$, the spatial profiles of the mode functions are different from those of the lower values of a_{CsRb}, and are shown in Figs. 5(d)–5(f). At around $a_{\mathrm{CsRb}} \approx 300a_0$, the mode functions begin to resemble the structure of ϕ_{Rb}, and the transformation is complete at $a_{\mathrm{CsRb}} \approx 380a_0$ when the mode goes soft.

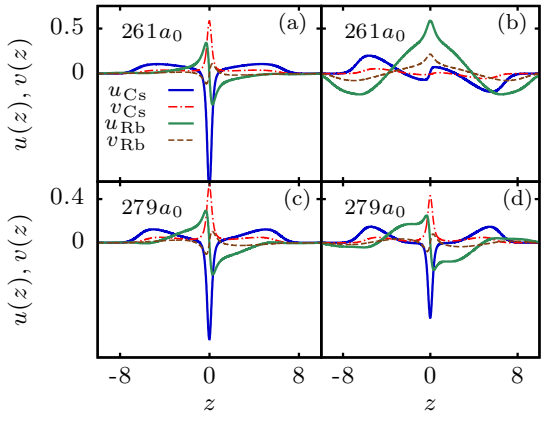

FIG. 4. (Color online) Variation in the nature of mode evolution near mode crossing and collision. (a), (b) Quasiparticle amplitudes corresponding to the anomalous and fourth excited mode, respectively, at $a_{\mathrm{CsRb}} = 261a_0$ when the modes cross each other. (c), (d) Quasiparticle amplitudes corresponding to the anomalous and sixth excited mode, respectively, at $a_{\mathrm{CsRb}} = 279a_0$ when the modes collide. For better visibility u_{Cs} and u_{Rb} are scaled by a factor of 2.5. In the plots u's and v's are in units of $a_{\mathrm{osc}}^{-1/2}$.

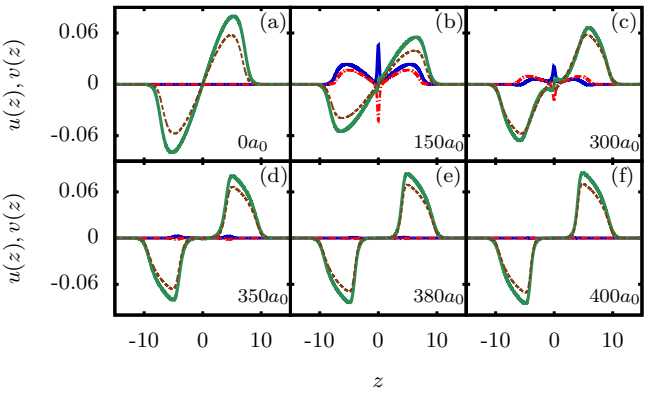

FIG. 5. (Color online) Evolution of quasiparticle amplitudes corresponding to the Rb Kohn mode as a_{CsRb} is increased from 0 to $400a_0$. (a) At $a_{\mathrm{CsRb}} = 0$, it is a Kohn mode of the Rb condensate. (b)–(d) In the domain $0 < a_{\mathrm{CsRb}} \lesssim 350a_0$ the mode acquires admixtures from the Cs Kohn mode (nonzero u_{Cs} and v_{Cs}). (e), (f) At phase separation $310a_0 \lesssim a_{\mathrm{CsRb}}$ the mode transforms to a Goldstone mode: u_{Rb} and v_{Rb} resemble the profile of $n_{\mathrm{Rb}} = |\phi_{\mathrm{Rb}}|^2$ but with a phase difference. In the plots u's and v's are in units of $a_{\mathrm{osc}}^{-1/2}$.

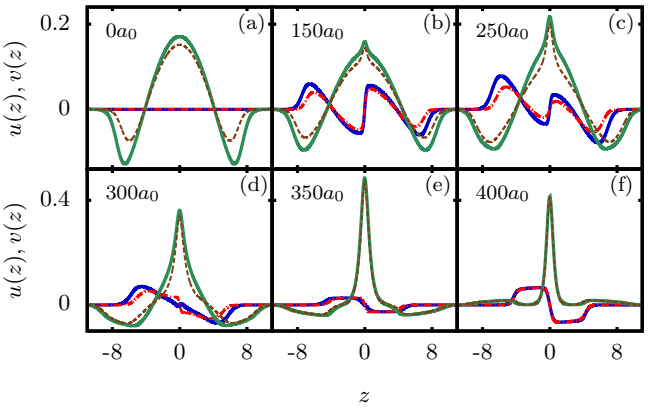

FIG. 6. (Color online) Evolution of the quasiparticle amplitudes corresponding to the fourth excited mode as a_{CsRb} is increased from 0 to $420a_0$. (a) At $a_{\mathrm{CsRb}} = 0$, it is the second excited mode of the Rb condensate. (b)–(d) In the domain $0 < a_{\mathrm{CsRb}} \lesssim 300a_0$ the mode acquires admixtures from the Cs Kohn mode (nonzero u_{Cs} and v_{Cs}). (e), (f) At phase separation $380a_0 \lesssim a_{\mathrm{CsRb}}$ the mode transforms to a Goldstone mode: $u_{\mathrm{Rb}}, v_{\mathrm{Rb}}$ and $u_{\mathrm{Cs}}, v_{\mathrm{Cs}}$ resemble the profile of $n_{\mathrm{Rb}} = |\phi_{\mathrm{Rb}}|^2$ and $n_{\mathrm{Cs}} = |\phi_{\mathrm{Cs}}|^2$ but with a phase difference. In the plots u's and v's are in units of $a_{\mathrm{osc}}^{-1/2}$.

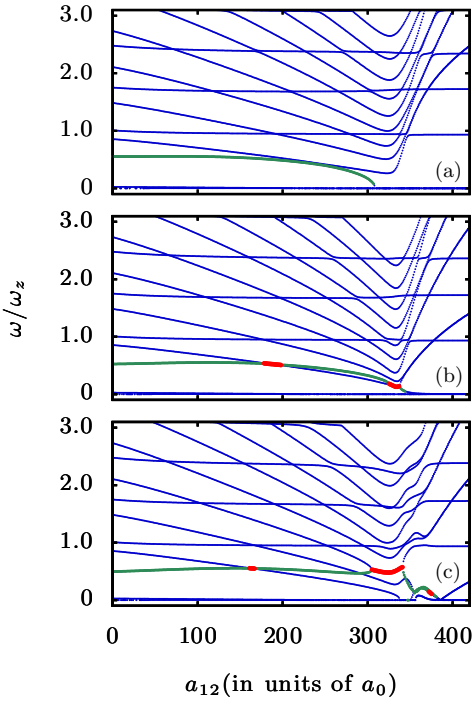

FIG. 7. (Color online) The evolution of the low-lying modes of the TBEC with a soliton for different mass ratios as a function of the interspecies scattering length a_{12} in the domain $0 \le a_{12} \le 420a_0$. The masses of the first and second species in each of the panels correspond to (a) 95 and 87, (b) 100 and 87, and (c) 105 and 87 amu, respectively. The number of atoms in each species is 10^3. The intraspecies scattering lengths of the first and second species are $a_{11} = 280a_0$ and $a_{22} = 100a_0$, respectively. The plots show only the real part of mode energies ω/ω_z.

D. Different mass ratios

To gain insight into the complex nature of the mode evolution in the Rb-Cs TBEC, we study the interplay of mass difference and intraspecies scattering lengths. For the set of aforementioned parameters the ground state of the TBEC after phase separation is of *sandwich* geometry, in which the species with the heavier mass (Cs) is at the center and flanked by the species with lighter mass (Rb) at the edges [61], albeit $a_{\mathrm{CsCs}} \gg a_{\mathrm{RbRb}}$. This geometry minimizes the trapping potential energy, and hence the total energy of the system. In contrast, for TBECs with $m_1 \approx m_2$, at phase separation, the species with the smaller intraspecies scattering length is surrounded by the other species. In this case the mode evolution in the presence of a soliton is devoid of any *mode collisions*. Thus, we attribute the pattern of mode collisions in the Rb-Cs TBEC binary condensate with a soliton to the interplay between mass difference and intraspecies scattering lengths.

To understand the transition in the mode evolution from $m_1 \approx m_2$ to a case similar to the Rb-Cs TBEC, we consider a test case where 87 amu $\le m_1 \le$ 125 amu and fix $m_2 = m_{\mathrm{Rb}}$. We then compute the evolution of the modes as a function of the interspecies scattering length as we increase m_1 from 87 amu to 125 amu in steps of 2 amu. For example, the mode evolution for three different values of m_1 (95, 100, and 105 amu) are shown in Fig. 7. From Fig. 7(a) it is evident that at $m_1 =$ 95 amu the anomalous mode goes soft at phase separation and becomes the third Goldstone mode of the system without any mode collisions. At $a_{12} \approx 300a_0$, the two species are partially miscible and the notch of n_1 at $z = 0$ due to the soliton is filled with the second species. For higher values of $a_{12} \approx 340a_0$, the energetically favorable state is of a *sandwich geometry* where the species with the heavier mass ($m_1 = 95$ amu) is at the edge of the trap and the species with lower mass ($m_2 = 87$ amu) occupies the center. It should, however be recalled here that $a_{11} > a_{22}$.

There is a major change in the nature of mode evolution, as shown in Fig. 7(b) for $m_1 = 100$: The anomalous mode collides with the second excited mode twice at $a_{12} \approx 180a_0$ and $320a_0$. The emergence of a bifurcation is evident in the second mode collision at $a_{12} \approx 320a_0$. On further increase of m_1, as shown in Fig. 7(c) for $m_1 = 105$, the trend of the mode collision begins to resemble that of the Rb-Cs mixture. In this case, the bifurcation arising from the collision between the anomalous and sixth excited mode is quite evident. Coming to the topology of the density profiles, prior to phase separation ($a_{12} \approx 300a_0$) n_1 and n_2 overlap with each other and the notch of the soliton is filled by the second species. At still higher values of a_{12}, n_2 from the edges migrates towards the notch of the soliton and the soliton gets topologically deformed. This is the energetically favorable density configuration. At $a_{12} \approx 380a_0$, the migration is complete and n_2 occupies the center of the trap and is surrounded by n_1 and the system is then phase separated. Here, it must be mentioned that without the soliton the density profile would be opposite: condensates with masses m_1 and m_2 occupy the center and edges, respectively. Thus, the presence of the soliton induces a change in the topology of the density profiles in TBECs. On further increase of m_1, the

energy of the anomalous mode increases with increasing a_{12} and the collision with the sixth mode occurs at higher energies.

V. CONCLUSIONS

In conclusion, we have examined the stability of solitons in single and two-component BECs. We have predicted that at zero temperature the presence of a soliton enhances the quantum depletion and fills up the notch of the soliton which makes it oscillatory unstable. In TBECs having a dark soliton with strong interspecies interaction, four Goldstone modes emerge in the excitation spectrum. We have also predicted that the TBECs with a soliton in one of the components oscillate while interacting even at zero temperature. This is due to the nonzero density of the other species within the notch of the dark soliton. We have also shown a soliton-induced change in the density profiles when the atomic masses of the two species differ widely. Based on a series of computations, we find an enhancement in the mass ratio at which the heavier species, with higher scattering length, occupies the central position at phase separation.

ACKNOWLEDGMENTS

We thank K. Suthar, S. Chattopadhyay, and S. Gautam for useful discussions. The results presented in the paper are based on the computations using the 3TFLOP HPC Cluster at Physical Research Laboratory, Ahmedabad, India. We also thank the anonymous referee for the thorough review and valuable comments, which contributed to improving the quality of the manuscript.

[1] W. H. Zurek, Nature (London) **317**, 505 (1985).
[2] W. H. Zurek, Phys. Rev. Lett. **102**, 105702 (2009).
[3] B. Damski and W. H. Zurek, Phys. Rev. Lett. **104**, 160404 (2010).
[4] G. Lamporesi, S. Donadello, S. Serafini, F. Dalfovo, and G. Ferrari, Nat. Phys. **9**, 656 (2013).
[5] A. Negretti and C. Henkel, J. Phys. B **37**, L385 (2004).
[6] A. Negretti, C. Henkel, and K. Mølmer, Phys. Rev. A **78**, 023630 (2008).
[7] S. Burger, K. Bongs, S. Dettmer, W. Ertmer, K. Sengstock, A. Sanpera, G. V. Shlyapnikov, and M. Lewenstein, Phys. Rev. Lett. **83**, 5198 (1999).
[8] J. Denschlag, J. E. Simsarian, D. L. Feder, C. W. Clark, L. A. Collins, J. Cubizolles, L. Deng, E. W. Hagley, K. Helmerson, W. P. Reinhardt, S. L. Rolston, B. I. Schneider, and W. D. Phillips, Science **287**, 97 (2000).
[9] Th. Busch and J. R. Anglin, Phys. Rev. Lett. **84**, 2298 (2000).
[10] Th. Busch and J. R. Anglin, Phys. Rev. Lett. **87**, 010401 (2001).
[11] S. Middelkamp, J. J. Chang, C. Hamner, R. Carretero-González, P. G. Kevrekidis, V. Achilleos, D. J. Frantzeskakis, P. Schmelcher, and P. Engels, Phys. Lett. A **375**, 642 (2011).
[12] M. A. Hoefer, J. J. Chang, C. Hamner, and P. Engels, Phys. Rev. A **84**, 041605 (2011).
[13] K. Kasamatsu and M. Tsubota, Phys. Rev. A **74**, 013617 (2006).
[14] S. Rajendran, P. Muruganandam, and M. Lakshmanan, J. Phys. B **42**, 145307 (2009).
[15] V. Achilleos, D. Yan, P. G. Kevrekidis, and D. J. Frantzeskakis, New J. Phys. **14**, 055006 (2012).
[16] C. Becker, S. Stellmer, P. Soltan-Panahi, S. Dorscher, M. Baumert, E.-M. Richter, J. Kronjager, K. Bongs, and K. Sengstock, Nat. Phys. **4**, 496 (2008).
[17] A. Weller, J. P. Ronzheimer, C. Gross, J. Esteve, M. K. Oberthaler, D. J. Frantzeskakis, G. Theocharis, and P. G. Kevrekidis, Phys. Rev. Lett. **101**, 130401 (2008).
[18] S. Stellmer, C. Becker, P. Soltan-Panahi, E.-M. Richter, S. Dörscher, M. Baumert, J. Kronjäger, K. Bongs, and K. Sengstock, Phys. Rev. Lett. **101**, 120406 (2008).
[19] A. E. Muryshev, H. B. van Linden van den Heuvell, and G. V. Shlayapnikov, Phys. Rev. A **60**, R2665(R) (1999).
[20] S. Middelkamp, G. Theocharis, P. G. Kevrekidis, D. J. Frantzeskakis, and P. Schmelcher, Phys. Rev. A **81**, 053618 (2010).
[21] M. Mochol, M. Płodzień, and K. Sacha, Phys. Rev. A **85**, 023627 (2012).
[22] P. G. Kevrekidis, R. Carretero-González, G. Theocharis, D. J. Frantzeskakis, and B. A. Malomed, Phys. Rev. A **68**, 035602 (2003).
[23] N. G. Parker, N. P. Proukakis, C. F. Barenghi, and C. S. Adams, J. Phys. B **37**, S175 (2004).
[24] H. Sakaguchi and B. A. Malomed, Phys. Rev. E **72**, 046610 (2005).
[25] Y. V. Kartashov, B. A. Malomed, and L. Torner, Rev. Mod. Phys. **83**, 247 (2011).
[26] R. Atre, P. K. Panigrahi, and G. S. Agarwal, Phys. Rev. E **73**, 056611 (2006).
[27] G. Theocharis, A. Weller, J. P. Ronzheimer, C. Gross, M. K. Oberthaler, P. G. Kevrekidis, and D. J. Frantzeskakis, Phys. Rev. A **81**, 063604 (2010).
[28] J. Dziarmaga and K. Sacha, Phys. Rev. A **66**, 043620 (2002).
[29] J. Dziarmaga, Z. P. Karkuszewski, and K. Sacha, Phys. Rev. A **66**, 043615 (2002).
[30] J. Dziarmaga and K. Sacha, Phys. Rev. A **67**, 033608 (2003).
[31] J. Dziarmaga, Z. P. Karkuszewski, and K. Sacha, J. Phys. B **36**, 1217 (2003).
[32] C. K. Law, P. T. Leung, and M.-C. Chu, J. Phys. B **35**, 3583 (2002).
[33] C. K. Law, Phys. Rev. A **68**, 015602 (2003).
[34] D. M. Gangardt and A. Kamenev, Phys. Rev. Lett. **104**, 190402 (2010).
[35] S. B. Papp, J. M. Pino, and C. E. Wieman, Phys. Rev. Lett. **101**, 040402 (2008).
[36] S. Tojo, Y. Taguchi, Y. Masuyama, T. Hayashi, H. Saito, and T. Hirano, Phys. Rev. A **82**, 033609 (2010).
[37] T.-L. Ho and V. B. Shenoy, Phys. Rev. Lett. **77**, 3276 (1996).
[38] S. Gautam and D. Angom, J. Phys. B **43**, 095302 (2010).
[39] S. Gautam and D. Angom, J. Phys. B **44**, 025302 (2011).
[40] K. Sasaki, N. Suzuki, D. Akamatsu, and H. Saito, Phys. Rev. A **80**, 063611 (2009).
[41] S. Gautam and D. Angom, Phys. Rev. A **81**, 053616 (2010).

[42] T. Kadokura, T. Aioi, K. Sasaki, T. Kishimoto, and H. Saito, Phys. Rev. A **85**, 013602 (2012).
[43] H. Takeuchi and K. Kasamatsu, Phys. Rev. A **88**, 043612 (2013).
[44] C. Ticknor, Phys. Rev. A **88**, 013623 (2013).
[45] A. Roy, S. Gautam, and D. Angom, Phys. Rev. A **89**, 013617 (2014).
[46] C. Ticknor, Phys. Rev. A **89**, 053601 (2014).
[47] P. Mason and S. A. Gardiner, Phys. Rev. A **89**, 043617 (2014).
[48] C. Hamner, J. J. Chang, P. Engels, and M. A. Hoefer, Phys. Rev. Lett. **106**, 065302 (2011).
[49] P. Öhberg and L. Santos, J. Phys. B **34**, 4721 (2001).
[50] P. Öhberg and L. Santos, Phys. Rev. Lett. **86**, 2918 (2001).
[51] P. G. Kevrekidis, H. E. Nistazakis, D. J. Frantzeskakis, B. A. Malomed, and R. Carretero-González, Eur. Phys. J. D **28**, 181 (2004).
[52] D. Schumayer and B. Apagyi, Phys. Rev. A **69**, 043620 (2004).
[53] R. J. Dodd, M. Edwards, C. W. Clark, and K. Burnett, Phys. Rev. A **57**, R32 (1998).
[54] A. Griffin, Phys. Rev. B **53**, 9341 (1996).
[55] P. Muruganandam and S. K. Adhikari, Comput. Phys. Commun. **180**, 1888 (2009).
[56] E. Anderson, Z. Bai, C. Bischof, S. Blackford, J. Demmel, J. Dongarra, J. D. Croz, A. Greenbaum, S. Hammarling, A. McKenney, and D. Sorensen, *LAPACK Users' Guide*, 3rd ed. (Society for Industrial and Applied Mathematics, Philadelphia, PA, 1999).
[57] A. Görlitz, J. M. Vogels, A. E. Leanhardt, C. Raman, T. L. Gustavson, J. R. Abo-Shaeer, A. P. Chikkatur, S. Gupta, S. Inouye, T. Rosenband, and W. Ketterle, Phys. Rev. Lett. **87**, 130402 (2001).
[58] R. W. Pattinson, T. P. Billam, S. A. Gardiner, D. J. McCarron, H. W. Cho, S. L. Cornish, N. G. Parker, and N. P. Proukakis, Phys. Rev. A **87**, 013625 (2013).
[59] A. Lercher, T. Takekoshi, M. Debatin, B. Schuster, R. Rameshan, F. Ferlaino, R. Grimm, and H.-C. Nägerl, Eur. Phys. J. D **65**, 3 (2011).
[60] K. Pilch, A. D. Lange, A. Prantner, G. Kerner, F. Ferlaino, H.-C. Nägerl, and R. Grimm, Phys. Rev. A **79**, 042718 (2009).
[61] D. J. McCarron, H. W. Cho, D. L. Jenkin, M. P. Köppinger, and S. L. Cornish, Phys. Rev. A **84**, 011603 (2011).

PHYSICAL REVIEW A **92**, 011601(R) (2015)

Thermal suppression of phase separation in condensate mixtures

Arko Roy[1,2] and D. Angom[1]
[1]*Physical Research Laboratory, Navrangpura, Ahmedabad 380009, Gujarat, India*
[2]*Indian Institute of Technology, Gandhinagar, Ahmedabad 382424, Gujarat, India*
(Received 9 February 2015; published 6 July 2015)

We examine the role of thermal fluctuations in binary condensate mixtures of dilute atomic gases. In particular, we use the Hartree-Fock-Bogoliubov theory with the Popov approximation to probe the impact of noncondensate atoms to the phenomenon of phase separation in two-component Bose-Einstein condensates. We demonstrate that, in comparison to $T = 0$, there is a suppression in the phase separation of the binary condensates at $T \neq 0$. This arises from the interaction of the condensate atoms with the thermal cloud. We also show that, when $T \neq 0$, it is possible to distinguish the phase-separated case from the miscible from the trends in the correlation function. However, this is not the case at $T = 0$.

DOI: 10.1103/PhysRevA.92.011601 PACS number(s): 03.75.Hh, 67.60.Bc, 03.75.Mn, 67.85.Bc

Phase separation in a two-component fluid is ubiquitous in nature, and the transition from a miscible to immiscible phase is a quintessential example of critical phenomena. One classic example is a temperature-driven phase separation in the cyclohexane-aniline mixture [1]. It is then natural to ask, what are the similarities and differences in the binary mixtures of quantum fluids? Recent experimental advances in binary Bose-Einstein condensates (BECs) of dilute atomic gases provide an ideal testbed to address such a question. In the case of binary mixtures of BECs or two-species BECs (TBECs), tuning the interaction through Feshbach resonances [2,3] can render it miscible or immiscible. Using improved experimental techniques, over the last decade, TBECs have been achieved in mixtures of two different alkali-metal atoms [4–8], or two different isotopes [2,9,10] and atoms of the same element in different hyperfine states [11–14]. The remarkable feature of phase separation in TBECs has been successfully observed in ^{85}Rb - ^{87}Rb [9,10] and ^{87}Rb - ^{133}Cs [7] condensate mixtures.

The criterion for phase separation, derived from the Thomas-Fermi (TF) approximation at zero temperature [15], is that the intraspecies (U_{11},U_{22}) and interspecies interaction (U_{12}) strengths must satisfy the inequality $U_{12}^2 > U_{11}U_{22}$. However, experiments are conducted at finite temperatures, and, therefore, deviations from the criterion are to be expected. Theoretical studies on the effects of thermal clouds on phase separation have been carried out for homogeneous binary Bose gases using Hartree-Fock theory [16] and a large-N approximation [17]. The phase separation of trapped binary mixtures at finite temperatures has also been examined using the local-density approximation [18]. In this Rapid Communication we address this issue by using the Hartree-Fock-Bogoliubov theory with the Popov approximation (HFB-Popov) [19] to account for the thermal fluctuations. It is a gapless formalism satisfying the Hugenholtz-Pines theorem [20] and can be employed to compute the energy eigenspectra of the quasiparticle excitations of the condensates.

The method has been validated extensively in single-species BECs, and we have used it in our recent works to examine the effect of quantum fluctuations in TBECs [21]. In the present work, we systematically study the role of thermal fluctuations in the phenomenon of phase separation in trapped TBECs. Our studies reveal that at $T \neq 0$, the constituent species in the TBEC undergo phase separation at a higher U_{12} than the value predicted based on the TF approximation at $T = 0$. Consistent with experimental observations of a dual-species condensate of ^{87}Rb and ^{133}Cs [7], our theoretical investigations show that even when the phase-separation condition is met, there is a sizable overlap between the two species. We attribute this to the presence of a thermal cloud, which has a profound effect on the miscibility-immiscibility transition. At $T = 0$, the TBECs are coherent throughout the spatial extent of the condensate, however, when $T \neq 0$, coherence decays and is reflected in the correlation function. This implies that at $T = 0$, the miscible or immiscible phases are indistinguishable from the trends in the correlation function. But, for $T \neq 0$, the miscible-immiscible transition and the associated changes in the density profiles have a characteristic signature in the form of correlation functions. There is a smooth crossover between correlation functions when the transition occurs. Interspecies Feshbach resonances of ultracold bosons have been experimentally demonstrated for Na-Rb [22], K-Rb [23], and Cs-Rb [24] mixtures, but a Bose-condensed mixture of Na-Rb is yet to observed experimentally. The Cs-Rb condensate mixture is a stepping stone towards the production of a quantum gas of dipolar RbCs molecules, as, unlike the KRb molecule, the rovibrational ground state of the RbCs molecule is stable against an exchange of atoms. Considering this, we focus our study on the finite-temperature effects in the Cs-Rb condensate mixture. Other than tuning the interspecies, it is also possible to steer the condensate mixture through the miscible-immiscible transition using intraspecies Feshbach resonance. An example is the tuning of the intraspecies interaction of ^{85}Rb in ^{85}Rb - ^{87}Rb [9,10], and for this system, too, we have examined the suppression of phase separation at $T \neq 0$ [25]. It must be emphasized that, as the background scattering length of ^{85}Rb is negative, it is possible to obtain ^{85}Rb BECs [26] only with the use of the Feshbach resonance [27].

Theory. We consider a cigar-shaped TBEC, where the frequencies of the harmonic trapping potential satisfy the condition $\omega_\perp \gg \omega_z$ with $\omega_x = \omega_y = \omega_\perp$. In this case, the radial excitation energies are large and assume the radial degrees of freedom are frozen for which $\hbar\omega_\perp \gg \mu_k$. So, the dynamics and hence the excitations occur only along the axial direction, z axis, of the trap. In the mean-field regime, using the HFB-Popov approximation [21,28], a pair of coupled generalized one-dimensional (1D) Gross-Pitaevskii

(GP) equations describe the dynamics and density distributions of the TBEC. The combined form of the equations is

$$\hat{h}_k\phi_k + U_{kk}[n_{ck} + 2\tilde{n}_k]\phi_k + U_{12}n_{3-k}\phi_k = 0, \quad (1)$$

where $\hat{h}_k = (-\hbar^2/2m_k)\partial^2/\partial z^2 + V_k(z) - \mu_k$ is the one-body part of the Hamiltonian, with $k = 1,2$ as the species label. The strengths of the coupling constants are given by $U_{kk} = (a_{kk}\lambda)/m_k$ and $U_{12} = (a_{12}\lambda)/(2m_{12})$, where, for cigar-shaped traps, $\lambda = \omega_\perp/\omega_z \gg 1$. Without loss of generality, for stable configurations, the intraspecies scattering lengths a_{kk} and the interspecies scattering length a_{12} are considered as positive (repulsive). Under the HFB approximation, the Bose field operators are decomposed as $\hat{\Psi}_k = \phi_k + \tilde{\psi}_k$, where the ϕ_k's are the stationary solutions of Eq. (1) obtained by evolving the solution in imaginary time, with $n_{ck}(z) \equiv |\phi_k(z)|^2$. The field operator $\tilde{\psi}_k(z)$ represents the fluctuation part of $\hat{\Psi}_k(z)$, and it incorporates both quantum and thermal fluctuations. The fluctuation operators, both quantum and thermal, are functions of the elementary excitations of the system, which solve the coupled Bogoliubov–de Gennes equations,

$$\hat{\mathcal{L}}_1 u_{1j} - U_{11}\phi_1^2 v_{1j} + U_{12}\phi_1(\phi_2^* u_{2j} - \phi_2 v_{2j}) = E_j u_{1j}, \quad (2a)$$

$$\hat{\underline{\mathcal{L}}}_1 v_{1j} + U_{11}\phi_1^{*2} u_{1j} - U_{12}\phi_1^*(\phi_2 v_{2j} - \phi_2^* u_{2j}) = E_j v_{1j}, \quad (2b)$$

$$\hat{\mathcal{L}}_2 u_{2j} - U_{22}\phi_2^2 v_{2j} + U_{12}\phi_2(\phi_1^* u_{1j} - \phi_1 v_{1j}) = E_j u_{2j}, \quad (2c)$$

$$\hat{\underline{\mathcal{L}}}_2 v_{2j} + U_{22}\phi_2^{*2} u_{2j} - U_{12}\phi_2^*(\phi_1 v_{1j} - \phi_1^* u_{1j}) = E_j v_{2j}, \quad (2d)$$

where $\hat{\mathcal{L}}_1 = (\hat{h}_1 + 2U_{11}n_1 + U_{12}n_2)$, $\hat{\mathcal{L}}_2 = (\hat{h}_2 + 2U_{22}n_2 + U_{12}n_1)$, and $\hat{\underline{\mathcal{L}}}_k = -\hat{\mathcal{L}}_k$. Here, u_{kj}'s and v_{kj}'s are the Bogoliubov quasiparticle amplitudes corresponding to the jth energy eigenvalue. The quantities $\tilde{n}_k(z) \equiv \langle\tilde{\psi}_k^\dagger(z,t)\tilde{\psi}_k(z,t)\rangle$ and $n_k(z) = n_{ck}(z) + \tilde{n}_k(z)$ are defined as noncondensate and total density, respectively. To solve the above eigenvalue equations, the u_{kj}'s and v_{kj}'s are decomposed into a linear combination of harmonic oscillator eigenstates. The order parameters ϕ_k's and the noncondensate densities $\tilde{n}_k$'s are then the self-consistent solutions of the coupled Eqs. (1) and (2). The thermal components, in terms of the quasiparticle amplitudes, are

$$\tilde{n}_k = \sum_j \left\{[|u_{kj}|^2 + |v_{kj}|^2]N_0(E_j) + |v_{kj}|^2\right\}, \quad (3)$$

where $N_0(E_j) = (e^{\beta E_j} - 1)^{-1}$ with $\beta = 1/(k_B T)$ is the Bose factor of the jth quasiparticle mode at temperature T. More detailed descriptions of the decomposition and derivation of the relevant equations are given elsewhere [25]. In this Rapid Communication we examine the role of temperature in the phase separation of TBECs. For this, a measure of phase separation is the overlap integral,

$$\Lambda = \frac{[\int n_1(z)n_2(z)dz]^2}{[\int n_1^2(z)dz][\int n_2^2(z)dz]}. \quad (4)$$

The miscible phase is when $\Lambda = 1$ and signifies a complete overlap of the two species, whereas the binary condensate is completely phase separated when $\Lambda = 0$ [29].

In terms of the Bose field operator $\hat{\Psi}_k$, the normalized first-order or the off-diagonal correlation function, which is also a measure of the phase fluctuations, is

$$g_k^{(1)}(z,z') = \frac{\langle\hat{\Psi}_k^\dagger(z)\hat{\Psi}_k(z')\rangle}{\sqrt{\langle\hat{\Psi}_k^\dagger(z)\hat{\Psi}_k(z)\rangle\langle\hat{\Psi}_k^\dagger(z')\hat{\Psi}_k(z')\rangle}}. \quad (5)$$

It can also be expressed in terms of off-diagonal condensate and noncondensate densities as

$$g_k^{(1)}(z,z') = \frac{n_{ck}(z,z') + \tilde{n}_k(z,z')}{\sqrt{n_k(z)n_k(z')}}, \quad (6)$$

where

$$n_{ck}(z,z') = \phi_k^*(z)\phi_k(z'),$$

$$\tilde{n}_k(z,z') = \sum_j \{[u_{kj}^*(z)u_{kj}(z') + v_{kj}^*(z)v_{kj}(z')]N_0(E_j) + v_{kj}^*(z)v_{kj}(z')\}.$$

At $T = 0$, when the entire system is coherent and characterized by the presence of a condensate only, then $g_k^{(1)} = 1$ within the extent of the condensate, whether it is in the miscible or in the immiscible regime. So, one cannot distinguish between the two phases from the nature of the correlation functions of the individual species. However, at $T \neq 0$, a clear signature of a miscible-immiscible transition of the density profiles is reflected in the form of correlation functions.

The thermal suppression of phase separation is generic to any binary condensate mixture. However, for comparison with experimental realizations, we consider the ^{133}Cs - ^{87}Rb BEC mixture with ^{133}Cs labeled as species 1 and ^{87}Rb as species 2. Hereafter, for brevity, we drop the mass numbers and write these as Cs and Rb. The intraspecies scattering lengths are $a_{11} = a_{Cs} = 280a_0$ and $a_{22} = a_{Rb} = 100a_0$, the interspecies scattering length is $a_{12} = a_{CsRb} = 295a_0$ with $N_{Cs} = N_{Rb} = 5 \times 10^3$, and a_0 is the Bohr radius. To form a quasi-1D trap we take $\omega_{z(Cs)} = 2\pi \times 4.55$ Hz and $\omega_{z(Rb)} = 2\pi \times 3.89$ Hz; $\omega_{\perp(Cs)} = 50\omega_{z(Cs)}$ and $\omega_{\perp(Rb)} = 50\omega_{z(Rb)}$. For this value of $\omega_\perp$, the temperature along the radial direction is $\hbar\omega_\perp/k_B \approx 11$ nK, and the tight confinement condition is valid as $\mu_k/\hbar\omega_\perp \approx 10^{-2}$. In addition to this, the healing length $\xi_k \gg 1/n_k$. Thus the system is in the weakly interacting TF regime [30] and the mean-field description through the GP equation is valid. For this parameter set, the ground-state density distribution is phase separated with species 1 at the center and surrounded by species 2 at the edges. We refer to this configuration of density profiles as a *sandwich* type. This choice of parameters is consistent with the experimental parameters of a recent work on quasi-1D TBECs of different hyperfine states of ^{87}Rb [31], in which the dynamical evolution of mixtures of quantum gases has been observed. It should be emphasized here that *sandwich*-type density profiles are applicable only to trapped systems. In uniform systems, at phase separation, the energetically preferred states are the symmetry-broken density profiles, where one species is entirely to the left and the other is entirely to the right. We refer to this configuration of density profiles as a *side-by-side* type. In the present work, we demonstrate the role of thermal clouds in *sandwich*-type density profiles since these are unique to trapped systems and are experimentally pertinent. For homogeneous binary condensates, using a periodic boundary condition with $\omega_z = 0$ in our computations, we do get side-by-side density profiles at

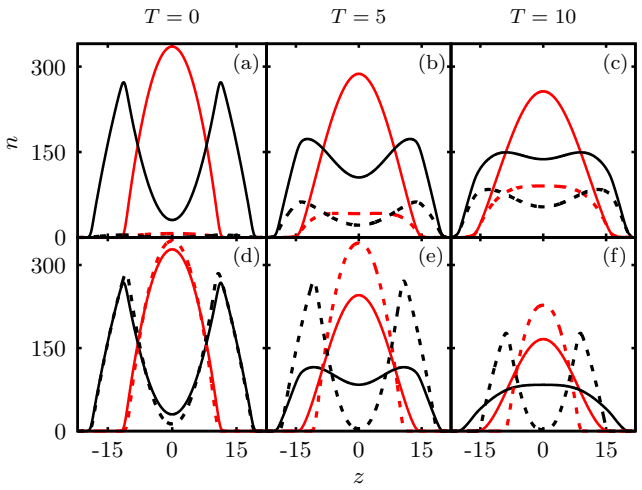

FIG. 1. (Color online) The suppression of phase separation in ^{87}Rb - ^{133}Cs TBECs at $a_{12} = 295a_0$. (a)–(c) The solid and dashed red (black) lines represent $n_{\rm Cs}(n_{\rm Rb})$ and $\tilde{n}_{\rm Cs}(\tilde{n}_{\rm Rb})$, respectively, at $T = 0$, 5, and 10 nK. (d)–(f) The solid red (black) lines represent $n_{c\rm Cs}(n_{c\rm Rb})$ at $T = 0$, 5, and 10 nK, respectively. The dashed red (black) lines $n_{c\rm Cs}(n_{c\rm Rb})$ at $T = 0$ with the same number of condensate atoms at $T = 0$, 5, and 10 nK, respectively. Here, n and z are measured in units of $a_{\rm osc}^{-1}$ and $a_{\rm osc}$, respectively.

phase separation. As an example, the density profiles are shown in Ref. [25], and these are consistent with the results reported in previous works [32]. In the computations, the spatial and temporal variables are scaled as $z/a_{\rm osc(Cs)}$ and $\omega_{z(\rm Cs)}t$ to render the equations dimensionless.

At $T = 0$, in TBECs, as mentioned earlier, the criterion for phase separation is $U_{12} > \sqrt{U_{11}U_{22}}$. With the parameters of Cs-Rb TBECs, consider keeping $a_{\rm Cs}$ and $a_{\rm Rb}$ fixed, but varying $a_{12} = a_{\rm CsRb}$ through a magnetic Feshbach resonance [24]. The condition for phase separation, using the TF approximation, is then $a_{12} > 261a_0$. When $a_{12} = 0$, the TBEC is noninteracting and the two species are completely miscible, in which case $\Lambda = 1$. On increasing a_{12}, the extent of overlap between the two species decreases, and hence Λ decreases. For instance, at $a_{12} = 50a_0$, $\Lambda = 0.97$, and it decreases monotonically with $\Lambda \to 0$ at complete phase separation. At $a_{12} = 295a_0$, just at the onset of phase separation, $\Lambda = 0.14$. As shown in Fig. 1(a), the density profiles corresponding to the two species have an interfacial overlap, and the interaction parameters satisfy the phase-separation condition. Furthermore, at phase separation, $n_{c\rm Cs}(0)$ is maximum, whereas $n_{c\rm Rb}(0) \approx 0$ and the species do not have significant overlap. In other words, Cs at the center of the trap is flanked by Rb at the edges and $\Lambda \approx 10^{-1}$. It is also to be mentioned here that for phase separation, there is a considerable difference between the values of a_{12} derived from the TF approximation and the numerical solution of the GP equation. This can be attributed to large gradients in condensate densities, which are ignored in the TF approximation.

Suppression of phase segregation. For $T \neq 0$, the Bose factor $N_0 \neq 0$, so in addition to the quantum fluctuations, the noncondensate densities $\tilde{n}_k$ have contributions from the thermal cloud as well. The condensate atoms n_{ck} then interact with $\tilde{n}_k$ of both species, and modify n_{ck} of both species. For illustration, at $T = 5$ nK and $a_{12} = 295a_0$, the total and noncondensate density profiles are shown in Fig. 1(b). Compared to the density profiles in Fig. 1(a), there is a remarkable change in $n_{c\rm Rb}$ as a result of the finite temperature: $n_{c\rm Rb}(0) > 0$. Thus, keeping all the parameters the same, but taking $T = 5$ nK, the two species have substantial overlap, as shown in Fig. 1(b), and Λ becomes $\approx$0.55. In other words, the finite temperature transforms the phase-separated TBECs at $T = 0$ to a partially miscible phase. The degree of overlap increases with temperature, and at $T = 10$ nK, the TBEC is miscible as $\Lambda \approx 0.77$. Thus, with an increase in temperature, the density of the thermal cloud increases and the *phase separation is suppressed*. This is evident from Fig. 1(c), which shows the plots of the corresponding total and noncondensate density profiles. Thus, a_{12} has to be greater than $295a_0$ at $T \neq 0$ for phase separation to occur. To confirm that the suppression is a consequence of nonzero temperature, we identify and compute the number of condensate atoms in each species, and use these numbers for $T = 0$ computations. Despite the difference in the numbers of atoms, from the plots in Figs. 1(d)–1(f), the TBEC retains the immiscible profiles at zero temperature. This implies that without the thermal cloud, there are no deviations from the usual phase-separation condition. For comparison, plots of n_{ck} from the finite-temperature cases are also shown in the figure.

To investigate the spatial coherence at equilibrium, we examine the nature of the first-order correlation function $g_k^{(1)}(z,z')$ as defined in Eq. (6). As expected, the profile of $g_k^{(1)}(z,z')$ depends on the interplay between the interaction strength and temperature. As stated earlier, at $T = 0$, there is perfect coherence in the Cs-Rb TBEC and $g^{(1)}_{\rm Cs/Rb}(0,z) = 1$ within the spatial extent of the condensates. This is independent of whether the TBEC is in the miscible or immiscible regime. For simplicity and based on the symmetry of the system, we consider $g^{(1)}_{\rm Cs/Rb}(0,z)$ with $z \geq 0$, and plots at different temperatures are shown in Fig. 2. At $T = 0$ the form of the $g^{(1)}_{\rm Cs/Rb}(0,z)$ remains unchanged as the system undergoes a dramatic transition from the miscible to immiscible phase. This is evident from the plot in Fig. 2(a). However, when $T \neq 0$, unlike the zero-temperature case, $g^{(1)}_{\rm Cs/Rb}(0,z)$ is maximum at $z = 0$ and decays to zero with z. This is due to the noncondensate atoms, which modify the nature of

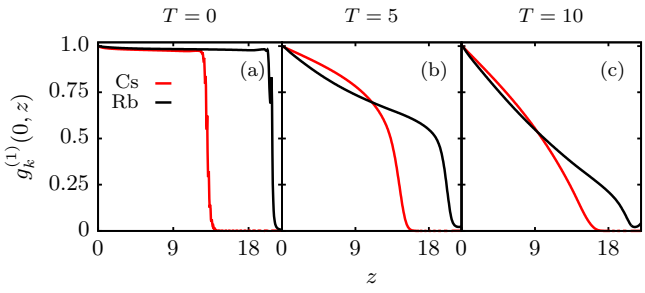

FIG. 2. (Color online) (a)–(c) The first-order spatial correlation function, $g^{(1)}_{\rm Cs/Rb}(0,z)$ with $z \geq 0$, of ^{87}Rb - ^{133}Cs TBECs at equilibrium for $a_{12} = 295a_0$ at $T = 0$, 5, and 10 nK, respectively. Here, z is measured in units of $a_{\rm osc}$.

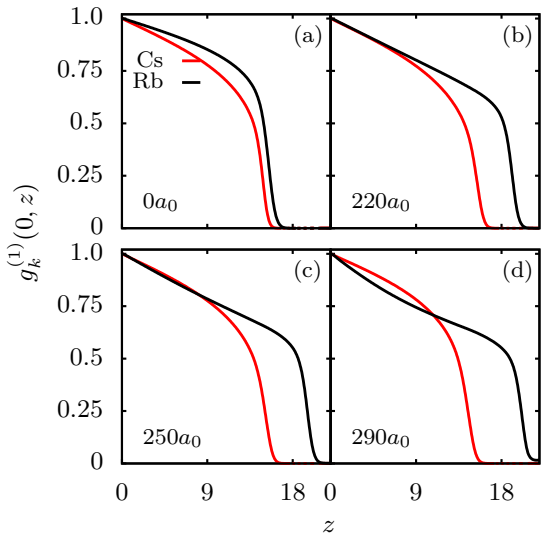

FIG. 3. (Color online) (a)–(d) The first-order spatial correlation function, $g^{(1)}_{\mathrm{Cs/Rb}}(0,z)$ with $z \geq 0$, of ^{87}Rb - ^{133}Cs TBECs at equilibrium at $T = 5$ nK for $a_{12} = 0,220,250,290a_0$, respectively. Here, z is measured in units of a_{osc}.

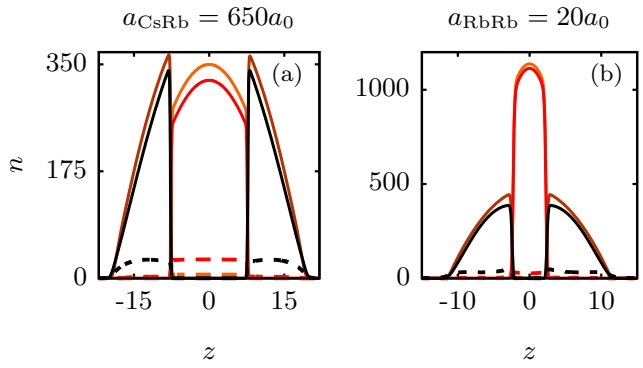

FIG. 4. (Color online) Density profiles showing complete phase separation at $T = 0$ and 10 nK. (a) Phase separation in ^{87}Rb - ^{133}Cs TBECs for $a_{12} = 650a_0$. The solid and dashed orange (brown) lines represent $n_{c\mathrm{Cs}}(n_{c\mathrm{Rb}})$ and $\tilde{n}_{c\mathrm{Cs}}(\tilde{n}_{c\mathrm{Rb}})$, respectively, at $T = 0$. The solid and dashed red (black) lines represent $n_{c\mathrm{Cs}}(n_{c\mathrm{Rb}})$ and $\tilde{n}_{c\mathrm{Cs}}(\tilde{n}_{c\mathrm{Rb}})$, respectively, at $T = 10$ nK. (b) Phase separation in ^{85}Rb - ^{87}Rb TBECs for $a_{12} = 20a_0$. The solid and dashed orange (brown) lines represent n_c and $\tilde{n}$ of ^{85}Rb (^{87}Rb), respectively, at $T = 0$. The solid and dashed red (black) lines represent n_c and $\tilde{n}$ of ^{85}Rb (^{87}Rb), respectively, at $T = 10$ nK. Here, n and z are measured in units of a_{osc}^{-1} and a_{osc}, respectively.

coherence in the system. The rate of decay of the $g^{(1)}_{\mathrm{Cs/Rb}}(0,z)$ increases with temperature, and this is evident from the plots of $g^{(1)}_{\mathrm{Cs/Rb}}(0,z)$ at $T = 5$ and 10 nK, as shown in Figs. 2(b) and 2(c), for $a_{12} = 295a_0$. We also observe a dramatic variation in $g^{(1)}_{\mathrm{Cs/Rb}}(0,z)$ at fixed temperature, but the value of a_{12} is steered from the miscible to immiscible regime. At the outset, when the TBEC is miscible at $a_{12} = 0$, $g^{(1)}_{\mathrm{Rb}}(0,z)$ decays to 0 at a larger distance than $g^{(1)}_{\mathrm{Cs}}(0,z)$, as shown in Fig. 3(a). This is because n_{Rb} has a larger spatial extent than n_{Cs}. As a_{12} is increased, the TBEC undergoes a phase transition from the miscible to sandwich-type density profile. Along with this, the distance at which $g^{(1)}_{\mathrm{Rb}}(0,z)$ falls off to zero increases with an increase in a_{12}. On the contrary, the distance at which $g^{(1)}_{\mathrm{Cs}}(0,z)$ falls off to zero decreases with an increase in a_{12}. This causes the $g^{(1)}_k(0,z)$ of the individual species to cross each other at a certain z_0. At z_0, the two species have equal $g^{(1)}_{\mathrm{Cs/Rb}}(0,z_0)$, and this is a characteristic signature of the immiscible phase. These features are shown in Figs. 3(b)–3(d). It deserves to be mentioned here that z_0 increases, and $g^{(1)}_{\mathrm{Cs/Rb}}(0,z_0)$ decreases with an increase in a_{12}. In addition, there is a dramatic difference in the decay rates of $g^{(1)}_{\mathrm{Cs/Rb}}(0,z_0)$; it is much faster in Cs. This is attributed to the fact that both $n_{c\mathrm{Rb}}$ and $\tilde{n}_{\mathrm{Rb}}$ increase along z within the bulk of the Cs-Rb TBECs, whereas in Cs, around the origin, $n_{c\mathrm{Cs}}$ decreases but $\tilde{n}_{\mathrm{Cs}}$ increases. This trend is similar to a single-species Cs condensate. The presence of Rb does not affect the nature of $g^{(1)}_{\mathrm{Cs}}(0,z)$ in Cs-Rb TBECs. Around the point of phase separation, $n_{c\mathrm{Rb}}(0)$ in a Cs-Rb TBEC is distinctly different from a single-species Rb condensate, and so is the nature of $g^{(1)}_{\mathrm{Rb}}(0,z)$ [25].

Segregation independent of temperature. In the domain of large a_{12}, $U_{12} \gg \sqrt{U_{11}U_{22}}$, $\Lambda \approx 0$, and the phase segregation is more prominent. However, due to the geometry of the TBEC, the mean-field approximation is still valid. In this domain the interfacial overlap is minimal and the TBECs assume a sandwich-type density profile. The system is then equivalent to three coupled condensate fragments, and, as a result, the Bogoliubov analysis shows the presence of three Goldstone modes [28]. For the Cs-Rb TBECs considered here, the background interspecies scattering length $a_{\mathrm{CsRb}} = 650a_0$ satisfies the above condition. With this value of a_{12}, at $T = 0$, as shown in Fig. 4(a), the Cs condensate lies at the center of the trap and the Rb condensate at the edges. So, at the center, $n_{\mathrm{Rb}}(0) = 0$ and $n_{\mathrm{Cs}}(0)$ is maximum. With an increase in a_{12}, there is a decrease in the number of noncondensate atoms arising from quantum fluctuations. This is a manifestation of a smaller overlap between the condensates at the interfaces. On the contrary, for a single-species BEC, with an increase in the intraspecies interaction strength, the number of noncondensate atoms due to quantum fluctuations increases [21]. When $T \neq 0$, the thermal density $\tilde{n}_k$ interacts with the condensate clouds through intraspecies and interspecies interactions. But, due to the large a_{12}, the interspecies interaction energy is much larger than the intraspecies interaction energy. This makes $n_{\mathrm{Rb}}(0) \approx 0$, and there is little overlap of the thermal cloud of one species with the condensate of the other species, such that $\Lambda < 0.1$. Thus, there is *no thermal suppression* in the domain of large a_{12}. We observe similar results in the case of ^{85}Rb - ^{87}Rb TBECs as well, where the intraspecies interaction of ^{85}Rb is decreased to obtain completely phase-separated density profiles. These are shown in Fig. 4(b).

Conclusions. At finite temperatures, to examine the properties of binary condensates in the neighborhood of phase separation, it is essential to incorporate the thermal component. In general, there is a delay or suppression of phase separation due to the thermal component, and we have examined this in detail with the Cs-Rb binary condensate as an example. In this system, the transition is driven by tuning the interspecies interaction, and similar results are obtained in the ^{85}Rb - ^{87}Rb binary condensate, where tuning the intraspecies interaction

of ^{85}Rb induces the transition. The binary condensate mixtures of dilute atomic gases are different from the classical binary fluids which undergo a miscible-immiscible transition with temperature as the control parameter. First, the variation of temperature in TBECs is applicable only below the lower of the two critical temperatures. Second, each species has two subcomponents, the condensate and noncondensate atoms. The condensate or the superfluid components are coherent, but the noncondensate components are incoherent and are similar to the normal gas. Third, there are spatial density variations of all the components due to the nature of the confining potential and diluteness of the atomic gas. Fourth, beyond a certain critical value of interaction strength or in the $U_{12} \gg \sqrt{U_{11}U_{22}}$ domain, temperature does not alter the density profiles. Finally, the transition to the phase-separated domain at finite temperatures is associated with a distinct change in the profile of the correlation function. Our results provide an explanation of the experimentally observed density profiles at phase separation [7]. Even when the phase-separation condition is satisfied, there is a finite overlap between the two species at finite temperature which is due to the presence of a thermal cloud. Our findings clearly demonstrate the dominance of thermal fluctuations over quantum fluctuations, which causes the suppression of phase segregation in TBEC experiments.

We thank K. Suthar, S. Chattopadhyay, and S. Gautam for useful discussions. The results presented here are based on the computations using the 3TFLOP HPC Cluster at the Physical Research Laboratory, Ahmedabad, India.

[1] H. Stanley, *Introduction to Phase Transitions and Critical Phenomena*, International Series of Monographs on Physics (Oxford University Press, Oxford, UK, 1971).
[2] S. Inouye, M. R. Andrews, J. Stenger, H.-J. Miesner, D. M. Stamper-Kurn, and W. Ketterle, Nature (London) **392**, 151 (1998).
[3] C. Chin, R. Grimm, P. Julienne, and E. Tiesinga, Rev. Mod. Phys. **82**, 1225 (2010).
[4] G. Modugno, M. Modugno, F. Riboli, G. Roati, and M. Inguscio, Phys. Rev. Lett. **89**, 190404 (2002).
[5] G. Thalhammer, G. Barontini, L. De Sarlo, J. Catani, F. Minardi, and M. Inguscio, Phys. Rev. Lett. **100**, 210402 (2008).
[6] A. Lercher, T. Takekoshi, M. Debatin, B. Schuster, R. Rameshan, F. Ferlaino, R. Grimm, and H.-C. Nägerl, Eur. Phys. J. D **65**, 3 (2011).
[7] D. J. McCarron, H. W. Cho, D. L. Jenkin, M. P. Köppinger, and S. L. Cornish, Phys. Rev. A **84**, 011603 (2011).
[8] B. Pasquiou, A. Bayerle, S. M. Tzanova, S. Stellmer, J. Szczepkowski, M. Parigger, R. Grimm, and F. Schreck, Phys. Rev. A **88**, 023601 (2013).
[9] S. B. Papp, J. M. Pino, and C. E. Wieman, Phys. Rev. Lett. **101**, 040402 (2008).
[10] S. Tojo, Y. Taguchi, Y. Masuyama, T. Hayashi, H. Saito, and T. Hirano, Phys. Rev. A **82**, 033609 (2010).
[11] D. M. Stamper-Kurn, M. R. Andrews, A. P. Chikkatur, S. Inouye, H.-J. Miesner, J. Stenger, and W. Ketterle, Phys. Rev. Lett. **80**, 2027 (1998).
[12] J. Stenger, S. Inouye, D. M. Stamper-Kurn, H.-J. Miesner, A. P. Chikkatur, and W. Ketterle, Nature (London) **396**, 345 (1998).
[13] C. J. Myatt, E. A. Burt, R. W. Ghrist, E. A. Cornell, and C. E. Wieman, Phys. Rev. Lett. **78**, 586 (1997).
[14] L. E. Sadler, J. M. Higbie, S. R. Leslie, M. Vengalattore, and D. M. Stamper-Kurn, Nature (London) **443**, 312 (2006).
[15] C. Pethick and H. Smith, *Bose-Einstein Condensation in Dilute Gases* (Cambridge University Press, New York, 2008).
[16] B. V. Schaeybroeck, Physica A **392**, 3806 (2013).
[17] C.-C. Chien, F. Cooper, and E. Timmermans, Phys. Rev. A **86**, 023634 (2012).
[18] H. Shi, W.-M. Zheng, and S.-T. Chui, Phys. Rev. A **61**, 063613 (2000).
[19] A. Griffin, Phys. Rev. B **53**, 9341 (1996).
[20] N. M. Hugenholtz and D. Pines, Phys. Rev. **116**, 489 (1959).
[21] A. Roy and D. Angom, Phys. Rev. A **90**, 023612 (2014).
[22] F. Wang, D. Xiong, X. Li, D. Wang, and E. Tiemann, Phys. Rev. A **87**, 050702 (2013).
[23] A. Simoni, F. Ferlaino, G. Roati, G. Modugno, and M. Inguscio, Phys. Rev. Lett. **90**, 163202 (2003).
[24] K. Pilch, A. D. Lange, A. Prantner, G. Kerner, F. Ferlaino, H.-C. Nägerl, and R. Grimm, Phys. Rev. A **79**, 042718 (2009).
[25] See Supplemental Material at http://link.aps.org/supplemental/10.1103/PhysRevA.92.011601 for details.
[26] S. L. Cornish, N. R. Claussen, J. L. Roberts, E. A. Cornell, and C. E. Wieman, Phys. Rev. Lett. **85**, 1795 (2000).
[27] J. L. Roberts, N. R. Claussen, J. P. Burke, C. H. Greene, E. A. Cornell, and C. E. Wieman, Phys. Rev. Lett. **81**, 5109 (1998).
[28] A. Roy, S. Gautam, and D. Angom, Phys. Rev. A **89**, 013617 (2014).
[29] P. Jain and M. Boninsegni, Phys. Rev. A **83**, 023602 (2011).
[30] D. S. Petrov, G. V. Shlyapnikov, and J. T. M. Walraven, Phys. Rev. Lett. **85**, 3745 (2000).
[31] S. De, D. L. Campbell, R. M. Price, A. Putra, B. M. Anderson, and I. B. Spielman, Phys. Rev. A **89**, 033631 (2014).
[32] B. Van Schaeybroeck, Phys. Rev. A **78**, 023624 (2008).